Politecnico di Torino

ScuDo
Scuola di Dottorato ~ Doctoral School
WHAT YOU ARE, TAKES YOU FAR

Doctoral Dissertation
Doctoral Program in Energy Engineering (36^{th}cycle)

Development of a High-Order Finite Volume code for turbomachinery applications

By

Nicola Rosafio

******

Supervisor(s):
Prof. D.A. Misul, Supervisor

Doctoral Examination Committee:
Prof. S. Ravelli, Referee, University of Bergamo
Prof. M. Manna, Referee, University of Naples
Prof. M. Marconcini, University of Florence
Dr./Eng. P. Adami, GE Aerospace
Prof. D. Simoni, University of Genoa

Politecnico di Torino
2024

Declaration

I hereby declare that, the contents and organization of this dissertation constitute my own original work and does not compromise in any way the rights of third parties, including those relating to the security of personal data.

Nicola Rosafio
2024

* This dissertation is presented in partial fulfillment of the requirements for **Ph.D. degree** in the Graduate School of Politecnico di Torino (ScuDo).

Dedicated to my family, my girlfriend, my friends and all those who supported me throughout the path.

Abstract

Numerical simulations are of vital importance to the development of turbomachinery components. While experimental investigations serve as main contributors to the analysis of the performance of turbomachines, the presence of challenging conditions during testing, such as high temperatures, high-Reynolds number and strong compressibility effects, make the exploration of large design spaces almost prohibitive. Moreover, a certain level of uncertainty still exists due to the presence of measuring devices, which inherently represent a disturb for the incoming flow, especially in high-speed regions, along with underlying assumptions necessary to obtain derived quantities. For these reasons, fostered by increasing computational resources, a numerical approach needs to work in conjunction with experimental investigations, allowing for initial assessments of design features, along with providing insights into local flow features which cannot be directly measured. In the present work of thesis, the development of a high-order Finite-Volume code for turbomachinery applications is detailed. The work starts from an existing solver developed at the University of Florence, which has been largely revisited to implement state of the art modeling and solution strategies, which are of interest for the study of turbomachinery components. The first part of the thesis reviews the original solution strategy of the code HybFlow, addressing some inherent weaknesses reported by its developers. In the second chapter of the thesis, the implementation of a parallel linear solver is detailed, focusing on the analysis of two different preconditioners to allow the speed-up of the nonlinear convergence for steady-state problems. In particular, three different linear solution algorithms are compared for laminar and turbulent computations: an Algrebraic Multigrid preconditioned GMRES, an ILU preconditioned GMRES and the point/block implicit solver LU-SSOR.
In the third chapter of the thesis, the extension of the code to higher-order reconstruction methods is detailed and assessed over both reference test-cases and turbomachinery simulations. Two different reconstruction methods are compared.

The first method is based on a Least-Square reconstruction, where flow gradients and high-order derivatives are computed all together, while guaranteeing the preservation of variables mean value. The second method is based on a Successive Correction, where high-order derivatives are computed from lower-order ones over a compact reconstruction stencil.
The last chapter of the thesis addresses the application of the solver to a new open-source low-pressure turbine blade test case, studied in the framework of European project SPLEEN. The chapter details two-dimensional, three-dimensional and unsteady characterization of the cascade.

Eventually, some open points of the current implementation will be discussed, along with the strategies for further advancements of the code performance and capabilities, in view of its application towards high-fidelity simulations.

Contents

List of Figures

List of Tables

Nomenclature

Greek Letters

β	Flow angle
δ	Kronecher delta
ε	Generic increment
γ	Specific heat ratio
λ	Jacobian matrix eigenvalue
μ	Molecular viscosity
ν	Kinematic viscosity
Ω	Rotational speed (Vorticity)
ω	Relaxation factor (Total pressure loss coefficient)
Φ	Generic quantity (Gradient limiter)
ρ	Density
τ	Shear stress (numerical time)
ξ	Kinetic energy loss coefficient

Symbols

AMG	Algebraic Multigrid
C	True chord

C_D Dissipation coefficient

C_f Skin friction coefficient

$C_{\omega s}$ Streamwise vorticity coefficient

C_{ax} Axial chord

CD Drag coefficient

CD_f Friction drag coefficient

CD_p Pressure drag coefficient

CFL Courant-Friedrichs-Lewy number

CFT Turbulent Courant-Friedrichs-Lewy number

E Specific total energy

G Pitch

$GMRES$ Generalized Minimal Residual

H Enthalpy (Cascade height)

ILS Integral length scale

ILU Incomplete Lower/Upper Factorization

is Isentropic

k Reconstruction order (Turbulent kineric energy)

K_S Acceleration paramenter

L Characteristic length

LSQ Least Square

$LU-SSOR$ Lower/Upper Symmetric Successive Over-Relaxation

Ma Mach number

Ma Reynolds number

N_{CPU} Number of processors

N_{DOF} Number of degrees of freedom

N_{el} Total number of elements

N_{faces} Total number of faces

$N_{profile}$ Total number of elements over the profile

S Curvilinear coordinate

s Entropy

S_0 Curvilinear length

SCM Successive Correction Method

SR Stretching ratio

T Temperature

t Physical time

TI Turbulence intensity

V Volume

VR Viscosity ratio

y^+ Non-dimensional wall distance

Vectors and Matrices

A Generic matrix

D Diagonal matrix

D Lower triangular matrix

F Inviscid fluxes

G Viscous Fluxes

I Identity matrix (Interpolation operator)

J	Jacobian matrix
P	Preconditioner matrix (Reconstruction matrix)
Q	Conservative variables
R	Residual vector (Restriction operator)
r	Distance vector
S	Source term
U	Velocity (Upper triangular matrix)
W	Primitive variables (Weighting Matrix)
x	Linear system unknown vector

Chapter 1

Overview of the HybFlow solver and thesis motivation

HybFlow is a cell-centered Finite-Volume solver which was developed at the Department of Industrial Engineering of the University of Florence. It is a three-dimensional flow solver, where 2D cases can be treated by using a single layer extrusion of 2D grids. The code uses unstructured grids composed of different element topologies: hexahedrons, prisms, pyramids and tetrahedrons. The choice of unstructured grids allows to provide an efficient discretization of complex domains, typically arising from turbomachinery problems. In this chapter, we will review the major characteristics of the code at its initial status, while the developments carried out during the thesis will be introduced in the last section of the present chapter and eventually discussed thoroughly in the remaining of the thesis.

1.1 Navier-Stokes equations in conservative form

Hybflow solves the compressible form of the Navier-Stokes equations:

$$\frac{\partial \mathbf{Q}}{\partial t} + \nabla \cdot (\mathbf{F} - \mathbf{G}) = \mathbf{S} \tag{1.1}$$

The vector $\mathbf{Q}$ contains the conservative variables, while the vectors $\mathbf{F}$ and $\mathbf{G}$ represent the inviscid and viscous fluxes, respectively.

$$\mathbf{Q} = \begin{bmatrix} \rho \\ \rho U_1 \\ \rho U_2 \\ \rho U_3 \\ \rho E \end{bmatrix} \qquad \mathbf{F\text{-}G} = \begin{bmatrix} \rho U_k \\ \rho U_1 U_k + p\delta_{1k} - \tau_{1k} \\ \rho U_2 U_k + p\delta_{2k} - \tau_{2k} \\ \rho U_3 U_k + p\delta_{3k} - \tau_{3k} \\ \rho E U_k + p U_k - \tau_{kh} U_h + q_k \end{bmatrix} \tag{1.2}$$

The terms τ_{ij} correspond to the elements of the compressible viscous stress tensor while q_i, is the conductive heat flux vector:

$$\tau_{ij} = 2\mu\left(\frac{1}{2}\left(\frac{\partial U_i}{\partial x_j} + \frac{\partial U_j}{\partial x_i}\right) - \frac{1}{3}\frac{\partial U_j}{\partial x_j}\right) \qquad q_i = -k\frac{\partial T}{\partial x_i} \tag{1.3}$$

The vector quantity **S**, represents a generic source term employed in the case of rotating components. In these cases, the equation are solved in a relative frame of reference and additional fictitious forces are added. The source term vector modifies the momentum balance and energy equations and, assuming a rotating about the x-axis, it takes the following form:

$$\mathbf{S} = \begin{bmatrix} 0 \\ 0 \\ \rho\Omega^2 y + 2\rho\Omega z \\ \rho\Omega^2 z - 2\rho\Omega y \\ \rho\Omega^2 (U_2 y + U_3 z) \end{bmatrix} \tag{1.4}$$

In order to fully close the system of equations, the ideal gas law is used to model the gas behavior, while uniform conductivity and viscosity are assumed for the computation of the viscous terms in the momentum and energy equations.

1.2 Spatial discretization

The code employs a second order, cell-centered Finite Volume method to perform the integration of NS equations over the domain:

$$\sum_{i=1}^{N_{el}} \left(V_i \frac{\partial \mathbf{Q}_i}{\partial t} + \sum_{j=1}^{N_{face,i}} \mathbf{F}_{ij} \right) = \sum_{i=1}^{N_{el}} \left(\sum_{j=1}^{N_{face,i}} \mathbf{G}_{ij} + V_i \mathbf{S}_i \right) \tag{1.5}$$

In Eq. 1.5, V_i represents the cell volume, while $\mathbf{Q}_i$ is the mean value of the conservative variables in the for the cell i. For a second order scheme, the latter correspond to the values of the solution variables in the cell center. The fluxes contribution has been split into an inviscid term $\mathbf{F}_{ij}$ and a viscous term $\mathbf{G}_{ij}$, which represent a numerical approximation to the non-linear residuals $\mathbf{R}$. The second order numerical approximation of the fluxes requires a consistent numerical integration of both the inviscid and viscous terms. For second order approximation, the integration is based on a single point integration, corresponding ti the center of each cell's face, where solution variables and its gradients are reconstructed, namely $\mathbf{F}_{ij} = \mathbf{F}_{ij}(\mathbf{Q}_C)$ and $\mathbf{G}_{ij} = \mathbf{G}_{ij}(\mathbf{Q}_C, \nabla(\mathbf{Q})_C)$

As far as inviscid fluxes are considered, the solution in the face centers is reconstructed by means of a limited linear approximation:

$$\mathbf{Q}_C = \mathbf{Q}_i + \Phi_i \nabla \mathbf{Q}_i \cdot \mathbf{r}_{ic} \tag{1.6}$$

where $\nabla\mathbf{Q}$ represent solution gradients stored in the cell center, while Φ_i is a gradient limiter. The vector $\mathbf{r}_{ic}$ is the distance vector from cell center 'i' and face center 'C'. The solution gradients can be approximated by two different methods: a Least-Square procedure ([1]) or a Green-Gauss method, where the averaged solution gradients are computed by means of the divergence theorem.

On the other hand, the limiter is enforced as:

$$\Phi_{ij} = \begin{cases} \min\left(1, \frac{Q_{max}-Q_i}{Q_{ij}-Q_i}\right) \; for\; Q_{ij} > Q_i \\ \min\left(1, \frac{Q_{min}-Q_i}{Q_{ij}-Q_i}\right) \; for\; Q_{ij} < Q_i \\ 1 \; for\; Q_{ij} = Q_i \end{cases} \tag{1.7}$$

where Q_{max} and Q_{min} are respectively the maximum and minimum value of the solution in the neighborhood of the cell 'i'. The gradient limiter of the cell is then found as $\min_j(\Phi_{ij})$. The limiting procedure avoids undershoots/overshoots in the reconstruction phase, bounding the reconstructed face values in between the minimum and maximum value found in the neighborhood of each cell. This allows

to enforce solution monotonicity, which could lead to an unbounded scheme (at least disregarding the stabilizing effects of the viscous terms). Upon reconstructing the solution value in the face center, the inviscid fluxes are approximated by means of the approximate Riemann solver proposed by Roe in [2].

As far as viscous gradients are considered, the numerical flux computation requires the definition of the solution values and gradients at the face center. To this end, the solution gradients are approximated by means of a finite difference formulation. The component of the gradient normal to the face is computed as follows:

$$\frac{\partial Q}{\partial n} = \frac{1}{|\mathbf{r}_{iC}| + |\mathbf{r}_{jC}|} \left[\frac{|\mathbf{r}_{iC}|}{|\mathbf{r}_{jC}|}(Q_j - Q_C) + \frac{|\mathbf{r}_{jC}|}{|\mathbf{r}_{iC}|}(Q_i - Q_C) \right] \tag{1.8}$$

where Q_C is an inverse distance weighted average of the cell solution Q_i and Q_j:

$$Q_C = \frac{|\mathbf{r}_{iC}|Q_j + |\mathbf{r}_{jC}|Q_i}{|\mathbf{r}_{iC}| + |\mathbf{r}_{jC}|} \tag{1.9}$$

Boundary conditions are imposed in a weak form, namely modifying the right-hand side (RHS) of the discretized equations, accounting for local viscous and inviscid fluxes over the boundaries of the domain.

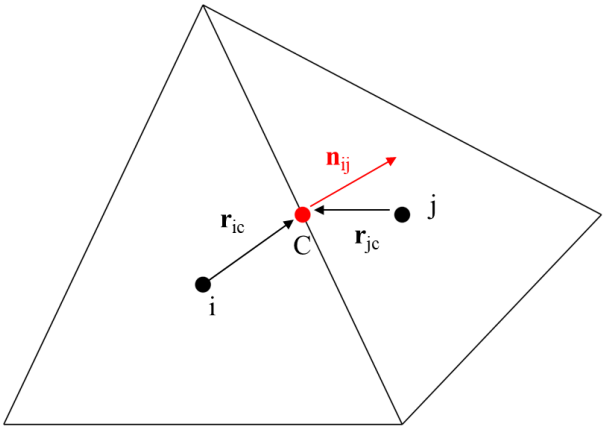

Fig. 1.1 Spatial discretization

1.3 Solution method

1.3.1 Steady and Unsteady NS solver

The full system of NS equations can be then reduced to following form:

$$\frac{\partial \mathbf{Q}}{\partial t} + \mathbf{R(Q)} = \mathbf{0} \tag{1.10}$$

where **R(Q)** represents the nonlinear residual found upon summing the contributions from the inviscid and viscous terms, along with the source vector for the case of rotating reference frames.

In the case of steady simulations, the code adopts a damped Newton method to find the solution to the nonlinear system of equations. In particular, the solution is marched in a numerical time according to the following iterative procedure:

$$\left[\frac{\mathbf{I}}{\Delta\tau} + \frac{\partial \mathbf{R}^*\mathbf{(Q)}}{\partial \mathbf{Q}}\right]^n \Delta\mathbf{Q}^n = -\mathbf{R(Q)}^n \tag{1.11}$$

The introduction of the diagonal damping term ($\frac{\mathbf{I}}{\Delta\tau}$) improves the stability of the Newton method, especially during the first iterations of the simulation, where the flow is dominated by the non-linearities. The damping term $\Delta\tau$ is computed according to the typical numerical time stepping technique, where the numerical time step is computed based on the grid topology and the local flow characteristics (speed of acoustic waves):

$$\Delta\tau = CFL\frac{L}{\lambda_{max}} \tag{1.12}$$

L represents a characteristic length scale of the cell, which in HybFlow is computed based on the distance between cell centers and face centers, while λ_{max} is the maximum wave propagation speed.

On the other hand the residual vector Jacobian is approximated by means of a 1^{st} order finite difference method, where the derivatives are computed by means of an imposed perturbation:

$$\frac{\partial R_i}{\partial Q_j} = \frac{R_i(Q_j + \varepsilon_j) - R_i(Q_j)}{\varepsilon_j} \tag{1.13}$$

The scalar ε_j is an imposed perturbation value, which in the initial configuration of the solver is taken equal to 10^{-3}.

The linear system matrix is stored in a Sparse Vector Format, pre-allocating the number of non-zero columns during the initial steps of the computation. The linear system arising at each iteration is then solved in HybFlow by using a multi-block approach which allows for a low-memory requirement and easy parallelization of the code. The general idea is to subdivide the whole grid into a certain number of blocks (greater than the number of processors). The solution is marched implicitly inside each block, while the couling between the blocks is performed in an explicit manner. For this reason, the solver only needs to store the linear matrix associated to a single block, while the coupling between the blocks themselves is obtained after updating the fluxes at each numerical time-step. The main advantage of the method is that the solution can be marched independently from block to block, which allows easiness in parallel implementations and also reduces the memory requirements as each processor can store a single block matrix at a time. The definition of the blocks is performed during a pre-processing phase of the simulation with in-house routines, which attempt at reducing the number of interfaces between blocks, while guaranteeing a uniform distribution of the load among all the blocks. After the block decomposition, a Cuthill-Mckee reordering of the cells is performed to reduce the bandwidth of the linear matrix. The parallelization is based on the MPI library, which enables the solution communication between different processors.

Unsteady problems can instead be tackled by means of an implicit solver, using a dual time-stepping technique, or an explicit solver. The dual time stepping technique consists in adding a fictitious numerical time derivative (in similar fashion to the damped Newton method), to improve the stability of the linear solver at each flow iteration. The unsteady NS system of equations can be written as:

$$\frac{\partial \mathbf{Q}}{\partial t} + \left(\frac{\partial \mathbf{Q}}{\partial \tau} + \mathbf{R(Q)} \right) = 0 \tag{1.14}$$

The time derivative is approximated by means of an implicit second order backward difference, which leads to the following expression:

$$\frac{3\mathbf{Q}^t - 4\mathbf{Q}^{t-1} + \mathbf{Q}^{t-2}}{2\Delta t} + \mathbf{R}(\mathbf{Q}^t) = 0 \tag{1.15}$$

Table 1.1 Explicit methods coefficient

Index	Two Stage		Four Stage	
	b_i	c_i	b_i	c_i
1	0.5	0.0	0.10893125722541	0.17985400977138
2	1.0	0.0	0.132017014921526	0.14081893152111
3			0.38911623225517	0.08255631629428
4			-0.59203884581148	0.65804425034331
5			0.47385028714844	0.31862993413251
6			0.48812405426094	0.0

At each time step, the residual vector is approximated by marching the solution in a numerical time, in a similar fashion to the one reported in Eq. 1.11. The algorithm iteratively finds the solution at each physical time step, driving numerical time derivative term to 0. This allows to find an approximate value of the residual vector at instant t.

The time advancement can also be handled in an explicit manner. The code adopts two different methodologies to handle the explicit problem, namely a two-stage predictor corrector and a 6-stage 4th order Runge-Kutta approach.

The two approaches can be reduced to the following form:

$$\mathbf{q}_0 = \mathbf{Q}^n \qquad \mathbf{F}_0 = \mathbf{R}(\mathbf{q}_0) \tag{1.16}$$

$$\mathbf{q}_i = \mathbf{q}_{i-1} + \Delta t b_i \mathbf{F}_{i-1} \qquad \mathbf{F}_i = \mathbf{R}(\mathbf{q}_i + \Delta t c_i \mathbf{F}_{i-1}) \tag{1.17}$$

The coefficients adopted in the two methods are shown in Tab. 1.1

1.3.2 Low Mach number preconditioning

The application of compressible solvers to simulations characterized by Low Mach number in most of the domain results in convergence difficulties and low accuracy due to the upwind nature of compressible schemes such as the one proposed by Roe [2]. Convergence difficulties are related to the fact that the propagation of acoustic waves occurs at a speed equal to $\sqrt{\frac{\partial \rho}{\partial p}} >> V$, where V represents the local speed of the flow. This increases the stiffness of the residuals Jacobian matrix, hindering

solver convergence. On the other hand it can be proved that artificial viscosity of the Roe's scheme is $\propto \frac{1}{Ma}$. A Low Mach preconditioning similar to those proposed by Turkel [3] and Weiss and Smith [4] is then adopted in the code to improve the convergence rate of the solver for low-speed flows and correct the non-physical behavior of the Roe's scheme.

Recalling the Euler equations written in conservative variables, the system is transformed into an equivalent one using primitive variables $\mathbf{W} = \{p\ U_1\ U_2\ U_3\ T\}^T$:

$$\mathbf{J}\frac{\partial \mathbf{W}}{\partial t} + \nabla \cdot \mathbf{F} = 0 \tag{1.18}$$

The Jacobian matrix $\mathbf{J}$ defines the transformation from conservative variables to primitive variables:

$$\mathbf{J} = \frac{\partial \mathbf{Q}}{\partial \mathbf{W}} = \begin{Bmatrix} \rho_p & 0 & 0 & 0 & \rho_T \\ \rho_p U_1 & \rho & 0 & 0 & \rho_T U_1 \\ \rho_p U_2 & 0 & \rho & 0 & \rho_T U_2 \\ \rho_p U_3 & 0 & 0 & \rho & \rho_T U_3 \\ \rho_p H - 1 & \rho U_1 & \rho U_2 & \rho U_3 & \rho_T \end{Bmatrix} \tag{1.19}$$

where:

$$\rho_p = \frac{\partial \rho}{\partial p}|_s \qquad \rho_T = \frac{\partial \rho}{\partial T}|_p \tag{1.20}$$

The low Mach number preconditioning consists in substituting the Jacobian matrix with a different one with the aim of equalizing its eigenvalues. The system is then transformed into the following one, where a parameter Θ is substituted for the acoustic speed $\frac{\partial \rho}{\partial p}$:

$$\mathbf{J}_{LM}\frac{\partial \mathbf{W}}{\partial t} + \nabla \cdot \mathbf{F} = 0 \qquad \mathbf{J}_{LM} = \begin{Bmatrix} \Theta & 0 & 0 & 0 & \rho_T \\ \rho_p U_1 & \rho & 0 & 0 & \rho_T U_1 \\ \rho_p U_2 & 0 & \rho & 0 & \rho_T U_2 \\ \rho_p U_3 & 0 & 0 & \rho & \rho_T U_3 \\ \rho_p H - 1 & \rho U_1 & \rho U_2 & \rho U_3 & \rho_T \end{Bmatrix} \tag{1.21}$$

The final system is then expressed again in conservative variables $\mathbf{Q}$ via a multiplication by the inverse of the real Jacobian matrix $\mathbf{J}$:

$$\frac{\partial \mathbf{Q}}{\partial t} + \mathbf{J}\mathbf{J}_{LM}^{-1} \nabla \cdot \mathbf{F} = 0 \tag{1.22}$$

The variable Θ is defined as:

$$\Theta = \frac{\gamma}{T} + \frac{1-\gamma}{V_{ref}^2} \tag{1.23}$$

where:

$$V_{ref}^2 = \max(V^2, \varepsilon^2 V_{sound}^2) \qquad \gamma = \max\left(1, \left(\frac{Ma^2}{Ma_{lim}^2}\right)^n\right) \tag{1.24}$$

where T is the local temperature, V_{ref} is a reference velocity, while n, ε and Ma_{lim} are adjustable parameters which control the blending between the Low Mach approach and the fully compressible one.

1.3.3 Turbulence solver

The effect of turbulent dissipation is modeled in HybFlow using common eddy-viscosity closure models, while Favre-averaging is adopted considering the compressible nature of the simulated flows. To this end, additional conservation laws for the turbulence variables are solved in a sequential manner with respect to the NS equations. The general conservation law of a scalar quantity Φ can be written as:

$$\frac{\partial \rho \Phi}{\partial t} + \frac{\partial (\rho U_j \Phi)}{\partial x_j} = P_\Phi - D_\Phi + \frac{\partial}{\partial x_j}\left[(\mu + \mu_\Phi)\frac{\partial \Phi}{\partial x_j}\right] \tag{1.25}$$

where U_j comes from the Favre-averaging of the flow field velocity. P_Φ and D_Φ represent general production and destruction terms, respectively, while μ_Φ is an additional, model-dependent, viscosity contribution.

Turbulence scalar equations present additional difficulties. In particular, for wall-bounded flows, adopting $k-\omega$ type models, the condition number of the Jacobian matrix deriving from the discretization the ω increases depending on wall vicinity. Moreover, the presence of production terms affects the diagonal dominance of the linear system matrix, which deteriorates the linear solver convergence.

In general, the solution strategy of the additional transport equation in the original version of the code is similar to the one reported for NS equations, but some modifications are present to deal with the stiffness of the system arising after the linearization of the conservation law. In particular, at each flow iteration, the turbulence problem is solved for a predefined number of numerical times, before the turbulent solution is updated and passed to the NS solver. In order to guarantee that the turbulence and the flow variables are marched at equal rates, the damping term of the Newton solver is modified accordingly. In particular, the pseudo-time step used for the turbulence equations is defined as:

$$\Delta\tau_{turb} = CFT\frac{L}{\lambda_{max}} \tag{1.26}$$

where $CFT = \frac{CFL}{n_{turb}}$, where n_{turb} is the number of turbulent iterations before solution update.

The computation of viscous fluxes for the additional conservation laws follows the same scheme used for flow variables. On the other hand, the inviscid fluxes are computed by means of a 1^{st} order upwind scheme, namely:

$$F_{\Phi,ij} = \begin{cases} \rho_1 \mathbf{U}_i \cdot \mathbf{n}_{ij} \Phi_i \ for \ \mathbf{U}_i \cdot \mathbf{n}_{ij} \geq 0 \\ \rho_j \mathbf{U}_j \cdot \mathbf{n}_{ij} \Phi_j \ for \ \mathbf{U}_j \cdot \mathbf{n}_{ij} < 0 \end{cases} \tag{1.27}$$

This strategy provides higher stability, compared to fully 2^{nd} order schemes, and improves the convergence rate of the turbulent flow field. The computation of production/destruction terms dependent on the flow gradients, the spatial derivatives obtained for the flow reconstruction are used.

The solution of the additional scalar transport equations is shown in Fig. 1.2. The solution of the scalar quantities is marched in a segregated manner with respect to the flow variables. While this methodology has proved to lead to slightly different results compared to a fully-coupled approach (where additional scalar equations are solved coupled with the flow equations), it provides higher flexibility as new turbulence models can be added without modifying the overall structure of the solver.

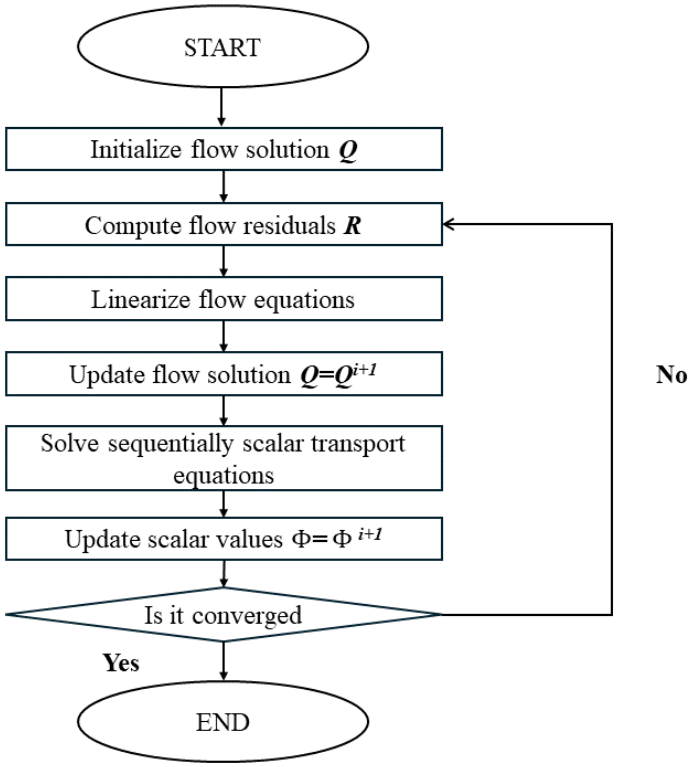

Fig. 1.2 Solution procedure

1.4 Motivations of the present work

The present work of thesis is devoted to the extension of the solver capability both in terms of accuracy, range of simulated flows and overall performance.

The first part of the present work is dedicated to the analysis of the implicit solution algorithm, especially for steady-state convergence. The multi-block approach has the main advantage of requiring low memory for the storage of the linear system matrix in a block format. Despite this, the explicit interface treatment prevents the code from a robust linear convergence as the solution is marched in the numerical time. The problem is exacerbated by the high number of block divisions, which in the typical configuration of the solver exceed the number of processor in parallel applications. An example of this behavior can be found in Chapter 2, where the increase of block divisions for building a preconditioner is shown to increment the number of linear iterations required to achieve a converged solution at each Newton iteration. When the block-division is used as a non-linear solver (as in the original version of HybFlow), it may hinder non-linear convergence. The second chapter of the thesis details the implementation of a new fully-implicit linear solver which is tested over laminar and turbulent test cases of interest for the development of the code.

In his thesis, Carnevale [5] analyzed the solver accuracy over some simple test cases, while implementing a Large Eddy Simulation (LES) module in HybFlow. The issue related to the code accuracy is raised after the implementation of subgrid models. Carnevale implies that the poor performance of the LES solver in reproducing pin-fin arrays is to be attributed to the excessive numerical dissipation of the original scheme implemented in the code. It is opinion of the present author that the reduced accuracy of the code for some test cases also needs to be attributed to the lack of transparency of the solver to processor boundaries. As a matter of fact, the reconstruction stencil becomes one-sided to avoid parallel communication among processors during the reconstruction phase of the solution (see Fig. 1.3). In this work, the accuracy issue has been tackled by extending the solver capabilities to higher-order (higher than second) reconstruction for FV solvers, while providing an ordered communication between processors before the reconstruction phase.

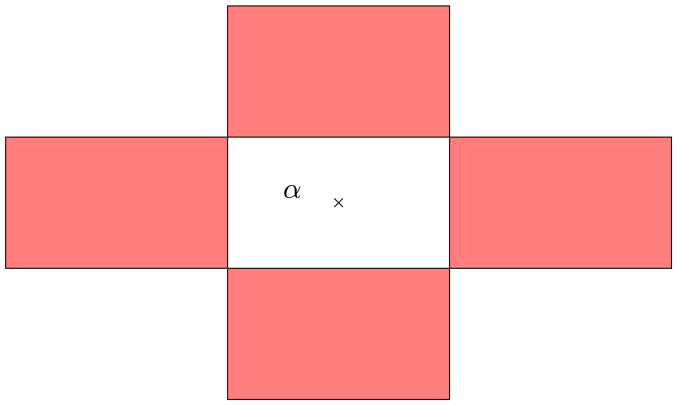

(a)

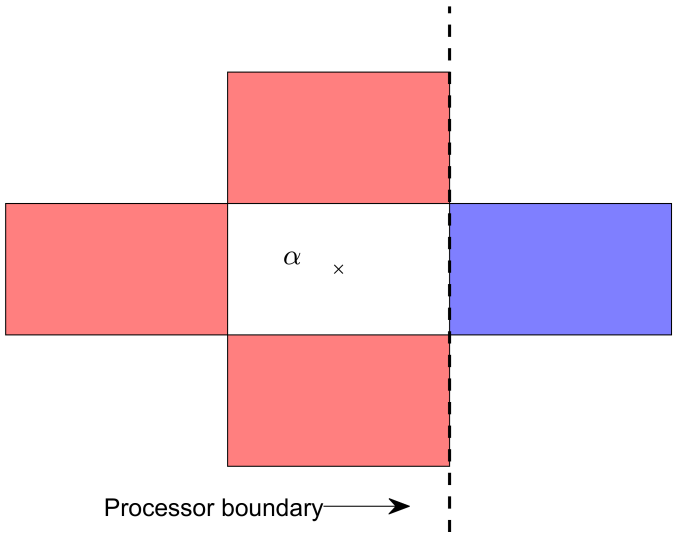

(b)

Fig. 1.3 Modification of the reconstruction stencil for a sample cell: (a) Serial computation, (b) Parallel computation - blue cell is removed from the reconstruction stencil

Chapter 2

Iterative method

The second chapter of the thesis is devoted to the introduction of an efficient iterative solution method applied to implicit discretization methods, which is essential for the development of CFD solvers developed for the study of industrial test cases. As a matter of fact, in most applications, the solver is used to find steady solutions with implicit methods, which allow to comply with the clustered cells in high gradients regions (like in the wall vicinity) and coarser discretizations in the free-stream. The chapter is organized as follows:

- The first part of the chapter gives an introduction to the Jacobian forming procedure, along with the parallel implementation of the GMRES linear solver
- The second part of the chapter describes the application of preconditioning methods to the GMRES solver. In particular two different preconditioners will be discussed and analyzed: Additive-Schwarz Method with ILU factorization (ILU(0)) and Aggregation based Algebraic Multigrid (AMG)
- The last part of the chapter provides an analysis of the linear solution strategy over a laminar and a turbulent test case, addressing the cost of the GMRES compared to simpler linear solvers and the impact of the CFL over the solution cost

2.1 Introduction to the iterative method

The discussion of the linear solver implementation will mainly regard the solution of steady-state problems. Hence, we will consider the solution of the steady state NS equations (Eq. 2.1), where the contributions of the viscous and inviscid fluxes, and the source term have been clustered into the residual vector **R(Q)**.

$$\mathbf{R(Q)} = \mathbf{0} \tag{2.1}$$

The non-linear system is solved by means of a damped Newton method (Eq. 2.2), introduced in Chapter 1, with the linearization of the non-linear NS equations and the addition of a damping term for stability reasons:

$$\left[\frac{\mathbf{I}}{\Delta\tau} + \frac{\partial \mathbf{R}^*\mathbf{(Q)}}{\partial \mathbf{Q}}\right]\Delta\mathbf{Q} = -\mathbf{R(Q)} \tag{2.2}$$

In general, the Jacobian term can be computed in different ways. The first option is to use an exact Jacobian matrix, in which case $\mathbf{R}^*$ corresponds to the non-linear residuals vector **R**, regardless of the order of accuracy of the code. This is the approach used by the authors in [6]. Despite this, the exact Jacobian computation can be lengthy, and for higher-order computations, the sparsity pattern of the matrix can be more complex. This increases the level of fill-in of the Jacobian, negatively affecting the overall computational time for a linear iteration. A different strategy is instead reported by Xu et al. in [7]. The authors suggest using an automatic differentiation of the residual vector based on matrix coloring, while using a blended (among first and second order) Jacobian to build the linear system preconditioner. Mavriplis ([8]) instead reports the usage of a first order simplified Jacobian even for second order computations. This same strategy has been adopted for the present thesis, providing no modification with respect to the original linearization strategy implemented in HybFlow. The Jacobian matrix is formed and stored after a finite difference evaluation of residual derivatives (Eq. 2.3) .

$$\frac{\partial R_i}{\partial Q_j} = \frac{R_i(Q_j + \varepsilon_j) - R_i(Q_j)}{\varepsilon_j} \tag{2.3}$$

The value of the perturbation can impact the Jacobian matrix, though. As a matter of fact, the value of ε_j should be chosen considering that if the value is too high, the per-

turbation method might not be adequate to provide a proper first order approximation of the Jacobian matrix. On the other hand, a low value of the perturbation can lead to wrong approximation to the derivative due to round-off errors. For these reasons, the perturbation level is determined locally for each cell and variable according to Eq. 2.4.

$$\varepsilon_j = \min(\varepsilon_{rel,j} * Q_j, \varepsilon_{abs}) \tag{2.4}$$

The values used are $\varepsilon_{rel,j}$=1×10^{-6} and ε_{abs}=1×10^{-8}.

The linear system arising from the Newton linearization is solved by means of a GMRES solver ([9]). The full algorithm is the reported in Alg. 1.

Algorithm 1 GMRES algorithm

1: Set $v_0 = b - Ax_0$, $\beta = ||r_0||$ and $v_1 = r_0/\beta$
2: **for all** $j \in \{1,\ldots,m\}$ **do**
3: Compute $w_j = Av_j$
4: **for all** $i \in \{1,\ldots,j\}$ **do**
5: Compute $h_{ij} = (w_j, v_i)$
6: Compute $w_j = w_j - h_{ij}v_i$
7: **end for**
8: $h_{j+1,j} = ||w_j||$
9: $v_{j+1} = w_j/h_{j+1,sj}$
10: **end for**
11: Compute y_m as the minimizer of $||\beta e_1 - Hy||$
12: Compute x_m as $x_m = x_0 + V_m y_m$

The algorithm finds the solution to the linear system in a Krylov sub-space whose basis is formed by the vectors v_m, which are all mutually orthogonal. It can be proved that the solution found at each linear iteration minimizes the 2-norm of the residual vector in the 'available' subspace. The GMRES is more stable than other linear solvers based on point-implicit or line implicit relaxations, but is more memory intensive due to the necessity of storing the Krylov vectors v_m during the solution phase. An additional drawback of Krylov methods is related to the size of the sub-vectors. As a matter of fact, when the number of Krylov iterations starts increasing, the following sub-vectors need to be orthogonalized against more previous sub-vectors. In Alg. 1, the orthogonalization steps are performed using a Modified Grahm Schmidt algorithm (lines from 4 to 8). Apart from increasing the

computational cost, an increasing number of sub-vectors leads to additional memory required for their storage. One of the possible remedies to the memory requirements of the GMRES is the adoption of a matrix-free approach (see [10] for example). As a matter of fact, since the build-up of sub-vectors involves only products between the Jacobian matrix and the sub-vectors, the Jacobian matrix can be built on the fly rather than assembled and stored in memory. From a practical point of view, the matrix-free approach consists in substituting the products involving the Jacobian matrix, with a local perturbation of the residual vector.

In the current implementation, the Jacobian matrix is stored as it gives the possibility to build local preconditioners to enhance the convergence speed of the linear solver. In order to counterbalance the high memory requirements, of the GMRES, in HybFlow a Restarted approach is adopted. The principle behind the restarted GMRES is to flush the Krylov sub-vectors after a prescribed number of iterations. The modification to Alg. 1, consists in prescribing a maximum value to the number of Krylov vectors to form the sub-space of the linear solution (m). After the threshold is reached, a new subspace is built using the final approximate solution x_m as initial value and eventually the algorithm is restarted. The procedure has a threefold effect. The memory requirements are reduced as a maximum number of Krylov vectors are stored during the linear solution which cannot be exceeded. The second effect is that, since each new Krylov vector is orthogonal to the previous available ones, the linear iterations after the Krylov subspace is restarted are faster as every new Krylov vector needs to be orthogonalized against a lower number of available ones. The third effect, is that the restart procedure removes information from the basis of the Krylov space built at each previous restart. For this reason, the convergence of the GMRES can be negatively impacted as the mutual orthogonality of the sub-vectors is lost ([11]).

In general, linear iterations continue until a linear tolerance is met. Different values are common in the literature with 0.1 (as in [12] and [7]) and 0.01 (as in [13]) being the most common ones. A good trade-off between the linear accuracy and the non-linear convergence rate of the code depends on the relative speed of the linear solver and the Newton method. As a matter of fact, tight linear tolerances increase the computational time for a single non-linear iteration. But as will be seen in Sec. 2.3, this also stabilizes the computation as a better approximate solution is found at each non-linear iteration.

To test the performance of the overall solution strategy (damped Newton + linear solver), the GMRES has been compared with a simpler point-implicit smoother: the Lower-Upper Symmetric Successive Over-Relaxation method (LU-SSOR). The LU-SSOR is a variant of the Gauss-Seidel method, where an approximate solution to the linear system is found using the iterative method defined in Eq. 2.5.

$$\begin{cases} Ax = f \\ A = D + L + U \\ x^{i+1} = (D + \omega L)^{-1}(\omega f - [\omega U + (\omega - 1)D]x^i) \end{cases} \tag{2.5}$$

The method is based on the common splitting of the linear system matrix A, into D (a diagonal matrix), L (a lower triangular matrix) and U (an upper triangular matrix). The difference with respect to the Gauss-Seidel iteration is in the presence of a scalar ω which can be used to improve the convergence rate of the method (ω>1) or to stabilize it (ω<1). For ω=1, the Gauss-Seidel iteration is recovered. As far as the application of the method to the CFD solver is considered, the matrices are regarded as composed of blocks for each cell. The inversion of the diagonal block is performed by means of a LU factorization and is applied by means of a forward and backward substitution to the right-hand side. The same holds for the matrices L and U which are never built. Throughout the activity, the value of ω has been set equal to 0.75.

2.2 Preconditioning

The linear system arising from the damped Newton linearization can lead to a linear matrix characterized by a high condition number, especially for highly stretched grids. In this scenario, the GMRES algorithm might stall, eventually oscillating around an incomplete solution. The preconditioning also serves another purpose. The cost of a GMRES iteration can be very costly compared to simpler solvers, like point-implicit methods, depending on the number of available Krylov vectors. In this case, the preconditioner is necessary to reduce the number of iterations necessary to reach the specified tolerance at each non-linear step. The preconditioner to the linear system takes the form of Eq. 2.6, where the first line refers to a left-preconditioner

and the second line refers to a right-preconditioner.

$$\begin{aligned} \mathbf{PAx} &= \mathbf{Pb} \\ \mathbf{AP}^{-1}\mathbf{Px} &= \mathbf{b} \end{aligned} \tag{2.6}$$

In order to improve the convergence rate of the linear system solution, the matrix **P**, needs to be as close as possible to $\mathbf{A}^{-1}$. Moreover, the preconditioner should be fast to compute so that the overall convergence time of the method is not hindered by the additional computational steps required to form **P**. In the present activity, two types of preconditioners have been implemented based on Domain Decomposition and Multilevel method, respectively.

2.2.1 Domain decomposition method

Domain decomposition methods were introduced as means for the solution of partial differential equations. The basic idea is to divide the problem into subdomains which are iteratively solved to obtain a final solution for the whole problem. In order to maintain the coupling between the subdomains, the method requires that some level of information is passed among the various subdomains. A sample domain decomposition is shown in Fig. 2.1, where Ω indicates the subdomains, while Γ indicates the interface between them.

Considering a sample problem $Bu(\mathbf{x}) = f$ over a domain $\Omega = \Omega 1 + \Omega 2$ with Dirichlet boundary conditions applied on the boundary ($u = u_{BC}$ on $\partial\Omega$), a domain decomposition method is based on the coupled set of equations to be solved iteratively, after an initial approximation to the solution is available u^m:

$$\begin{cases} Bu^{m+1}(\mathbf{x}) = f & \mathbf{x} \in \Omega 1 \\ u^{m+1}(\mathbf{x}) = u^m(\mathbf{x}) & \mathbf{x} \in \Gamma 1 \\ u^{m+1}(\mathbf{x}) = u_{BC} & \mathbf{x} \in \partial\Omega 1/\Gamma 1 \end{cases} \tag{2.7}$$

$$\begin{cases} Bu^{m+1}(\mathbf{x}) = f & \mathbf{x} \in \Omega 2 \\ u^{m+1}(\mathbf{x}) = u^m(\mathbf{x}) & \mathbf{x} \in \Gamma 2 \\ u^{m+1}(\mathbf{x}) = u_{BC} & \mathbf{x} \in \partial\Omega 2/\Gamma 2 \end{cases} \tag{2.8}$$

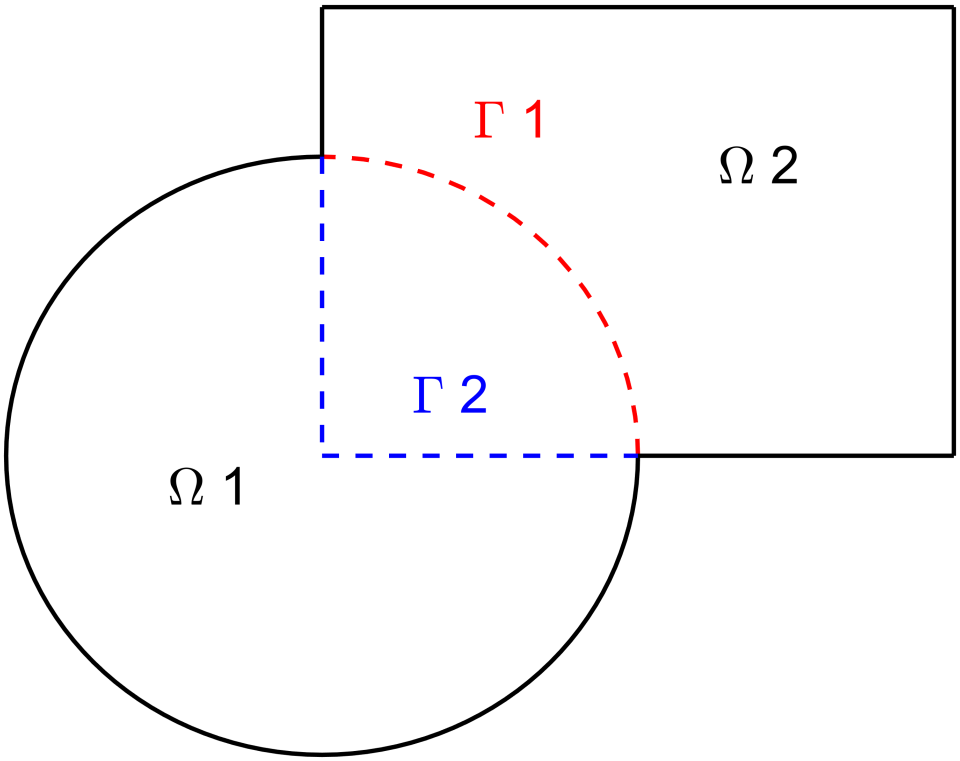

Fig. 2.1 Domain decomposition.

The second equation in each system defines the coupling between the two subdomains, which takes the form of a boundary condition over the interface.

Different classes of domain decomposition techniques have been discussed in the literature, which can be grouped in two different categories (Fig. 2.2):

- Overlapping methods
- Non-overlapping methods

In the case of overlapping methods, subdomains are built in such a way that a certain amount of overlap between the subdomains is provided. In CFD applications, the need of an overlap between subdomains, coincides with defining a certain number of layers of cell to exchange coupling information between the subdomains, typically 1- or 2-layers overlap are used. In the case of non-overlapping methods, no overlapping layer is added to the subdomains and the solution is marched explicitly inside each of the subdomains, while the coupling is obtained through the specification of boundary conditions at the subdomain interface.

Typically, overlapping methods retain better convergence properties because of the increased exchange of information between the subdomains ([14]). On the other hand, the performance of non-overlapping methods tends to deteriorate as the number of subdomains increases because of the addition of an increased number of explicit interfaces. Despite this, the implementation of non-overlapping methods is straightforward, especially in parallel applications, where the decomposition of the mesh among the processors already offers the availability of the subdomains. Another classification of the domain decomposition methods depends on the type of information exchanged among the subdomains. If the coupling (with reference to 2.8) at the iteration $m+1$ occurs using solution at instant m, then the methods are called *Additive*. On the other hand, if the coupling between subdomains takes advantage of the current solution from the iteration $m+1$ (which requires a sequential solution for the subdomain problems), then the methods are called *Multiplicative*.

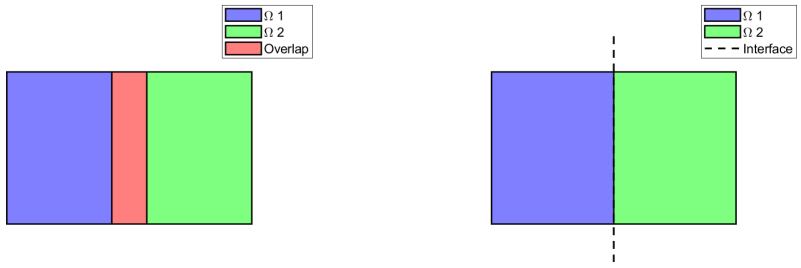

Fig. 2.2 Domain decomposition methods. (a): Overlapping method, (b): Non-overlapping method

Despite being developed for the solution of Partial Differential Equations (PDE), domain decomposition methods have become increasingly popular also when applied to the solution of linear systems. In the CFD field, the methods became increasingly popular in the 90's and early 2000's ([15, 16]), while being among the most popular methods for building linear system preconditioners ([7]) and parallel solvers ([17]) nowadays . The main advantage is that, since an explicit coupling between various subdomains allows to progress the solution over the full domain, only the subdomain matrix needs to be stored, leading to non-negligible savings in memory requirements. When applied to a linear system, a domain decomposition method (of the same type of Eq. 2.7 and 2.8) takes the general form of Eq. 2.9, if the unknowns are appropriately ordered.

$$\mathbf{Au} = \begin{bmatrix} A_{\Omega 1} & & A_{\Omega 1\Gamma} \\ & A_{\Omega 2} & A_{\Omega 2\Gamma} \\ A_{\Gamma\Omega 1} & A_{\Gamma\Omega 2} & A_{\Gamma\Gamma} \end{bmatrix} \begin{bmatrix} x_{\Omega 1} \\ x_{\Omega 2} \\ x_{\Gamma} \end{bmatrix} = \begin{bmatrix} f_{\Omega 1} \\ f_{\Omega 2} \\ g \end{bmatrix} = \mathbf{f} \tag{2.9}$$

The blocks on the diagonal $A_{\Omega i}$ define the local system matrix of each of the subdomains, while the blocks out of the diagonal A_{Γ} define the dependence of the inner solution of the subdomains ($x_{\Omega i}$) on the interface solution A_{Γ}. On the RHS, the term g couples the two domains by means of interface conditions. This type of system can be solved in different ways like Schur complement, or alternating procedures.

In this thesis we will deal with the Additive Scharwz method with a single cell overlap. In this case, the solution between the subdomains is marched explicitly (alternating), fixing the solution of the first cell across the interface. In this scenario, all the blocks out of the diagonal become null and the coupling between the subdomains is achieved by means of the RHS g, which takes the form of a non-linear residual (sum of a viscous flux and an inviscid flux). The implementation of the Additive Schwarz method as a preconditioner to the linear system solver (GMRES) in HybFlow can be schematized as follows:

1. Define a certain number of subdomains Ω_i. This is achieved in by means of graph-partitioning method
2. Define the restriction operator $\mathbf{R}_i$, which maps the global domain $\mathbf{Q}$ to the local subdomain $\mathbf{Q}_i$. The operator $\mathbf{R}_i^T$ will be the extension operator, mapping the local subdomain $\mathbf{Q}_i$ to the global one $\mathbf{Q}$. $\mathbf{R}_i^T$ is the transpose of $\mathbf{R}_i$
3. Find the local domain matrix $\mathbf{A}_i$=$\mathbf{R}_i^T$ $\mathbf{A}$ $\mathbf{R}_i$
4. Assemble the preconditioner matrix $\mathbf{P}_{DD}$=$\sum_{i=1}^{N_i} \mathbf{A}_i^{-1}$

The additive method with no overlap is equal to a block-Jacobi method, where the block corresponds to the local subdomain.

At step 3), the method requires finding an approximate inverse to the local subdomain matrix, namely $\mathbf{A}_i^{-1}$. While an exact inversion is costly, it is possible to use an approximate inverse. We use a ILU factorization with 0 level of fill-in (Alg. 2).

Algorithm 2 ILU(0) algorithm

for all $i \in \{2 \cdots N\}$ **do**
  for all $k \in \{1 \cdots i-1\}$ and $A_{ik} \neq 0$ **do**
    $w = A_{ik}/A_{kk}$
    for all $j \in \{k+1 \cdots N\}$ and $A_{ij} \neq 0$ **do**
      $A'^{-1}_{ij} = A_{ij} - w \times A_{kj}$
    end for
    $A'^{-1}_{ik} = w$
  end for
end for

From a practical point of view, the restriction operator and the extension operator are never built in the code as the domain decomposition is performed during a pre-processing phase of the grid, and cells are re-numbered according to the local block. Moreover, none of the steps requires communication between processors, as blocks are locally assigned to processors and the split of a block among different processors is not allowed. In general $N_{blocks} \neq N_{proc}$. The block division used in the code is performed using the C-library *metis* ([18]), while the integration with the Fortran subroutine of the preprocessing is performed using the Fortran interface available at [19]. A sample block partition is shown in Fig. 2.3.

The assessment of domain decomposition as a preconditioner to the parallel GMRES solver has been performed on the laminar flow over the NACA0012 profile. The simulations have been run at Ma=0.5, Re=5,000. These conditions have been thoroughly tested in the literature to assess the accuracy and convergence speed of CFD solvers. The analysis has been performed using two different meshes, namely M1 and M2. The setup of the simulations is summarized in Tab. 2.1. All the simulations are run using an adaptive strategy for the control of the CFL number. While the adaption provides a faster non-linear convergence of the Newton solver, it also allows to test the effect of the preconditioning over a wide range of damping parameters. The adaption of the CFL is performed according to a simple exponential law (Eq. 2.10), where CFL_0 indicates the CFL at the first iteration and β controls the rate of increase of the CFL. The min function is used to set a limit to the CFL. All the results of the present Chapter have been obtained by setting CFL_0 and CFL_{max} equal to 1.0 and 10^6, respectively. On the other hand, β was set equal to 1.1.

$$CFL_i = \min(CFL_0 * \beta^{i-1}, CFL_{max}) \tag{2.10}$$

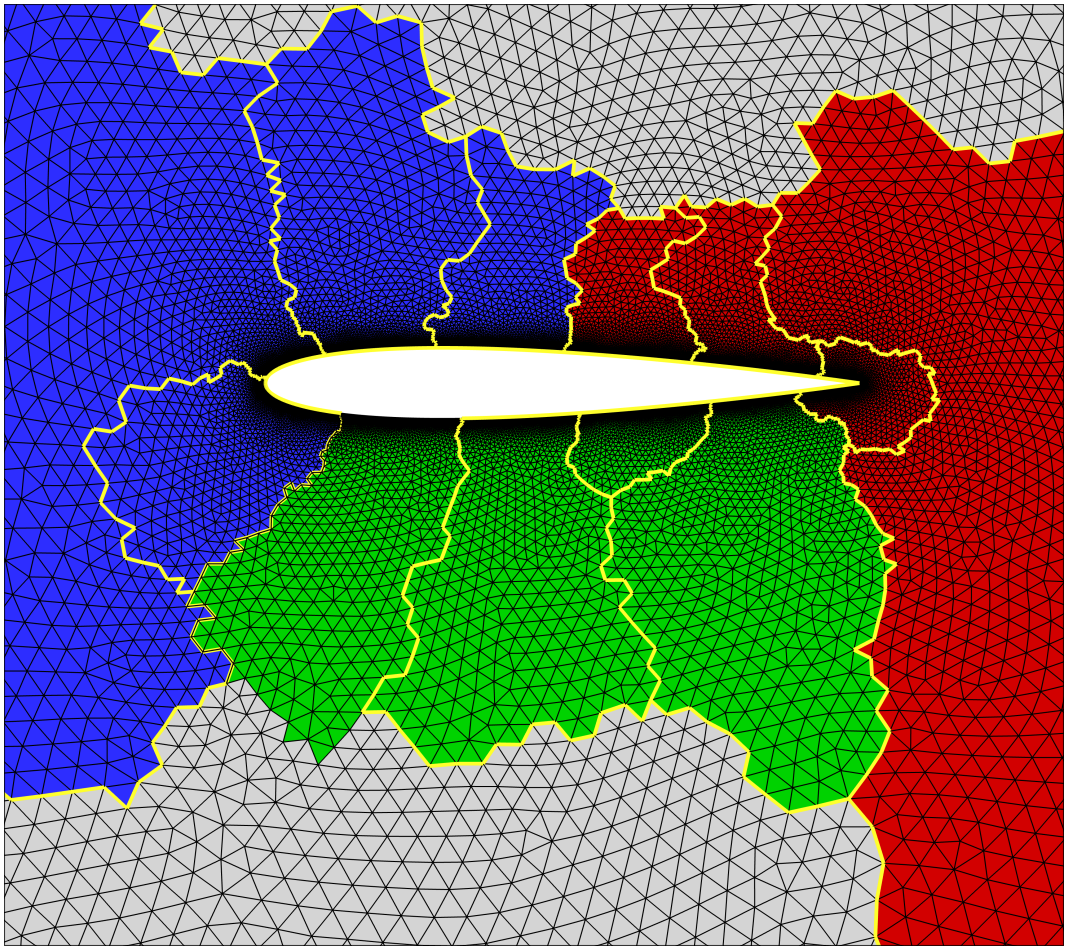

Fig. 2.3 Block division (yellow bold line) among processors (solid contour)

Table 2.1 NACA0012 - Simulation setup

Mesh	N_{el}	Reconstruction order	N_{proc}	Ma	Re	CFL
M1	49234	0	4	0.5	5,000	Adaptive
M1	49234	1	4	0.5	5,000	Adaptive
M2	180228	0	4	0.5	5,000	Adaptive

Figure 2.4 shows the effect of the block partitioning on the evolution of the density residuals against the non-linear iterations, along with the CFL and the number of linear iterations required at each non-linear iteration.
The non-linear evolution of the residuals is not affected by the block partitioning, as the linear solution hardly affects the non-linear evolution of the solution, provided that a certain tolerance in the linear solver is met. This aspect is analyzed later in the thesis. Moreover, the block partitioning also hardly affects the number of linear iterations required at each Newton step. As a matter of fact, for a limited number of blocks, the number of linear iterations does not vary much. The highest number is found for N_{blk}/N_{proc}=8.

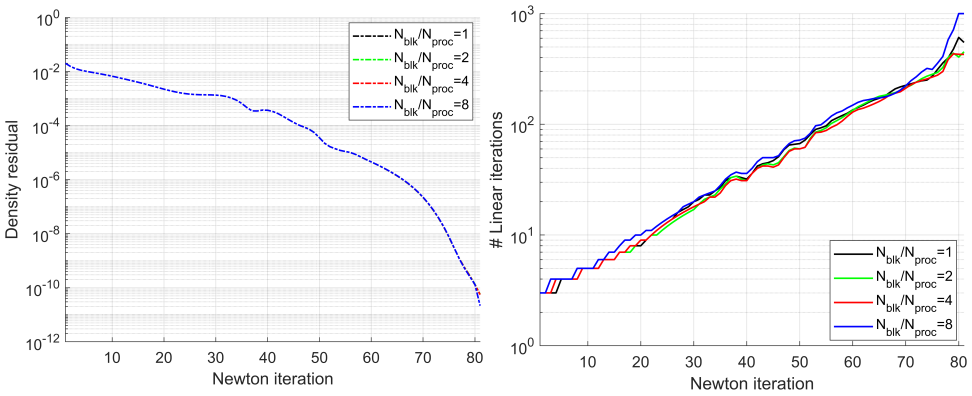

(a) (b)

Fig. 2.4 Effect of block partitioning 1^{st} order: NACA M1

This aspect is evidenced further in Fig. 2.5, where the same configuration is run using a much finer mesh and a higher number of blocks per processor. While similar considerations regarding the non-linear solution can be drawn as occurring in mesh M1, the effect of block partitioning over the processor is quite evident for N_{blk}/N_{proc}=128, especially over the last iterations of the simulations. As a matter of fact, the number of linear iterations required at each Newton step is roughly 20-25% higher than those required by the preconditioner adopting N_{blk}/N_{proc}=1.

Moreover, because of the lower diagonal dominance of the linear system matrix in the case of high CFL values reached when the simulation is close to convergence, the preconditioner also affects the non-linear path of the simulation at i=80, which corresponds to the iteration where the linear solver does not achieve the prescribed tolerance as the maximum number of linear iterations is met.

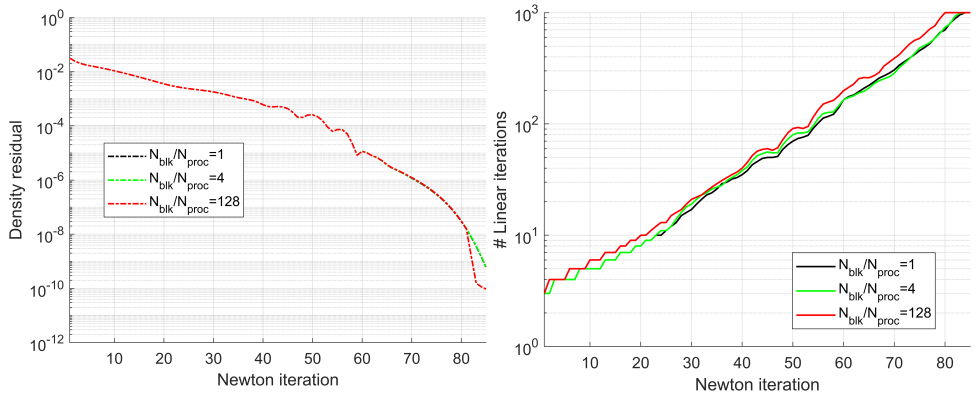

(a) (b)

Fig. 2.5 Effect of block partitioning 1^{st}: NACA M2

Eventually an additional simulation is run using a 2^{nd} order discretization, initialized from the converged 1^{st} order solution. In this case, the linear solver requires fewer iterations compared to the 1^{st} order solution because of the better initialization of the flow. In this case also the effect of the number of blocks is limited.

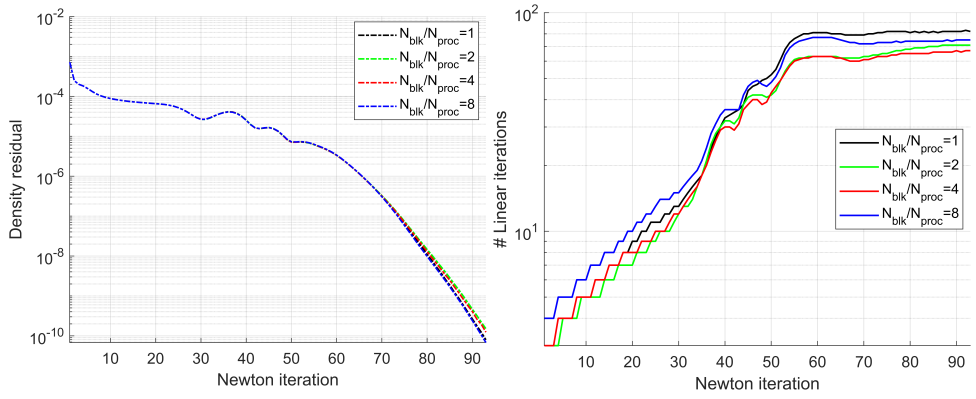

(a) (b)

Fig. 2.6 Effect of block partitioning 2^{nd} order: NACA M1

The assessment of the domain decomposition as a preconditioning method to the linear solver is summarized in Tab. 2.2, where the convergence time for each of

the studied configurations is shown. The variability of the total convergence time of the code when the Schwarz Additive preconditioner is coupled with the GMRES, is small. The fastest solution over mesh M1 is achieved when $N_{el}/N_{blk} \approx 3000$. This is adduced to the slight reduction of the total number of linear iterations necessary to achieve convergence at each non-linear step. It is thought that the lower number of iterations can be adduced to the different sparsity pattern of the linear system matrix after the block decomposition and cell reordering.

In the current implementation, the number of blocks is formed before their assignment to a certain processor. From a computational perspective, it would be better to use a double decomposition of the domain. As a matter of fact, *metis* partitioning algorithms tend to minimize the communication cost between different processors. For this reason, when $N_{blk} \neq N_{proc}$, it is suggested to apply a first decomposition for the overall domain to minimize the cost for parallel communication. A second decomposition, internal to the subdomains, would be necessary to generate the blocks for the Schwarz preconditioner. This second methodology has been tested throughout the thesis, but it was found that when large 3D domains are partitioned, the internal partitioning loop can lead to non-adjacent cells in the blocks, which impact negatively the performance. Moreover, as will be shown in Sec. 2.3, the Schwarz preconditioner might not be the best option in terms of computational time and stability. Hence, for robustness reasons, it was decided that the default utilization of the Schwarz preconditioner features $N_{blk} = N_{proc}$.

Table 2.2 Convergence time

N_{el}	Order	N_{proc}	N_{blk}/N_{proc}	N_{el}/N_{blk}	GMRES	Time [s]
49264	1	4	1	12316	(0.01,100,10)	310.56
	1	4	2	6158	(0.01,100,10)	322.72
	1	4	4	3079	(0.01,100,10)	311.1
	1	4	8	1540	(0.01,100,10)	420.88
49264	2	4	1	12316	(0.01,100,10)	152.57
	2	4	2	6158	(0.01,100,10)	141.72
	2	4	4	3079	(0.01,100,10)	108.58
	2	4	8	1540	(0.01,100,10)	165.64

2.2.2 Algebraic Multigrid

The idea behind multilevel methods is that many iterative linear solvers (especially point-implicit methods) are quite effective in reducing high frequency errors, but quite inefficient in reducing low frequency ones. For this reason, multilevel methods exploit the construction of coarse levels where original low frequency errors become of high-frequency. Hence, the latter can be efficiently resolved and eventually convergence is accelerated. For practical interests, multilevel methods can be used in a twofold way. The first possibility is to apply multilevel methods to the solution of the NS equations. In this case the multilevel method serves as a non-linear solver. This strategy is often referred to as Full-Approximation Storage (FAS). On the other hand, multilevel methods can be used as linear solvers/preconditioners to speed up the solution of the linear system arising at each Newton step. While similar in terms of computational steps, the effect of the two strategies on the non-linear convergence of the problem is quite different. In this section, only applications to steady problems will be discussed, while the extension to implicit unsteady solutions is trivial. The starting point of a multigrid method is the definition of the non-linear residuals of the NS equations on a fine grid:

$$\mathbf{R}_h(\mathbf{Q}_h) = 0 \tag{2.11}$$

where the subscript h indicates the fine level (or in general the current grid level when more than 2 levels are used to build the multigrid scheme). The application of the FAS strategy to this problem requires the definition of a coarse grid 'c' where a correction equation is solved to improve the convergence of the solution of the fine grid level:

$$\mathbf{R}_c(\mathbf{Q}_c) = \mathbf{R}_c(\mathbf{I}_h^c \mathbf{Q}_h^1) - \mathbf{I}_h^c \mathbf{R}_h(\mathbf{Q}_h^1) \tag{2.12}$$

where $\mathbf{R}_c$ and $\mathbf{Q}_c$ are the non linear residuals and solution on the coarse grid, $\mathbf{Q}_h^1$ is an approximate solution on the fine grid and $\mathbf{I}_h^c$ is an interpolation operator which maps the solution from the fine grid to the coarse grid. After the solution to the mapped residuals is found on the coarse grid, a correction step is necessary to interpolate the coarse grid solution to the fine grid one:

$$\mathbf{Q}_h^2 = \mathbf{Q}_h^1 + \mathbf{I}_c^h \left(\mathbf{Q}_c - \mathbf{I}_h^c \mathbf{Q}_h^1\right) \tag{2.13}$$

where $\mathbf{I}_c^h$ is the interpolation operator which maps a coarse grid solution to the fine grid one. The main advantage of the method is that a sufficiently accurate solution on the fine grid can be found by solving a much smaller problem on a set of coarser grids. The FAS Multigrid is quite common in both commercial and academic ([20, 21]) compressible flow solvers.

Another possibility for the application of Multigrid methods in a CFD solver, is to apply them directly to the solution of the linear system at each Newton iteration. At each non-linear step the Newton method requires to find an approximate solution to the linearized residual equation:

$$\left[\frac{\mathbf{I}}{\Delta\tau}+\frac{\partial\mathbf{R}^*(\mathbf{Q})}{\partial\mathbf{Q}}\right]^n\Delta\mathbf{Q}^n=-\mathbf{R}(\mathbf{Q})^n=\mathbf{A}\mathbf{x}=\mathbf{b} \tag{2.14}$$

The application of the multigrid method to the linearized residuals corresponds to the following algorithm:

Algorithm 3 2-Levels Multigrid algorithm

1: Apply m pre-smoothing steps: $\mathbf{x}_h^i=\mathbf{x}_h^{i-1}+\mathbf{S}_h(\mathbf{b}_h-\mathbf{A}_h\mathbf{x}_h^{i-1})$
2: Define the residual and the error equation $\mathbf{r}_h=\mathbf{b}_h-\mathbf{A}_h\mathbf{x}_h$ and $\mathbf{A}_h\mathbf{e}_h=\mathbf{r}_h$
3: Restrict the residual equation to a coarse space $\mathbf{r}_c=\mathbf{I}_c^h\mathbf{r}_h$
4: Compute the coarse level matrix $\mathbf{A}_c=\mathbf{I}_c^h\mathbf{A}\mathbf{I}_h^c$
5: Find the coarse level correction $\mathbf{e}_c=\mathbf{A}_c^{-1}\mathbf{r}_c$
6: Prolongate the error to the fine level $\mathbf{e}_h=\mathbf{I}_h^c\mathbf{e}_c$
7: Apply n post-smoothing steps $\mathbf{x}_h^i=\mathbf{x}_h^{i-1}+\mathbf{S}_h(\mathbf{b}_h-\mathbf{A}_h\mathbf{x}_h^{i-1})$

In Alg. 3, since the multigrid method is applied to a linear problem, the restriction and prolongation steps can be directly applied to the error equation to build the respective coarse level counterparts of the error vector $\mathbf{e}_c$, the residual vector $\mathbf{r}_c$ and the coarse level matrix $\mathbf{A}_c$. The coarse grid correction does not require to find the exact solution to the error equation, so a general linear iterative solver can be used to find $\mathbf{e}_c$. It is common to use fast smoothers on the coarse level in order to balance the time necessary to build and apply the prolongation and restriction operators.

While both strategies have seen a certain level of success in the CFD community, in the present work of thesis, only the application of the multigrid in a linear manner has been tested. As a matter of fact, the application of the non-linear multigrid as a solver for the N-S equations leads to fast steady-state convergence, it also hinders the reduction of residuals to machine-precision ([8]).

The definition of the coarse levels, and consequently of the prolongation and restriction operators can be tackled with two different approaches. When the combination of fine levels unknowns to build coarse levels, is defined based on the grid itself, the multigrid method is referred to as Geometric. On the other hand, for linear solvers, the combination of fine levels unknown is based on the characteristic of the fine level matrix, then the multigrid method is defined as Algebraic. In this case, no additional grid is necessary to build coarse spaces. This comes as an advantage in the case of complex domains and irregular grids, where it is difficult to define a grid hierarchy for the definition of coarse levels. For this reason, the Aggregation Based variant of the Multigrid method has been implemented in the code.

In order to fully define the multigrid linear solver, the following steps have to be followed:

- Define the prolongation and restriction structure
- Define prolongation and restriction weights
- Define coarse level smoother

As previously said, the coarse level variables are basically defined upon availability of the linear system matrix A_h. The first step for the definition of the method, requires defining a suitable set of unknown variables on the coarse space, which sets the structure for the prolongation and restriction operators. While different methods have been investigated in the literature (like the C/F splitting or maximum independent set, [22]), in the present work the construction of coarse spaces is defined according to the concept of strength of connection, in a similar fashion to the works of Raw ([23]) and Weiss et al. [4]. In particular, for a given real number θ_h we need to check the following inequality:

$$-A_{ij} \geq \theta_h |\min_k A_{ik}| \tag{2.15}$$

When the inequality is satisfied, the unknowns i and j are said strongly negatively connected. Another suitable definition is to substitute $|\min_k A_{ik}|$ with $\sqrt{A_{ii}A_{jj}}$. For a given fine level unknown, we will define a subset S_i, which contains all the strongly connected variables to the unknown i. The final construction of the prolongation and restriction operator will then be based on Alg. 4. The algorithm performs a two-stage

grouping of fine level variables, based on the strength of connection, while trying to match the user specified n_{min} and n_{max}, which define the minimum and maximum number of cells per group, respectively. The strength of connection is defined in a slightly different manner with respect to Eq. 2.15. In particular, the absolute value is considered in place of the minus on the LHS. For this reason, the strong connections can also occur in the case of a positive entry in the linear system matrix. Moreover, an undirected graph is used to find the strong connectivity. As a matter of fact, the linear system arising in the CFD solver is non-symmetric ($A_{ij} \neq A_{ji}$ in general). In order to define if two variables are strongly connected, the inequality has to be satisfied at least in one sense (namely at least on one of the two entries A_{ij} and A_{ji}).

The first part of the algorithm handles the initial grouping of the cells. The second part performs a merging between existing groups in order to favor the formation of groups of similar size. The performance of the grouping algorithm is shown in Fig. 2.7, where the groups distribution is shown for both a laminar case and a turbulent case. The image refers to an already initialized flow field, which allows to visualize the performance of the algorithm over a sufficiently converged solution where the coupling between the cells has already been established. Both the steps, mainly the initial grouping and the subsequent merging of groups aim at distributing a number of cells per group corresponding to n_{min}, while n_{max} serves as major parameter for allowing the merging among the groups in the second step of the algorithm.

In the case of coupled equations, like in the case of the N-S equations, similarly to other implementation in CFD codes, the coupling between cells is define based on the density equation entry of the linear system matrix.

The prolongation operator is built by using the approach of unsmoothed aggregation, namely:

$$I^h_{c\,ij} = \begin{cases} 1 \; if \; i \in S_j \\ 0 \; if \; i \notin S_j \end{cases} \tag{2.16}$$

The restriction operator is instead built using the Galerkin method, namely:

$$I^c_{h\,ij} = I^h_{c\,ji} \tag{2.17}$$

while the coarse space matrix A_c is obtained as:

$$A_c = I^c_h A_h I^h_c \tag{2.18}$$

Algorithm 4 Aggregation algorithm

For each cell i define the strength of connection with other cells in the fine level grid S_i
Define the subset of non grouped fine levels variables: $U = i \in \{1, \ldots n\}$
for all $i \in U$ **do**
    Start a new group G
    Set $n_G = 0$
    for all $j \in S_i/U$ **do**
        Assign the cell j to G until $n_G < n_{max}$
        Set $n_G = n_G + 1$
        $U = U/j$
    end for
    if $n_G < n_{min}$ **then**
        for all $j \in G$ **do**
            for all $k \in S_j/U$ **do**
                Assign the cell k to G until $n_G < n_{min}$
                Set $n_G = n_G + 1$
                $U = U/k$
            end for
        end for
    end if
end for
for all $i \in G_i$ **do**
    Count number of strong connections between groups i and j, n_{ij}
    for all $m : n_{im} > 0$ **do**
        if $n_i < n_{max}$ **then**
            Find the group index k such that $n_{ik} = max_j n_{ij}$
            if $n_i + n_k < n_{max}$ **then**
                Merge groups i and k
                Set $n_i = n_i + n_k$
            end if
        end if
    end for
end for

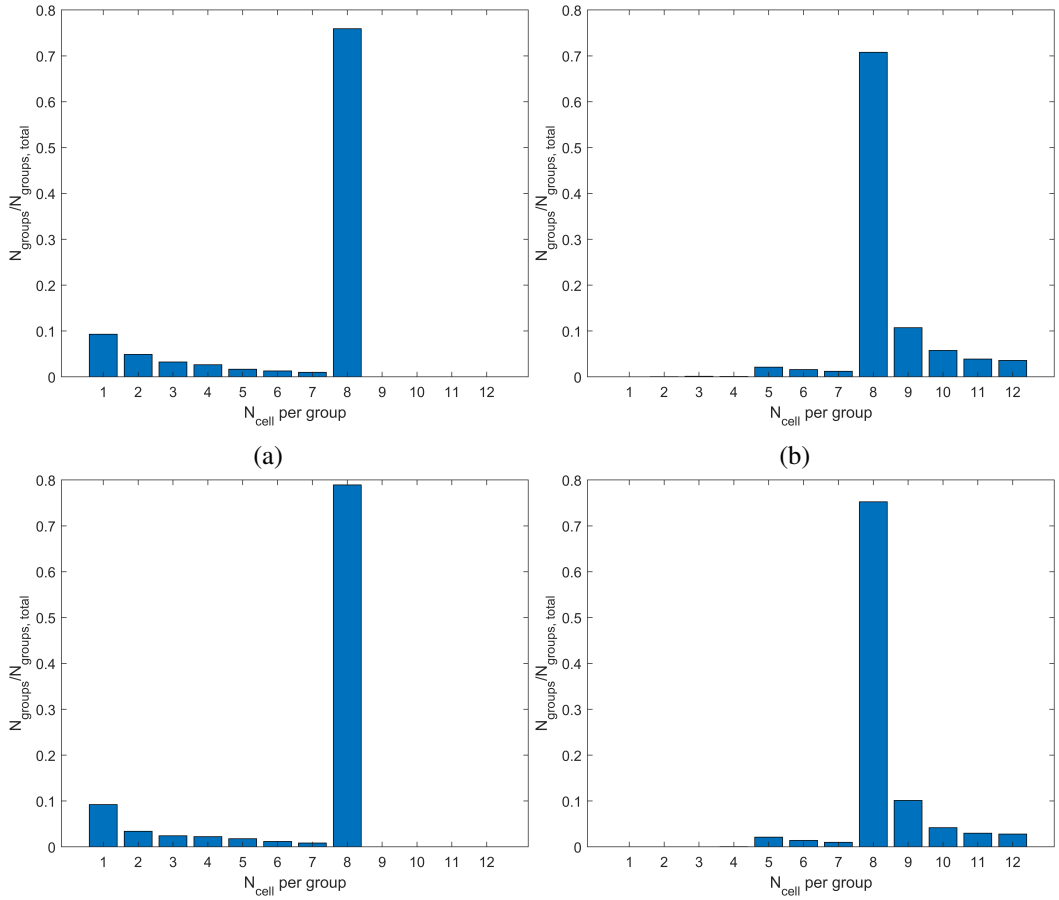

Fig. 2.7 Groups distribution: laminar flow over NACA0012 profile (top) and turbulent flow over LS89 high pressure vane (bottom) for n_{min}=8 n_{max}=12. First grouping (left) and distribution after merging (right)

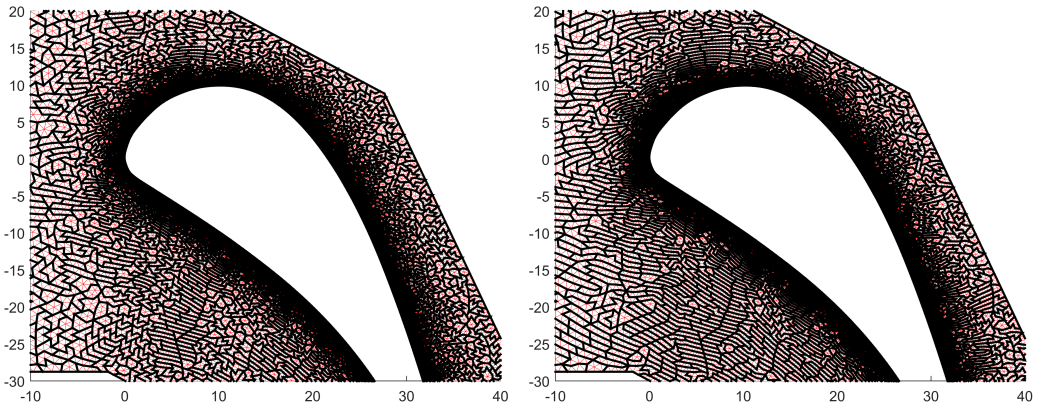

(a) (b)

Fig. 2.8 Effect of the strength parameter θ: 0.3 (a), 0.5 (b)

The second step for the Multigrid algorithm requires the definition of the strategy for visiting iteratively coarser and finer levels. In the present implementation, the common V cycle and W cycle strategies have been implemented. In the V cycle, the solution from finer levels is prolonged to coarser levels, until the last level is found. At that point, restriction operation take place to interpolate the coarse grid corrections to finer levels. In the W cycle, after the residuals have been prolonged to the coarsest level, the solution is prolonged and restricted back and forth between coarse and finer levels. The cycle is more demanding but is also more stable than the simpler V cycle.

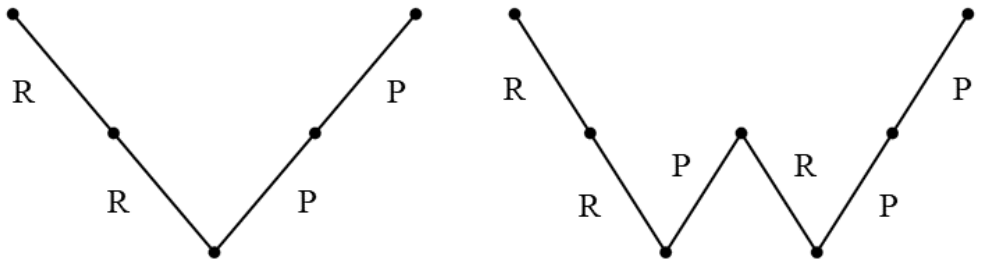

(a) (b)

Fig. 2.9 AMG cycles definition: V cycle (a) and W cycle (b). R: restriction, P: prolongation

Case	Toll	Time [-]
Fixed V cycle (0,4,2,1)	-	0.57
Toll V Cycle (0,20,20,1)	0.1	0.65
Fixed W cycle (0,4,2,1)	-	0.50
Toll W Cycle (0,20,20,1)	0.1	1.0

Table 2.3 Convergence time

The third step of the AMG cycle is to apply a smoother at each level, to reduce the error before any restriction/prolongation operation. As far as the smoother (linear solver) is regarded, the Lower-Upper Symmetric Successive Over Relaxation method was chosen (Eq. 2.19). The single iteration of the smoother is the following:

$$\mathbf{x}^{i+1} = (\mathbf{D} + \omega\mathbf{L})^{-1} \left\{ \omega\mathbf{b} - [\omega\mathbf{U} + (\omega - 1)\,\mathbf{D}]\,\mathbf{x}^{i} \right\} \tag{2.19}$$

In the case of coupled flow equations, the smoother is applied cell-wise, and the matrix $\mathbf{D}^{-1}$ is computed by means of a Lower-Upper decomposition of the diagonal block of the linear matrix $\mathbf{A}$. In the case of scalar transport equations, the smoother is applied point-wise. The choice was dictated by the easiness of implementation and the fast computational time associated to the forward/backward substitution associated with the LU decomposition of the matrix.

As far as the cycling strategy is concerned, it can be controlled in two different ways, which have been tested throughout the thesis. The first possibility is to control the convergence of the linear solver at each grid level. In this case, the restriction/prolongation operations take place only when a specified reduction of the linear residuals at the current level is achieved. Another possibility is to fix the cycle by specifying the number of smoothing steps to be performed before any prolongation/restriction operation. The effect of the control strategy for the cycling operation is shown in Fig. 2.10, where the number of linear iterations at each Newton step is shown for the two approaches.

The check has been performed using both a V and a W cycle shape, with aggressive coarsening (n_{min}=8) and the LU-SSOR smoother. It is shown that for the V cycle, despite increasing the overall number of linear iterations in correspondence of high CFL values, fixing the number of smoothing steps (to a low value), is already sufficient to guarantee proper convergence of the preconditioned GMRES.

On the other hand, for the W cycle, the number of iterations is preserved, while the increasing number of sweeps performed at each level leads to higher computational times. Hence, the analysis of the AMG as a preconditioner has been performed by fixing the number of smoothing steps rather than checking for a specified drop of the norm of linear residuals at each coarse level.

The AMG has been eventually tested to determine the effects of different cycle parameters on the convergence rate of the simulations: shape of the cycle (V or W), number of grouping levels, coarse grid smoother, number of smoothing steps at each cycle and number of allowed cells in a group. A sensitivity analysis to these parameters is shown in Appendix A, where the performance of the AMG as a preconditioner is tested for both laminar and turbulent solutions configurations.

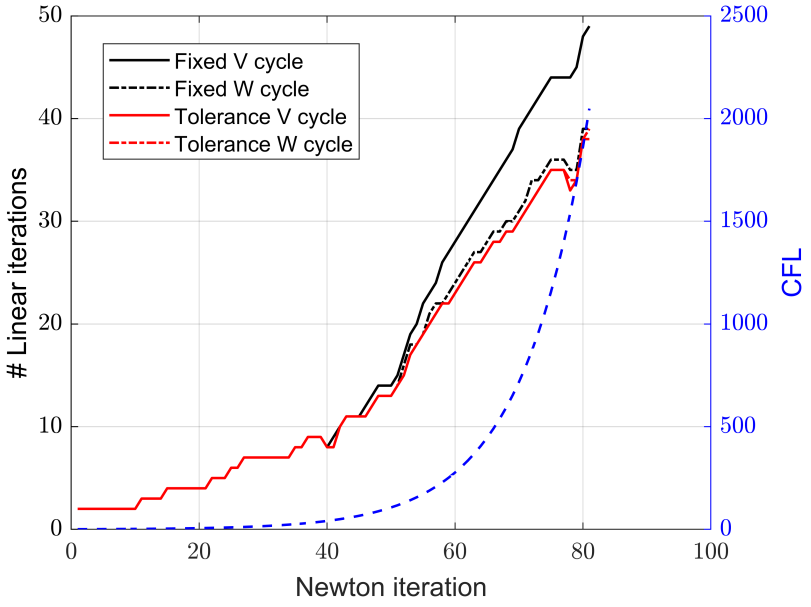

Fig. 2.10 Effect of cycling strategy on convergence

2.3 Analysis of the linear solvers

Once that the preconditioners and their setup have been analyzed, the convergence of the overall linear solver has been assessed using two different test-cases which are of interest for the applications of the code. The first one is the compressible NACA0012 airfoil run at Ma=0.5, Re=5000, which has been exploited for the analysis of the preconditioners in various works such as [6, 24, 25]. The second test case is the

turbulent high pressure vane LS89 studied by Arts et al. ([26]), which is of interest because represents the first application of the solvers for turbomachinery relevant test-cases. The analysis provided here-after aims at investigating the performance of the overall linear solver implemented in the code, assessing the influence of the preconditioner and of the parameters for the continuation of the Restarted GMRES, which has also been compared to LU-SSOR linear solver. The characteristics of the test cases used for the evaluation of the performance of the non-linear solution strategy are reported in Tab. 2.4.

Table 2.4 Test cases for the analysis of the linear solver

Case	Regime	Mesh type	N_{DOF}	N_{CPU}	Ma [-]
NACA M1	Laminar	2D triangular	49234	4	0.5
NACA M2	Laminar	2D triangular	180228	4	0.5
LS89 MUR43	Turbulent	2D hybrid	43756	4	0.83

The convergence time for the laminar test case are reported in Fig. 2.11 and Fig. 2.12 for the coarse and the fine mesh, respectively. The figures also show the effect over the convergence time of the linear tolerance. The AMG-preconditioned GMRES provides the lowest convergence time for $0.1<\varepsilon<0.001$, while the highest convergence time is reached for the LU-SSOR method at the tightest linear tolerance over the coarse mesh test case and using the ILU-preconditioned GMRES for the finest mesh. For both cases, Fig. 2.13 and 2.14 report the number of linear iterations at each non-linear step. At ε=0.1, all the methods tested present a wavy behavior in terms of number of inner iterations and in the density residuals drop (see Fig. 2.15). Despite providing the lowest convergence time, the low tolerance hinders the non-linear convergence of the code. This is particularly true for the ILU(0) GMRES and the LU-SSOR. The number of non-linear iterations by approximately 30% for both of them. For the AMG, the effect is less evident, where an increase of $\approx$ 25% of the Newton iterations is obtained compared to the ε=0.001 case. The increase in convergence time for tighter tolerances is easily addressed considering the variation of inner iterations for the three different solvers. For the finest mesh, the total number of inner iterations increases by $\approx$ 50% at every drop of the linear tolerance of one order of magnitude for the AMG. For the LU-SSOR and the ILU, the number of linear iterations required to convergence at each Newton iteration increases by a factor of $\approx$3. In general, the faster convergence time obtained by the AMG-GMRES, The better non-linear convergence of the method is adduced to

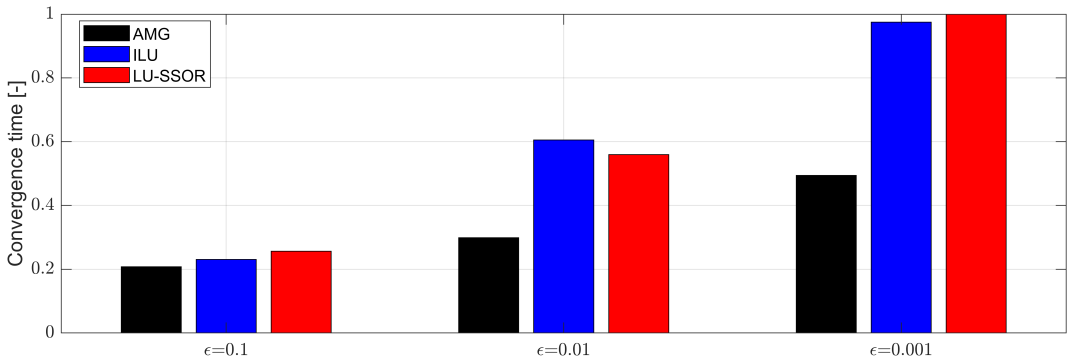

Fig. 2.11 Non-dimensional convergence time for NACA M1 test case

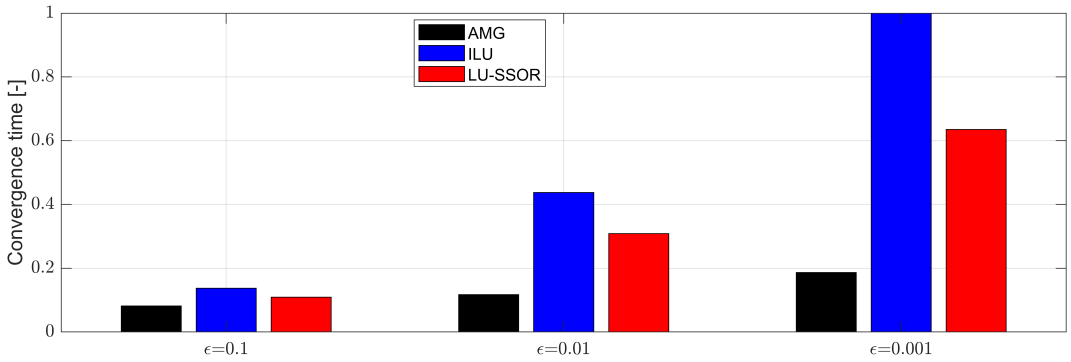

Fig. 2.12 Non-dimensional convergence time for NACA M2 test case

the fact that for high CFL numbers, the linear system matrix has higher condition number, being the diagonal damping of the Newton iteration lower. For this reason, the cell-coupling obtained with the coarsening algorithm succeeds in recovering cell-to-cell dependence during the preconditioning, which is probably lost when ILU(0) is used. On the other hand, the worse behavior in terms of convergence properties of the LU-SSOR solver could be expected for high CFL numbers due to its point-implicit characteristic.

Figure 2.16 shows the convergence time for the turbulent LS89 high-pressure turbine vane. For the turbulent test case, the results are slightly different from the laminar test case. As a matter of fact, the LU-SSOR provides the lowest computational time for the coarse linear tolerance, while the AMG-preconditioned GMRES is the fastest for the tightest linear tolerance. At moderate tolerances, the performance of the two solution strategies is the same. Similarly to laminar test case, the AMG proves to be a more reliable preconditioner to the GMRES compared to the ILU(0) factorization.

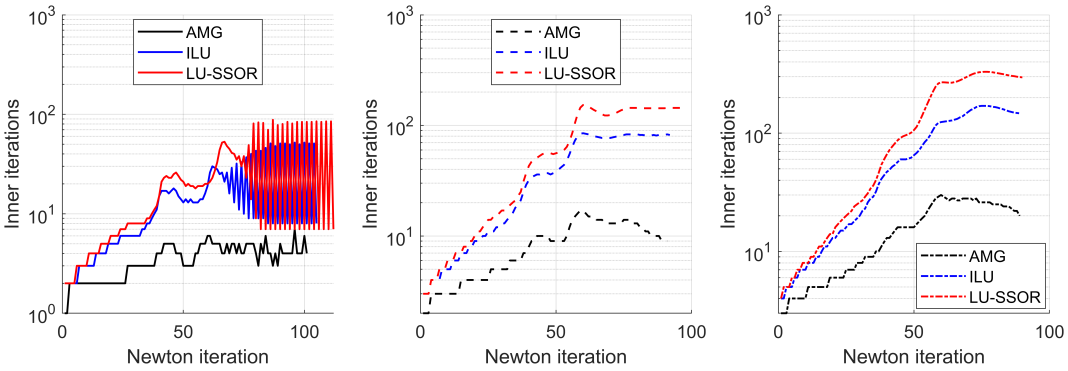

Fig. 2.13 Number of linear iterations at each Newton step - NACA0012 Mesh M1. From left to right: ε=0.1, ε=0.01, ε=0.001

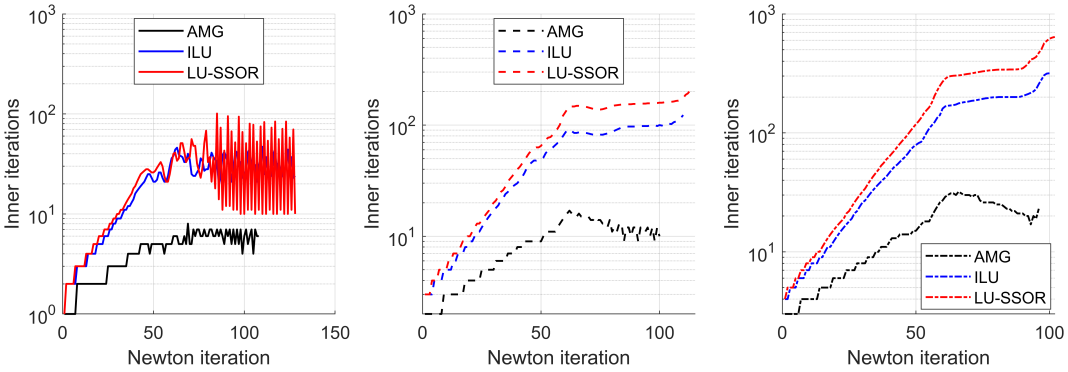

Fig. 2.14 Number of linear iterations at each Newton step - NACA0012 Mesh M2. From left to right: ε=0.1, ε=0.01, ε=0.001

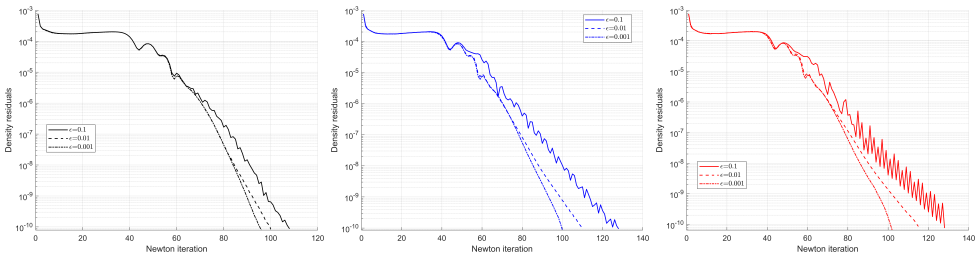

(a) AMG GMRES (b) ILU(0) GMRES (c) LU-SSOR

Fig. 2.15 Density residuals convergence - NACA0012 M2

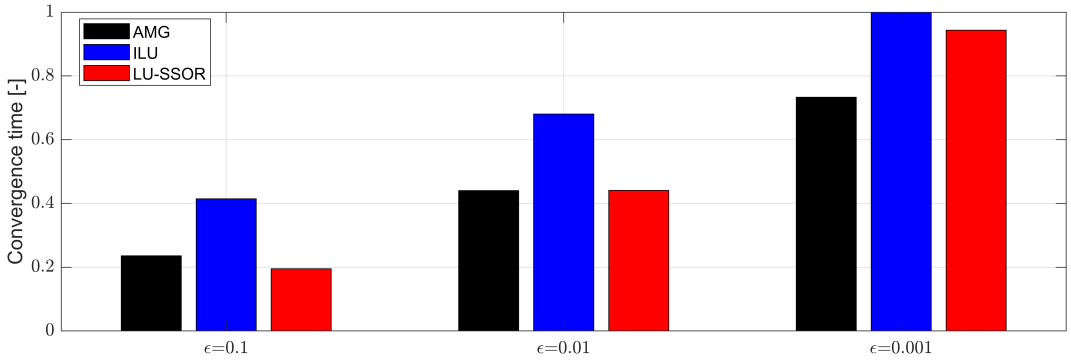

Fig. 2.16 Non-dimensional convergence time for LS89 MUR43 test case

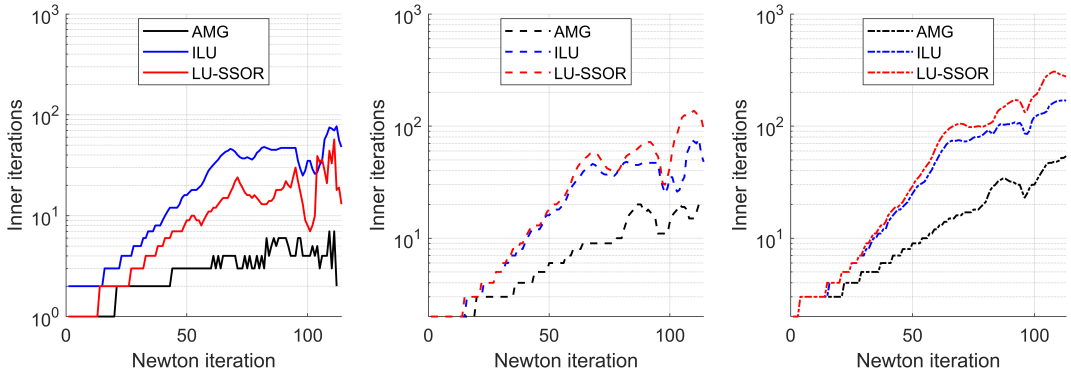

Fig. 2.17 Number of linear iterations at each Newton step - LS89 MUR43

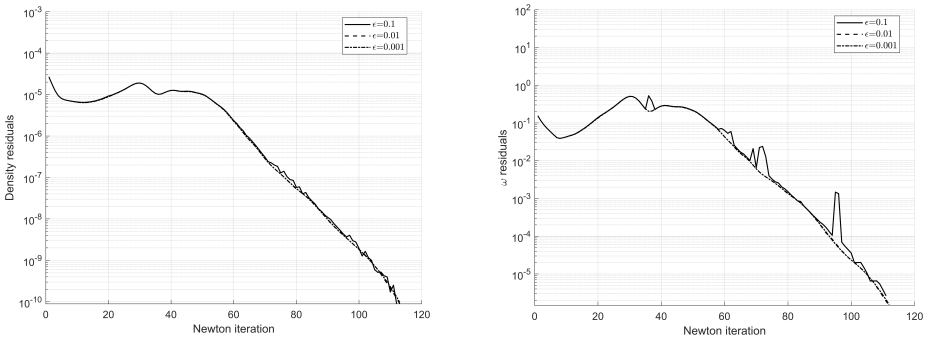

(a) Density residuals

(b) ω residuals

Fig. 2.18 Residuals convergence - AMG-GMRES

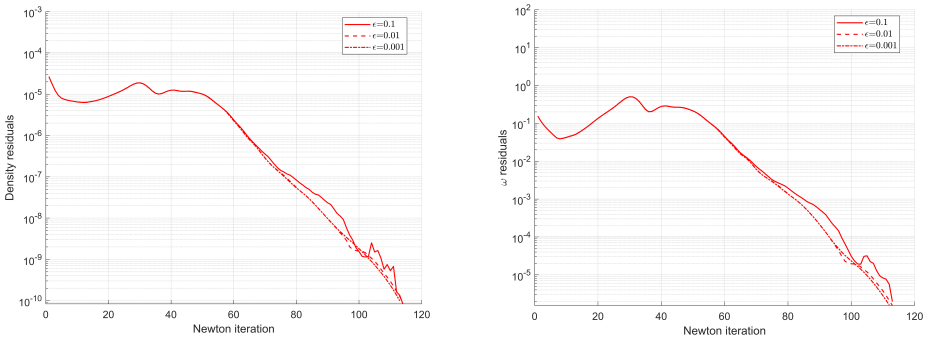

(a) Density residuals

(b) ω residuals

Fig. 2.19 Density residuals convergence LU-SSOR - LS89

In order to analyze the sources for the different behavior of the code for the different characteristics of the linear solver, a breakdown of the cost of each operation in the solution phase is presented both for the NACA and the LS89 test cases in Fig. 2.20. The breakdown of the costs of different phases of the solution process considers the following terms:

- Linear Solver: either GMRES or LU-SSOR; this contribution also accounts for the application of the right-preconditioner in the GMRES
- ILU(0) factorization cost
- Build-up of coarse space for the AMG: grouping between cells and application of restriction and prolongation operators to the linear matrices
- AMG solver: solution of the correction equations over the coarse spaces

The profiling was performed running the same simulations shown in the previous part of the chapter, using a 0 level of optimization during the compilation of the code. This is thought to be the reason behind the slight difference between the performance of the solvers, compared one to the other, which is noticeable from the turbulent test case. The profiling is performed using a moderate linear tolerance, set to 0.01.

The LU-SSOR solver time is the sum of the inner iteration time and the set-up for the block-ILU factorization of cell diagonal blocks. The latter is negligible with respect to the iteration cost itself (<0.2%). Thus the reported results only refer to the iteration cost, while the factorization costs have been considered negligible. The AMG spends the lowest time in the GMRES routine, due to the noticeably lower

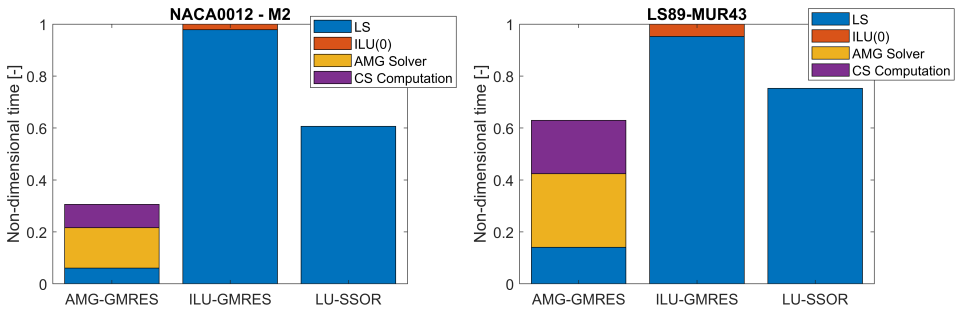

Fig. 2.20 Breakdown of computational costs for convergence: LS - Linear Solver, ILU(0) - ILU Factorization, AMG Solver - Application of the AMG cyclying strategy, CS Computation - Computation of the coarse space and related matrices

number of inner iterations required at each non-linear step. The total time spent in the GMRES accounts for roughly 20% of the total linear solution time, both for the turbulent and the laminar test cases, while roughly 80% of the time is spent to construct the coarse space and to apply the preconditioning. On the other hand, the ILU(0) preconditioner is less efficient compared to the AMG. Despite the lower time necessary to build the preconditioner ($\approx$4 times faster than the AMG), the high number of linear iterations required to achieve convergence hinders the overall performance of the solver. Comparing the laminar and the turbulent test cases, the performance of the AMG compared to the other two cases is slightly worse. This is related to the build-up of coarse matrices for turbulent variables and also to the fact that the number of iterations required to achieve convergence for the turbulent variables is generally lower than the ones required for flow variables, thus the efficiency of a more expensive preconditioner is not counterbalanced by a substantial reduction of the overall solution cost at each iteration. It must also be underlined that, for a low number of inner iterations, the cost for the orthogonalization of the GMRES is lower because of the lower number of Krylov vectors. For this reason, the AMG reduces an already low number of inner iterations. This is quite different from the laminar case, where the number of inner iterations required by ILU(0) preconditioned GMRES is around the maximum number allowed before restarting, where the cost of a single GMRES iteration is the highest.

The latter aspect is analyzed by measuring the time necessary to perform the various steps of the building and the application of the preconditioner during the solution phase. The analysis is performed over a single iteration run at CFL=10,000 over a converged solution. This mimics the behavior of code close to non-linear

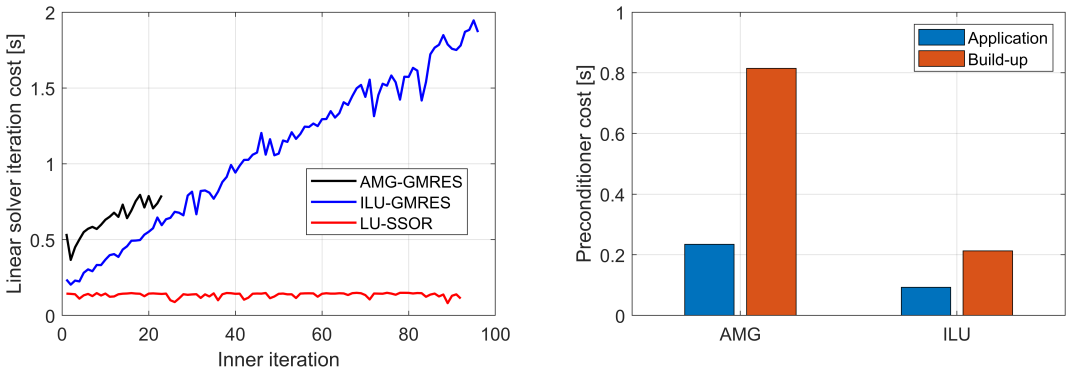

Fig. 2.21 Breakdown of computational costs for a single iteration for the NACA airfoil test-case

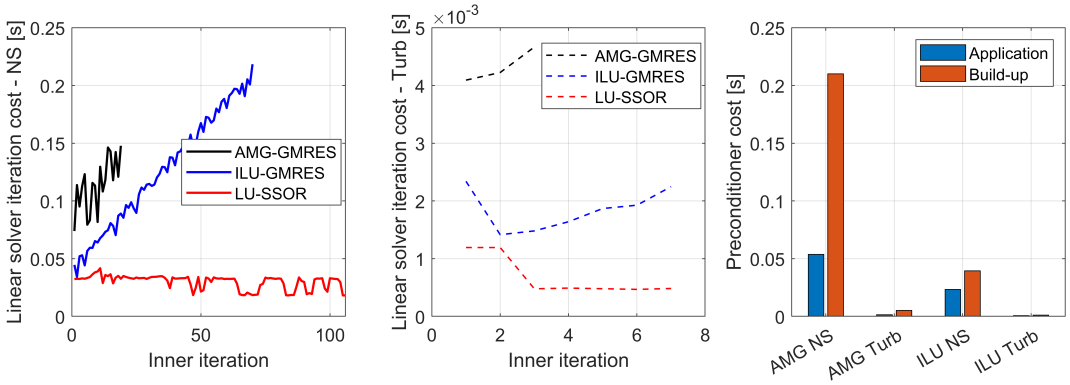

Fig. 2.22 Breakdown of computational costs for a single iteration for the LS89 vane test-case

convergence when the ramp of the CFL is active. Moreover, the cost of each GMRES iteration at each new Krylov vector addition is shown.

Figures 2.21 and 2.22 report the results of the analysis for the laminar and the turbulent test case, respectively. While the iterations of the of the LU-SSOR present the same cost over the full non-linear iteration solution, the cost of the GMRES linearly increases with the number of Krylov vectors built at each inner iteration. The cost of each GMRES iteration reported in the figure take into consideration both the application of the preconditioner and the bare GMRES iterations. As mentioned before, the reason behind the worse performance of the ILU(0) preconditioner against the AMG is related to the increased number of linear iterations. As a matter of fact, despite the increase of overall build-up cost for the AMG, and also the cost for the application of the coarse correction ($\approx 40\%$ more demanding than the ILU triangular solver application), the low number of inner iterations allows for an overall speed-up of the computation. For the LU-SSOR solver, the cost of each inner iteration is

almost constant. Yet again, its performance against the AMG-GMRES depends on the reduction of inner iterations required by the latter at each non-linear step.

Looking at the turbulent test-case results, it is noticeable that as far as the flow solution is considered, similar considerations to the laminar case can be drawn. The main difference is that regardless of the preconditioner, the GMRES takes less inner iterations than the LU-SSOR but at a higher cost. On the other hand, the turbulent field solution (in this case for the k equation), requires a low number of inner iterations compared to the NS equations. For this reason, the cost of the build-up and the application of the AMG can lead to an increased computational burden, which affects its performance compared to the other solvers.

The last comparison between the solvers is performed for a fixed CFL=20.0, with a linear tolerance equal to ε=0.01. As a matter of fact, the CFL ramp might not be optimal for more involved test cases and it might lead to solver divergence. So this analysis is necessary to establish the performance of the solvers for cases where the ramp is not suitable and the CFL number cannot be increased over a certain threshold. The results are reported in Fig. 2.23 and 2.24, for the NACA0012 airfoil and the LS89 vane, respectively. As the number of inner iterations required by the Newton method decreases, the build-up of the preconditioner and its application throughout the GMRES iterations become the main cost for the linear solver. Both for the turbulent and the laminar test-cases, the LU-SSOR yields the fastest computational time compared to the GMRES solver. For the laminar test case, Fig. 2.21 shows that the cost for the build up of the AMG coarse space is approximately equivalent to the cost of two GMRES iterations, while the applications of the AMG correction takes between 50% and 30% of the overall iteration cost, over the first ten non-linear iterations. For the ILU-GMRES case, the build-up of the preconditioner costs less than a single GMRES iteration, while the application of the triangular solver takes between 25% and 15% of the total GMRES iteration cost. Similar considerations can be drawn for the turbulent test case. Eventually, the choice of the solver is mainly dictated by the non-linear continuation strategy (either at constant CFL or using a ramp, whose parameters need to be optimized depending on the applications).

Eventually Tab 2.5 reports the cost for the storage of the linear system matrix for the different solvers. The increase in RAM requirements is normalized by the memory cost associated to the storage of the linear system matrix. The ILU(0) preconditioner requires almost 1.5 times the memory requested for assembling the

Table 2.5 Memory usage increase

Case	AMG-GMRES	ILU-GMRES	LU-SSOR
NACA	≈ 0.21	≈ 0.5	≈ 0.12

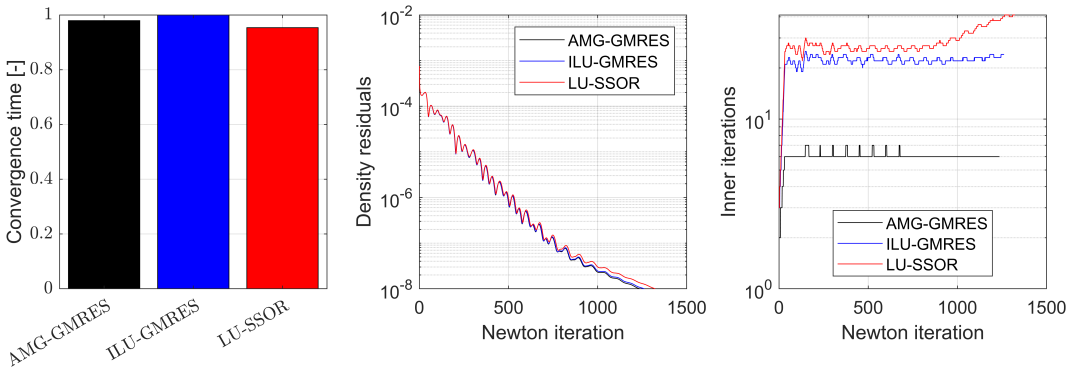

Fig. 2.23 NACA0012 M2 - CFL=20.0

linear system matrix as the 0-level of fill-in induces the same non-zero structure for the Jacobian matrix and the preconditioner. The memory increase is associated with the storage of the LU factorization, while the same sparsity pattern of the matrix **A** can be used. A slight difference needs to be considered as all the entries necessary for the parallel solution are not stored for the preconditioning, but their effect on the memory requirement is negligible. The LU-SSOR additional memory requirement is instead related to the inversion of 5×5 blocks for each cell, summing up to more than 10 % of the Jacobian matrix. A higher memory usage is instead required for storing AMG coarse matrices and prolongation and restriction operators. The former takes around 21 % of the Jacobian matrix, while ≈ 2 % of the memory is required to store operators necessary to interpolate from coarse to fine levels.

The comparison of the predictions of the NACA0012 airfoil and some results found in the literature, for the same test case, are shown in Tab. 2.6. The pressure and skin drag coefficients are compared to the findings of other Finite Volume based solvers. The predictions of Hybflow are reasonably close to the results of other researchers. It must he said that the employed grid is not tailored for the simulation of external aerodynamic flows, which can explain the difference with the predictions reported in [27] and [28].

A comparison of the loading prediction of the LS89 with the experimental findings is shown in Fig. 2.25. While the front loading of the blade is correctly

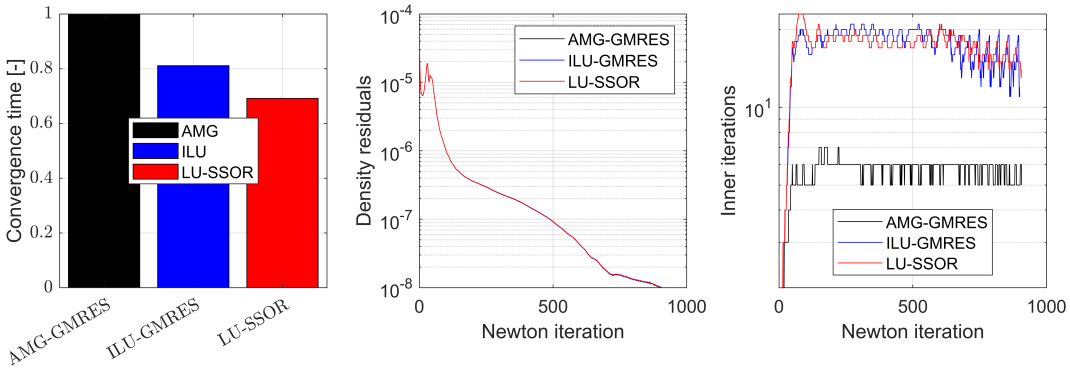

Fig. 2.24 LS89 MUR43 - CFL=20.0

Table 2.6 NACA0012 - Comparison with literature predictions

Method	N_{DOF}	Order	$C_{D,p}$	$C_{D,f}$	C_D
FVM Hybflow	1.8×10^5	2	0.00229	0.0330	0.0559
FVM [28]	5.2×10^5	2	0.00228	0.0328	0.0556
FVM [27]	3.1×10^6	2	0.00228	0.0327	0.0555
FVM [29]	$3.0\text{-}16.4\times10^5$	2	0.002249-0.02297	0.03247-0.03291	0.0554
SVM [30]	3.4×10^4	5	0.00222	0.0324	0.0546

captured, the proper acceleration in the aft region is not reached. This is induced by the usage of a uniform pressure at the outlet boundary, which prevents from a proper acceleration of the flow over the SS. As it was reported in [31], the use of the experimental pressure measured as outlet boundary condition allows to retrieve a better prediction of the loading compared to a uniform static pressure condition.

The last assessment of the solvers regards its speed-up in parallel applications. While all the previous analysis has been performed using 4 processors, the scalability of the code using both the preconditioned GMRES and the LU-SSOR solvers has been analyzed on the laminar test case. The speed-up is assessed using a constant CFL=5.0 over 100 iterations. Results of the speed-up of the solver are reported in Fig. 2.26, where the solvers performance is compared to a reference speed-up. The reference solution is the obtained on 4 processors. While the LU-SSOR achieves a a good scalability compared to the perfect speed-up, the AMG-GMRES instead slightly loose performance as the number of processors is increased. It stabilizes at around 80% of the perfect scalability.

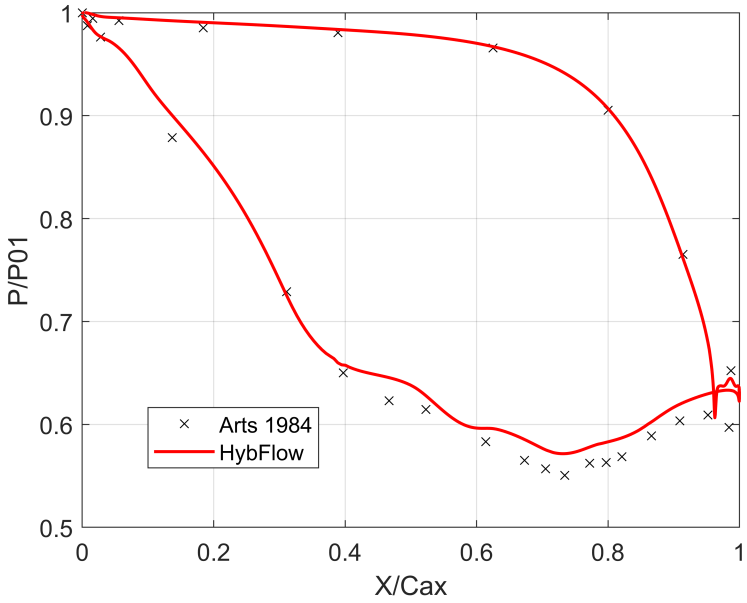

Fig. 2.25 LS89 MUR43: Loading prediction

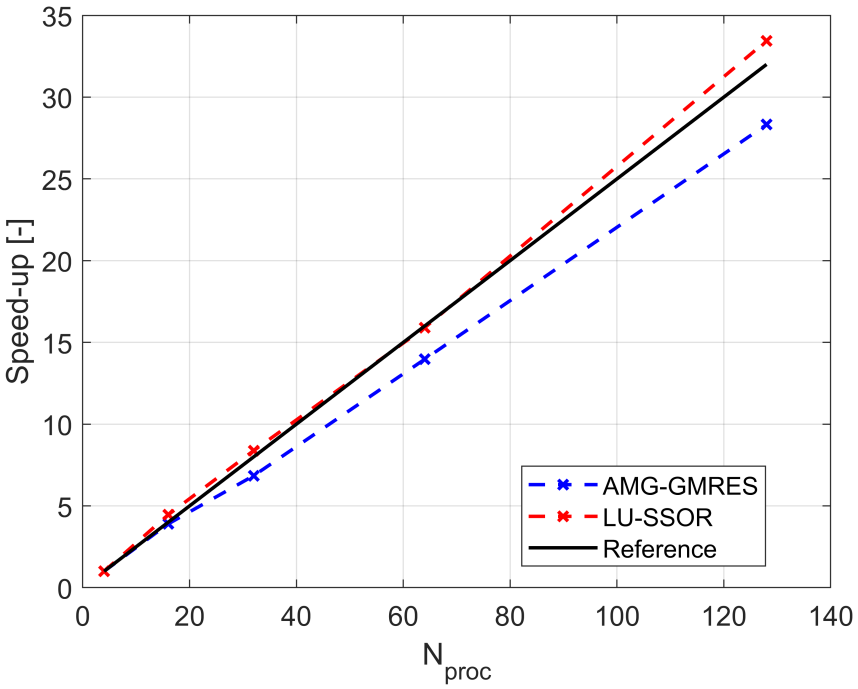

Fig. 2.26 Hybflow speed-up

Chapter 3

High-Order Reconstruction

The third chapter of the thesis is devoted to the extension of the code to higher order discretization. The latter has been a major trend in the recent development of CFD codes, providing advantages in terms of computational time and accuracy compared to lower order ones (second order). The chapter is organized as follows:

- First an introduction to high-order methods is presented, highlighting potential advantages over lower order ones
- The implementation of two different high-order reconstruction developed for unstructured Finite-Volume solvers is discussed
- The application of the high-order methods is compared for a series of inviscid, viscous and turbomachinery test cases, pointing out potential advantages compared to typical second order discretization

3.1 Introduction to High Order Reconstruction

The introduction of high-order methods for numerical solver has seen a major increase in popularity over the last two decades, as potential advantages both in terms of accuracy and overall computational time (for a specified threshold error) can be achieved ([32]). The development of high-order methods has seen major applications both in the context of Discontinuous-Galerkin, Finite-Elements and Spectral Elements methods. Some examples of high-order discretization methods

for turbomachinery applications can be found in the work of Brunet et al. [33] and Cassinelli et al. [34]. On the other hand, higher order Finite Volume codes have been somehow limited in this sense.

The typical approach enforced in FV solvers stems from the work of Barth and Friederickson [35], who introduced the possibility of generating high-order schemes upon availability of a k-exact reconstruction of the flow variables, which can be expressed by means of Taylor series about a specified point. In most of later development of FV methods, a k-exact reconstruction is typically enforced by means of polynomial shape functions of order k. The determination of polynomial coefficients can be then carried with two different approaches. The most common procedure is to adopt a certain reconstruction stencil, while minimizing the reconstruction error associated to mean flow variables or their point-wise values over the full reconstruction stencil. Examples of this approach can be seen in the works by Cueto et al. [36], who proposed a high-order reconstruction based on a Moving-Least Square method with exponential weighting kernel and in the work by Antoniadis et al. [37] where a high-order mean preserving reconstruction is implemented by means of Legendre polynomials. Another possible strategy is the method of successive derivatives. In this case, the polynomial coefficients can be obtained by means of successive differentiation of "available" lower order derivatives ([38, 39]) and a backward correction step necessary to preserve the accuracy of flow gradients.

Despite the potential advantages of high-order reconstruction schemes, some drawbacks still exist, the biggest coming from the necessity to guarantee a monotone solution and in general related to avoid overshoots/undershoots close to flow field discontinuities. This problem is addressed in the literature by means of two different strategies. On one-hand, there is the possibility of developing Essentially-Non-Oscillatory (ENO) schemes, also in the form of Weighted ENO (as in [40]) or Centered ENO (as in [27]). While in the former cases, the monotonicity of the solution is enforced by using different reconstruction stencils at the cost of evaluating polynomial coefficients over different groups of reconstruction cells, the latter adopts a smoothness indicator which allows to individuate regions of non-smooth solutions where high-order polynomial terms can be dropped. Besides the computational advantage of having a fixed stencil, CENO schemes are also uniformly accurate in regions where the solution is smooth. On the other hand, monotonicity can be enforced by means of gradient limiters, which can be used to build a Monotonic Upwind scheme (MUSCL) as in the work by Michalak and Gooch [41]. Additional

disadvantages related to high-order methods is the inherent complexity related to the management of high-order polynomial approximations. The necessity of reconstructing solution variables by means of polynomials requires the definition of "extended" reconstruction stencils (with respect to second order computations). The problem is exacerbated by the fact that the determination of reconstruction coefficients is reduced to an over-determined linear problem, whose characteristic matrix features a very high condition number. An alleviation to the problem is the use of large reconstruction stencils as in [37] or [42]. In parallel computations, this means that the overall communication pattern is more complex as the knowledge of the solution in "further" cells is necessary to accomplish a consistent and possibly centered polynomial approximation.

Analysis of high-order solutions shows that the theoretical order of discretization can be fully achieved as long as the geometry is discretized with meshes which are consistent with the order of discretization of the solution variables. According to [38], this problem is more typical of DG and FEM discretization based codes, while it can be ignored in FV discretizations. The reasoning is that the elements adopted in DG and FEM are typically bigger compared to those used in FV methods because of the presence of internal degrees of freedom. Moreover, the work of Menasria et al. [43] shows that while an increased accuracy is obtained using curved boundaries, the advantage compared to straight ones is still limited. Despite the absence of a satisfactory procedure to generate curved boundaries for HybFlow, the effect of adopting curved elements is shown for the smooth inviscid bump, discussed later in the chapter. All the other cases, including turbomachinery blades and vanes employ linear meshes, which as will be shown, can prevent the code from achieving the formal order of accuracy.

The last complication related to the implementation of higher-order discretization methods is related to implicit/dual time-stepping techniques for steady/unsteady convergence. As a matter of fact, as the reconstruction stencil is increased in size, a higher-order Jacobian might be necessary to recover a proper convergence in the Newton method. The side effects are related to the increased memory requirements for the methods, as the number of non-zero entries in the linear matrix increases along with the bandwidth of the matrix itself. A consistent approach for the generation of the Jacobian matrix was shown by Hoshyari et al. [44]. This aspect has been neglected in the present thesis, meaning that the implicit advancement is still based on a 1^{st} order Jacobian. This strategy was found to somehow limit the possibility to

increase the CFL, especially for fourth order discretization, but has been neglected as it would have required a major modification of the structure of the code and the parallel implementation.

In the remaining of the chapter, we will mainly deal with the k-exact reconstruction concept proposed by Gooch [45], which will be here-after referred to as LSQ, and Haider [46] which will be here-after referred to as SCM.

3.1.1 Least Square Reconstruction

One of the first methods for the implementation of high-order reconstruction of flow variables for unstructured FVM solvers was presented by Gooch [45]. The Least Square procedure (LSQ) consists in finding a polynomial approximation to the flow variables which is mean-preserving, while adopting a compact reconstruction stencil. In this case compact refers to the use of a reconstruction stencil which comprises cells in the vicinity of the target reconstruction element. In order to do this, the LSQ procedure minimizes the reconstruction error of a flow variable polynomial over the full reconstruction stencil. The results of the minimization procedure will be the derivatives of the flow variables, used to implement the high-order reconstruction. We begin by considering the reconstruction of the flow variables in the cell α, using its neighboring cells as reconstruction stencil (V_β). The reconstruction error associated to the mean value of the polynomial approximating the flow variable Φ_α over the cell $\beta \in N_\alpha$ can be defined as:

$$E_{\beta,\alpha} = \frac{1}{V_\beta} \int_{\Omega_\beta} P_\alpha(\mathbf{x} - \mathbf{x}_\alpha) dV - \overline{\Phi}_\beta \tag{3.1}$$

where P_α represents the interpolating polynomial for the variable $\Phi(\mathbf{x})$, centered in the point $\mathbf{x}_\alpha$. The integral of the polynomial P_α can be computed as:

$$\int_{\Omega_\beta} P_\alpha(\mathbf{x}-\mathbf{x}_\alpha)dV = \Phi(\mathbf{x}_\alpha) + \left.\frac{\partial\Phi}{\partial x}\right|_{\mathbf{x}_\alpha} \frac{1}{V_\beta}\int_{\Omega_\beta}(x-x_\alpha)dV + \left.\frac{\partial\Phi}{\partial y}\right|_{\mathbf{x}_\alpha} \frac{1}{V_\beta}\int_{\Omega_\beta}(y-y_\alpha)dV + \left.\frac{\partial\Phi}{\partial z}\right|_{\mathbf{x}_\alpha} \frac{1}{V_\beta}\int_{\Omega_\beta}(z-z_\alpha)dV + \left.\frac{\partial^2\Phi}{\partial x^2}\right|_{\mathbf{x}_\alpha} \frac{1}{2V_\beta}\int_{\Omega_\beta}(x-x_\alpha)^2dV + \left.\frac{\partial^2\Phi}{\partial x\partial y}\right|_{\mathbf{x}_\alpha} \frac{1}{V_\beta}\int_{\Omega_\beta}(x-x_\alpha)(y-y_\alpha)dV \ldots \tag{3.2}$$

Simplifying geometric terms, Eq. 3.2 can be rewritten as:

$$\int_{\Omega_\beta} P_\alpha(\mathbf{x}-\mathbf{x}_\alpha)dV = \Phi(x_\alpha) + \left.\frac{\partial\Phi}{\partial x}\right|_{\mathbf{x}_\alpha} \widehat{x}_{\alpha\beta} + \left.\frac{\partial\Phi}{\partial y}\right|_{\mathbf{x}_\alpha} \widehat{y}_{\alpha\beta} + \left.\frac{\partial\Phi}{\partial z}\right|_{\mathbf{x}_\alpha} \widehat{z}_{\alpha\beta} + \frac{1}{2}\left.\frac{\partial^2\Phi}{\partial x^2}\right|_{\mathbf{x}_\alpha} \widehat{x^2}_{\alpha\beta} + \left.\frac{\partial^2\Phi}{\partial x\partial y}\right|_{\mathbf{x}_\alpha} \widehat{xy}_{\alpha\beta} \ldots \tag{3.3}$$

where the geometric terms $\widehat{x^n y^m z^k}_{\alpha\beta}$ are defined as:

$$\widehat{x^l y^m z^n}_{\alpha\beta} = \frac{1}{V_\beta}\int_{\Omega_\beta} \left[(x-x_\beta)+(x_\alpha-x_\beta)\right]^l \left[(y-y_\beta)+(y_\alpha-y_\beta)\right]^m \left[(z-z_\beta)+(z_\alpha-z_\beta)\right]^n dV = \sum_{a=0}^{l}\sum_{b=0}^{m}\sum_{c=0}^{n} \binom{l}{a}\binom{m}{b}\binom{n}{c} (x_\beta-x_\alpha)^a (y_\beta-y_\alpha)^b (z_\beta-z_\alpha)^c \overline{x^{l-a}y^{m-b}z^{n-c}}_\beta \tag{3.4}$$

with $\overline{x^{l-a}y^{m-b}z^{n-c}}_\beta$ indicating the moments of inertia of the cell β. When the evaluation of the reconstruction error is performed over the whole set of cells contained in the reconstruction stencil of the cell α, an over-determined system of linear equations arises (Eq. 3.5).

$$\begin{bmatrix} 1 & \overline{x_\alpha} & \overline{y_\alpha} & \overline{z_\alpha} & \overline{x_\alpha^2} & \dots \\ 1 & \widehat{x_{\alpha 1}} & \widehat{y_{\alpha 1}} & \widehat{z_{\alpha 1}} & \widehat{x_{\alpha 1}^2} & \dots \\ 1 & \widehat{x_{\alpha 2}} & \widehat{y_{\alpha 2}} & \widehat{z_{\alpha 2}} & \widehat{x_{\alpha 2}^2} & \dots \\ 1 & \widehat{x_{\alpha 3}} & \widehat{y_{\alpha 3}} & \widehat{z_{\alpha 3}} & \widehat{x_{\alpha 3}^2} & \dots \\ 1 & \widehat{x_{\alpha 4}} & \widehat{y_{\alpha 4}} & \widehat{z_{\alpha 4}} & \widehat{x_{\alpha 4}^2} & \dots \\ \vdots & \vdots & \vdots & \vdots & \vdots & \vdots \end{bmatrix} \begin{pmatrix} \Phi \\ \frac{\partial \Phi}{\partial x} \\ \frac{\partial \Phi}{\partial y} \\ \frac{\partial \Phi}{\partial z} \\ \frac{1}{2}\frac{\partial^2 \Phi}{\partial x^2} \\ \vdots \end{pmatrix} = \begin{pmatrix} \overline{\Phi_\alpha} \\ \overline{\Phi_1} \\ \overline{\Phi_2} \\ \overline{\Phi_3} \\ \overline{\Phi_4} \\ \vdots \end{pmatrix} \tag{3.5}$$

The equations can be further simplified centering the expansion in the cell baricenter:

$$x_\alpha = \int_{\Omega_\alpha} x dV, \;\; y_\alpha = \int_{\Omega_\alpha} y dV, \;\; z_\alpha = \int_{\Omega_\alpha} z dV \tag{3.6}$$

With this choice, the first order moments of inertial are 0, at least analytically, and some terms in the Taylor series expansion can be dropped during the numerical implementation of the reconstruction procedure.

The linear system can be eventually solved to obtain the reconstruction coefficients in the Taylor expansion. It must be noted that the first line in Eq. 3.5 is added to obtain a mean-preserving high order reconstruction, meaning that the flow variables derivatives will be coherent with their mean value in each cell. In order to guarantee the conservation of the mean value, the first line is solved exactly by means of Gaussian elimination procedure, while the remaining part of the linear system can be solved by minimizing the reconstruction error by means of a Moore-Penrose pseudo-inverse.

Considering a three-dimensional implementation of the reconstruction procedure 3,9 and 19 unknown derivatives arise respectively for k=1, k=2 and k=3 polynomial orders. In order to guarantee a sufficient number of equations, the reconstruction stencil can be iteratively increased by adding neighboring cells. To this end, we can define a 1^{st} grid neighborhood (also called Von Neumann neighborhood) for a generic cell *i* as:

Definition. $N_\alpha^{(1)} \triangleq \{\, \beta \mid \beta \textit{ is adjacent to } \alpha \,\} \cup \alpha$

A generic k^{th} grid neighborhood can be defined as:

Definition. $N_\alpha^{(k)} \triangleq \bigcup_{j=1,k} N_\alpha^{(j)}$

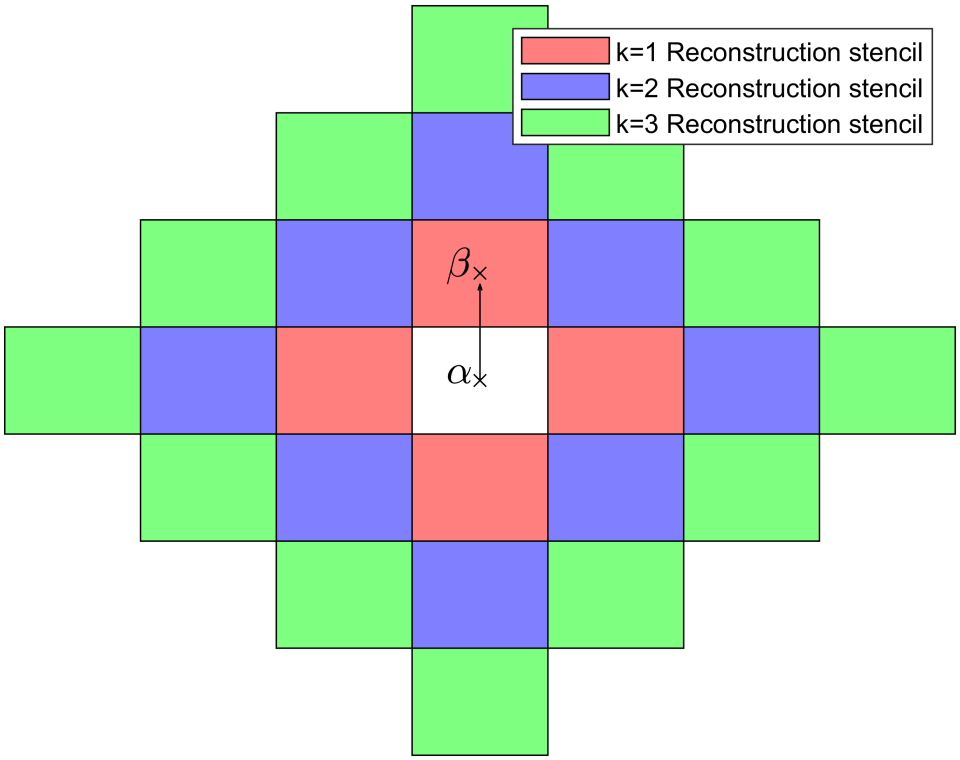

Fig. 3.1 Reconstruction stencil

The reconstruction stencil adopted for variable order reconstructions is shown in Fig. 3.1

3.1.2 Successive Correction Method

The main drawback of the LSQ mean-based method introduced in Sec. 3.1.1 is related to parallel applications. Considering a 4^{th} order reconstruction stencil (k=3) (Fig. 3.1), the LSQ procedure requires that both the solution state and the geometric information of each cell in the reconstruction stencil are available upon the computation of higher order derivatives. On highly parallel applications, the communication pattern between processors is hence affected by the reconstruction order. The Successive Correction Method (SCM) overcomes this limitation by using a compact reconstruction stencil and approximating higher order derivatives from available lower order ones.

The implementation followed during the development of HybFlow, follows the original SCM proposed by Haider et al. in [46]. For compactness reasons, the

description of the method follows the same notation used in the referenced paper, which is more compact than the one used for the LSQ procedure.

Similarly to the method proposed by Gooch, the starting point for the definition of a high order reconstruction using the SCM method is a Taylor expansion of the flow variable about a point (which is again chosen to be the cell center):

$$\begin{aligned}\Phi(x) = \Phi(x_\alpha) + \sum_{j=1}^{k} \frac{1}{j!} \sum_{i_1 i_j=1}^{d} \frac{\partial \Phi}{\partial x_{i_1} \dots \partial x_{i_j}}|_{x=x_\alpha} \left(x_{i_1} x_{\alpha,i_1}\right) \dots \left(x_{i_j} x_{\alpha,i_j}\right) = \\ = \Phi(x_\alpha) + \sum_{j=1}^{k} \frac{1}{j!} \mathbf{D}^{(j)} \left(x_{i_1} x_{\alpha,i_1}\right) \dots \left(x_{i_j} x_{\alpha,i_j}\right)\end{aligned} \tag{3.7}$$

where all the derivatives have been grouped in the operator $\mathbf{D}^{(j)}$. Thus the mean value of the function $\Phi(x)$ can be computed over a different cell γ can be expressed as:

$$\begin{aligned}\overline{\Phi} = \Phi_\alpha + \sum_{j=1}^{k} \frac{1}{j!} \mathbf{D}^j|_{x=x_\alpha} \mathbf{z}_{\alpha\gamma}^{(j)} = \\ = \Phi(x_\alpha) + \sum_{j=1}^{k} \frac{1}{j!} \sum_{i_1 i_j=1}^{d} z_{\alpha\gamma,i_1\dots i_j}^{(j)} \frac{\partial \Phi}{\partial x_{i_1} \dots \partial x_{i_j}}|_{x=x_\alpha}\end{aligned} \tag{3.8}$$

where $\mathbf{z}_{\alpha\gamma}^{(j)}$ is a geometric term, which accounts for the cell centers position and moments of inertia:

$$z_{\alpha\gamma,i_1\dots i_k}^{(j)} = \frac{1}{V_\gamma} \int_{\Omega_\gamma} (x_{i_1} - x_{\alpha,i_1}) \dots (x_{i_k} - x_{\alpha,i_k}) dV \tag{3.9}$$

By definition, we have the following:

- $z_{\alpha\gamma}^{(0)} = 1$ denoting the integral of the identity function over the volume
- $z_{\alpha\gamma,i_1\dots i_3}^{(1)} = (\mathbf{x}_\gamma - \mathbf{x}_\alpha)_{i_1\dots i_3}$ denoting center-to-center distance
- $z_{\alpha\gamma,i_j,i_1\dots i_3}^{(2)} = \frac{1}{V_\gamma} \int_{\Omega_\gamma} (\mathbf{x} - \mathbf{x}_\alpha)_{i_j} (\mathbf{x} - \mathbf{x}_\alpha)_{i_1\dots i_3} dV$ denoting second order moments of inertia of the cell γ centered in $\mathbf{x}_\alpha$

On the other hand, the reconstruction of flow variables derivatives can be accomplished upon introducing a k-exact reconstruction operator which maps the cell mean variables to the derivatives computation:

$$\sum_{\beta \in N_\alpha} w^{(m|k)}_{\alpha\beta,i_i \ldots i_m} \overline{\Phi}_\beta = \frac{\partial \Phi}{\partial x_{i_1} \ldots \partial x_{i_j}}|_{x=x_\alpha} \tag{3.10}$$

The mapping $w^{(m|k)}_{\alpha\beta}$ returns a k-exact m^{th} derivative of the variable Φ. Comparing Eq. 3.7 and Eq. 3.10, it is possible to introduce the reconstruction error associated to the m^{th} k-exact derivative as:

$$\sum_{\beta \in N_\alpha} w^{(m|k)}_{\alpha\beta} \overline{u}_\beta - D^{(m)}|_{x=x_\alpha} = \sum_{l=k+1}^{j} \frac{1}{l!} \sum_{\beta \in N_\alpha} w^{(m|k)}_{\alpha\beta} (z^{(l)}_{\alpha\beta} \cdot D^{(l)}|_{x=x_\alpha}) \tag{3.11}$$

Eq. 3.11 represents the building block of the method as it allows to iteratively compute and correct lower order derivatives after higher order ones are available. As a matter of fact, the LHS represents the correction which needs to be applied to the available lower order derivatives $\sum_{\beta \in N_\alpha} w^{(m|k)}_{\alpha\beta} \overline{u}_\beta$, upon the availability of higher order ones $D^{(l)}|_{x=x_\alpha}$. It must be noted that the correction depends on the definition of a single reconstruction stencil N_α, which can be chosen to be equal to the Von Neumann stencil in order to reduce communications during parallel applications of the reconstruction method.

The last step of the algorithm consists in finding a reconstruction method (mapping) which allows the computation of higher order derivatives, from lower order ones. Using the same notation adopted previously, the higher order derivative mapping can be found as:

$$\mathbf{R} D^{(k+1)}|_{x=x_\alpha} = D^{(k)}|_{x=x_\alpha} \begin{pmatrix} w^{(k+1\,k)}_{\beta_1}[\overline{\Phi}] - w^{(k+1\,k)}_{\alpha}[\overline{\Phi}] \\ \vdots \\ w^{(k+1\,k)}_{\beta_n}[\overline{\Phi}] - w^{(k+1\,k)}_{\alpha}[\overline{\Phi}] \end{pmatrix} \tag{3.12}$$

where **R** is the inverse of a reconstruction matrix. Since k+1-exact k derivatives are not available before the computation of k+1-exact k+1 derivatives, the RHS can be substituted using Eq. 3.11. Eq. 3.12 thus becomes:

$$\left(\mathbf{R}+\mathbf{C}^{k+1}\right) D^{(k+1)}|_{x=x_\alpha} = \begin{pmatrix} w_{\beta_1}^{(kk)}[\overline{\Phi}] - w_{\alpha}^{(kk)}[\overline{\Phi}] \\ \vdots \\ w_{\beta_n}^{(kk)}[\overline{\Phi}] - w_{\alpha}^{(kk)}[\overline{\Phi}] \end{pmatrix} \tag{3.13}$$

The difference between Eq. 3.12 and Eq. 3.13 lies in the RHS which is now expressed in terms of k-exact k derivatives, and in the addition of a new matrix **C**, necessary to recover the consistency between the order of discretization of k+1 derivatives on the LHS and the k derivatives on the RHS. The entries of matrix **C** are the following:

$$\begin{aligned} C_{ij}^{k+1,i_1\ldots i_k} = h_{\alpha\beta,j} + \frac{1}{(k+1)!}\sum_{\gamma\in N_\beta} w_{\beta\gamma}^{(k|k)} \sum_{n=1}^{d} z_{\beta\gamma i_1\ldots i_k n} + \\ -\frac{1}{(k+1)!} + \sum_{\gamma\in N_\alpha} w_{\alpha\gamma}^{(k|k)} \sum_{n=1}^{d} z_{\alpha\gamma i_1\ldots i_k n} \end{aligned} \tag{3.14}$$

The coefficients $h_{\alpha\beta,j}$ indicate reconstruction coefficients for the j^{th} derivative, which depend on the method chosen for the computation of successive derivatives. In the present implementation, the original version proposed by Haider, where successive derivatives are computed by means of finite difference, has been implemented in the code so that the coefficients $h_{\alpha\beta}$ correspond to distances between cell centers.

The method implemented in the code is extended up to the 3^{rd} order reconstruction (k=2). The algorithm is based then on the following 3 steps:

- Compute 1-exact 1^{st} order derivatives, which is performed using a LSQ procedure
- Compute 2-exact 2^{nd} order derivatives via Eq. 3.13
- Apply the correction step (Eq. 3.11) to compute 2-exact 1^{st} order derivatives

It is important to notice that the method only uses information (flow mean state and derivatives) coming from a fixed reconstruction stencil (in this case the Von Neumann neighborhood). Information regarding cells from outside of the Von Neumann stencil only appear when building the matrix **C** through the terms $w_{\beta\gamma}\, z_{\beta\gamma}$, which require accessing the reconstruction stencil of the cell β. Despite this, the

terms only depend on the grid geometrical characteristics, so they can be computed during the initial pre-processing of the grid and no additional communication among processors is necessary during the solution phase.

On the other hand, since a correction phase of lower order derivatives is necessary, the communication between processors occurs three times. The first communication is required to exchange the flow state among processors before carrying out the computation of the 1-exact first order derivative. The second communication occurs before the correction step, where the first order derivatives are exchanged to compute 2-exact 2^{nd} order derivatives. The last communication occurs to propagate the 2-exact 1^{st} order derivatives.

3.1.3 Final remarks on the reconstruction procedure

As previously described, from a practical perspective, the implementation of the two methods in parallel has a major difference, regarding the number of solution variables which are accessed at run-time for the generation of approximating polynomials. The communication stencil and the reconstruction stencil for both methods are shown in Fig. 3.2 for a third order reconstruction. While the overall reconstruction stencil necessary for the LSQ method needs to be accessed at run-time to generate the RHS vector of the reconstruction equation, for the SCM the reconstruction stencil and the communication-stencil are different. As a matter of fact, higher order neighbors are necessary for the construction of derivative correction equation only through their geometrical characteristics, which in HybFlow are pre-computed during the pre-processing of the grid. On the other hand, higher order derivatives only access the von-Neumann neighborhood at run-time at the increased expense of more communication steps.

The solution of the reconstruction equation, or the successive-derivative and the correction equations all yield a problem of the form:

$$\mathbf{P}\,\mathbf{d} = \mathbf{b} \tag{3.15}$$

where $\mathbf{P}$ is a n$\times$m rectangular matrix, with n>m, $\mathbf{d}$ is a vector of unknowns representing the derivatives of flow variables (or its higher order approximation for the correction equations), while the RHS $\mathbf{b}$ depends on the specific equation to be

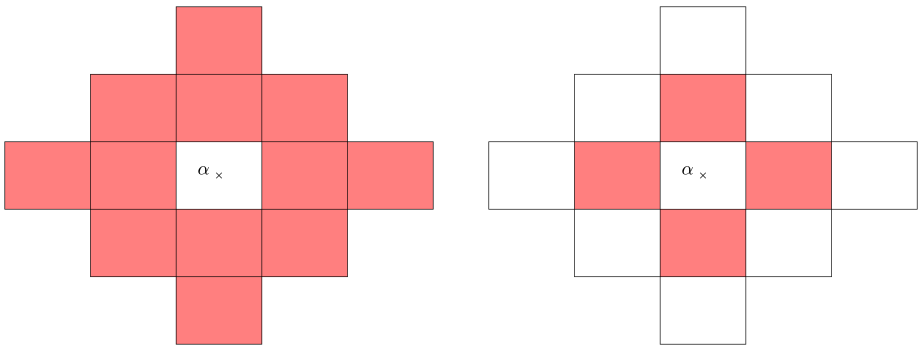

Fig. 3.2 Comparison of communication stencil (red) and overall reconstruction stencil (white) for k=2 reconstruction: (a) LSQ, (b) SCM

solved. The original set of equations is modified in HybFlow by a twofold correction. The first one regards the application of a weighting matrix on the RHS and on the LHS of the linear system. The weighting was originally suggested by Gooch in [45] to build a Weighted Essentially Non Oscillating (WENO) reconstruction stencil, by assigning a low weight to the equations associated with sharp variations of the solutions and in general at a high distance from the target cell. The same procedure is used in HybFlow, even though the weighting adopted comes after the work of Mavriplis [47], who showed that the LSQ reconstruction performs better when an inverse distance weighting is applied. The weighting is applied only to the case of LSQ reconstruction system (for the SCM this corresponds to the computation of the first derivatives, while it is not applied to the finite difference method adopted for computing higher order approximations). A second modification to the system is instead applied according to the work of Jalali and Gooch [48]. The authors show that when the aspect ratio of cells (in their case two-dimensional triangular cells) increases, so does the condition number of the matrix **P**. For this reason, a scaling of the matrix columns is implemented so that the eigenvalues of the system are balanced and the cut-off errors associated with the numerical inversion are minimized. The overall system of equations is then rewritten in the following form:

$$\mathbf{P}\,\mathbf{d} = \mathbf{b} \Rightarrow \mathbf{W}\,\mathbf{P}\,\mathbf{D}\,\mathbf{D}^{-1}\mathbf{d} = \mathbf{W}\,\mathbf{b} \tag{3.16}$$

The matrix **W** is the n×n weighting matrix, while the matrix **D** accounts for the column scaling:

$$W_{ij} = \begin{bmatrix} w_{11} & 0 & \dots & 0 \\ 0 & w_{22} & \dots & 0 \\ \vdots & \vdots & \vdots & 0 \\ 0 & 0 & 0 & w_{nn} \end{bmatrix} \tag{3.17}$$

$$D_{ij} = \begin{bmatrix} \max_i P_{i1} & 0 & \dots & 0 \\ 0 & \max_i P_{i2} & \dots & 0 \\ \vdots & \vdots & \vdots & 0 \\ 0 & 0 & 0 & \max_i P_{im} \end{bmatrix} \tag{3.18}$$

where $w_{ii} = \frac{1}{|d_{\alpha i}|}$.

In HybFlow, the solution to this equation is found by minimizing the norm-2 of the error vector (**e=b-$\tilde{\mathbf{P}}^{-1}$ d**) by means of the Moore-Penrose inverse of the matrix $\tilde{\mathbf{P}}$, which is defined as **W P D**. The pseudo-inverse matrix is obtained as a QR decomposition **$\tilde{\mathbf{P}}$=QR** where **Q** is an ortho-normal matrix, while **R** is an upper triangular matrix. The decomposition is obtained using the Grahm-Schmidt orthogonalization which is used in the GMRES algorithm as well. Since the decomposition is inherently dependent only on the geometrical characteristics of the cells, the pseudo-inverse matrix is computed at the first iteration of the solver, while the RHS of the equation is updated at every iteration, depending on the solution vector.

In order to provide a consistent discretization scheme, additional modifications to the original solver regard the implementation of consistent methods for the computation of both viscous and inviscid fluxes. The first modification applies to the integration rule necessary to obtain the overall flux through a face of the mesh. For high-order integration, Gauss quadrature formulas applying to both triangular faces and quadrilateral faces have been implemented during the pre-processing of the grid. These shapes are sufficient for the range of grids to be dealt with within HybFlow, which comprises only triangles and rectangles as cell faces. The Gauss quadrature formula can be expressed as:

$$\int_S \mathbf{F} \cdot \mathbf{n} dS = \sum_{i=1}^{N_i} w_i \mathbf{F}_i \cdot \mathbf{n} \tag{3.19}$$

The previous formulation assumes that the normal to the face is uniform, which is the case of linear elements. As stated in the introduction to the chapter, curved elements treatment has not been implemented in the framework of the present thesis. For this reason the integration rules depend only on the order of reconstruction of the flow variables while the normal vector to each face remains constant over the quadrature points. For second order reconstruction (k=1), the formula reduces to the original method implemented in HybFlow, where the flux integral is using a single-point quadrature formula. The point corresponds to the face center, while the weight corresponds to the face area. The number of quadrature points necessary to enforce a consistent integration of the fluxes, depends on the order of reconstruction. In particular, the use of N_p quadrature points allows an exact integration of polynomials of degree m. Tab. 3.1 and 3.2 report the quadrature rules over reference elements which have been implemented in HybFlow, respectively for triangular elements and quadrilateral elements. The quadrature formulas have been retrieved from [49] for triangular elements and from [50] for quadrilateral elements. It must be noted that the position of the points for a triangular faces are reported in terms of area coordinates (as provided in the referenced paper). The reference elements are instead shown in Fig. 3.3.

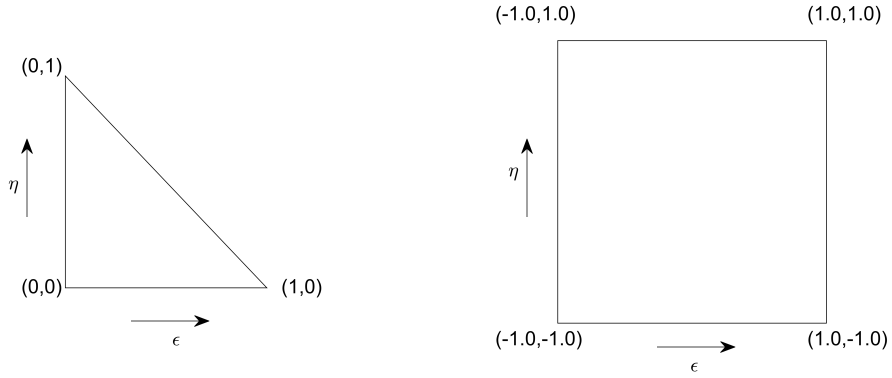

Fig. 3.3 Reference elements for quadrature points and weights: (a) Triangular element, (b) Quadrilateral element

The second modification to the code refers to the implementation of the viscous fluxes. The original method based on finite difference is correct only for a linear

Table 3.1 Quadrature points and weights for triangular faces

N_p	m	A_1	A_2	A_3	w
4	3	1/3	1/3	1/3	-0.5625
		0.6	0.2	0.2	0.5208333
		0.2	0.6	0.2	0.5208333
		0.2	0.2	0.6	0.5208333
6	4	0.8168475729	0.0915762135	0.0915762135	0.1099517436
		0.0915762135	0.8168475729	0.0915762135	0.1099517436
		0.0915762135	0.0915762135	0.8168475729	0.1099517436
		0.1081030181	0.4459484909	0.4459484909	0.2233815869
		0.4459484909	0.1081030181	0.4459484909	0.2233815869
		0.4459484909	0.4459484909	0.1081030181	0.2233815869

Table 3.2 Quadrature points and weights for quadrilateral faces

N_p	m	ε	η	w
4	3	$-1/\sqrt{3}$	$-1/\sqrt{3}$	1.0
		$-1/\sqrt{3}$	$1/\sqrt{3}$	1.0
		$1/\sqrt{3}$	$1/\sqrt{3}$	1.0
		$1/\sqrt{3}$	$-1/\sqrt{3}$	1.0
9	5	$-\sqrt{3/5}$	$-\sqrt{3/5}$	25/81
		0	$-\sqrt{3/5}$	40/81
		$\sqrt{3/5}$	$-\sqrt{3/5}$	25/81
		$-\sqrt{3/5}$	0	40/81
		0	0	64/81
		$\sqrt{3/5}$	0	40/81
		$-\sqrt{3/5}$	$\sqrt{3/5}$	25/81
		0	$\sqrt{3/5}$	40/81
		$-\sqrt{3/5}$	$\sqrt{3/5}$	25/81

reconstruction. For this reason, the computation of the viscous fluxes is modified to account for the variation of flow solution gradients over the face quadrature points according to the work of Jalali and Gooch [51]:

$$\nabla\Phi_i = \frac{\nabla\Phi_i^+ + \nabla\Phi_i^-}{2} + \eta\frac{(\Phi_i^+ - \Phi_i^-)}{|\mathbf{x}^+ - \mathbf{x}^-|}\mathbf{n} \tag{3.20}$$

where the superscripts $^+$ and $^-$ refer to the left and right reconstructed gradients, while second term imposes a relaxation which accounts for the solution jump across the quadrature point, which depends also on the distance between the cell centers ($\mathbf{x}^+$ and $\mathbf{x}^-$). The value of the relaxation parameter η is equal to 1.

3.2 Inviscid test cases

3.2.1 Inviscid vortex advection

The first test case used for testing the high-order reconstruction implementation is the inviscid advection of an isothermal vortex, with an underlying uniform flow. The test case admits an analytical solution, which is the transport of the vortex at the uniform velocity of the "external" flow field, while any modification to the vortex structure is adduced to numerical diffusion. The isothermal vortex is defined according to the following set of equations:

$$P = P_\infty\left(1 - a\exp(\frac{-r}{2\sigma^2})\right) \tag{3.21}$$

$$T = T_\infty \tag{3.22}$$

$$v_\Theta = \sqrt{\frac{aRT}{\sigma^2}\frac{\exp(\frac{-r}{2\sigma^2})}{1 - a\exp(\frac{-r}{2\sigma^2})}} \tag{3.23}$$

The quantity v_Θ indicates the circumferential velocity of the vortex field, while the parameters a and σ control the shape of the vortex. The flow field is initialized using the volumetric average of the conservative variables, and transporting the flow field for approximately 7.5 convective time steps. The Mach number of the flow is 0.5. The solution is run using a structured mesh made of squares, which is extruded by one layer in one dimension. The convergence for the test case is shown in Fig.

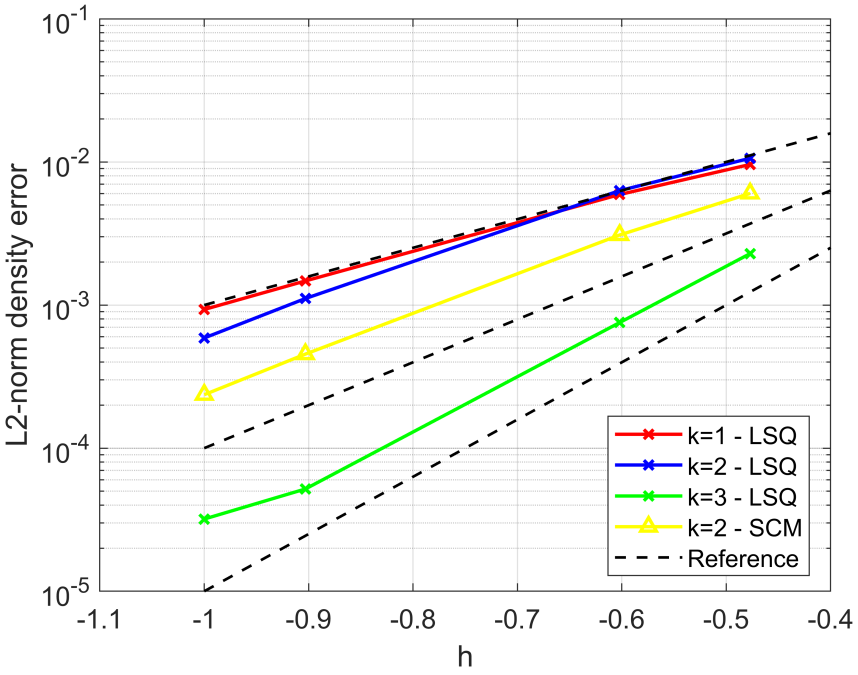

Fig. 3.4 Inviscid vortex advection: error convergence

3.4. The nominal order of convergence can be instead retrieved from Tab. 3.3. The results are reported for the fourth order explicit time integration. It was checked that the time-integration method does not affect the results. While for k=1 and k=2 simulations reach the nominal order of convergence (in the case of the LSQ this nominal convergence is reached in the last mesh size interval), for k=3, the situation is slightly different. The rate of convergence of the error is ≈3.9 over the first three meshes, while it decreases slightly over the last interval. The SCM method yields better results than the LSQ reconstruction, both in terms of slope and overall error for this test case. It must also be said that the latter does nor provide the correct convergence when the vortex is not properly discretized by enough elements. The convergence order for the inviscid vortex test case are reported in Tab. 3.3.

3.2.2 Smooth Gaussian bump

The second inviscid test case is the smooth Gaussian bump. The test case aims at evaluating the performance of the high order reconstruction method over a curved surface. The numerical domain is shown in Fig. 3.5. The upper and the lower surfaces are solid walls. At the inlet, the total pressure is prescribed along with the

Mesh	h	k	ε_{LSQ}	ε_{SCM}	r_{LSQ}	r_{SCM}
M1	1/3	1	9.22×10^{-05}	-	-	-
M2	1/4	1	3.50×10^{-05}	-	1.68	-
M3	1/8	1	2.17×10^{-06}	-	2.00	-
M4	1/10	1	8.67×10^{-07}	-	2.06	-
M1	1/3	2	1.13×10^{-04}	3.63×10^{-05}	-	-
M2	1/4	2	3.98×10^{-05}	9.53×10^{-06}	1.8	2.32
M3	1/8	2	1.23×10^{-06}	2.06×10^{-07}	2.50	2.77
M4	1/10	2	3.46×10^{-07}	5.58×10^{-08}	2.85	2.93
M1	1/3	3	5.23×10^{-06}	-	-	-
M2	1/4	3	5.70×10^{-07}	-	3.85	-
M3	1/8	3	2.69×10^{-09}	-	3.86	-
M4	1/10	3	1.02×10^{-09}	-	2.17	-

Table 3.3 Inviscid vortex advection - Order of convergence

total temperature and an inlet angle equal to 0°. At the outlet, a static pressure is prescribed to reach a Mach number equal to 0.5. The numerical domain is defined according to the following exponential equation.

$$y(x) = 0.0625e^{-25x^2} \tag{3.24}$$

It extends from -1.5 to 1.5 in the x-direction and from 0 to 0.8 in the y-direction. The test case has been simulated using a 1-layer extrusion of quadrilateral elements. The convergence of the method is tested according using the L2-norm of the entropy error. Being the flow inviscid, the analytical solution yields a null entropy increase. The entropy error is defined as:

$$L2 = \sqrt{\frac{\int_{\Omega}\left(\frac{p/\rho^{\gamma}-p_{\infty}/\rho_{\infty}^{\gamma}}{p_{\infty}/\rho_{\infty}^{\gamma}}\right)^2 dV}{V}} \tag{3.25}$$

The result of the high-order scheme applied to the bump is shown in Fig. 3.6. It is shown that the code achieves the formal order of accuracy in the region between -2.2≤h≤-1.6 for k=1 and k=2. For k=3, the slope is 3.25, which is lower than the what would be expected. For the finest mesh, all the methods converge to the same error. Similar results are obtained with a third order scheme implemented via the

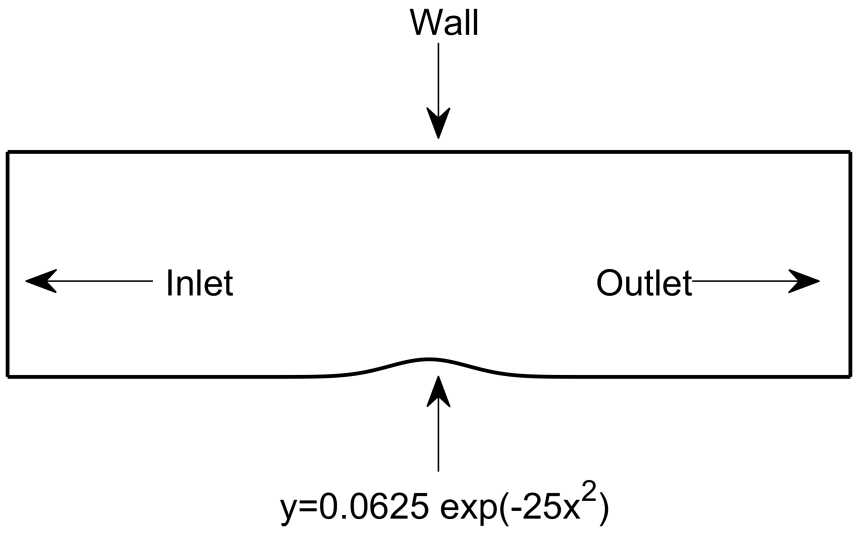

Fig. 3.5 Inviscid bump - Numerical domain

SCM method, even though the error level is lower than the one obtained with the LSQ method.

The possible reason behind this behavior is related to the presence of linear edges. This possibility has been investigated by running an additional set of simulations implementing a treatment for the curved boundaries elements over the lower surface of the bump. The implementation of curved boundaries is obtained by using a third order polynomial interpolation of the lower surface. An example of the curved boundary treatment is shown in Fig. 3.7, which shows the deviation of the curved boundary from the linear boundary over a convex portion of the bump. The implementation of the curved treatment yields two modifications in the computation of both inviscid fluxes and moments of inertia. On one hand, the normal vector is no longer uniform over the cell face, so it cannot be taken out of the integral for flux computations (see Eq. 3.19). On the other hand, the integral needs to be modified to take into consideration the different length of the curve and of the linear edge. This is accomplished by transforming the curved element into a linear element, by means of Serendipity transformation ([52]). This yields the following formulation for surface integral computation:

$$\int_{S_{curv}} \mathbf{F}(\mathbf{x}) \cdot \mathbf{n}(\mathbf{x}) dS = \int_{S_{ref}} ||\mathbf{J}|| \mathbf{F}(\eta) \cdot \mathbf{n}(\eta) dS' = \sum_{i=1}^{N_i} w_i ||\mathbf{J}||_i \mathbf{F}_i \cdot \mathbf{n}_i \tag{3.26}$$

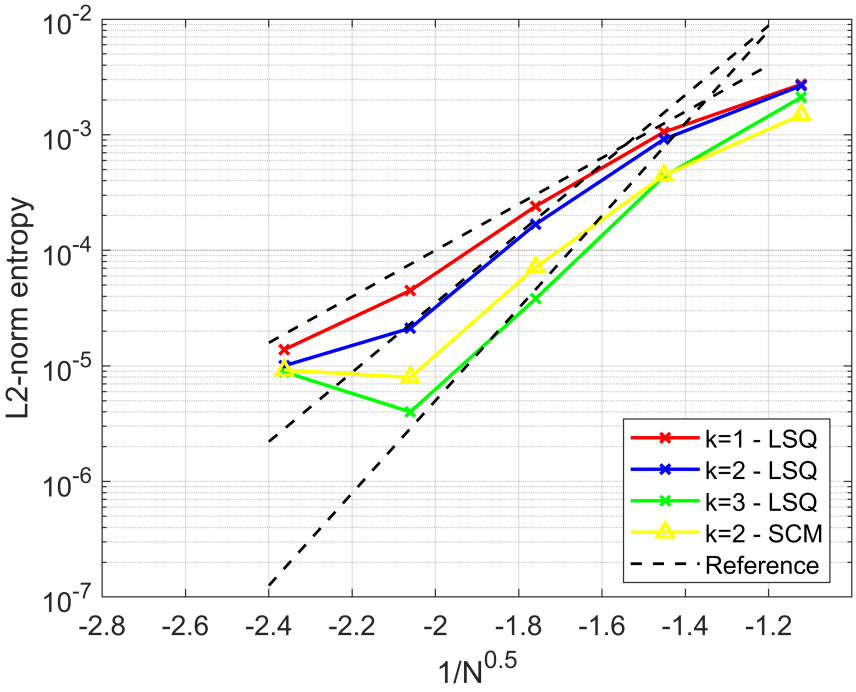

Fig. 3.6 Inviscid bump: error convergence for linear edges

The results obtained with the curved treatment are shown in Fig. 3.8. After the curved element introduction, all the simulations converge at a slightly higher rate than the formal order of accuracy. Similarly to the straight mesh case, the SCM retains a slightly lower error compared to the LSQ procedure.

It must be said that the bump is the only test case in which a curved treatment of the boundaries has been tested, because of the relatively uniformity of the meshes used in this test case. On the other hand, for turbomachinery flows, the strict requirements in terms of mesh spacing in the near-wall region leads to highly stretched grids, which would require curving also faces of cells which are directly adjacent to the wall. This is necessary to avoid edge intersections after the routine for curved faces is run. Since such a procedure was not developed, care has been taken to guarantee a proper definition of surface curvature for the set of blades investigated in the thesis. The convergence order for the inviscid vortex test case are reported in Tab. 3.4.

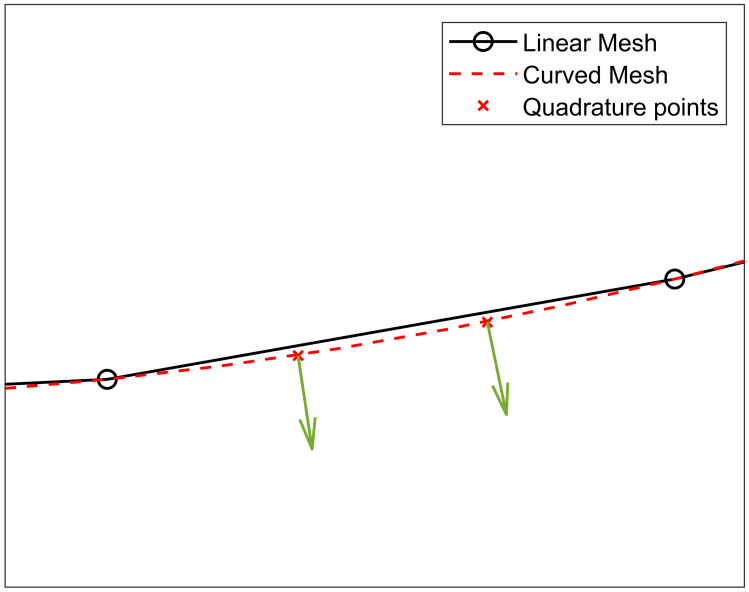

Fig. 3.7 Implementation of curved mesh treatment

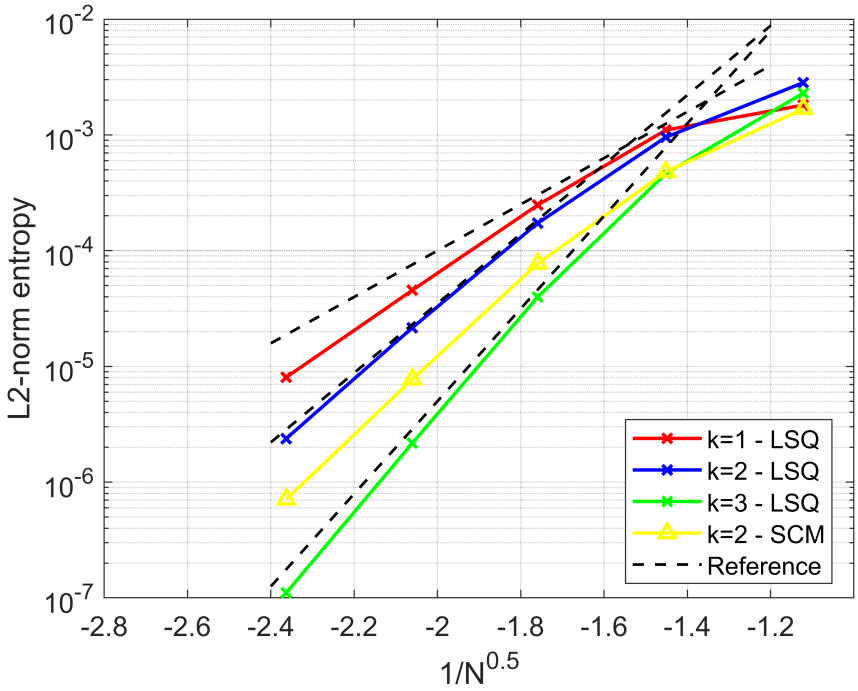

Fig. 3.8 Inviscid bump: error convergence with curved edges

			Linear Edges		Curved Edges	
Mesh	$\log_{10}(1/N^{0.5})$	k	r_{LSQ}	r_{SCM}	r_{LSQ}	r_{SCM}
M1	-1.12	1	-	-	-	-
M2	-1.45	1	1.25	-	0.65	-
M3	-1.76	1	2.08	-	2.10	-
M4	-2.06	1	2.42	-	2.44	-
M5	-2.36	1	1.68	-	2.49	-
M1	-1.12	2	-	-	-	-
M2	-1.45	2	1.40	1.59	1.43	- 1.65
M3	-1.76	2	2.39	2.58	2.41	- 2.58
M4	-2.06	2	2.99	3.16	2.99	- 3.32
M5	-2.36	2	1.07	-0.2	3.16	- 3.42
M1	-1.12	3	-	-	-	-
M2	-1.45	3	2.08	-	2.1	-
M3	-1.76	3	3.44	-	3.47	-
M4	-2.06	3	2.25	-	4.19	-
M5	-2.36	3	-1.14	-	4.26	-

Table 3.4 Smooth Gaussian bump - Order of convergence

3.3 Viscous test cases

The viscous test-cases reported here-after have all been studied using the $k-\overline{v^2}-\omega$ model by Lopez and Walters [53]. A summary of the model is reported in Appendix C. Considering the variable reconstruction order of the present Finite-Volume code, care must be taken in the definition of the source terms in the equations. As a matter of fact, similarly to other eddy-viscosity based turbulence models, the $k-\overline{v^2}-\omega$ makes use of the Boussinesq approximation to account for the Reynolds stresses. The latter are then dependent on the definition of average (in the volume sense) of velocity gradients, through the flow strain S. Moreover, the model damps near-wall oscillations by means of the destruction terms D_k and $D_{\overline{v^2}}$ which depend on the gradients of $\sqrt{k}$ and $\sqrt{\overline{v^2}}$, respectively. The current implementation of the model exploits the LSQ reconstruction procedure for all flow and turbulence variables. As far as the $\sqrt{k}$ and $\sqrt{\overline{v^2}}$ are regarded, the cell averaged values are obtained from a point-wise conversion of the the value of k and $\overline{v^2}$. Upon computing cell-centered velocity and turbulence gradients, one possible strategy for the computation of source terms is to directly use them. This means that the LSQ method is used both for reconstruction purposes and for the computation of source terms. Despite this, as

suggested by [1], the ability of the LSQ reconstruction to yield correct predictions of the cell-center gradients depends on the weighting, especially on highly stretched grids. This could lead to a worse definition of volume average gradients adopted in the source terms. For this reason, in the present activity, the use of the LSQ reconstruction based gradients, will be compared to a second approach based on the of Green-Gauss theorem:

$$\nabla U_j = \frac{1}{V_j} \int_{\partial V_j} U_j dS \tag{3.27}$$

The surface integral of the flow variables is computed using the same Gauss quadrature rules employed for flux computations as:

$$\int_{\partial V_j} U_j dS = \sum_{i=1}^{N_{face,j}} \sum_{k=1}^{N_{quad}} U_{ik} \times w_{ik} \tag{3.28}$$

where w_{ik} and U_{ik} are the weight and variable value in the $k-th$ quadrature point of the $i-th$ face, respectively. The face value U_{ik} is computed as the arithmetic mean of the left and right LSQ reconstruction of U in the quadrature point

$$U_{ik} = \frac{U_{ik}^{-} + U_{ik}^{+}}{2} \tag{3.29}$$

3.3.1 Flat plate with zero pressure gradient

The first test case used for the validation of implementation of the method for viscous flow solutions is a transitional flat plate with zero-pressure gradient. The model can be retrieved from the classic ERCOFTAC database. The model setup enforces a symmetry condition over the upper wall and upstream of the plate LE, while the plate itself is modelled as a viscous wall. At the inlet plane, the boundary condition is specified by means of flow velocity, while at the outlet plane, the static pressure is enforced. The characteristics of the meshes adopted for the simulations are reported in Tab. 3.5. A view of the meshes is present in Fig. 3.9.

The value of the reported y^+ is computed by means of the experimental friction velocity u_τ. This choice allows to report a value of the wall distance parameter independent from the prediction of the wall shear stress. The friction velocity is taken in the fully turbulent region, at Re_x=3.82$\times$ 10^5. The convergence of the solution by varying the reconstruction order is assessed on the first three meshes

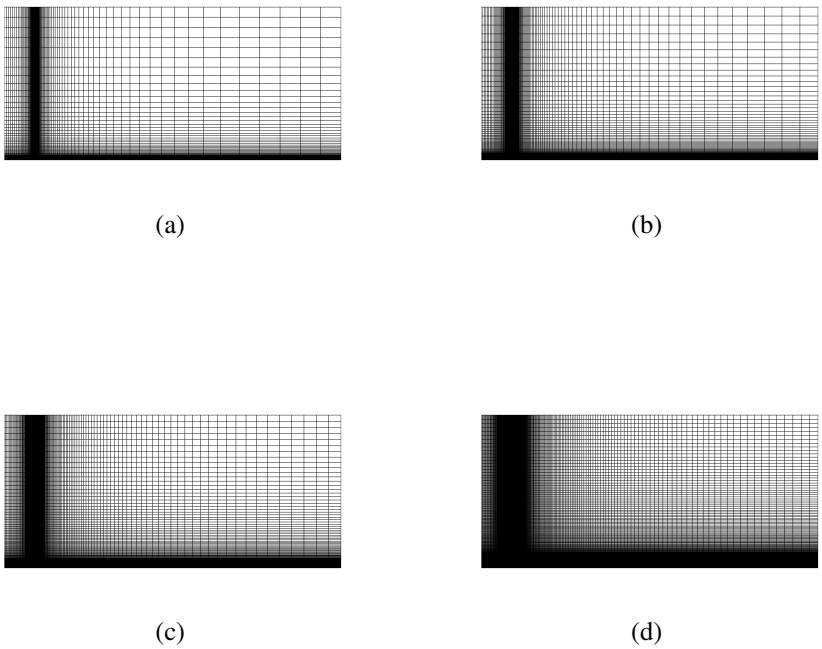

(a) (b)

(c) (d)

Fig. 3.9 Flat plate - Mesh details: (a) M1, (b) M2, (c) M3, (d) M4

Mesh	N_{DOF}	y^+
M1	7128	≈ 3.0
M2	15617	≈ 1.5
M3	33654	≈ 0.75
M4	96720	≈ 0.38

Table 3.5 Flat plate - Mesh characteristics

	T3A	T3B
U [m/s]	5.4	9.4
TI [%]	3.3	6.5
VR	12.0	100.0

Table 3.6 Flat plate - Boundary conditions

(M1, M2 and M3), while the fourth mesh is used to check the converged solution at k=1.

The experimental conditions which have been simulated refer to the test cases T3A and T3B (see Tab. 3.6 for the boundary conditions). The values of the turbulence intensity and the viscosity ratio reported in the table refer to the quantities at the LE of the blade, and have been retrieved from [53]. The inlet values can be calculated by integrating two coupled ordinary differential equations for the variable $\overline{v}^2$ and ω:

$$U_\infty \frac{d\overline{v}^2}{dx} = -\omega \overline{v}^2 \tag{3.30}$$

$$U_\infty \frac{d\omega}{dx} = -C_{\omega 2}\omega^2 \tag{3.31}$$

The effect of the discretization method for the source terms is checked using the T3B test case. Figure 3.10 reports the predictions of the skin friction coefficient using the flow and turbulence gradients computed through the LSQ. For the coarsest mesh, the use of a higher order reconstruction has the main advantage of enabling boundary layer transition, even though a relevant over-prediction of the skin friction coefficient is present at the end of transition location. This occurs for both k=2 and k=3. On the other hand, at k=1, the transition process is weak and the skin friction coefficient is largely under-predicted, which is adduced to the large mesh in wall vicinity. On the intermediate mesh M2, all the simulations properly predict the transition length regardless of the reconstruction order. It must be noted that for

higher reconstruction orders, the transition point moves downstream and away from experimental measurements. Still the three simulations present differences at the end of the transition, where k=2 overpredicts the skin friction coefficient. On the fine mesh M3 instead, the higher order simulations converge to the same predictions, while for k=1 the transition point moves closer to the experimental measurements. Moreover all the simulations succeed in predicting the shear in the fully turbulent region. The results obtained over mesh M4 confirm that the simulations enforcing k=3 converge to the same result obtained with a very fine mesh (M4), which features roughly $3\times$ and $6\times$ the number of elements compared to mesh M3 and M3. The results over mesh M1 confirm the fact that the reconstruction order cannot make up for an insufficient geometrical discretization. Eventually all this simulations tend to overpredict the axial position of the transition onset despite reproducing the transition length. It is thought that while this is a shortcoming of the solver compared to the original model of Lopez and Walters, the difference might be recovered with a slight calibration of the constants.

Another set of simulations enforces the Green-Gauss theorem for the computation of gradients which are to be used in the source terms. The results obtained with this methodology are instead shown in Fig. 3.11. The figure also reports the results obtained with the SCM method using k=2. For the coarsest mesh, the change of strategy for the computation of the source terms yields similar results to the plain LSQ gradients. As a matter of fact, the skin friction coefficient is still underestimated at k=1, while for k=2 and k=3 the transition occurs over a length similar to the experimental one, but the skin friction is largely overestimated (up to 25% higher than the measured value) in the turbulent region. For the intermediate mesh, the predicted values are closer to the experiment for all tested reconstruction orders, being the best agreement achieved for k=3. The skin friction at the end of the transition process is slightly underestimated (5.5×10^{-3} compared to the measured 5.7×10^{-3}), but the turbulent region as well as the transition length are captured. For mesh M3 the results have almost converged both in terms of spatial discretization and reconstruction. The difference between the predictions at k=1 and higher orders lies in the lower C_f at the end of transition. The comparison of the predictions at k=3 LSQ and the results using M4, indicates that the solution is converged. Most notably this method allows to correctly capture the transition process, differently from the plain LSQ gradient computation. It must be noted that the results obtained with the SCM method are in good agreement with the results obtained using a fourth order

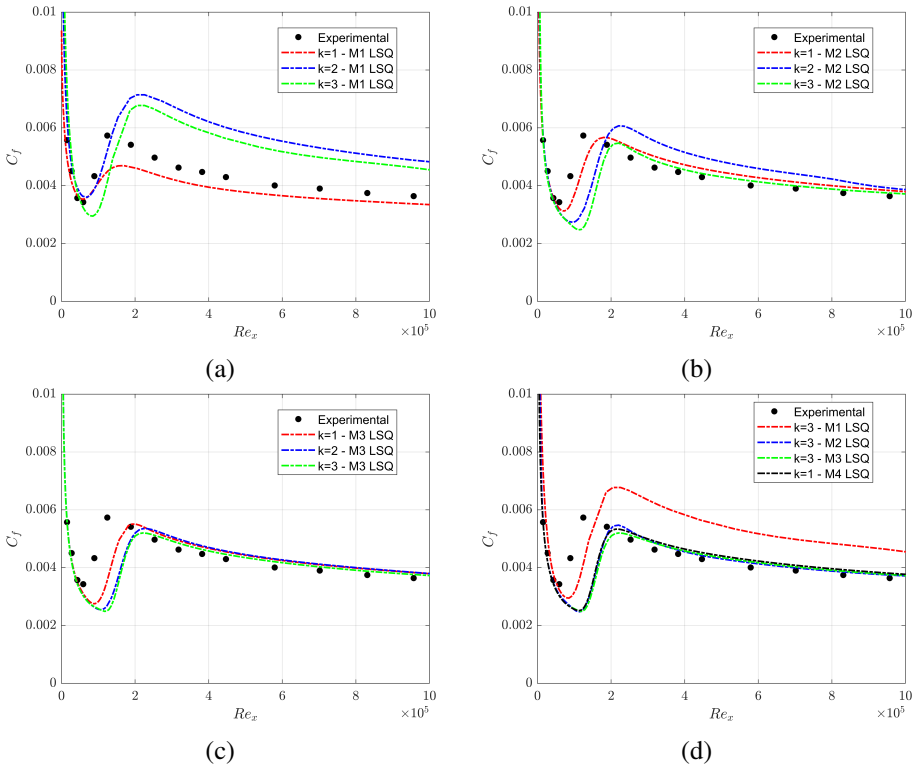

Fig. 3.10 T3B - Skin friction coefficient prediction using LSQ gradients for the computation of source terms: (a) M1 predictions, (b) M2 predictions, (c) M3 predictions, (d) k=3 predictions

discretization and the LSQ method, proving to be superior at least for the simple test cases reported so far in the thesis.

The full comparison between the two computation methods for the source terms are shown in Tab. 3.7 and 3.8. The first one reports the predictions of the axial distance based Reynolds number at the transition onset, along with the normalized transition length. The second table reports instead the corresponding predictions of the skin friction coefficient, compared with the experimental findings.

The last set of simulations reproduced the flow conditions of the test T3A. This test case features a lower turbulence intensity compared to the T3B, which leads to an increased transition length ($Re_x \approx 7 \times 10^4$). In this case, the effect of higher order discretization is tested over a case with lower flow gradients. The simulations for the T3A enforce the Green-Gauss computation of the source terms. Now the effect of the reconstruction method is even stronger. As a matter of fact, for k=1 the transition of the boundary layer is weak and there is an overall under-prediction of the skin friction

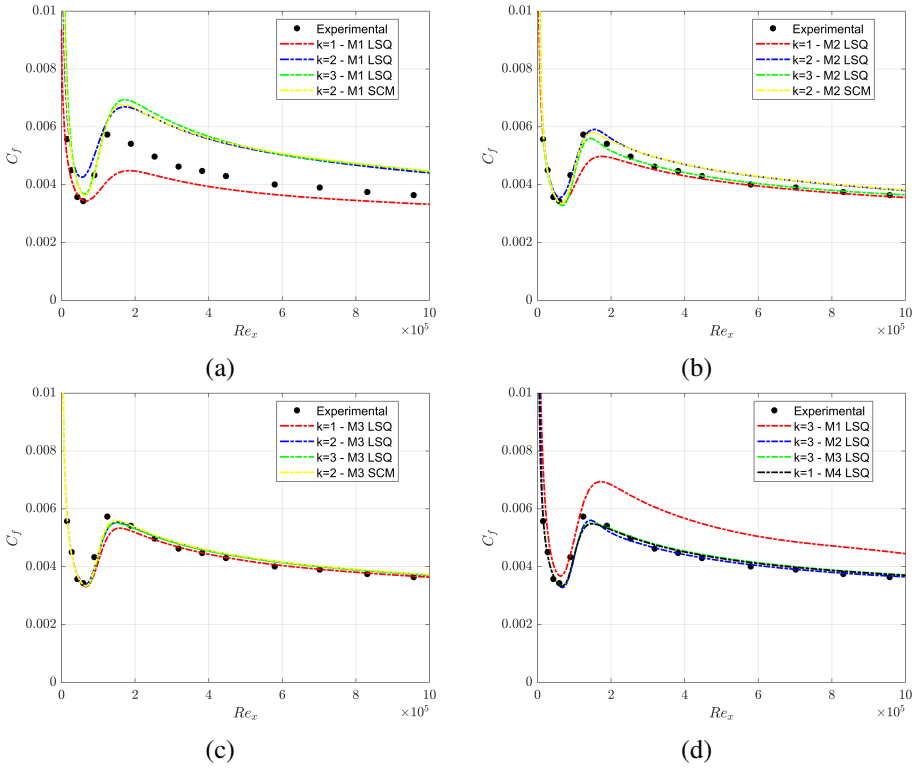

(a) (b) (c) (d)

Fig. 3.11 T3B - Skin friction coefficient prediction using Green-Gauss theorem for the computation of source terms: (a) M1 predictions, (b) M2 predictions, (c) M3 predictions, (d) k=3 predictions

Experimental		$Re_{x,length}$ $\approx$ 60,000		$Re_{x,onset}$ $\approx$ 65,000	
		LSQ Gradient		Green-Gauss Method	
Mesh	k	$Re_{x,onset}$	$Re_{x,length}$	$Re_{x,onset}$	$Re_{x,length}$
M1	1	58,000	110,000	60,000	85,000
M1	2	70,000	130,000	60,000	100,000
M1	3	85,000	120,000	60,000	100,000
M2	1	74,000	90,000	64,000	100,000
M2	2	90,000	140,000	60,000	100,000
M2	3	110,000	90,000	60,000	90,000
M3	1	91,000	100,000	64,000	90,000
M3	2	110,000	120,000	64,000	80,000
M3	3	115,000	100,000	64,000	80,000
M1	2 - SCM	-	-	60,000	100,000
M2	2 - SCM	-	-	60,000	95,000
M3	2 - SCM	-	-	64,000	80,000

Table 3.7 T3B Flat plate - Predictions based on LSQ and GG theorem - Streamwise Reynolds number

Experimental		Cf_{onset} $\approx$ 0.0034		Cf_{length} $\approx$ 0.0057	
		LSQ Gradient		Green-Gauss Method	
Mesh	k	Cf_{onset}	Cf_{length}	Cf_{onset}	Cf_{length}
M1	1	$\approx$ 0.0035	0.0047	0.0034	0.0044
M1	2	$\approx$ 0.0036	0.0071	0.0043	0.0069
M1	3	$\approx$ 0.0030	0.0067	0.0037	0.0069
M2	1	$\approx$ 0.0031	0.0056	0.0033	0.0048
M2	2	$\approx$ 0.0027	0.0061	0.0036	0.0059
M2	3	$\approx$ 0.0025	0.0054	0.0035	0.0058
M3	1	$\approx$ 0.0028	0.0055	0.0033	0.0053
M3	2	$\approx$ 0.0025	0.0054	0.0033	0.0056
M3	3	$\approx$ 0.0025	0.0052	0.0033	0.0056
M1	2 - SCM	-	-	0.0037	0.0067
M2	2 - SCM	-	-	0.0035	0.0059
M3	2 - SCM	-	-	0.0033	0.0056

Table 3.8 T3B Flat plate - Predictions based on LSQ and GG theorem - Skin friction coefficient

Experimental		$Re_{x,onset}$ $\approx$ 155,000	$Re_{x,length}$ $\approx$ 125,000
		Green-Gauss Method	
Mesh	k	$Re_{x,onset}$	$Re_{x,length}$
M1	1	97,500	155,000
M1	2	97,500	130,000
M1	3	155,000	150,000
M2	1	126,000	160,000
M2	2	126,000	140,000
M2	3	155,000	145,000
M3	1	165,000	125,000
M3	2	165,000	140,000
M3	3	162,500	120,000
M1	2 - SCM	155,000	125,000
M2	2 - SCM	165,000	140,000
M3	2 - SCM	162,500	120,000

Table 3.9 T3A Flat plate - Predictions based on GG theorem - Streamwise Reynolds number

coefficient. At k=2, the transition process occurs, but is anticipated compared to the experiments, while the simulation correctly retrieves the shear in the turbulent region. At k=3 instead, both the transition onset and length are captured properly and small overestimation of end of transition location exists. A similar situation occurs on mesh M3, where for k=1 and k=2, the onset gets closer to the experimental location, but is still anticipated with respect to the experimental measurements. On the other hand, the predictions for k=3 are similar to the corresponding case using M1. The results obtained on mesh M4 confirm the fact that the fourth order predictions obtained on mesh M3 are converged, while a small discrepancy at the end of transition is present for meshes M1 and M2. This difference with respect to the T3B test case is probably induced by the fact that the elements are clustered in the vicinity of the LE of the flat plate, while the mesh is coarsened downstream. Similarly to the T3B test case, the third order reconstruction achieved by means of the SCM method converges to the fourth order results obtained with the LSQ. Normalized transition onset positions and length, along with the corresponding skin friction coefficients are reported in Tab. 3.9 and 3.10, respectively.

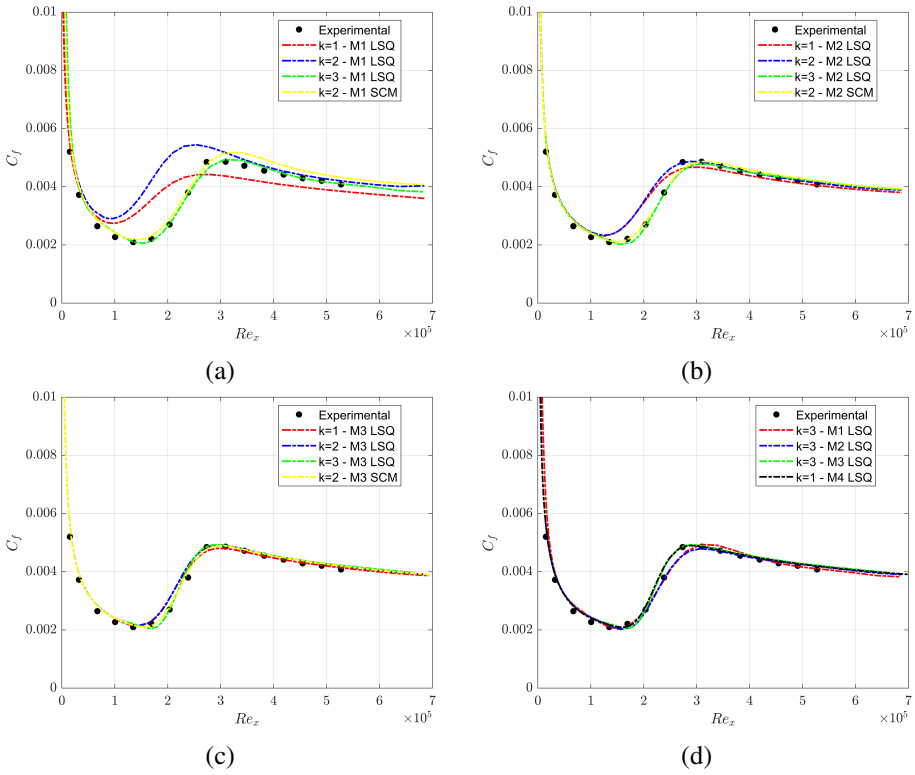

Fig. 3.12 T3A - Skin friction coefficient prediction using Green-Gauss theorem for the computation of source terms: (a) M1 predictions, (b) M2 predictions, (c) M3 predictions, (d) k=3 predictions

		Experimental		Green-Gauss Method	
Mesh	k	Cf_{onset}	Re_{length}	Cf_{onset}	Cf_{length}
M1	1	≈ 0.0021	≈ 0.0049	0.0027	0.0044
M1	2	≈ 0.0021	≈ 0.0049	0.0029	0.0054
M1	3	≈ 0.0021	≈ 0.0049	0.0021	0.0049
M2	1	≈ 0.0021	≈ 0.0049	0.0023	0.0046
M2	2	≈ 0.0021	≈ 0.0049	0.0023	0.0048
M2	3	≈ 0.0021	≈ 0.0049	0.002	0.0049
M3	1	≈ 0.0021	≈ 0.0049	0.0022	0.0048
M3	2	≈ 0.0021	≈ 0.0049	0.0022	0.0049
M3	3	≈ 0.0021	≈ 0.0049	0.0021	0.0049
M1	2 - SCM	≈ 0.0021	≈ 0.0049	0.0021	0.0051
M2	2 - SCM	≈ 0.0021	≈ 0.0049	0.002	0.0049
M3	2 - SCM	≈ 0.0021	≈ 0.0049	0.0022	0.0049

Table 3.10 T3A Flat plate - Predictions based on GG theorem - Skin friction coefficient

C[mm]	93.01
C_{ax} [mm]	79.97
β_1	32.7
$M_{2,is}$	0.65
$Re_{2,is}$ [$*10^3$]	[100:250]
TI [%]	0.8

Table 3.11 T106C blade characteristics

Mesh	N_{DOF}	y^+	$N_{profile}$
M1	14760	<1	231
M2	44656	<1	440
M3	80516	<1	513

Table 3.12 T106C - Mesh characteristics

3.3.2 T106C low pressure turbine blade

The T106C represents a high-speed, high-lift low pressure turbine blade which has been thoroughly investigated at the von Karman Institute for Fluid Dynamics. All the details of the test case can be retrieved from the work of Michálek et al. [54], while some details are given here. The profile has been used in the literature as a benchmark for the prediction of separation induced transition using transition models ([55–57]). The most important characteristics of the blade are reported in Tab. 3.11. The profile features the formation of a separation bubble in the aft region of the SS for the selected range of Reynolds number. Differently from the previous test cases, the profile has been simulated using hybrid grids, employing quadrilateral elements in the near-wall region and triangular elements in the free-stream. The characteristics of the mesh are reported in Tab. 3.12, while a close-up view of the LE and TE details is provided in Fig. 3.13

The CFD results are compared to experimental measurements for loading, wake and skin friction coefficient, respectively in Fig. 3.14, 3.16, 3.15. The latter is computed as:

$$C_f = \frac{\tau_{wall}}{0.5\rho_{2,is}U_{2,is}^2} \tag{3.32}$$

The simulations do not properly predict the loading in the region X/C_{ax}<0.4. This type of disagreement is common in the literature and can be adduced to either

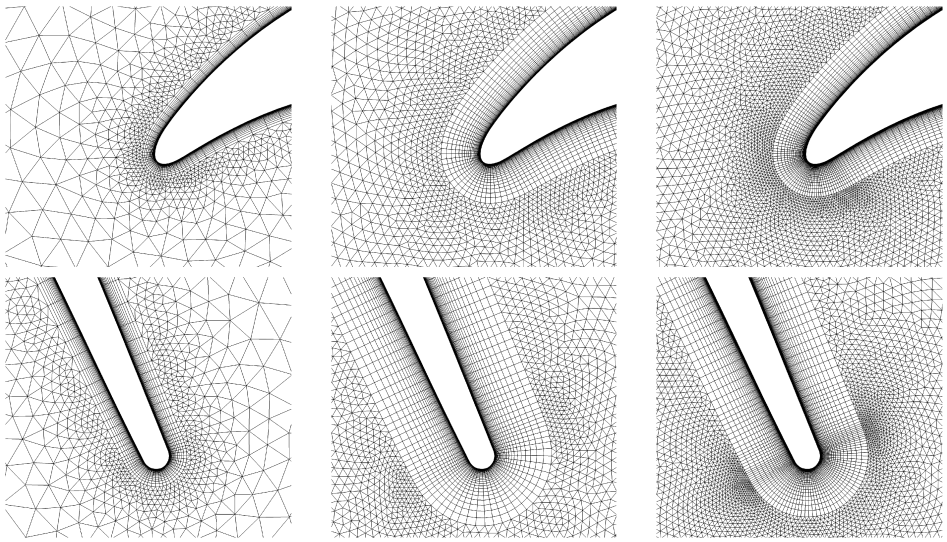

(a) (b) (c)

Fig. 3.13 T106C - LE and TE mesh details: (a) M1, (b) M2, (c) M3

a mismatch in the inlet flow angle (with respect to the one reported in the paper) as supposed by Hillewaert et al. in [58], or due to three-dimensional effects which are not simulated here (see Hu et al. [59]). The predictions of the loading are in agreement with the experimental values at $Re_{2,is}$=100,000, apart from a small peak of the isentropic Mach number in the region 0.83X/C_{ax}<0.85. The increment of the reconstruction order and the elements count leads to a reduction in the peak Mach number. The coarsest mesh, with k=1, also features a faster pressure recovery close to the TE region, indicating that the separation bubble has reattached. On the same mesh, for k=2, the velocity peak reduces, while the loading distribution gets closer to the experimental measurements, matching the pressure recovery in the aft region of the SS. A similar conclusion can be drawn from the loading predictions at $Re_{2,is}$=160,000. While the acceleration up to the peak velocity point is the same for all tested meshes and discretization orders, the recovery predicted using k=1 on M1 is still faster than the experiments. At higher Reynolds, the predictions of the loading are all similar, and no evident effect on the loading is present.

The loading predictions and the differences seen at various reconstruction order, mesh density and Reynolds numbers can be explained with the distribution of the skin friction coefficient shown in Fig. 3.15. At the lowest Reynolds number, the structure of the separation bubble can is affected by both the mesh and the discretiazion order. For M1 and k=1, the separation point occurs later than the other cases ($S/S_0 \approx 0.6$)

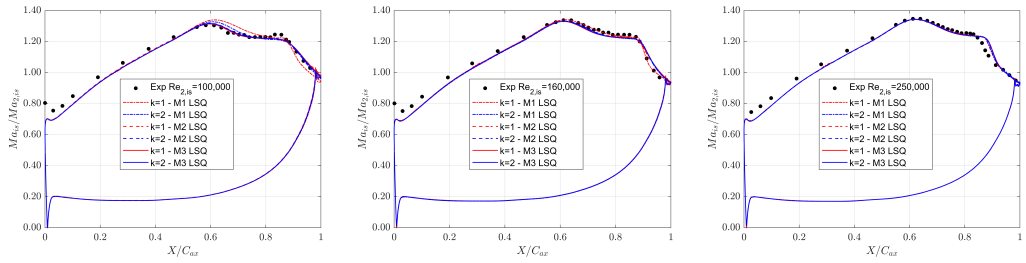

(a) (b) (c)

Fig. 3.14 Loading predictions at various Reynolds numbers: (a) $Re_{2,is}$=100,000, (b) $Re_{2,is}$=160,000, (c) $Re_{2,is}$=250,000

and a reattachment point is present at roughly $S/S_0 \approx 0.9$. On the other hand, the other setups predict an open bubble, which induces a slower pressure recovery close to the TE and a better overall matching with the experimental results. For k=2, on the coarsest mesh, the separation bubble is still open, even though a fully converged solution is found only for the finest mesh. The intermediate mesh M2, predicts the same separation point location as M3, but only for k=2, the skin friction coefficient prediction is satisfactory up to the recovery point ($S/S_0 \approx 0.85$). While the behavior at $Re_{2,is}$=160,000 is similar to the lowest Reynolds case, at $Re_{2,is}$=250,000 all the simulations predict a reattachment of the flow. Also in this case, the coarsest mesh predicts a faster reattachment induced by the insufficient discretization. At k=2 and M1 the skin friction tends towards the predictions of finer meshes, managing to reproduce the value for S/S_0>0.9. In this case a fully convergent solution is achieved for k=2 both on the intermediate and the finest mesh.

As far as the losses are concerned, all the results are reported in Fig. 3.16. The experimental data are not present in the original paper and are retrieved from the work of Benyahia [60]. It is shown that the increase in the order of accuracy has virtually no effect on the prediction of the blade's wake. Due to the coarse mesh, all predictions at M1 yield a wide wake, with an evident underprediction of the peak loss. Better predictions are found for M2 and M3, showing a trend for a reduction of the wake width and an increase of the peak loss. The best predictions are obtained at high-Reynolds, with lower losses induced by the lower shape factor of the boundary layer. Higher mispredictions are present at low Reynolds, where the wake shows the typical behavior of RANS models.

Eventually, the predictions obtained with the SCM method and the LSQ method are compared in Fig. 3.17 and 3.18, respectively for the wake total pressure losses

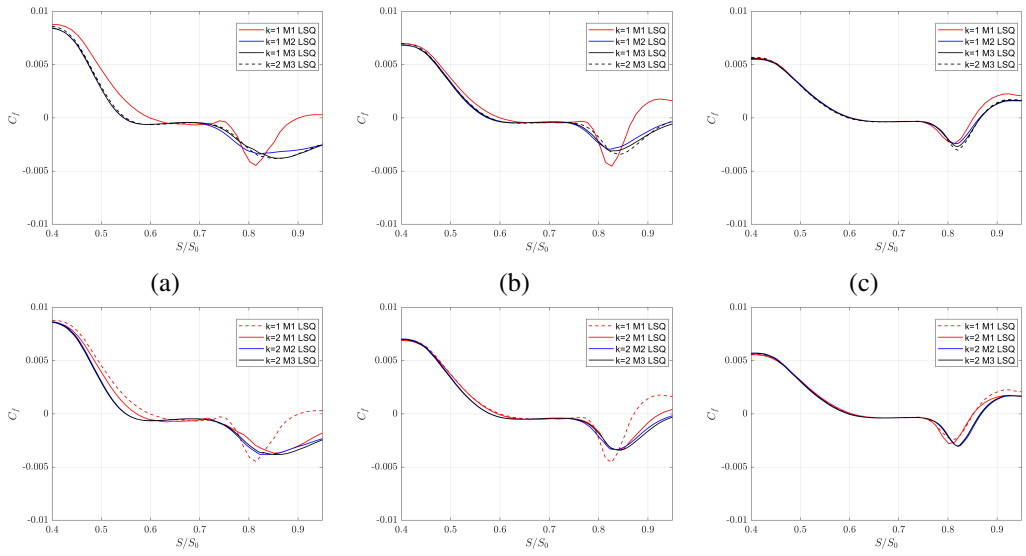

Fig. 3.15 Skin friction coefficient predictions at various Reynolds numbers: (a)-(d) $Re_{2,is}$=100,000, (b)-(e) $Re_{2,is}$=160,000, (c)-(f) $Re_{2,is}$=250,000

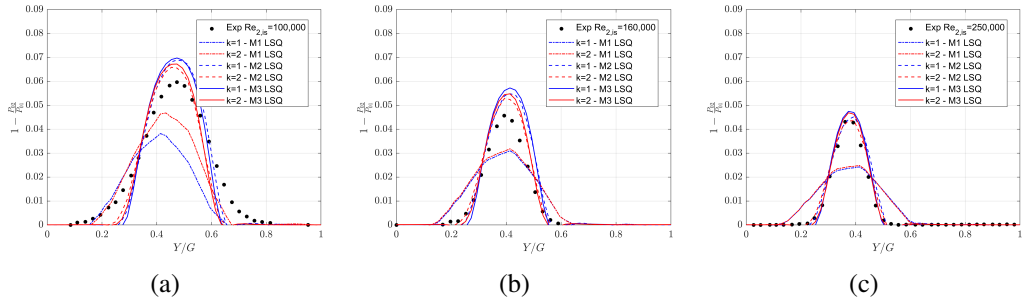

Fig. 3.16 Wake at various Reynolds numbers: (a) $Re_{2,is}$=100,000, (b) $Re_{2,is}$=160,000, (c) $Re_{2,is}$=250,000

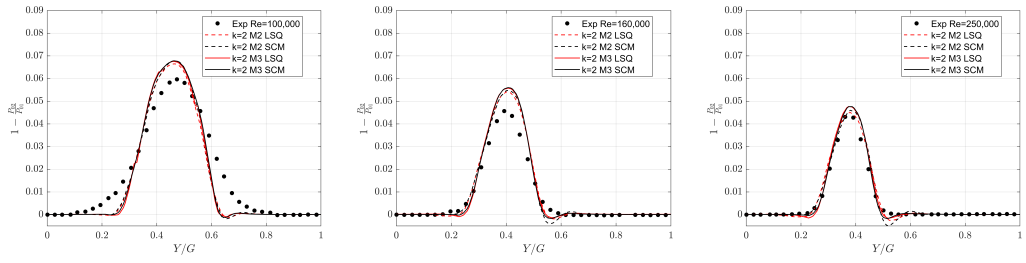

(a) (b) (c)

Fig. 3.17 Total pressure losses using the high order SCM method: (a) $Re_{2,is}$=100,000, (b) $Re_{2,is}$=160,000, (c) $Re_{2,is}$=250,000

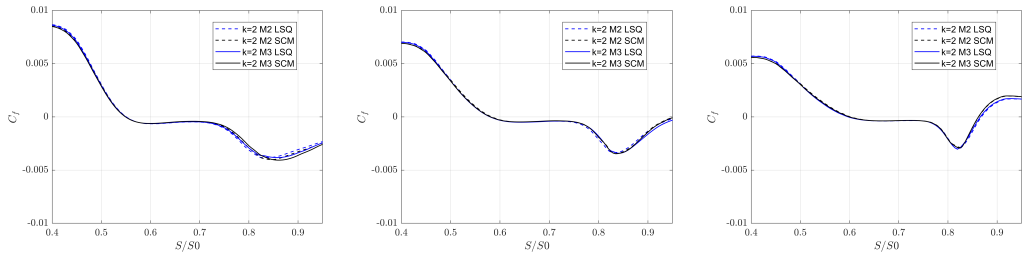

(a) (b) (c)

Fig. 3.18 Skin friction coefficient predictions using the high order SCM method: (a) $Re_{2,is}$=100,000, (b) $Re_{2,is}$=160,000, (c) $Re_{2,is}$=250,000

and the skin friction coefficient. The predictions of the loading are omitted for brevity as the same pressure distribution is predicted by both method. The results are shown for the medium and the fine mesh only, as the method was found to be unstable for the coarsest mesh. The results presented for the SCM method are very similar to the predictions retrieved using the LSQ. Some minor differences arise both in the prediction of the wake and in the skin friction coefficient. As far as the wake is considered, while the peak position and value are in accordance between the two methods, mainly depending on the number of elements, the third order computations on mesh M2 feature an increase of total pressure at the interface between the wake and the free-stream flow. This is present for $Re_{2,is}$=160,000 at Y/G=0.58 and for $Re_{2,is}$=250,000 at Y/G=0.55. The difficulty in properly reproducing the region, at least compared to the LSQ method, along with the convergence difficulties on the coarse mesh are probably induced by the use of a finite difference method for extension to higher order derivatives during the reconstruction phase.

		Experimental	HybFlow		
Mesh	k	$1-\frac{P_{06}}{P_{01}}_{max}$	$1-\frac{P_{06}}{P_{01}}_{max}$	S_{sep}	S_{rea}
M1	1	0.060	0.040	0.0.6	0.9
M1	2	0.060	0.041	0.574	0.99
M2	1	0.060	0.070	0.58	-
M2	2	0.060	0.066	0.58	-
M2	2-SCM	0.060	0.067	0.58	-
M3	1	0.060	0.070	0.58	-
M3	2	0.060	0.067	0.58	-
M3	2-SCM	0.060	0.067	0.58	-

Table 3.13 T106C - $Ma_{2,is}$=0.9,$Re_{2,is}$=100,000

		Experimental	HybFlow		
Mesh	k	$1-\frac{P_{06}}{P_{01}}_{max}$	$1-\frac{P_{06}}{P_{01}}_{max}$	S_{sep}	Cf_{min}
M1	1	0.046	0.034	0.6	-0.0045
M1	2	0.046	0.034	0.56	-0.0037
M2	1	0.046	0.056	0.547	-0.0034
M2	2	0.046	0.054	0.547	-0.0038
M2	2-SCM	0.046	0.055	0.547	-0.0041
M3	1	0.046	0.058	0.547	-0.0038
M3	2	0.046	0.056	0.547	-0.0038
M3	2-SCM	0.046	0.056	0.547	-0.0041

Table 3.14 T106C - $Ma_{2,is}$=0.9,$Re_{2,is}$=160,000

		Experimental	HybFlow		
Mesh	k	$1-\frac{P_{06}}{P_{01}}_{max}$	$1-\frac{P_{06}}{P_{01}}_{max}$	S_{sep}	S_{rea}
M1	1	0.043	0.026	0.6	0.85
M1	2	0.043	0.027	0.6	0.85
M2	1	0.043	0.046	0.6	0.865
M2	2	0.043	0.045	0.6	0.870
M2	2-SCM	0.043	0.046	0.6	0.862
M3	1	0.043	0.048	0.6	0.867
M3	2	0.043	0.048	0.6	0.867
M3	2-SCM	0.043	0.048	0.6	0.862

Table 3.15 T106C - $Ma_{2,is}$=0.9,$Re_{2,is}$=250,000

Test	MUR237	MUR218
C[mm]	67.647	67.647
β_1 [°]	0	0
P_{out} [bar]	1.179	1.19
$Ma_{2,is}$	0.775	0.760
$Re_{2,is}$ [*10^3]	1000	1000
TI [%]	6	4
VR []	75	50

Table 3.16 LS89 characteristics

Mesh	N_{DOF}	y^+	$N_{profile}$
M1	12158	<1	250
M2	23027	<1	300
M3	46966	<1	683

Table 3.17 LS89 - Mesh characteristics

3.3.3 LS89 high pressure turbine vane

The last test case devoted to the analysis of the code's accuracy is the LS89 high pressure turbine vane. Differently from the results shown in Chapter 2, heat transfer test cases are shown. The two test-cases selected for the analysis are the MUR218 and the MUR237, which have been already investigated in the context of similar modeling strategies for boundary layer transition ([61]). The main characteristics of the blade, along with the operating conditions are shown in Tab. 3.16. The boundary conditions for turbulence quantities refer to the LE values, and are defined in the same way reported for the flat plate case. The three different meshes adopted for the investigation of the heat transfer are shown in Fig. 3.19 and the main characteristics are reported in Tab. 3.17. For this test case, only the results obtained with the LSQ method have been reported as the SCM method has been found to be unstable.

For the MUR218 (Fig. 3.20), the experiments are run at a free-stream turbulence intensity equal to 4%, which induces boundary layer transition at approximately S=60mm. CFD predicts a slightly later transition, at S=67mm. Differently from the T106C, the increase in mesh density seems to be prevalent over the increase of the reconstruction order. M1 and M2 show a slower increase in the Nusselt number downstream of transition, while the same behavior is not captured increasing the reconstruction order. On the pressure side, Nusselt number is predicted fairly up to

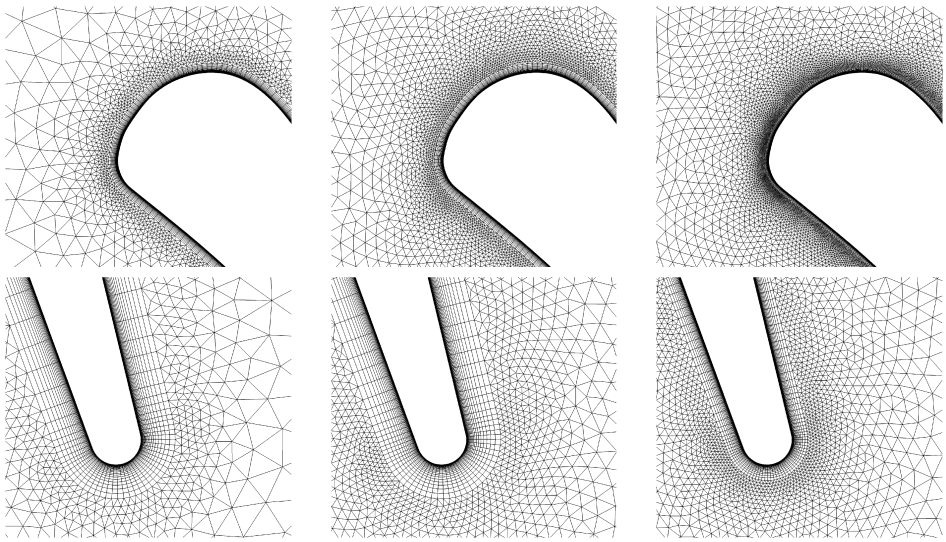

(a) (b) (c)

Fig. 3.19 LS89 - LE and TE mesh details: (a) M1, (b) M2, (c) M3

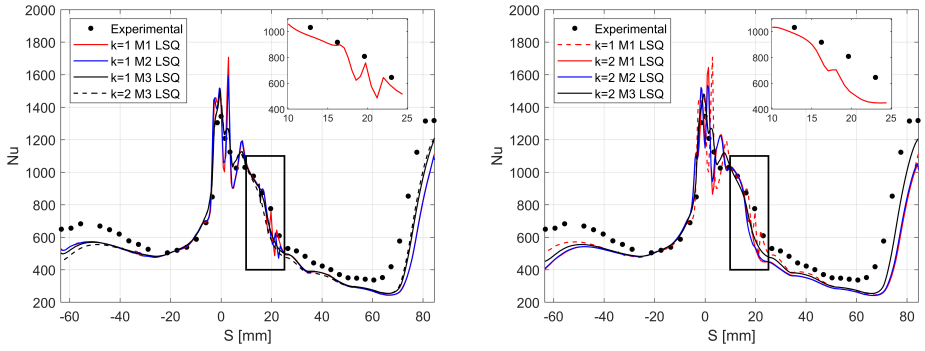

(a) (b)

Fig. 3.20 LS89 - MUR218: (a) second order discretization, (c) third order discretization

S=20mm but is underestimated downstream. The figure also reports a magnification of the heat transfer coefficient in the region 10mm<S<25mm, where the effect of the discretization order is the most evident. In this part of the blade, spurious peaks arise when the coarse mesh M1 is adopted along with a k=1 reconstruction. These peaks are instead limited for k=2, which is possibly induced by the increase in the reconstruction stencil.

Figure 3.21 shows the MUR237 predictions. The higher turbulence intensity yields a faster transition, where the transition point is located at S=40mm approximately. In this case, CFD does not yield a satisfactory prediction of the Nusselt number over the SS, while underestimating the PS heat transfer (to a higher extent

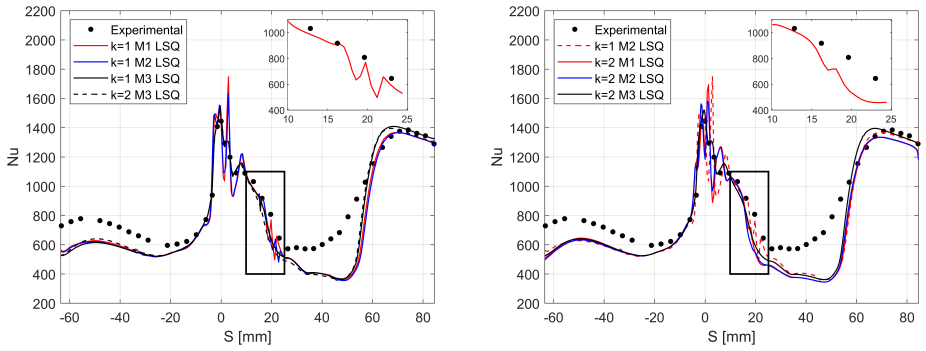

(a) (b)

Fig. 3.21 LS89 - MUR237: (a) second order discretization, (c) third order discretization

compared to the MUR218). Transition occurs at S=52mm, which is delayed compared to the experiments. It is important to highlight that the present predictions are in line with the results reported by Walters and Cokljat [61], where a similar version of the turbulence model is used. Similarly to the MUR218, the high order discretization allows to avoid evident wiggles in the Nusselt number over the SS. On the other hand, the peaks present at the LE can be removed only using finer discretization. Eventually it is concluded that the performance of high order discretization for heat transfer test-cases is limited compared to pure aerodynamics. A possible motivation lies in the choice of conservative variables, which requires a variable transformation for the computation of temperature derivatives.

Chapter 4

Analysis of high-speed LPT: the SPLEEN test case

The final chapter of the thesis details the application of the code to the analysis of the SPLEEN-C1 cascade. The test case is a ultra-high speed rotor blade airfoil, experimentally investigated at the von Karman Institute for Fluid Dynamics in the context of the EU-funded SPLEEN (Secondary and Leakage Flow Effects in High-Speed Low-Pressure Turbines) project. The numerical activity was dedicated to the evaluation of the code in reproducing the flow field occurring in linear cascades operated at low Reynolds conditions. The chapter is organized as follows:

- An initial introduction to Low Pressure Turbines (LPT) flow field, along with modeling aspects of low-Reynolds flows
- Discussion of steady, two-dimensional simulations aimed at testing the performance of the code in reproducing the transitional high-speed flow characteristics of the low-pressure turbine airfoil
- Analysis of the three-dimensional flow field developing throughout the cascade, addressing the development of secondary flow structures under representative inlet boundary layer profiles
- Analysis of the unsteady flow field reproducing the interaction of the cascade midspan section with the wakes generated by an upstream wake generator using both a sliding-mesh treatment for the bar and blade domains and imposing the experimental wake of the bar as a boundary condition for the blade simulation

4.1 Introduction to Low-Pressure Turbine flow topology and modelling

4.1.1 Profile losses

Modern aero-engine designs are characterized by the design of high-lift and high-speed low pressure turbines. The high-lift configuration allows to extract more work per stage, which in turn benefits the engine reducing both the weight and dimensions ([62]). Despite this, such configurations typically work at low-Reynolds number (below 100,000 when operated in cruise conditions) which leads to a laminar boundary layer over the suction side of the blade. In combination with adverse pressure gradients in the aft region of the suction side, laminar boundary layers are also prone to separation. The development of the profile boundary layer, along with the downstream wake mixing represent roughly one third of the overall loss for axial machine designs ([63]).

Under certain conditions, a laminar boundary can undergo transition to a turbulent state. The process can occur through several mechanisms which can be divided into four different modes: natural, by-pass, separation-induced and wake-induced.
The natural transition is a slow transition mode, typically occurring when the free-stream turbulence intensity is below 1 %. In general, a laminar boundary layer is subject to flow disturbances which can be amplified/damped over a certain range of frequencies. The amplification of flow disturbance in a laminar boundary layer gives origin to a two-dimensional flow perturbation which is referred to as Tollmien-Schitling waves ([64]). The waves go through additional amplification, and start developing in spanwise direction, becoming three-dimensional. Eventually the waves will lead to the formation of turbulent spots, which merge together and form a turbulent boundary layer [65].

The by-pass transition occurs at higher value of free-stream turbulence intensity. In this case, the disturbances propagate from the free-stream into the laminar boundary layer and the natural instability promoted by T-S waves is by-passed ([66]). In this case the transition mechanisms is completely dominated by the formation and propagation of turbulent spots inside the boundary layer, which is a three-dimensional phenomenon in nature.

The separation induced transition occurs in the case of separated boundary layers. This mode of transition is typical for LPT working under uniform/steady boundary conditions, in the aft region of the SS where an adverse pressure gradient is present. The separation-induced transition occurs when the Kelvin-Helmotz instabilities occurring in a separated shear layer are amplified, eventually triggering the transition of the boundary layer. The occurrence of transition favors the mixing of the "dead air region" with the free-stream. This process leads to the reattachment of the flow and fast pressure recovery. Depending on the local Reynolds number and the adverse pressure gradients, the separation induced transition can promote a fast reattachment of the separation bubble. In this case, it is referred to as 'short'. Short separation bubbles occur typically for Reynolds numbers in the range $240<Re_{\theta,sep}<320$ and mild adverse pressure gradients. The fast reattachment occurs because the K-H roll-up interacts with the flow in the vicinity of the wall. The exchange of momentum between the near-wall flow and the outer shear layer promotes the transition of the boundary layer and eventually a reattachment of the bubble itself. For very low Reynolds number ($Re_{\theta,sep}<240$) and strong adverse pressure gradient, the interaction between the near-wall flow and the K-H instabilities interaction is no more present. Because of the low momentum exchange between the near-wall flow and the shear layer at the top of the dead air region, the transition is slower compared to the short bubble case. In the case of an eventual reattachment the bubble is referred to as "long", while in the case of no reattachment, the bubble is referred to as "open". This last scenario is the most detrimental for turbine performance because an open bubble also thickens the wake and aerodynamic losses increase ([54]).

The last mode of transition is the wake induced mode, which typically occurs in unsteady environments like turbomachinery components. The wake induced transition stems from the downstream propagation of wakes shed from upstream components. A wake is characterized by regions of increased turbulence traveling at a lower speed with respect to neighboring "clean" flow region. A scheme of the wake kinematics is provided in Fig. 4.1, where the velocity defect of the wake region is associated to the so-called "negative jet" ([67]) in the flow reference frame. According to Pfeil et al. [68], the wake induced transition is caused by the propagation of turbulent spots from the wake into the boundary layer, which occurs in correspondence of the negative jet region. The behavior of the boundary layer is in this case intermittent, due to the unsteady nature of wake passing events. It must be said that the impact of wake induced transition has been central in the research

of low-pressure turbine airfoils as it can favor boundary layer reattachment thus reducing profile losses.

The type of transition process promoting the formation of a turbulent boundary layer starting from a laminar state depends mainly on the rate of production of turbulence spots. The latter depends on various parameters:

- Reynolds number: it gives an estimation of the likelihood for a boundary layer to be laminar, transitional or turbulent
- Free-stream turbulence intensity: it promotes the production of turbulent spots in laminar boundary layers, favoring the transition process
- Pressure gradient: in the case of adverse pressure gradients, boundary layer are more susceptible to free-stream disturbances induced by certain turbulence levels, promoting its transition. On the other hand, a favorable pressure gradient stabilizes the boundary layer preserving its laminar state ([69]).

Mayle ([70]), provided a depiction to summarize the various effects in the case steady conditions, introducing a separation-criterion which determines the possibility of the flow to undergo separation and a stability-criterion which allows to determine flow conditions (pressure gradient, turbulence intensity and momentum thickness Re) under which the flow does not experience transition. For turbine blade applications, the study is further complicated by the presence of an unsteady flow field generated by upstream components (combustor/moving rows) and the fact that blade surfaces are curved. Convex surfaces are characterized by more stable boundary layers as the centrifugal force acting of flow particles further from the surface is higher than the centrifugal force acting on a particle closer to the surface itself. This prevents to some degree, mixing between the boundary layer and the free-stream region.

4.1.2 Endwall/Secondary losses

While the development of the boundary layer and the subsequent trailing edge wake are typically regarded as "profile losses", approximately 30-40 % of the losses generated in axial turbomachinery is related to the development of the flow in the endwall region [63]. The losses are attributed to two different effects, namely the development of the endwall boundary layer and the mixing loss associated

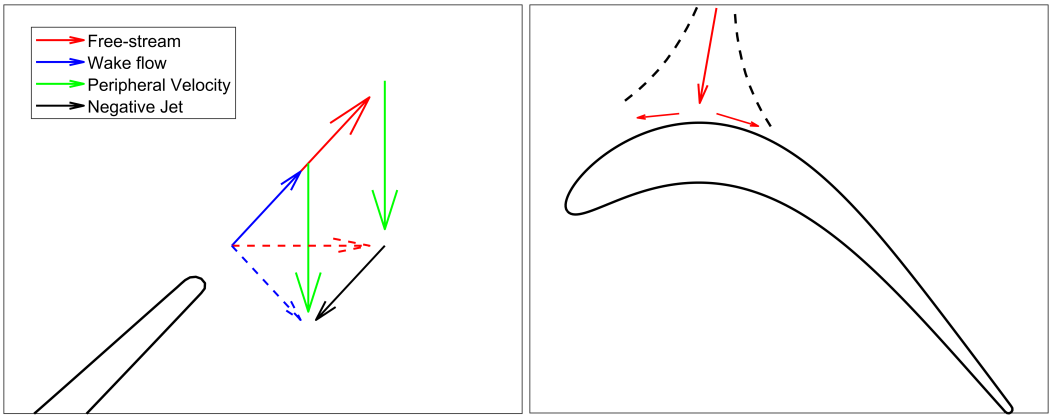

(a) (b)

Fig. 4.1 Negative jet model:(a) Velocity deficit of the wake, (b) Wake in the stream reference frame

with development and subsequent mixing of secondary flows. Their origin can be efficiently addressed by means of inviscid flow theory [71], which explains the generation of streamwise vorticity considering the kinematics (bending and stretching) of vortex filaments along with the variation of the blade circulation in the presence of incoming boundary layers. A comprehensive description of the overall secondary flow system can be found in the experimental works of Sieverding [72] and Wang et al. [73], while a schematic representation of the vortex system arising in axial turbomachinery is shown in Fig. 4.2. The most important structures are:

- Passage Vortex: the boundary layer developing over the endwall is characterized by a velocity defect with respect to the potential flow in the free-stream. Because of the low velocity, the centrifugal force is not able to withstand the blade-to-blade pressure gradient, pushing the flow towards the suction side of the blade, generating a branch of negative axial vorticity which develops throughout the cascade.

- Horseshoe Vortex: it is caused by the redistribution of the boundary layer vorticity under the potential effect imposed by the blade. When the boundary layer approaches the leading edge of the blade, flow material lines start bowing. This redirects the inlet pitchwise vorticity to the axial direction. Because of the overall conservation of vorticity (under inviscid flow assumptions), the two branches developing on the pressure side and on the suction side are characterized by a positive and negative axial vorticity respectively.

- Corner Vortex: it forms in the aft region of the SS. The formation of this vorticity region is adduced to the interaction between the horseshoe vortex and the boundary layer in the SS corner of the endwall. When the HV impinges on the SS, it starts migrating towards the midspan, while a new three-dimensional boundary layer forms in the corner. The sense of rotation of the corner vortex is opposite to the deflection of the cascade.
- Trailing Shed Vortex: it is adduced to the different circulation of the blade under an incoming boundary layer. The different loading and deflection of the flow in the endwall region cause a region of positive axial vorticity at the outlet plane

It is of general consensus that the overall strength and interaction mechanism between the aforementioned flow structures highly depends on the blade design and the incoming boundary layer characteristics. Hodson and Dominy [74], showed that the losses associated to secondary flows increase with the blade loading. Similarly, the works of Weiss and Fottner in [75] and Benner et al. in [76] indicate that losses increase for higher stagger angles, hence for front-loaded designs. On the other hand, the impact of incoming boundary layers is somewhat more subtle. While some analysis predict a small impact of the incoming boundary layer on the overall secondary flow structure (see [77] as an example), other works indicate that significant discrepancies in the endwall region arise when realistic boundary layers are fed to axial turbines (see [78]). In [79], the authors showed that laminar boundary layers, yield higher losses and residual vorticity compared the turbulent boundary layers.

The topic has also been addressed in various numerical works. Some examples are the work from Cui et al. ([80]), Pichler et al. ([81]) and Giovannini et al. ([82]). From a numerical standpoint, there is a general agreement that the definition of realistic boundary layers, both in terms of mean flow profiles and turbulence quantities is fundamental for the proper reproduction of the secondary vorticity/losses for low-pressure turbine applications.

4.1.3 Modeling issues

From a modeling point of view, the prediction of the transitional boundary layer developing in low-Reynolds conditions has been addressed by means of both high-

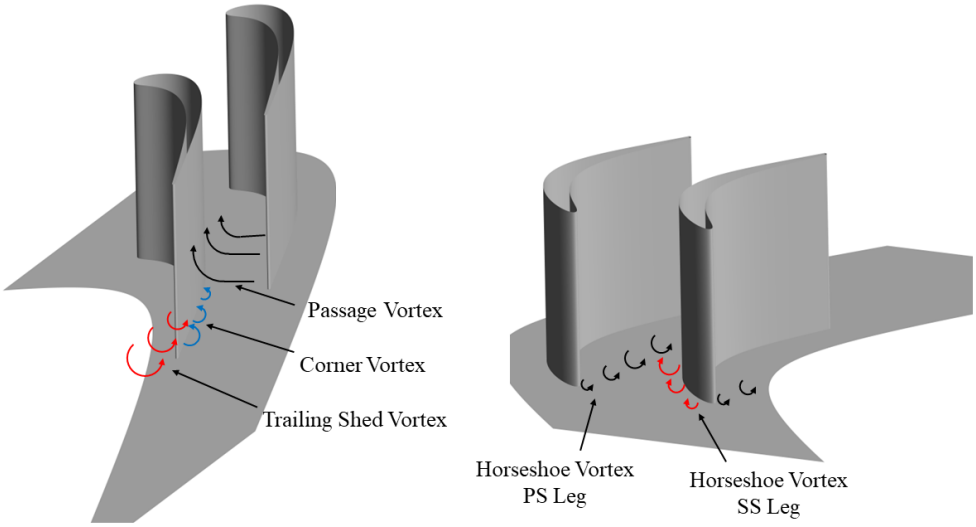

Fig. 4.2 Vortex system schematic

fidelity methods, like Direct Numerical Simulation (DNS) and Large Eddy Simulation (LES), and transition-sensitive RANS closures. The former methodology has proved to be reliable for the prediction of laminar/turbulent boundary layers arising in low-pressure turbine operating conditions ([83, 84]), because of the possibility to resolve local flow features responsible for boundary layer transition and wake mixing. On the other hand, RANS closure still represent the most adopted design tools for turbomachinery applications, as it provides a good trade-off between accuracy and overall computational time. In this case, local flow features are approached in 'averaged' sense, solving for the mean flow field. The transition mechanism is instead tackled by means of suitable modifications to production and destruction terms in the turbulent scalars equations. In general, transition-sensitive models developed for low-Reynolds applications can be divided in two families:

- Laminar Kinetic Enegy models: they are based on the concept of laminar kinetic energy which accounts for larger time-scales fluctuations which eventually feed turbulent eddies, promoting transition. The idea of LKE was first proposed by Mayle and Schulz [85] and represented the starting point for various types of closures ([86] and [61] are the most adopted in the turbomachinery community)

- Intermittency-based models: in this case the transition is enforced by means of flow intermittency, which indicates the probability of the boundary layer to either be in a laminar or turbulent state. The concept has served for the introduction of transition sensitive closures, being the one by Menter et al. ([87]) the most common in CFD

From a practical perspective, both approaches require additional variables, which provide the proper blending between a laminar solution and a fully-turbulent one. In the context of the present thesis, two different models have been employed for the simulation of the SPLEEN cascade. The first model is the $k-\overline{v^2}-\omega$ by Lopez and Walters [53], whose implementation was already described in Chapter 3. The other transition-sensitive model employed is the $\gamma-\tilde{Re}_{\theta t}$ by Langtry and Menter [88]. A general overview of both models and their implementation in HybFlow is given in Appendix C.

4.2 Introduction to the SPLEEN test case

The SPLEEN-C1 is a high-speed blade which has been thoroughly investigated in a wide range of operating conditions, spanning both subsonic and transonic Mach numbers, in low Reynolds conditions in the framework of the EU-funded project SPLEEN. A general overview of the blade characteristics and operating conditions is reported in Tab. 4.1. While, the full experimental characterization of the test case, for both steady and unsteady conditions can be found in the literature ([89–91]), a brief overview of the cascade and experimental data available is here reported.

The open database reports three different test campaigns. The first one is devoted to the analysis of the cascade performance under steady conditions, and no leakage flow from the cavity cassette. The cascade has been investigated for different ranges of Mach numbers (0.7-0.95) and Reynolds numbers (65,000-120,000). The second campaign details the performance under wake passing events, introducing an annular wake generator. The third campaign details the combined effect of wake passing and leakage flow. As mentioned in the introduction to the chapter, in the present thesis only the first two set of measurements have been used, while no simulation with both leakage flow and wake generator has been performed. The linear cascade geometry, along with the local coordinate system and the measurements plane is reported in

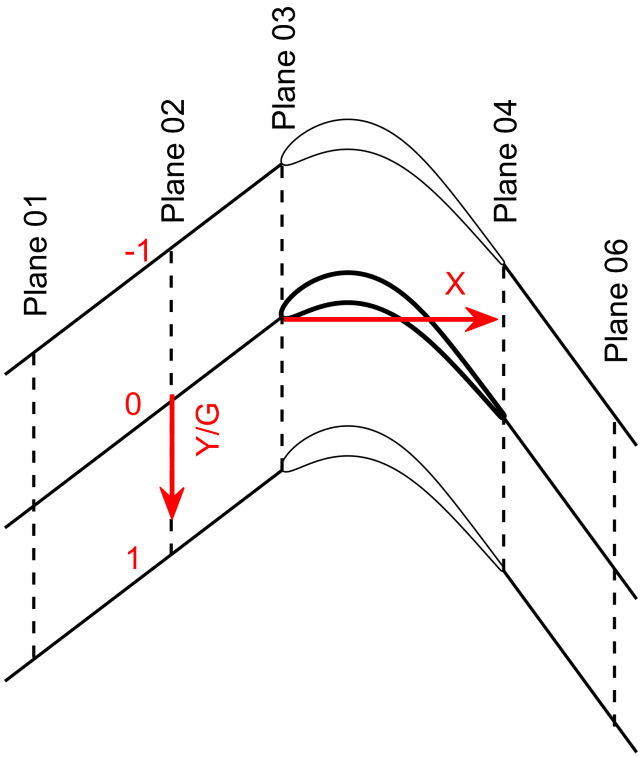

Fig. 4.3 Spleen cascade: measurement locations and coordinate system

Fig. 4.3. Plane 01 is located at X=-1.12 C_{ax}, corresponding to the axial position of the wake generator rake. Plane 02 is located at X=-0.5 C_{ax}. Measurements at this plane are used to characterize the inlet flow field to the cascade. The position of the plane corresponds with the cavity cassette introduced to study the effect of leakage flow on the cascade. Plane 03 and 04 respectively indicate the LE plane and the TE plane. The outlet measurement location is Plane 06, which is located at X=1.5 C_{ax}. The full description of the measurement methodology and the experimental dataset are openly available at [92].

4.3 2D Steady Simulations

The study of the SPLEEN cascade started from 2D steady simulations aiming at reproducing the midspan flow of the blade. The two-dimensional simulations have been used to assess mesh dependency and the performance of the implemented transition models in reproducing the losses and the loading distribution of the airfoil.

Table 4.1 SPLEEN-C1 Blade characteristics and steady operating conditions

C_{ax} [mm]	47.614
C [mm]	52.285
G/C [-]	0.63
H/C [-]	3.16
Inlet blade metal angle β_{m2} [°]	37.3
Outlet blade metal angle β_{m6} [°]	53.8
Incidence angle [°]	-1
Outlet isentropic Mach number [-]	0.70-0.95
Outlet isentropic Reynolds number [$\times 10^3$]	70-120
Freestream turbulence intensity [%]	$\approx$ 2.4

Table 4.2 Mesh characteristics

Name	Total Elements [$\cdot 10^3$]	Quadrilateral Layers	Profile Elements	Max y^+
M1	$\approx$50	25	305	0.12
M2	$\approx$70	25	573	0.12
M3	$\approx$90	25	737	0.12
M4	$\approx$100	25	763	0.12

Hybrid triangular/quadrilateral meshes were enforced for the the analysis, generated using the commercial mesh generator Centaur^{TM}. All the meshes were built in order to guarantee a max value of y^+<1.0 over the blade surface, guaranteeing a proper discretization of the blade curvature at the LE and TE of the airfoil. The details of the adopted meshes are summarized in Tab. 4.2, while Fig. 4.4 shows the LE/TE details of the grid, along with the refinement enforced until PL06.

The mesh dependency was assessed in terms of loading prediction and energy loss coefficient in the wake for the nominal operating point of the blade ($Ma_{6,is}$=0.9 and $Re_{6,is}$=70,000). The energy loss coefficient is defined as:

$$\xi = 1 - \frac{1 - \left(\frac{P_6}{P_{06}}\right)^{\frac{\gamma}{\gamma-1}}}{1 - \left(\frac{P_6}{P_{02}}\right)^{\frac{\gamma}{\gamma-1}}} \tag{4.1}$$

The results are shown in Fig. 4.5, where experimental measurements are also added for reference. While the predictions of the loading show little sensitivity to the adopted grid, the same does not hold for the total pressure deficit. As a matter of fact,

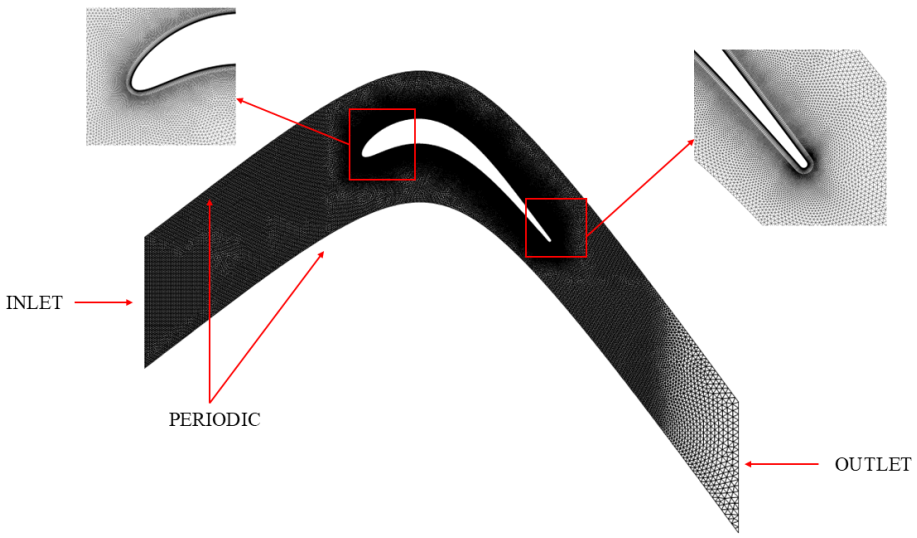

Fig. 4.4 Final mesh

a mesh independent distribution of the losses is achieved only for mesh M3. Coarser meshes yield a slightly thicker wake, with a lower loss value in the wake center.

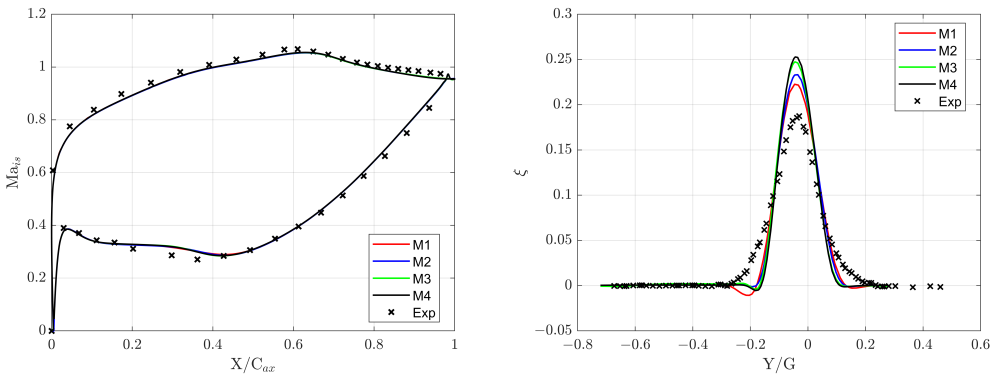

(a) (b)

Fig. 4.5 Mesh Sensitivity: Blade loading (a) and Energy loss coefficient (b)

4.3.1 Comparison with the experiments

Figure 4.6 reports the predictions obtained with the $\gamma - \tilde{Re}_{\theta t}$ and $k - \overline{v^2} - \omega$ transitional models for different combinations of isentropic Mach and Reynolds numbers. The cascade evidences the occurrence of two different separation bubbles. The first

one arises over the SS of the blade due to the pressure recovery, while a secondary separation bubble is present in the front region of the blade PS. While experiments seem to confirm the existence of the PS separation, the experimental size is probably smaller than the one predicted by CFD simulations, causing a mismatch in the pressure distribution over the front region of the blade. Among the two models, the $\gamma - \tilde{Re}_{\theta t}$ transition closure yields a faster reattachment of the PS separation, which in turn leads to a better agreement with the experimental measurements. As far as the diffusive region of the SS is concerned, the predictions yielded by the models evidence a different reaction to the onset and reattachment of the SS bubble. At $Ma_{6,is}$=0.7, the pressure recovery predicted by the $k - \overline{v^2} - \omega$ model indicates that the separation-induced transition mechanism predicted by the CFD is too slow, failing to retrieve the experimental deceleration. A similar behavior is present at intermediate Mach conditions ($Ma_{6,is}$=0.8) for $Re_{6,is}$=100,000-120,000, while a better agreement is present in low-Reynolds conditions. On the other hand, the $\gamma - Re_{\theta}$ model is able to adequately predict the loading, for the whole range of $Re_{6,is}$. At low-Mach, the experimental isentropic Mach distribution after the reattachment is correctly predicted, while it is underestimated at $Ma_{6,is}$=0.8 for all Reynolds numbers. Both models feature a general underestimation of the isentropic Mach number throughout the whole SS, even though the acceleration in the front part is correctly captured. As far as the high-Mach condition is concerned, the $k - \overline{v^2} - \omega$ and the $\gamma - \tilde{Re}_{\theta t}$ model yield similar predictions of the loading, matching the experimental measurements over the SS, still overpredicting the PS separation bubble.

Using the procedure detailed in [89], it is possible to infer the relationship between the mismatch in the loading and the size of the separation bubble. As a matter of fact, the approximate positions of the separation point, recovery point and reattachment point can be related to distribution of the isentropic velocity on the SS, and in particular to the the acceleration parameter $K_s = \frac{\nu}{U_{is}^2}\frac{\partial U_{is}}{\partial S}$ and its derivative. The position of the aforementioned points can be retrieved as follows:

- The position of the separation point 'Sep' can be related to a local minimum of the acceleration parameter
- The position of the recovery point 'Rec', where the separation bubble reaches its maximum size, can be approximately located in the following peak of the acceleration parameter

- The reattachment point 'Rea' is approximately located in the position of local peak of the acceleration parameter derivative ($\frac{\partial K_S}{\partial S}$)

The comparison between the numerical and experimental acceleration parameter is shown in Fig. 4.7, where the effect of a variation of both the Mach number and Reynolds number is evaluated. The Reynolds number retains a major effect on the acceleration parameter in the central region of the SS, but does change the loading distribution of the blade. The peak velocity (found in correspondence of K_s=0) is not affected by the Reynolds number, while the relative minimum found closer to the TE moves downstream when $\mathrm{Re}_{6,is}$ is increased. Moreover, the recovery point moves upstream in high-Reynolds conditions. The length of the separation bubble is thus lower. The faster diffusion close to the TE for $\mathrm{Re}_{6,is}$=70,000 is instead due to the later reattachment of the bubble itself. On the other hand, the Mach number affects the loading distribution in the front part of the cascade. The increase of the isentropic Mach moves the velocity peak downstream: at $\mathrm{Ma}_{6,is}$=0.7 the velocity peak is approximately located at S/S_0=0.37 while for $\mathrm{Ma}_{6,is}$=0.95 the velocity peak is instead located at S/S_0=0.6. In these conditions, the acceleration parameter exhibits a flatter curve after the peak velocity compared to the intermediate and low-Mach conditions. This indicates a smooth diffusion of the flow in the aft region of the SS, which is possible because the separation bubble affecting blade loading at $\mathrm{Ma}_{6,is}$=0.7-0.8 is almost suppressed. Thus, it retains a negligible effect on the isentropic velocity distribution. At $\mathrm{Ma}_{6,is}$=0.95, the blade also features the presence of a weak shock in the throat section of the passage. It is shown in Fig. 4.8, where numerical Schlieren of low- and high-Mach cases is shown. Because of its weakness, the shock does not affect the loading distribution to a major extent. As a matter of fact an evident reduction of the acceleration parameter is not present. Despite this, the shock will retain a major effect on the boundary layer quantities as will be shown later.

Low-Mach conditions represent the most difficult case to be reproduced using the implemented transition models, because of the longer diverging region over the SS, which favors the formation of the separation bubble. The $\gamma - \tilde{Re}_{\theta t}$ model demonstrate a satisfactory prediction of both separation and reattachment points compared to the experiments, even though the isentropic velocity is underpredicted close to the recovery point, possibly indicating that the size of the separation bubble is smaller compared to the experiments. The $k - \overline{v^2} - \omega$ predicts an open bubble at $\mathrm{Re}_{6,is}$=70,000 and reattaches in correspondence of the trailing edge at $\mathrm{Re}_{6,is}$=100,000.

The slow reaction to the presence of a separation bubble is possibly related to the fact that the model does not have any explicit trigger for separation induced transition. Hence, from a numerical standpoint, the turbulence production in the separated shear layer is not sufficient to favor its reattachment. This is a common problem in local transition models, which can be alleviated using non-local treatment of transition triggering terms (like in [86] and [93]), or non-physical values of the intermittency, for intermittency based models. This second strategy is instead adopted by the $\gamma - \tilde{Re}_{\theta t}$ model (see App. C). A similar behavior is present also at $Ma_{6,is}$=0.8. The most noteworthy result occurs for the lowest Reynolds number. In this case, the experimental diffusion is very slow in the aft region of the SS also an indication of separating boundary layer. An evident reattachment point is not present in the experiments (the diffusion starts to increase only downstream of $S/S_0 \approx 0.9$), nor in the numerical predictions as the diffusion rate is almost constant. Despite this, the prediction of a thicker boundary layer by the $k - \overline{v^2} - \omega$ allows to retrieve a better distribution of the loading closer to the TE.

The analysis of the prediction of the outlet flow field is instead presented in Tabs. 4.3 and 4.4, where the numerical mass-flow averaged energy loss coefficient and deviation angle, are respectively compared with experimental values. Both models satisfactory predict the averaged losses at the outlet plane, even though the $\gamma - \tilde{Re}_{\theta t}$ model exhibits a better agreement with the experiments. The maximum discrepancy is instead present for the $k - \overline{v^2} - \omega$ model, in correspondence of low-Mach, low-Reynolds conditions. The deviation angle is also well predicted, even though the values are very small. Experiments do not evidence significant changes over the range of measured conditions. Higher variability is present in CFD, evidencing that the deviation angle highly depends on the isentropic Mach number, and hardly depends on the isentropic Reynolds number. Despite the proper prediction of mass flow averaged values, Fig. 4.9 shows how the local flow field predicted by RANS highly deviates from the experimental one. Both models strongly over predict the energy loss coefficient in the center of the wake, while underestimating its spreading. Similarly to the mass-flow averaged performance, the misprediction highly depends on the Mach number. This behavior is common in literature and addressed to the inability of RANS models to properly predict wake mixing downstream of the blade. It is noteworthy to say that both models present a similar treatment of the wake region, implementing a cross-diffusion term. This indicates that the different prediction of the wake spreading and position is to be found in the upstream flow,

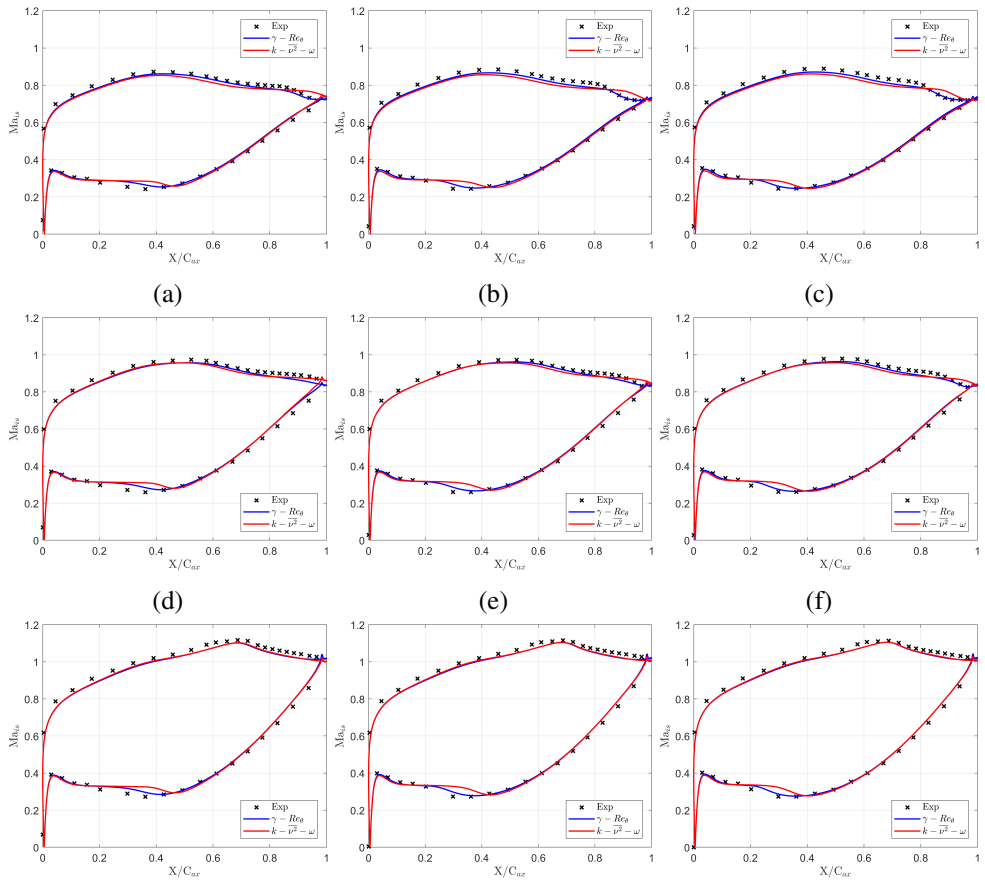

Fig. 4.6 Effect of operating conditions on blade loading: (a) $Ma_{6,is}$=0.7, $Re_{6,is}$=70,000, (b) $Ma_{6,is}$=0.7, $Re_{6,is}$=100,000, (c) $Ma_{6,is}$=0.7, $Re_{6,is}$=120,000, (d) $Ma_{6,is}$=0.8, $Re_{6,is}$=70,000, (e) $Ma_{6,is}$=0.8, $Re_{6,is}$=70,000, (f) $Ma_{6,is}$=0.8, $Re_{6,is}$=120,000, (g) $Ma_{6,is}$=0.95, $Re_{6,is}$=70,000, (h) $Ma_{6,is}$=0.95, $Re_{6,is}$=70,000, (i) $Ma_{6,is}$=0.95, $Re_{6,is}$=120,000

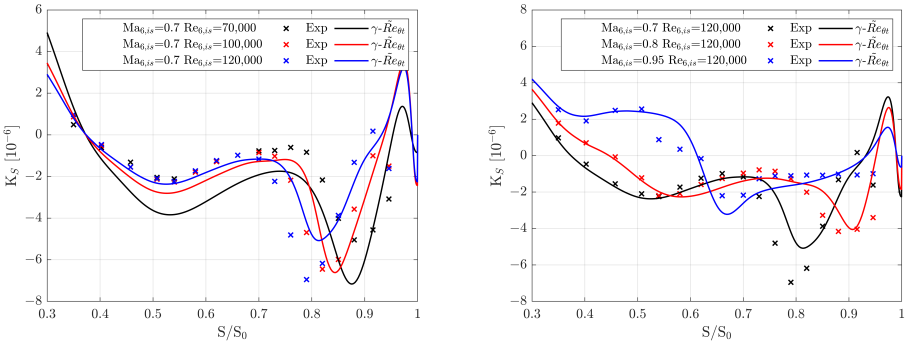

Fig. 4.7 Acceleration parameter: (a) Effect of the Reynolds number at $Ma_{6,is}$=0.7, (b) Effect of the Reynolds number at $Re_{6,is}$=120,000

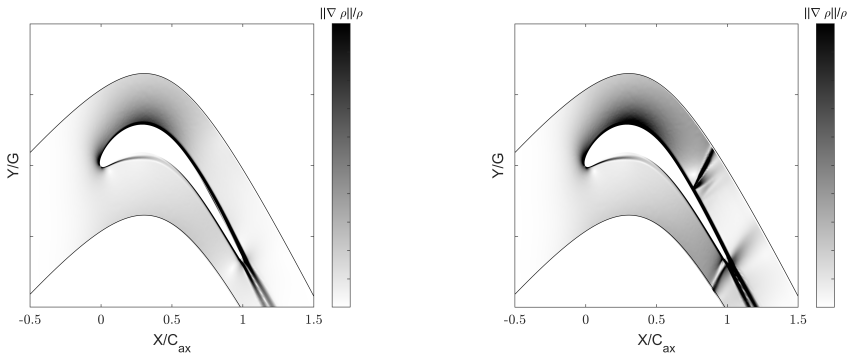

(a) $Ma_{6,is}$=0.7 (b) $Ma_{6,is}$=0.95

Fig. 4.8 Numerical Schlieren: (a) $Ma_{6,is}$=0.7, (b) $Ma_{6,is}$=0.95

Table 4.3 Energy losses coefficient - Plane 06.

$Ma_{6,is}$	$Re_{6,is}$	ξ Experimental	ξ $\gamma - \tilde{Re}_{\theta t}$	ξ $k - \overline{v^2} - \omega$
0.7	70,000	0.036	0.036	0.039
0.9	70,000	0.031	0.032	0.031
0.95	70,000	0.031	0.032	0.029
0.8	120,000	0.027	0.028	0.029
0.9	120,000	0.028	0.027	0.027

and in particular in the boundary layer close to the TE of the blade. As a matter of fact, thicker boundary layers can induce higher deficit of total pressure. This reasoning is confirmed by the evident mismatch between the experimental loss at $Ma_{6,is}$=0.7, $Re_{6,is}$=70,000 and the numerical predictions obtained with the $k - \overline{v^2} - \omega$ model. It was shown , while describing the loading, that the model is unable to trigger transition after the formation of the SS separation bubble, generating a thick boundary layer at the blade TE, before wake mixing.

4.3.2 Boundary layer analysis

A thorough description of the boundary layer allows to understand where the mismatch between the two given models arise. The first analysis will regard the prediction of the separation and reattachment points by the models over the range of experimental working conditions. The separation and reattachment points of the SPLEEN test-case are not available and can only be inferred from the loading

Table 4.4 Deviation - Plane 06.

$Ma_{6,is}$	$Re_{6,is}$	d [deg] Experimental	d [deg] $\gamma - \tilde{Re}_{\theta t}$	d [deg] $k - \nu^2 - \omega$
0.7	70,000	-0.7 ($\pm$ 0.4)	-0.4	-0.3
0.9	70,000	-0.9 ($\pm$ 0.4)	-0.2	-0.1
0.95	70,000	-0.9 ($\pm$ 0.4)	0.0	0.0
0.8	120,000	-0.9 ($\pm$ 0.4)	-0.4	-0.3
0.9	120,000	-0.9 ($\pm$ 0.4)	-0.2	-0.2

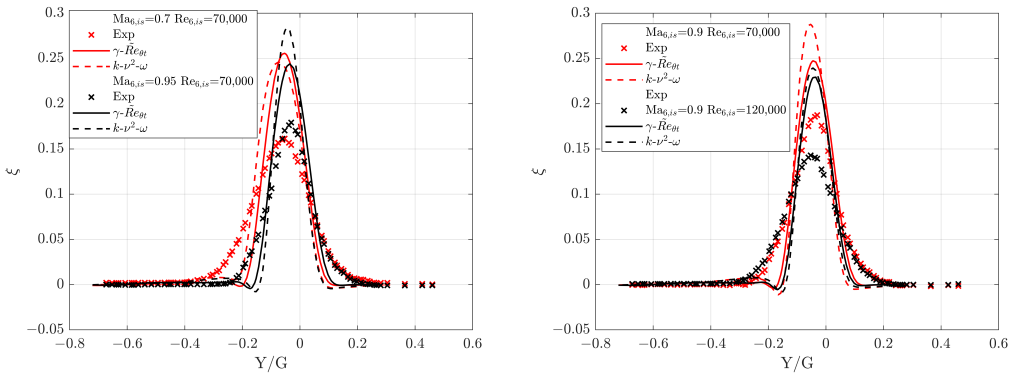

(a) (b)

Fig. 4.9 Effect of operating conditions on the prediction of the wake total pressure deficit: Effect of Mach number (a) and Effect of Reynolds number (b)

distribution. While the methodology is reliable to extract flow information from the isentropic velocity only, it does not allow to accurately define the separation and reattachment. In order to clarify this aspect, Fig. 4.10 reports the comparison between the separation and the reattachment positions obtained from the numerical loading and from the numerical wall shear stress. It is evident that while the loading criterion allows to locate the separation and reattachment point in the vicinity of the proper position, the length of the separation bubble would result in being higher than its value obtained from shear stress analysis. For this reason the comparison between the CFD predictions and experimental evidence is done against the correlations proposed by Hatman and Wang ([94]). It must be said that the correlations were obtained in subsonic conditions and for low levels of turbulence intensity (TI<0.6%). The analysis compares the prediction of the separation point and the bubble length (Reynolds at reattachment vs Reynolds at the separation point) against the available correlations for $Ma_{6,is}$=0.7-0.8 only. As far as the analysis of the reattachment point is concerned, Fig. 4.10c only provides results for the $\gamma - \tilde{Re}_{\theta t}$ model as the $k - \overline{v^2} - \omega$ does not consistently predict the reattachment of the boundary layer, thus these results have been omitted. The CFD shows the same trend as the correlations, but the bubble length is shorter. This is particularly true for the low-Reynolds number case (bottom-left region of the plot). This mismatch is probably due to the lower turbulence intensity used to obtain the correlations. Comparing the Reynolds number at the separation and the local acceleration parameter, it is evident that CFD predicts an early separation, even though the origin of this disagreement has not been identified.

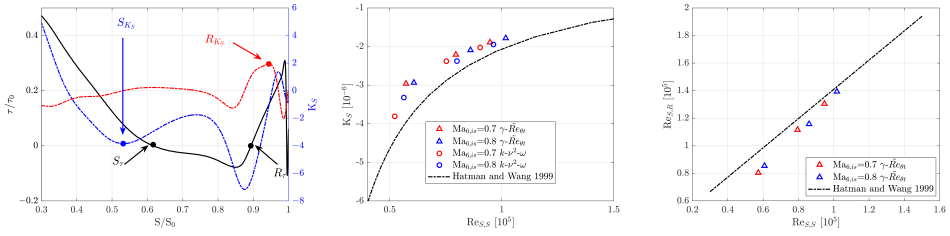

(a) (b) (c)

Fig. 4.10 Separation/Reattachment: Comparison with experimental correlations

Figure 4.11 compares the experimentally measured quasi-wall shear stress for three different operating conditions. The experimental measurements are normalized with respect to the first measurement point at S/S_0 =0.038. The isentropic Mach

number is also added to identify accelerating/decelerating regions over the SS. The discussion will start from low-Mach, low-Reynolds conditions. The $\gamma - \tilde{Re}_{\theta t}$ model predictions agree to some extent with the experimental trend. It must be said that the overprediction of the wall shear stress in the front part of the blade may be due to the choice of the normalization point. The separation of the flow occurs at $S/S_0 \approx 0.61$ while the reattachment occurs at $S/S_0 \approx 0.89$. The model overpredicts the wall shear stress after the reattachment. The $k - \overline{v^2} - \omega$ instead predicts an open separation and manages to properly retrieve the experimental wall shear stress. Despite this the misprediction of the loading indicates that the bubble is actually closed and the overall agreement is due to the impossibility to retrieve flow direction from hot film measurements. The slower reaction to the separation bubble from the $k - \overline{v^2} - \omega$ model is also evidenced for the other two operating conditions which, even if a reattachment point is predicted. At $\mathrm{Re}_{6,is}$=120,000, both models predict boundary layer separation slightly upstream of S/S_0 =0.6 which seems to be anticipated with respect to the experiments. The $\gamma - \tilde{Re}_{\theta t}$ predicts reattachment at $S/S_0 \approx 0.84$ and later the flow transitions to the turbulent state. The $k - \overline{v^2} - \omega$ predicts a reattachment point at $S/S_0 \approx 0.92$. At $\mathrm{Ma}_{6,is}$=0.95, the experimental measurements appear more scattered. The simulations yield the same predictions of the wall shear stress up to the separation point and also retrieve a sudden decrease of the wall shear stress occurring due to the presence of impinging shock. Downstream of impingement, the wall shear stress is very low both in the computations and in the experiments as the presence of the shock thickens the boundary layer (see Fig. 4.12). The transition is again faster for the $\gamma - \tilde{Re}_{\theta t}$. As a general remark, the two models predict the same behavior in the accelerating region, while differences occur in the separation and reattachment prediction.

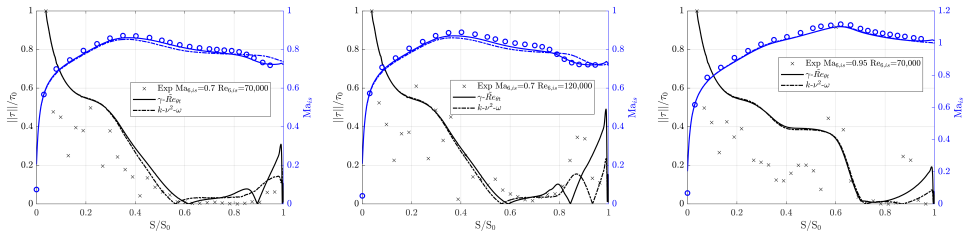

(a) (b) (c)

Fig. 4.11 Wall shear stress: (a) $\mathrm{Ma}_{6,is}$=0.7, $\mathrm{Re}_{6,is}$=70,000, (b) $\mathrm{Ma}_{6,is}$=0.7, $\mathrm{Re}_{6,is}$=120,000, (c) $\mathrm{Ma}_{6,is}$=0.95, $\mathrm{Re}_{6,is}$=70,000

Figure 4.12 compares the boundary layer shape factor from both models. It is computed integrating respectively the velocity and momentum deficit in the boundary up to the free-stream position. The latter is individuated using local flow vorticity. Similarly to the wall shear stress, the models yield similar predictions in the accelerating region, while major differences arise only downstream. At $Ma_{6,is}$=0.7, laminar flow exists in the front part, eventually separating in the diverging portion. The separation bubble of the $k-\overline{v^2}-\omega$ is much thicker and leads to an almost twice shape factor compared to the one predicted by the $\gamma-\tilde{Re}_{\theta t}$. The high shape factor of the $k-\overline{v^2}-\omega$ at low-Reynolds is due to the fact that the separation bubble is open. All the other cases instead evidence the presence of a reattaching flow undergoing transition. The high shape factor after reattachment ($\approx$2 for the $\gamma-\tilde{Re}_{\theta t}$) is due to the fact that the boundary layer is not in equilibrium yet. At $Ma_{6,is}$=0.95, the shape factor shows a peak at S/S_0 =0.33 upstream of the velocity peak at S/S_0 $\approx$0.65. Higher values of H are found later because of the shock impingement, with boundary layer thickening. The value of H at the TE is around 4 for the $k-\overline{v^2}-\omega$ and 3.5 for the $\gamma-\tilde{Re}_{\theta t}$. In the aft region, the shape factor predicted at $Ma_{6,is}$=0.7 by the $\gamma-\tilde{Re}_{\theta t}$ model is lower because of the separation induced transition mechanism which favors the formation of a turbulent boundary layer

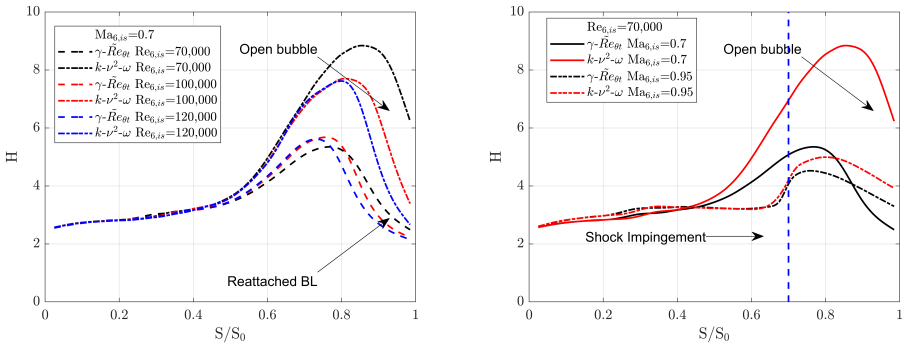

(a) (b)

Fig. 4.12 Shape Factor: $Ma_{6,is} = 0.7$ (a) and $Ma_{6,is} = 0.95$ (b)

4.4 3D Steady Simulations

The second part of the activity devoted to the analysis of the SPLEEN cascade, aims at investigating the endwall flow of the test-case under representative operating con-

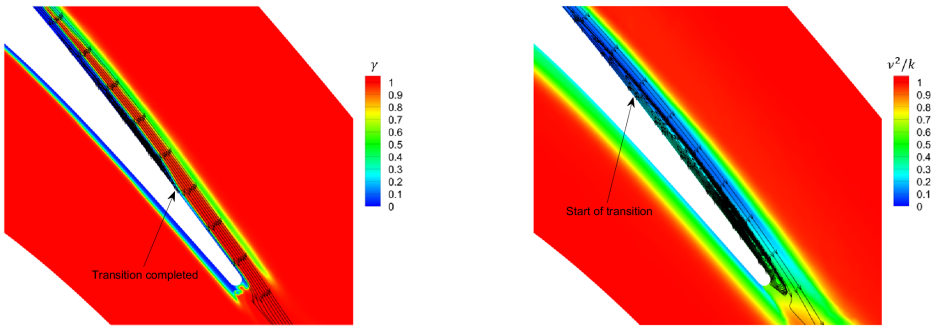

(a) (b)

Fig. 4.13 Streamlines: (a) $\gamma - \tilde{Re}_{\theta,t}$, (b) $k - \overline{v^2} - \omega$

ditions and inflow boundary layer profile. Considering the overall better agreement provided by the $\gamma - \tilde{Re}_{\theta t}$ transition model in the reproduction of the midspan flow field, it has been used for the simulations of the three-dimensional profiles. The analysis was conducted for three different operating conditions, trying to evidence the combined effect of the Reynolds and Mach number of the secondary flow structures and turbulence intensity distributions at the outlet measurement plane. The operating points used for the 3D analysis are:

- $Ma_{6,is}$=0.9, $Re_{6,is}$=70,000 representing nominal conditions
- $Ma_{6,is}$=0.7, $Re_{6,is}$=70,000 representing the low-Mach case
- $Ma_{6,is}$=0.9, $Re_{6,is}$=120,000 representing the high-Reynolds case

The setup of three-dimensional simulations is slightly different from the two-dimensional counterpart. As a matter of fact, the inlet of the numerical domain was moved to Plane 02, 0.5 C_{ax} upstream of the cascade. This modification allows to specify the experimentally measured boundary layer at the inlet of the cascade, reducing the error associated with its development for further positions of the inlet surface. The inlet conditions were prescribed using the experimental spanwise profile for total pressure and incidence angle, while maintaining the total temperature to a constant value. On the other hand, the turbulence specifications used in this thesis was retrieved from various measurements of the boundary layer flow accessed during a secondment at VKI, which have not been released in the open database ([92]) at the moment of writing this dissertation.

The first part of the analysis is dedicated to the effect of the turbulence specification inside the boundary layer profile. To this end, three different turbulence specifications have been used:

- T1 enforces the turbulence intensity retrieved from the experiments, assuming isotropic turbulence. The turbulent length scale at the inlet is instead uniform and defined according to the decay found at midspan
- T2 uses the same uniform profile for the turbulent length scale, while adopting an anisotropic assumption for the computation of the turbulence intensity retrieved from experimental data
- T3 uses the anisotropic turbulence intensity definition, along with a profile for the turbulent length scale which is retrieved from the experimental campaign. The profile is scaled to match the turbulence decay at midspan

The specified inlet conditions, in terms of spanwise profiles, are represented in Fig. 4.14.

Eventually, considering the symmetrical distribution of flow through the span of the cascade, only half domain was simulated, treating the upper boundary surface as an inviscid wall. Figure 4.15 shows the three-dimensional domain used for the investigation.

4.4.1 Grid sensitivity

Because of the additional effects related to the simulation of the secondary flow field, an additional grid sensitivity was performed on the three-dimensional test case. The aim is to characterize the effect of spanwise mesh spacing on the prediction of the secondary flow structures. All the three-dimensional meshes have been obtained as an extrusion of two-dimensional grids in the spanwise direction. The generated meshes do not enforce the same discretization used for the 2D simulations, as it was attempted to reduce the computational cost of the three-dimensional simulations in order to have more flexibility in the assessment of the boundary conditions. Nevertheless, all the meshes have been generated to target a $y^+<1$ both over the viscous endwall and the blade profile, while preserving a mesh independent solution in the two-dimensional region of the flow. The spanwise distribution of the grid was

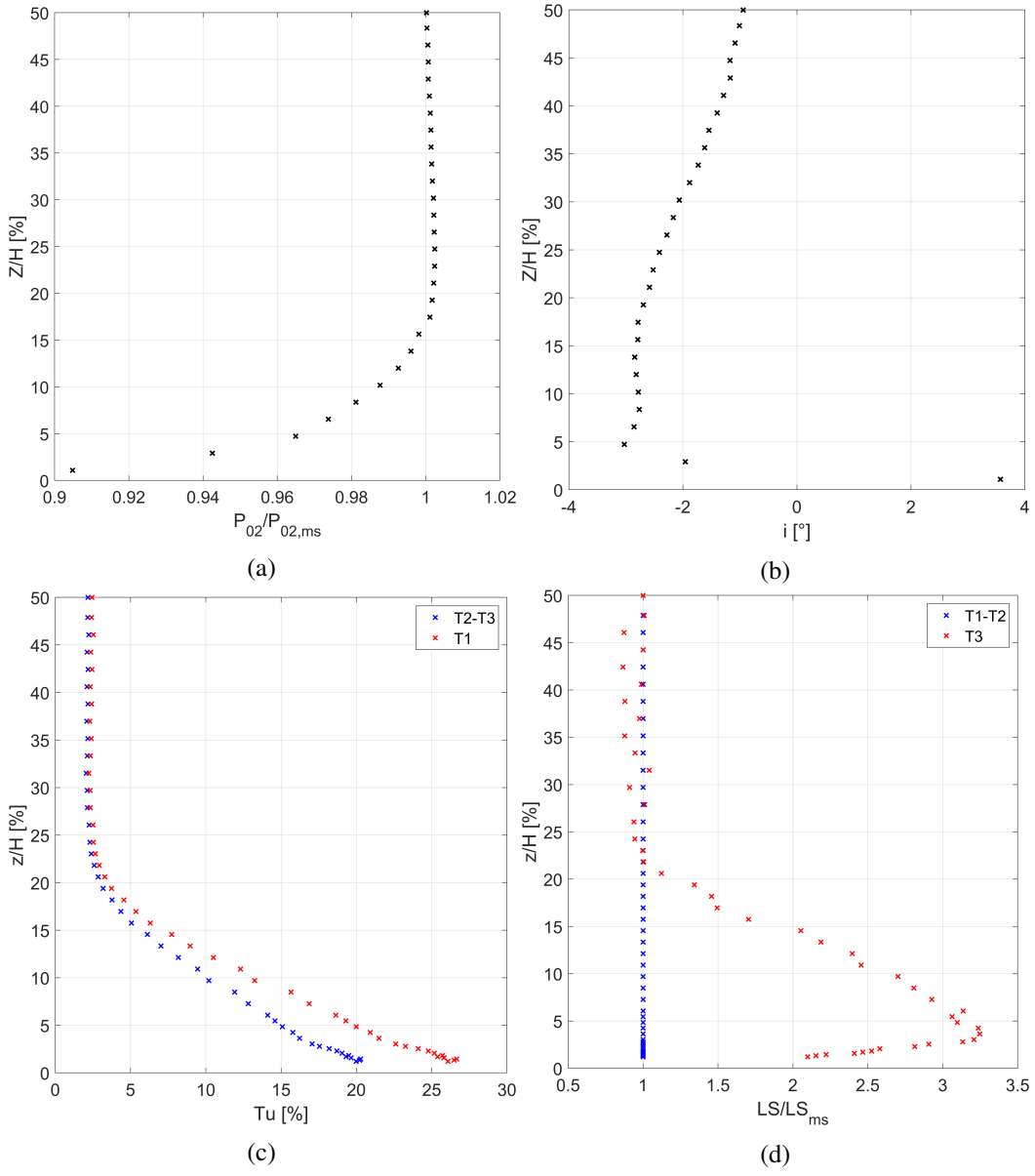

Fig. 4.14 Boundary conditions specification: (a) Total Pressure, (b) Incidence angle, (c) Turbulence intensity, (d) Integral length scale

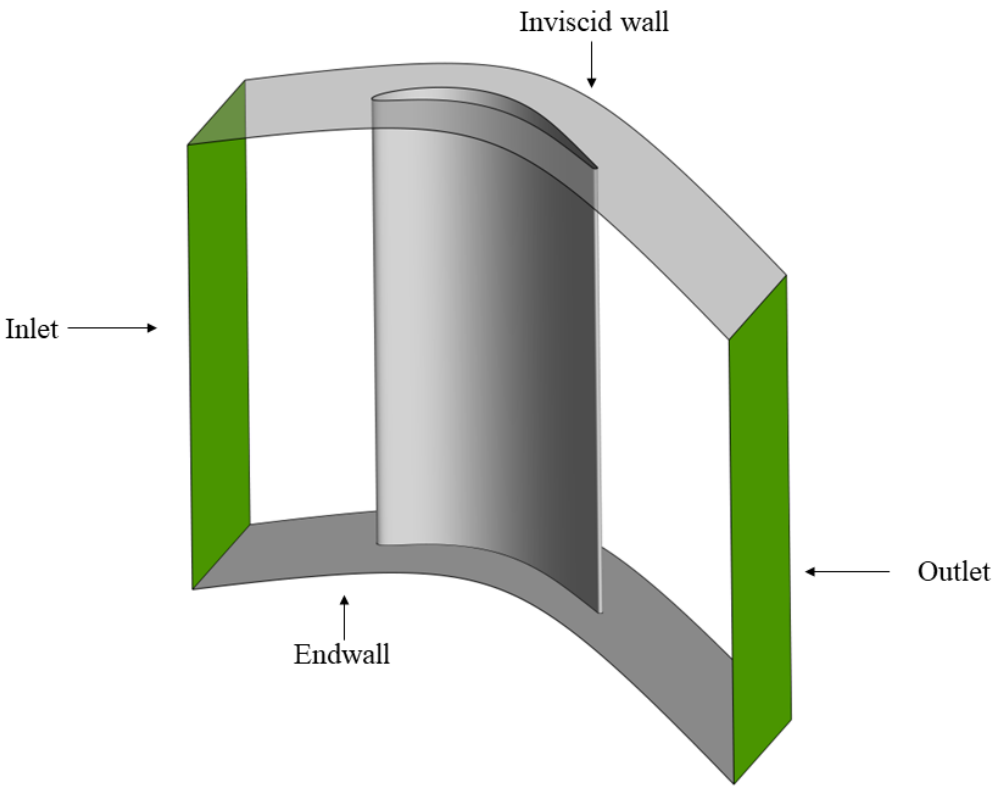

Fig. 4.15 Three-dimensional domain

obtained as a two-step extrusion: the boundary layer in the vicinity of the endwall was enforced using the thickness of the first layer, the stretching ratio (SR) in the spanwise direction and the total number of extrusion layers. The second step allowed to fill the remaining spanwise extension of the domain, calculating the expansion ratio of the cells in the spanwise direction from the total number of prescribed layers and from the thickness of the last extrusion layer in the endwall vicinity. The choice to use a two-pass extrusion is mainly motivated by the fact that it is possible to define an a-priori evolution law for the cells in the wall vicinity independently from the distribution of cells at higher spanwise positions. This allows to have a better control on the overall number of elements because the two regions of the flow are extruded independently one from the other, while the proper matching between the two extrusions is preserved. The main characteristics of the extruded grids are presented Fig. 4.16, along with the spanwise extrusion distribution in terms of mesh-index against the normalized spanwise position.

Name	SR	N_{layers}	Max y^+	N_{el}
M1	1.2	120	0.74	1.5M
M2	1.2	150	0.72	3.5M
M3	1.15	180	0.54	5.8M
M4	1.15	220	0.55	9.5M
M5	1.15	220	0.54	17.7M

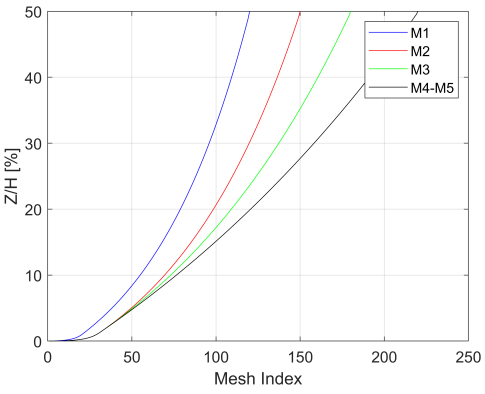

Fig. 4.16 Mesh characteristics

The mesh dependency was assessed in terms of loading predictions as well as Plane 06 measurements. In this case, the experimental targets are the flow angle and energy loss coefficient. This part of the study was performed using the turbulence profile T2, while flow conditions were reproducing the nominal operating point. As far as the loading is regarded, the mesh sensitivity is performed analyzing two different section, respectively close to the endwall and at midspan. The analysis is shown in Fig. 4.17. All the meshes exhibit similar predictions of the loading. As far as the free-stream flow is concerned, all meshes manage to capture the loading over the SS, up to X/C_{ax}=0.7. The flow diffusion in the aft region is instead faster compared to the experiments. All simulations predict a plateau in the region $0.2<X/C_{ax}<0.4$, over the PS of the blade. The loading is correctly captured even if

an overestimation of the isentropic Mach number is present in the TE region (around 0.03). The predictions of the free-stream flow field are similar to what has been shown in Sec 4.3, confirming that 3D effects retain little impact over the midspan flow. Moreover similar results have been already reported in the literature [95], using high-fidelity simulations (LES). It is assumed that the different prediction of the loading in the TE region is caused by a misprediction of the base pressure which would explain the increase in the isentropic Mach number over the SS.

The effect over the outlet flow field is shown in Fig. 4.18. The left figure shows the development spanwise development of the flow angle, normalized with respect to the midspan value. The right figure shows the energy loss coefficient. As far as the flow angle is considered, minor variations are present in the region around Z/H=10%. As the mesh is coarsened, the underturning slowly reduces close to its peak, and increasing in the region close to the midspan. The mesh density retains a higher effect close to the endwall at Z/H=2.5%. All meshes predict the same overturning trend values for low spanwise positions. The difference between the predictions and the experiments is constant, equal to $\approx 2^\circ$ for 2.5%<Z/H<5%. The variation over the peak in over-turning changes of about 0.2° as the mesh is refined. Regarding the energy loss coefficient, the main effect of the grid spacing regards the region around Z/H=7.5%, where the losses decrease as the mesh is refined. The effect is considered negligible, though.

Considering that effect of the mesh density on the loading predictions, as well as on the averaged outlet flow field, is negligible, the choice of the mesh was dictated by local distribution of flow features. This is shown in Fig. 4.19, where the losses distribution is shown for four different spanwise locations. While coarse meshes yield similar predictions in terms of mass-flow averaged pitchwise averaged losses, the same does not hold for local losses, both in the wake center (around the loss peak) and closer to the undisturbed flow. M4 and M5 yield the same prediction of the kinetic energy loss coefficient, so mesh M4 has been eventually selected for the final evaluation of the test-case. The details of the mesh used for the final simulations is instead shown in Fig. 4.20.

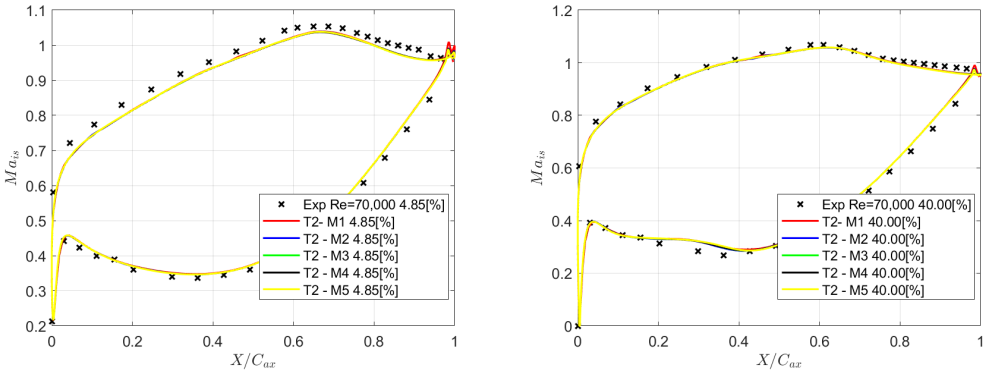

(a) (b)

Fig. 4.17 Mesh sensitivity - Loading prediction: (b) Z/H=4.85 %, (b) Z/H=40.00 %

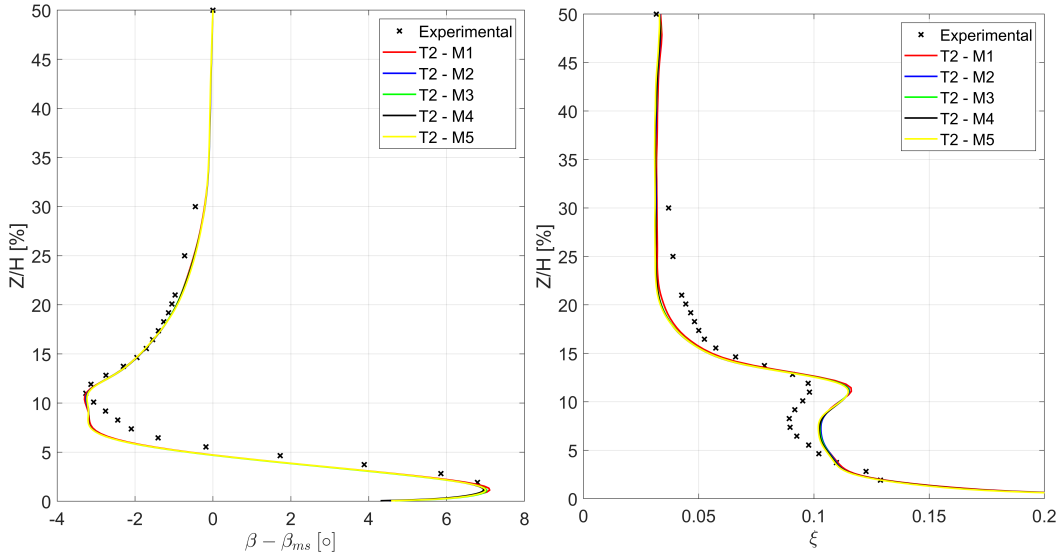

(a) (b)

Fig. 4.18 Mesh sensitivity - Plane 06: (a) Outlet angle, (b) Kinetic energy loss coefficient

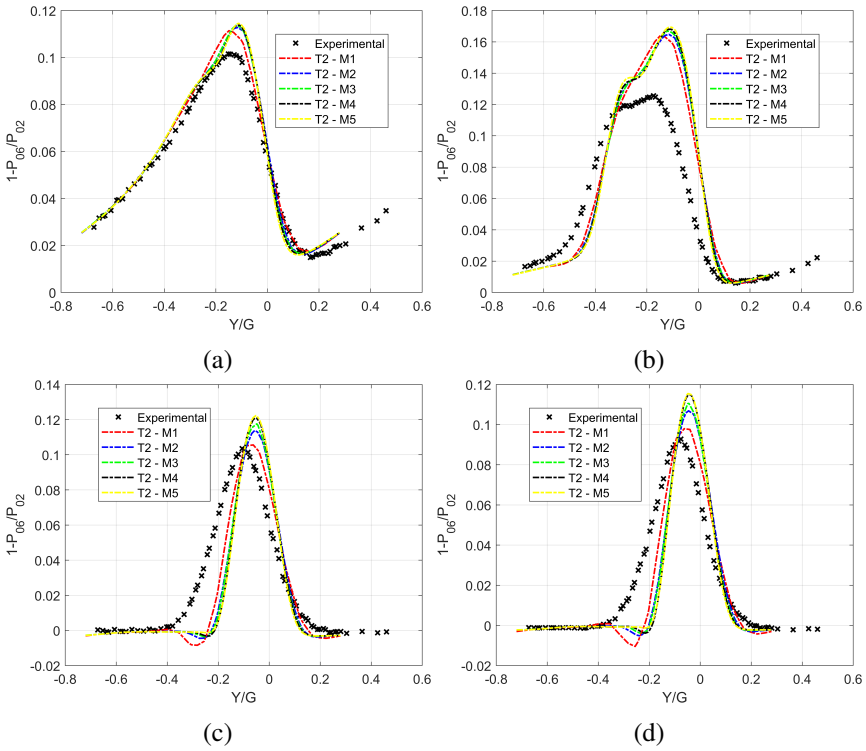

Fig. 4.19 Pitchwise resolved wake distribution: (a) Z/H=5%, (b) Z/H=10%, (c) Z/H=20%, (d) Z/H=30%

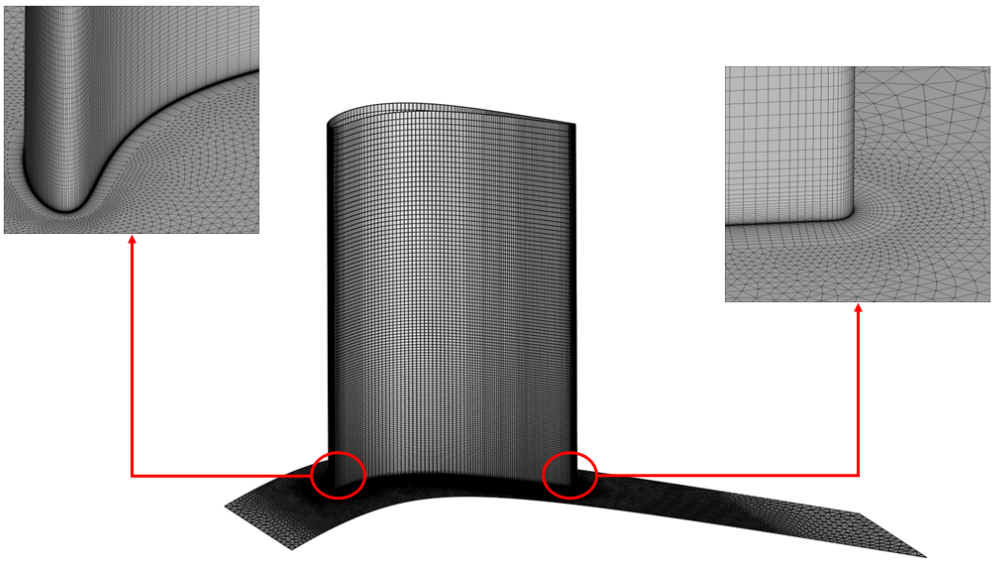

Fig. 4.20 Detail of M4 mesh.

4.4.2 Description of the secondary flow structure

The development of secondary flow structures under the developing blade and endwall boundary layers represents the major source of loss for a turbine cascade. For this reason it is important to investigate how they form throughout the cascade and interact with the free-stream flow. The secondary flow system in the endwall region is addressed first, visualizing the limiting streamlines and the static pressure over the endwall surface in Fig. 4.21. The streamlines evidence the presence of the horseshoe vortex, forming upstream of the LE of the blade and its bifurcation into a SS leg and a PS leg traveling towards the SS. The SS leg and the PS leg interact under the blade-to-blade pressure gradient. The impingement of the HV structure onto the SS blade marks the origin of the corner vortex (CV) in the aft region of the blade. The most interesting feature of the limiting streamlines is the presence of one single saddle point. Other researchers show that, depending on the incoming boundary layer, a couple of saddle points might be present (see numerical results from [81] and experimental results from [96]).

An overview of the secondary flow system is instead shown in Fig. 4.22b, where the secondary structures are identified by using isosurfaces of Q-criterion. The contours refer to the streamwise vorticity coefficient $C_{\omega s}$ defined in Eq. 4.2.

$$C_{\omega s} = \frac{\Omega_{ax} cos\left(\beta_{ms}\right) + \Omega_{y} sin\left(\beta_{ms}\right)}{V_{6,is}} C \tag{4.2}$$

The visualizations evidence five different structures developing throughout the cascade. The PS leg of the HV lifts up after reaching the SS of the blade. Its interaction with the blade boundary layer generates a counter-rotating vortical region: the Wall Vortex (WV). The Passage Vortex (PV) is co-rotating with the HVPS, induced by the pressure gradient in the blade-to-blade direction. In the figure it is indicated together with the HVPS. Also close to the hub, it is possible to discern the CV, which is also counter-rotating with respect to the HVPS. The fifth structure is the Trailing Shed Vortex (TSV) which is visible downstream of the cascade. It is induced by the total pressure deficit in the inlet boundary layer and the lower loading which is encountered in the endwall region of the cascade. There are other minor regions visible through the plot. One of them arises from the spanwise displacement of the WV and the HVPS. This vortical region is referred to as SCE2 after [97], and is co-rotating with the HVPS. It must be underlined that the HVPS and the PV

structures are typically regarded as a single one. This arises from the fact that, when looking at secondary flow structures at the outlet plane using loss coefficients, it might be difficult to discern them and a clear distinction of two vortical regions is not possible. In this case, it was decided to treat them as separate structures, because as will be shown later in the section, the presence of two different structures is also present in the experiments.

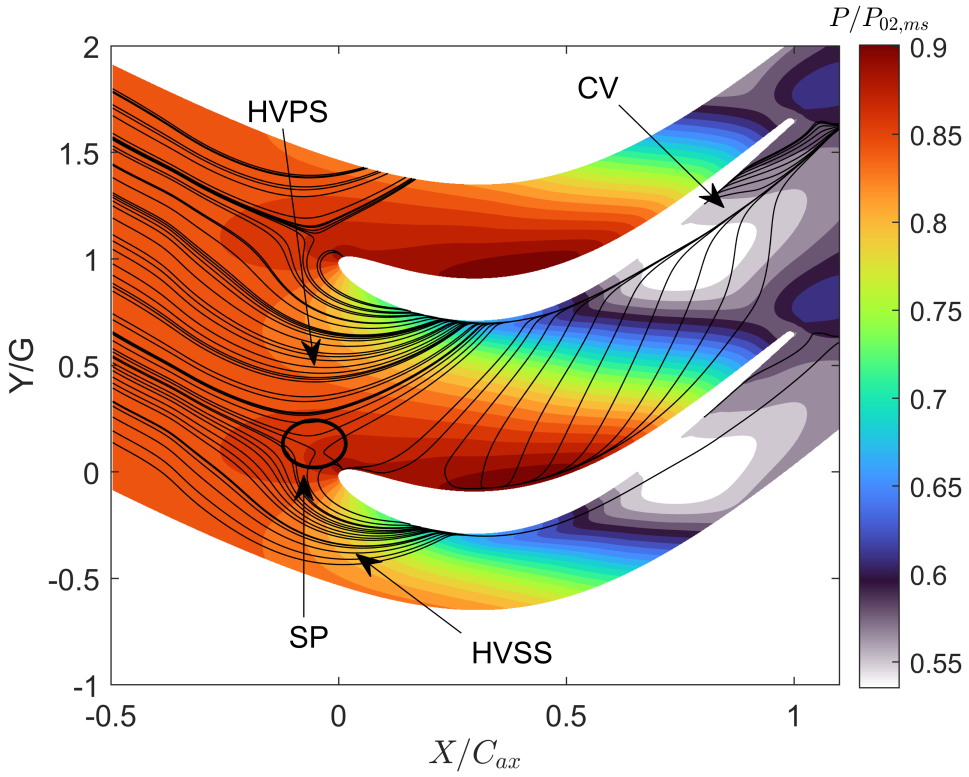

Fig. 4.21 Endwall limiting streamlines.

Figure 4.23 is useful to visualize the interaction between the secondary structures especially in the region close to the blade SS, shedding some light on the formation of the WV and the SCE2 structure. This is shown using three different axial slices, plotting contours of the streamwise vorticity coefficient. The first two figure show the migration in the spanwise direction of the HVPS. This corresponds to the flow separation in the corner between the blade and the endwall which foster the formation of the CV vortex. As they convect through the cascade, the structures get weaker due to the viscous dissipation. Moving to the axial location X/C_{ax}=0.7, the interaction of the HVPS with a thicker boundary layer in diverging portion of the SS generate what we call here the wall vortex WV. A similar distribution of the flow structures

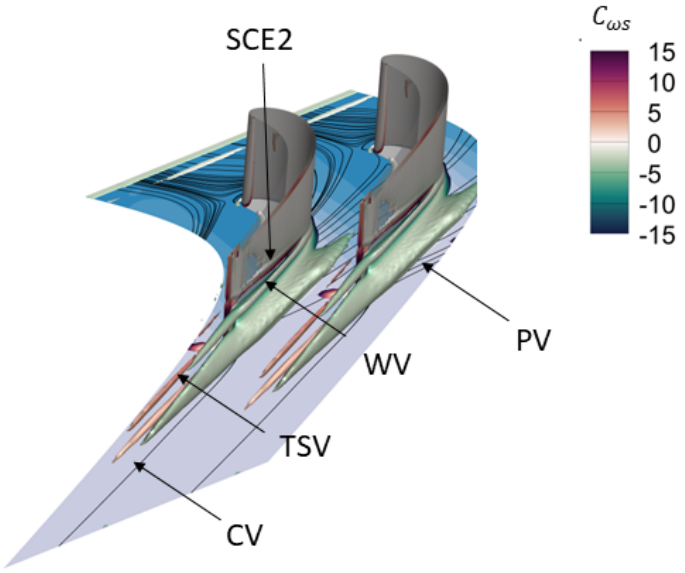

(a)

(b) Q criterion vortex visualization.

is reported in [98], even if it is shown using a loss coefficient. In the referenced paper, the WV is adduced to a separating boundary layer. In the present test case, the WV forms generally in the diverging region even when the separation bubble is not present. The formation of the SCE2 structure, which is more evident using the Q criterion visualization, rather than the streamwise vorticity, is instead related to the interaction between the WV and the HVPS. To the author knowledge, the strength of this structure depends on the strength of the HVPS and in general to the incoming boundary layer, as it may appear stronger with lower turbulence inlet intensity.

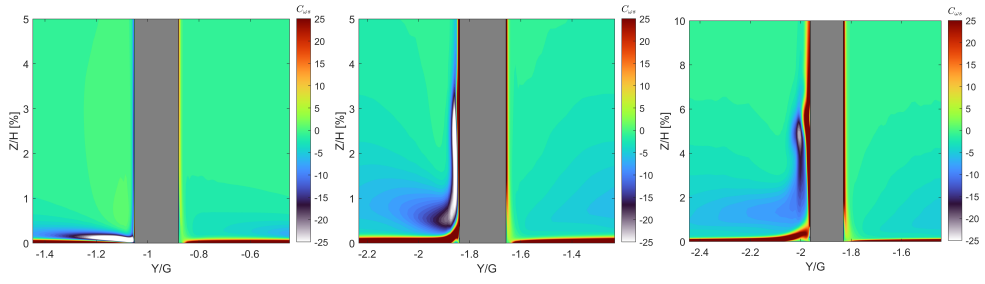

(a) (b) (c)

Fig. 4.23 Slices aligned with cascade axis: (a) X/C_{ax}=0.1, (b) X/C_{ax}=0.5, (c) X/C_{ax}=0.7

4.4.3 Effect of turbulence profile

The three turbulence profiles introduced earlier in the section, allow to understand the effect of inlet turbulence specification on the prediction of the cascade flow. The turbulence profiles used in this investigation feature different shapes, peaks of TI and profile of ILS, which in turn affects the decay of turbulence upstream of the LE of the blade. The total pressure and incidence angle profiles remain unvaried. The endwall flow is analyzed in Fig. 4.24, highlighting the different generation of the vortex system for the various profiles. T1 and T2 present the same inlet turbulent length scale, but different turbulence intensity distributions. It is shown that the endwall limiting streamlines structure is the same. As a matter of fact, the saddle point occurs in the same position, as well as the corner vortex, which provides the same amount of blockage at low span. Some differences instead arise when the profile T2 is compared to the profile T3, which instead features the same turbulence intensity, but a lower dissipation because of the higher length scale imposed at Plane 02. For a lower dissipation, the saddle point moves downstream due to the increased turbulence in the endwall region. Moreover, it is thought that the fuller boundary layer profile induced by the reduced dissipation, affects the formation of the corner vortex, reducing the blockage to the flow over the aft region of the SS.

The slight difference over the endwall limiting streamlines also yields a minor difference in the hub pressure distribution. The quantity is analyzed for nominal operating conditions in Fig. 4.25. The experimental points refer to the measurements acquired over two different passages, for this reason some axial positions report two different pressure values. All the profiles manage to reproduce the experimental distribution of the endwall pressure. Some differences arise at two different locations of the cascade, though. Close to the LE, both over the SS and the PS, the profile T3 predicts a higher loading compared to T1 and T2. The difference is 0.05 P_{02}. This is induced by the different separation system stemming from the horse-shoe vortex. The other difference arises in the aft region, where the SS acceleration is higher for T1 and T2. The max difference between the predicted endwall pressure profiles is at X/C_{ax}=0.8 and is around $0.075P_{02}$. This difference is adduced to the slightly different corner vortex system, which was shown to be smaller in for the profile T3. The differences arise close to the SS, because it is the region affected by the secondary flow system, while the PS pressure distribution is equal.

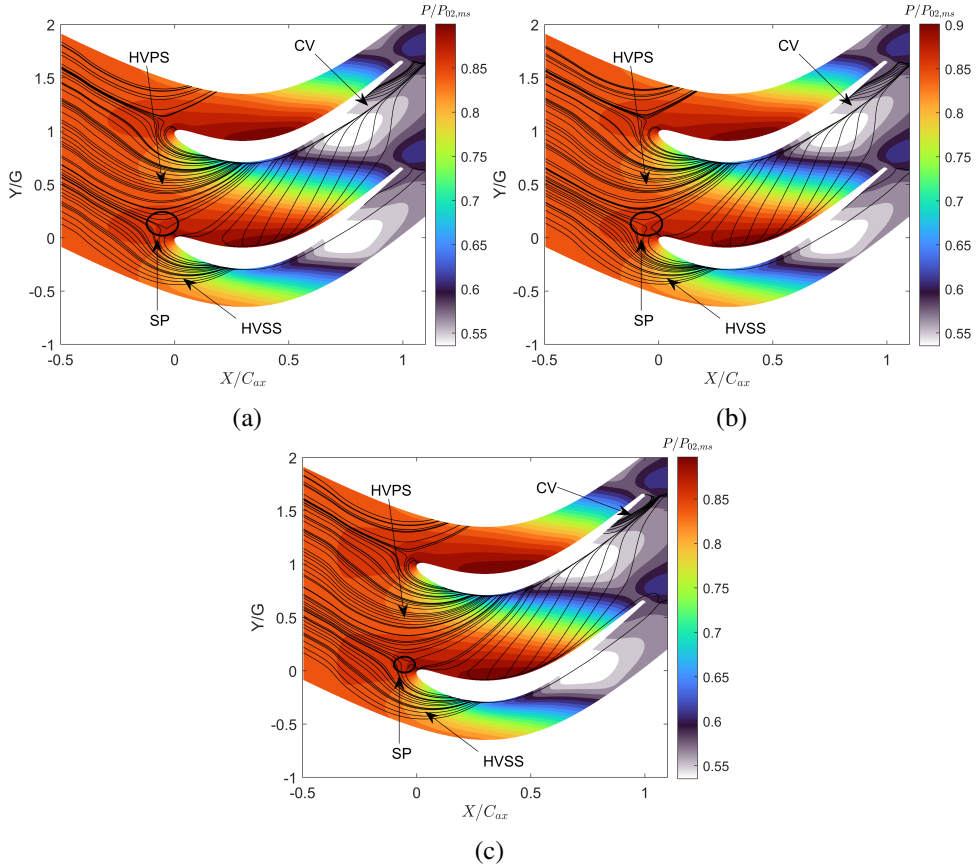

Fig. 4.24 Limiting streamlines over the endwall for the three tested turbulence conditions: (a) T1, (b) T2, (c) T3

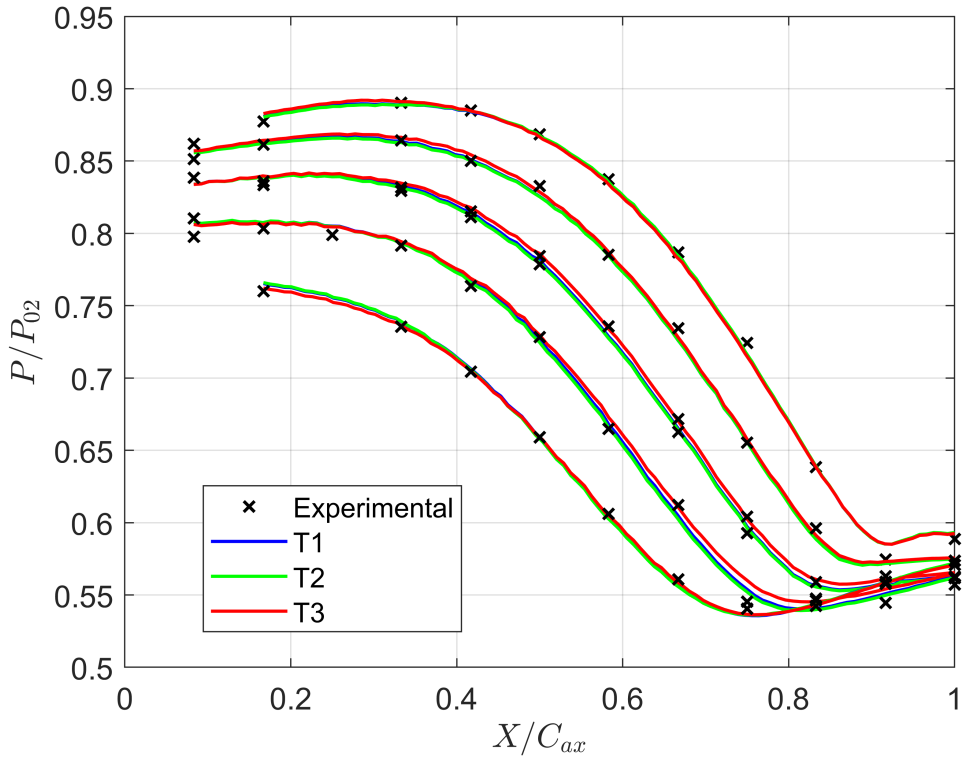

Fig. 4.25 Isolines of static pressure over the endwall

Figure 4.26 reports the prediction of the blade loading at various spanwise positions. Because of the similar structure of the secondary flow system, all the inlet turbulence profiles yield similar predictions of the loading across the span. The PS distribution is recovered correctly in the front part, with an exception for Z/H=20%. CFD yields a separation bubble in the front region for $0.2<X/C_{ax}<0.4$, similarly to the midspan plane, overestimating its size compared to the experimental measurements. This behavior occurs regardless of the specified inlet profiles. At Z/H=10%, the CFD recovers the experimental pressure side isentropic Mach, while the front acceleration is underestimated on the SS (the maximum difference with respect to the experiments is around 0.15 in the front region). The most remarkable difference occurs in the aft region. The fast recovery of the numerical simulations for $0.65<X/C_{ax}<0.85$, is induced by the developing secondary flows, as shown in Fig. 4.23. The measurements, indicate a slower pressure recovery, hinting at the fact that the impact of secondary flows on the loading is smaller that what the CFD approach used in the present thesis is able to predict. Differences in the predictions yielded by the profiles are instead present at lower span positions. At Z/H=1.21%, profile T3 features the highest isentropic velocity, peaking at Ma_{is}=1. This is thought to

be relative to the reduced blockage provided by the CV system, while all profiles recover limited differences at Z/H=4.85%.

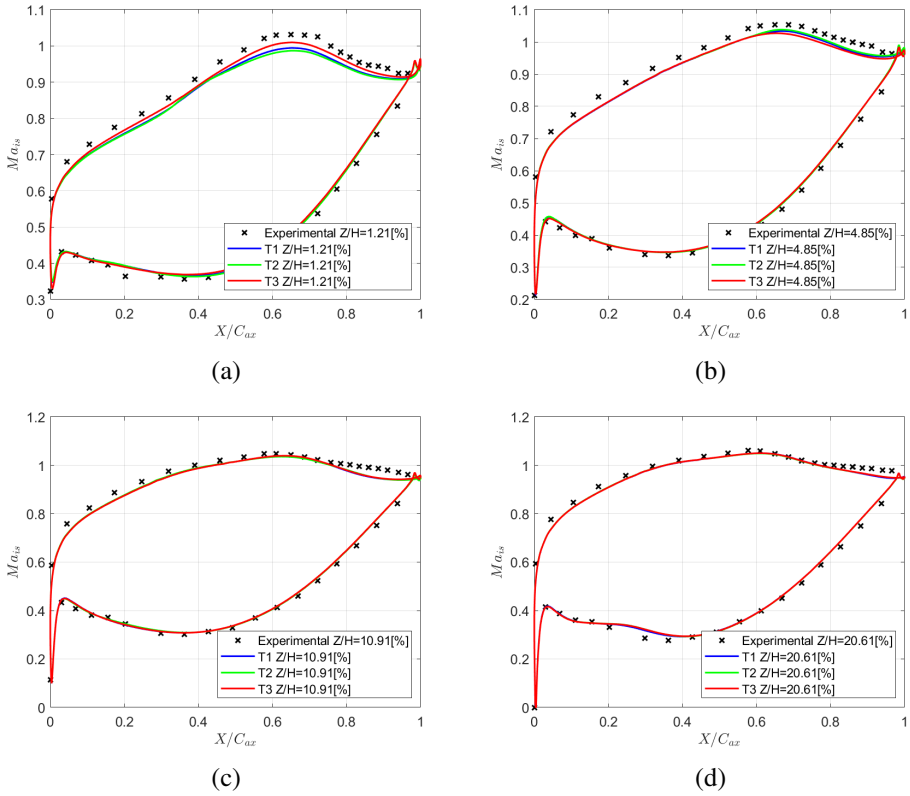

Fig. 4.26 Effect of turbulence profile on spanwise loading

Figure 4.27 reports the prediction of the outlet flow in terms of mass flow, pitchwise averaged loss and angle profiles. The latter is referred to the midspan value to remove systematic errors of the acquisition process, allowing an easier comparison with the CFD results. Profile T1 recovers the losses over the last two points close to the endwall, but is characterized by an overall misprediction of the trend. As a matter of fact, the loss profile in the region 3%<Z/H<10% is flat, evidencing a peak which which is not as marked as in the experimental setup. Above the loss peak, the numerical transition from the endwall region to the midspan flow matches the experimental one, occurring in the region 12.5%<Z/H<20%. Despite this, the overall loss prediction in the region is not satisfactory as CFD features an important overestimation of the losses close to the peak (ξ is around 0.11) and an underprediction for Z/H>15%. This can be partially attributed to the turbulence modeling (a comparison of RANS and ILES modeling by Gilbert et al. [99] shows

that the transition of RANS from the endwall to the midspan flow is faster), and partially to some real cascade effects which cannot be reproduced with a periodic setup.

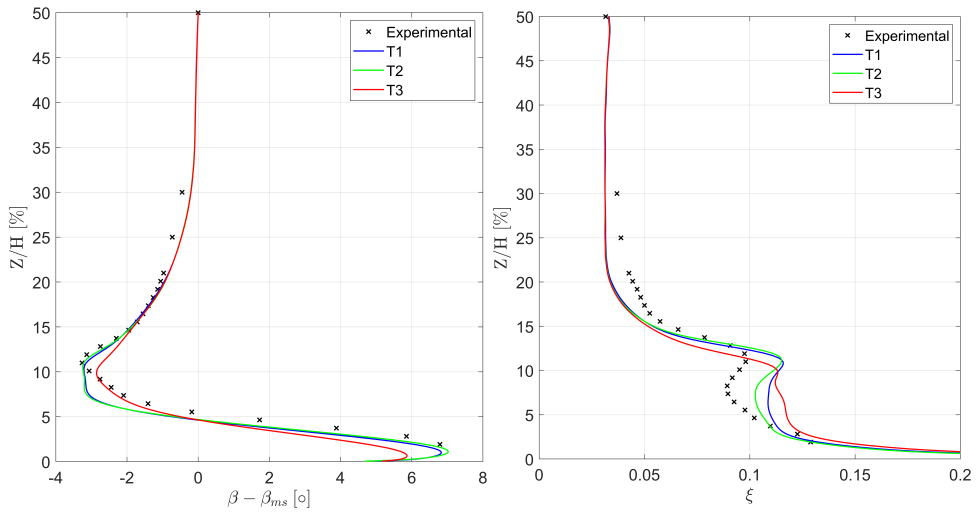

(a) (b)

Fig. 4.27 Effect of turbulence profile on outlet flow field: (a) Flow angle, (b) Energy loss coefficient

This is shown in Fig. 4.28 which compares the spatially resolved loss predictions and measurements. All simulations overpredict the main loss region, where the peak of losses is higher than 0.3, while the experimental measurements peak at 0.25. Only the CFD simulations implementing the turbulence profiles T1 and T2 manage to predict the losses associated to the Passage Vortex. The effect which is not reproduced is the skewing of the wake across the span, present in the experimental measurements. As far as the flow angle is considered, the numerical shape is in accordance with the measurements close to the max under-turning point. Closer to the endwall, the angle profile is flat for an extension of approximately 5%H, without matching the experiments. The agreement is again good close to the endwall, where the over-turning is closely captured.

Comparing with the other profiles, profile T2 yields similar prediction to T1 in terms of both flow angle and losses. The major difference occurs for 5.0%<Z/H<12.5%, which is the region between the endwall flow and peak of losses. The lower turbulence intensity specified at the inlet induces less turbulent mixing and lower losses at the outlet plane. On the other hand, the predictions yielded by profile T3 are characterized by a smooth loss profile with no evident peak. The loss is over-predicted in

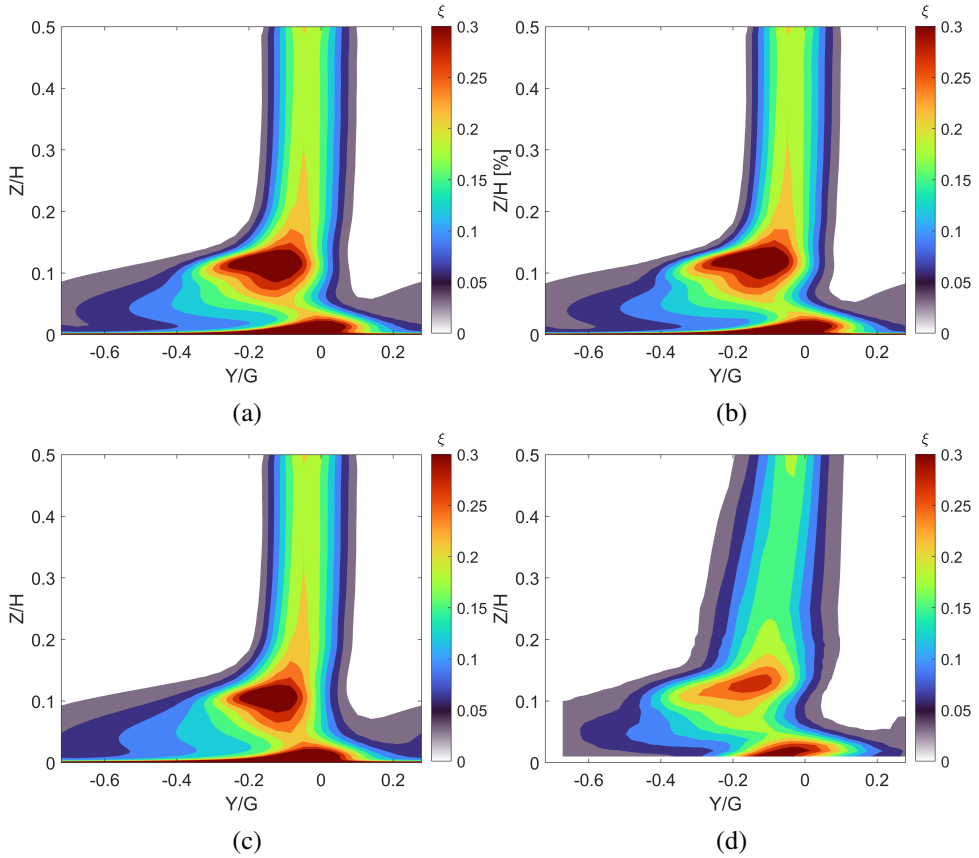

Fig. 4.28 Effect of turbulence profile on outlet kinetic energy loss coefficient: (a) T1, (b) T2, (c) T3, (d) Experimental

the endwall region due to the accumulation of low momentum flow at low spanwise positions, where the loss coefficient stabilizes at around 0.12. The profile of the losses can be explained using an argument regarding the generation of vorticity upstream of the blade and considering their transport throughout the cascade. With reference to Fig. 4.28, profile T1 and T2 evidence an important migration of the HVPS and related structures towards the span, transporting low-momentum flow towards higher spanwise positions. For the profile T3, the strength of the upstream vortex system is lower, the spanwise migration is inhibited and the low-momentum flow remains attached close to the endwall region. This is shown in Fig. 4.29, which compares the streamwise vorticity coefficient predicted by profiles T2 and T3 for two different axial locations: close to the blade LE and close to the TE. While the inlet vortex system is similar, the profile T2 features a higher spanwise migration of the HVPS. The vortex system remains stronger as the dissipation induced by turbulent viscosity decreases. On the other hand, the profile T3 yields higher dissipation of the HVPS, which in turn remains closer to the endwall. The different development across the cascade is in turn responsible for the different predictions present at Plane 06.

The outlet vorticity field is instead shown in Fig. 4.30. The isolines refer to the energy loss coefficient. It is the highest in correspondence of vortex cancellation regions (white part of the contours), where two counter-rotating structures interact, while it reduces in the core of the vortex structures. It is shown that the T2 profile, besides giving the a good overall prediction of the losses and flow deviation, also yields the most accurate prediction of the vortical field at the outlet. The intensity of the vortexes is overestimated approximately by a factor of 1.5. Nevertheless, the two vortex cores with negative streamwise vorticity corresponding to the HVPS and the PV and the two vortex cores corresponding to the WV+TSV and CV are all present in the CFD. Similarly to the losses and angles, the simulations implementing the turbulence profile T3 fails to predict the spanwise position of the vortex cores as well as the distribution of the negative vorticity region on the SS of the wake.

4.4.4 Effect of operating conditions

The effect of the operating conditions on the cascade performance was investigated by varying in turn the isentropic Reynolds and Mach number of the cascade. In order to impose the inlet boundary layer at the inlet of the cascade when the isentropic

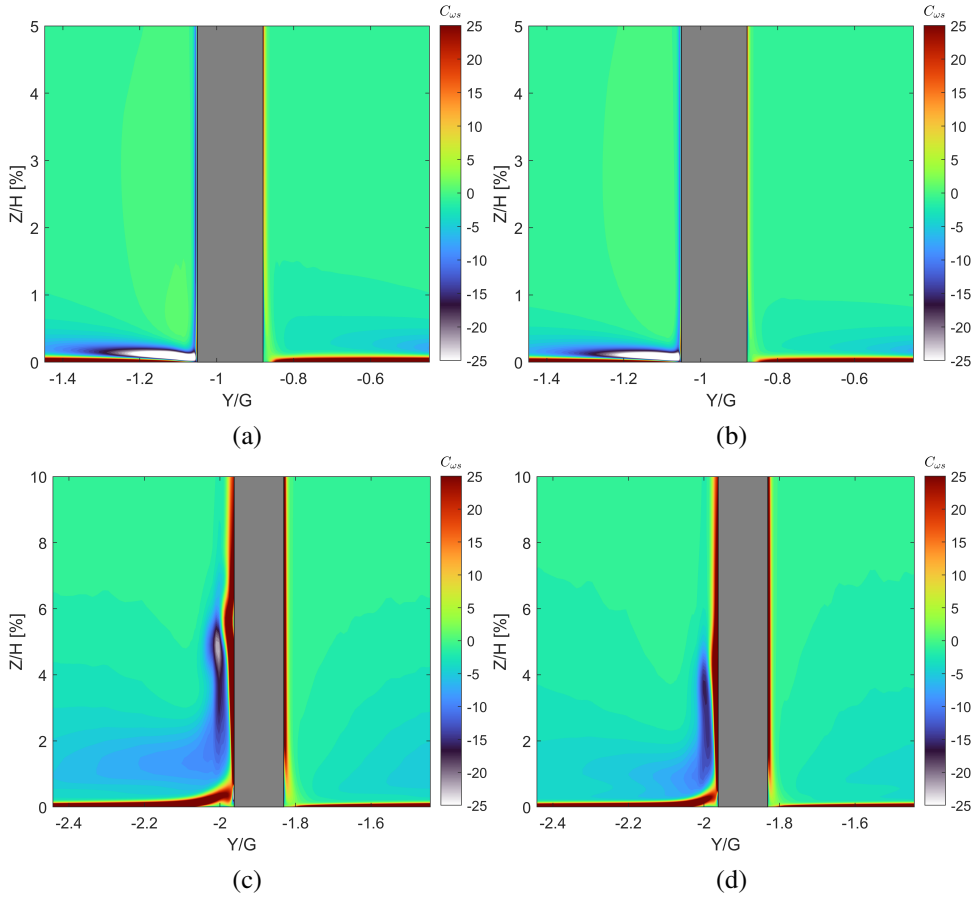

Fig. 4.29 Effect of turbulence profile on vorticity distribution in the cascade: (a) X/C$_{ax}$=0.1 T2, (b) X/C$_{ax}$=0.1 T3, (c) X/C$_{ax}$=0.7 T2, (d) X/C$_{ax}$=0.7 T3

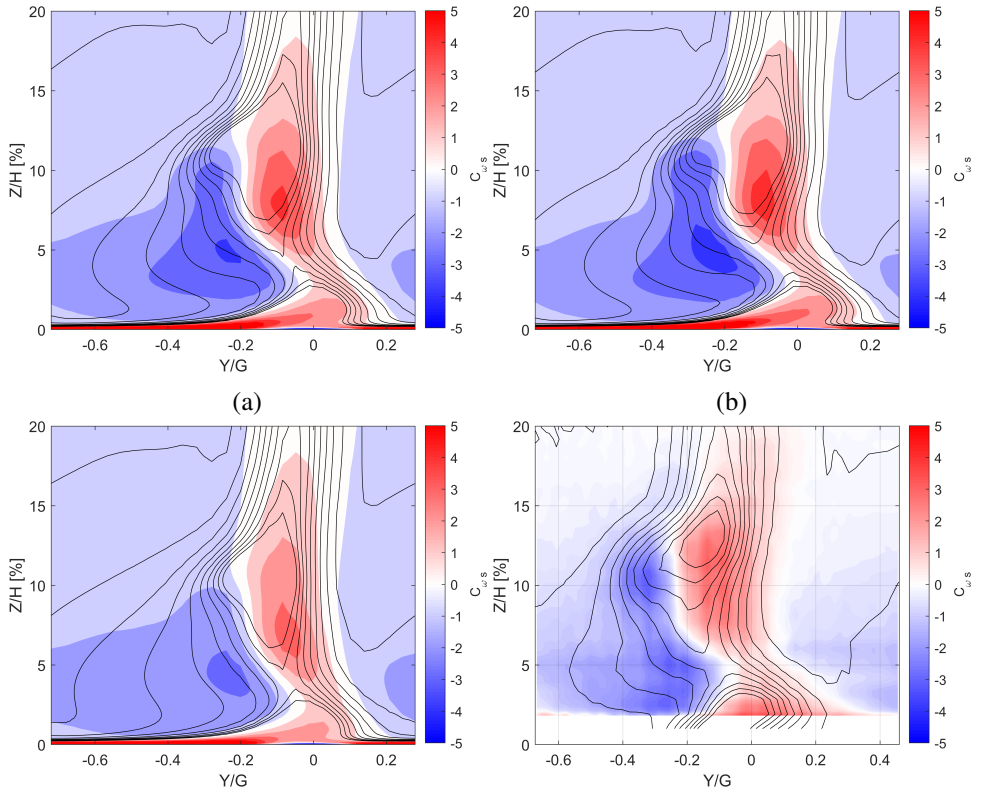

Fig. 4.30 Effect of turbulence profile on outlet vorticity: (a) T1, (b) T2, (c) T3, (d) Experimental

Mach number is varied, the total pressure distribution is modified according to the upstream midspan Mach number. This modification is necessary to enforce the same velocity profile in the boundary layer as shown in [89]. Moreover, the wrong definition of the total pressure distribution in the endwall region might modify flow entrance because of the inconsistency between the free-stream Mach number and the wall pressure, end eventually lead to flow ejection from the endwall region. The turbulence profile chosen for this part of the activity is the profile T2, because it gives the best overall agreement with the experimental measurements. The comparison between the predicted and the measured losses of the cascade for various operating conditions is shown in Fig. 4.31, along with the corresponding outlet flow angle profile. The agreement between the CFD and the experiments obtained at low Mach, nominal Reynolds is similar to what has already been discussed for the on-design conditions. There is an overall overestimation of the losses in the endwall region, while the strong secondary flows mark in the kinetic energy loss coefficient is still present in the peak loss region. There is an overall capability of the simulations in predicting the experimental trend. On the other hand the prediction at high-Reynolds features a different shape of the loss profile. The peak loss position is underestimated compared to the experiments (Z/H=12% and Z/H=12.5%), moreover, the shape is not correctly captured, having an almost uniform trend of losses in the endwall region, with a peak loss coefficient equal to 0.1. The spanwise position of the loss core depends on the isentropic Mach number. As a matter of fact, the latter affects the traveling time of the flow throughout the cascade. The lower the Mach, the stronger the spanwise migration induced by the lower velocity of the flow. Another drawback of the predictions concerns the blending between the endwall region and the midspan flow, which was also highlighted for nominal conditions. In this case, the highest misprediction occurs for the low-Mach case. This is probably induced by either the higher spanwise migration of the secondary flows or by the interaction of the latter with the separation bubble forming on the SS of the blade.

The comparison for the origin of the losses throughout the cascade can be done by analyzing the cumulative kinetic energy loss coefficient shown in Fig. 4.32. The accumulation of losses upstream of the LE accounts for the development of the inlet boundary layer, along with the separation of the HV. The blade region mainly accounts for the development of the profile losses and the endwall boundary layer, while the increase downstream is mainly due to wake/secondary flows mixing. The high-Re condition shows overall fewer losses compared to the nominal conditions,

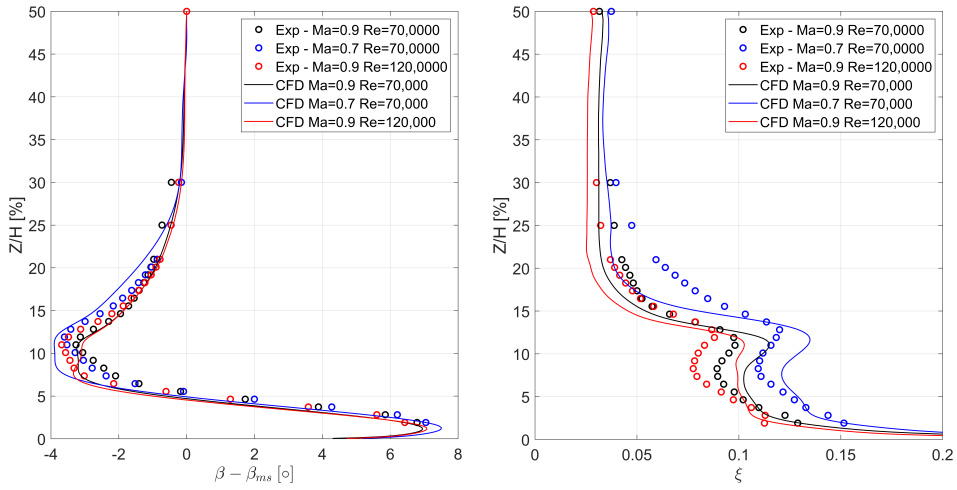

(a) (b)

Fig. 4.31 PL06 measurements comparison: (a) Flow angle, (b) Kinetic energy loss coefficient

thanks to the development of thinner boundary layers both over the endwall and over the profile. This is also makes a great difference in the wake mixing, where most of the losses are generated. For the low-Ma case instead, the losses increase mainly in the profile section due to the longer diffusion region over the SS (around 0.45 from LE to TE), while the difference remains more stable (around 0.05) downstream of the TE, hinting at the lower effect of the wake/secondary flow mixing in generating the loss difference between the various operating conditions.

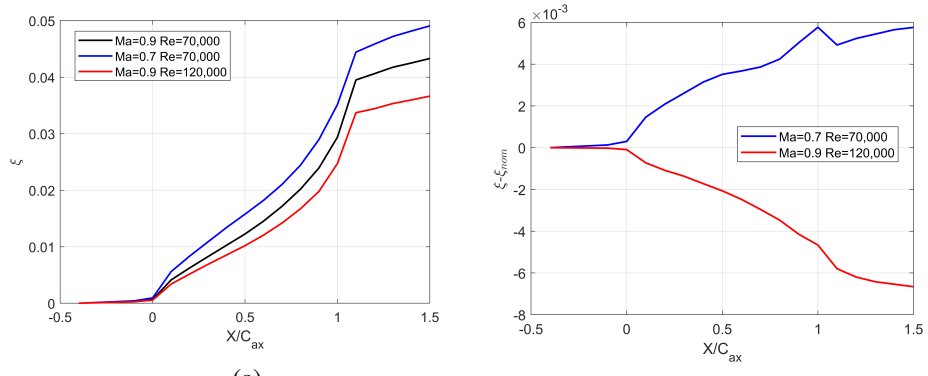

(a) (b)

Fig. 4.32 Axial development of the losses: (a) Kinetic energy loss coefficient, (b) Difference from nominal conditions

The origin of the losses can be efficiently tracked down using the dissipation coefficient (Eq. 4.3)

$$C_D = \frac{\tau_{ij}\frac{\partial U_i}{\partial x_j} + k\left(\frac{\partial T}{\partial x_j}\right)^2}{0.5\rho_{6,is}V_{6,is}^3 C_{ax}} \tag{4.3}$$

The dissipation coefficient represents a local measure of entropy generation (and thus of the losses) due to viscous phenomena: the work of shear stresses and heat transfer. The latter contribution is small in adiabatic test cases, but has been considered for consistency with entropy generation mechanisms. The dissipation coefficient is shown in Fig. 4.33. The isolines refer to the streamwise vorticity coefficient and are added to facilitate the localization of vortex cores positions, respectively to the loss generation positions. It must be pointed out that the contours have been saturated at 0.5 to improve visibility of the structures, while peaks can overcome the aforementioned value. At X/C_{ax}=0.9, the peaks of the dissipation coefficient coincide with the interaction between th secondary flow structures: HVPS-WV, SCE2-WV and SCE2 with the boundary layer over the blade. The loss is mainly concentrated over the SS where the secondary flows concentrate and where the boundary layer along the blade is thicker. The highest value of the coefficient are found in the endwall boundary layer and through the spanwise migration of the HVPS and the WV ($C_D \approx 1.1$). The PS and SS boundary layer and the interaction between the HVPS and the WV evidence similar peaks, of the order of 0.15. The loss associated with the HVPS and the PV is marginally lower, reaching a peak of the order of 0.05. For the low-Mach case, an overall increased thickness of the boundary layer generates more losses in the region, while a peak in the dissipation coefficient occurs over the SS due to the presence of a separation bubble interacting with the SCE2 structure. The losses generated trough the interaction between of the PV and the HVPS cores are one order of magnitude lower. The high Reynolds case has a similar distribution with respect to the nominal conditions. The biggest difference concerns the HVPS/WV interface which is less intense than the other cases. Moving downstream of the blade profile, at X/C_{ax}=1.1, the high loss region for Z/H>20% is related to the wake mixing, with a bigger contribution from the SS. The mixing between the WV and the HVPS is still present and accounts for similar losses with respect to the wake mixing on the PS. An additional loss region occurs on the PS side, above the CV. This loss is related to the development of the TSV. The loss associated with this structure is stronger for the low-Ma case, which is in agreement with the theory of vorticity amplification factors ([100]).

At the highest $Re_{6,is}$ the dissipation coefficient is lower in general, while no major development at X/C_{ax}=1.3 compared to X/C_{ax}=1.1. This is in agreement with Fig. 4.32, which shows how most of the interaction between the secondary flows is resolved in the TE region.

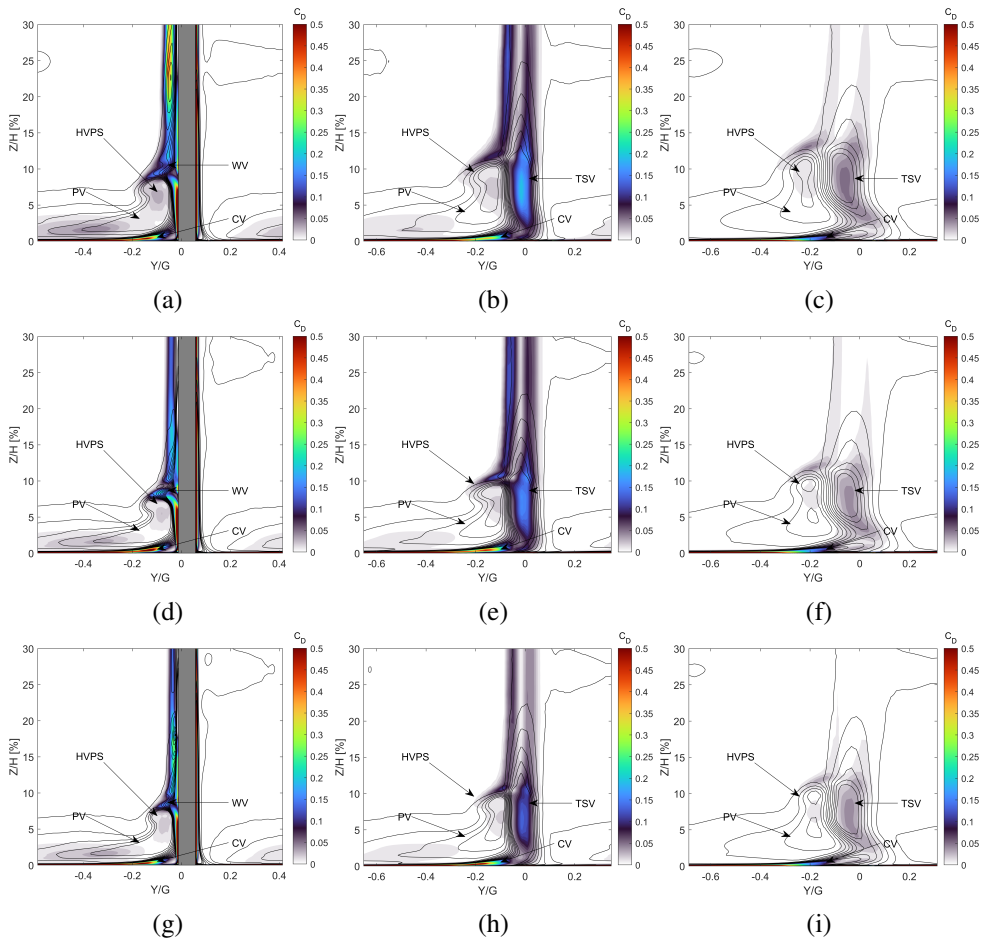

Fig. 4.33 Effect of operating conditions on the dissipation coefficient: X/C_{ax}=0.9, X/C_{ax}=1.1, X/C_{ax}=1.3 from left to right. Top row: $Ma_{6,is}$=0.7, $Re_{6,is}$=70,000. Middle row: $Ma_{6,is}$=0.9, $Re_{6,is}$=70,000. Bottom row: $Ma_{6,is}$=0.9, $Re_{6,is}$=120,000.

Figure 4.34 reports the prediction of the outlet turbulence intensity compared to the measurements obtained using PIV, along with the isolines of the streamwise vorticity coefficient. CFD manages to capture the overall flow field, even though some differences still exists due to the development of the flow under RANS closures. As shown in [101], the PIV flow field is more uniform than the one obtained with intrusive methods (5-Hole Probes), and also from RANS. The PIV allows to easily identify the CV and the PV and the TSV. The structures visible in the CFD (TSV,

HVPS and PV) are slightly more diffused in the PIV measurements, while still being present in the 5HP acquisitions. In the mixing region between the two vortices, the highest peak of turbulence is reached. RANS models manage to reproduce quite well the behavior of the *TI*, especially in the secondary flow. On the other hand, it is found that the experimental decay in the endwall region is stronger than the numerical one. This can be inferred by the turbulence level in the free-stream which goes down to 2% in the experiments, while reaching 3% in the CFD. Considering the effect of the operating conditions, the CFD manages to reproduce the experimental trend. As a matter of fact, the turbulence peak moves towards the span at low Mach, as a consequence of the spanwise migration of the secondary flows. On the other hand, the overall turbulence level found at low Mach is higher than the turbulence level at nominal conditions which is probably induced by the stronger secondary flows for the former case.

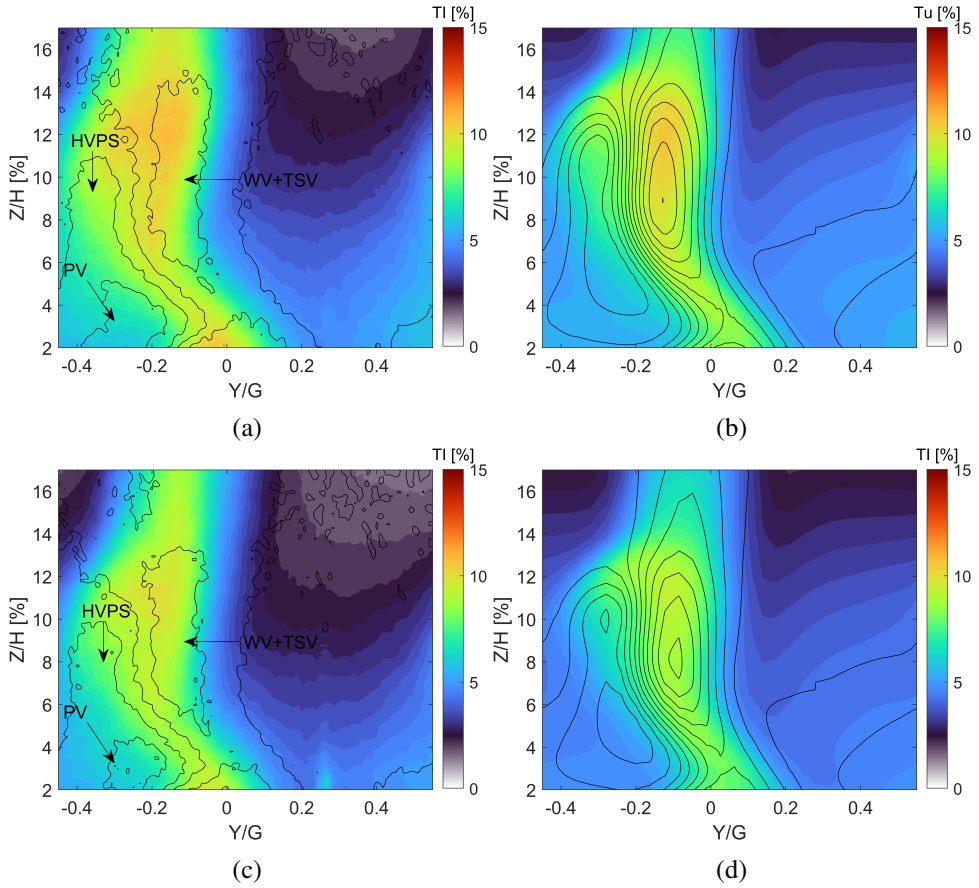

Fig. 4.34 Prediction of the outlet turbulence intensity. Left: PIV, right:CFD. Top: $Ma_{6,is}$=0.7, $Re_{6,is}$=70,000. Bottom: $Ma_{6,is}$=0.9, $Re_{6,is}$=70,000.

Eventually, the analysis of the 3D flow field will be concluded by comparing the loss budgets of the CFD, with the ones from the experiments and from existing correlations in the literature. The correlations are retrieved from the work of Coull [100], where the endwall loss contribution is basically adduced to two different effects: the development of the endwall boundary layer (ζ_{CD}) and the development of the secondary flows (ζ_{sec}). For consistency with the original paper, the losses are reported in terms of an energy loss coefficient which is defined as:

$$\zeta = \frac{(s_{6,mix} - s_{2,mix})T_{6,mix\ ms}}{(h_{06,mix} - h_{6,mix})} \tag{4.4}$$

where the subscript *mix* refers to a mixed out average, *ms* refers to the midspan value.

The loss contribution terms can be computed as follows:

$$\zeta_{CD} = 2C_D \left(\frac{A_{endwall}}{h\,s\,cos(\beta_6)}\right) \int \frac{\rho_{fs}}{\rho_6} \frac{T_6}{T_{fs}} \left(\frac{V_{fs}}{V_6}\right)^3 d\frac{A}{A_{endwall}} \tag{4.5}$$

$$AF_{PV} = M^* \left(\frac{V_6}{V_1}\right)^2 \left[\frac{\Delta T^* C_{ax}}{s\,cos(\beta_6} + \frac{|\frac{V_6}{V_1} sin(\beta_1) - sin(\beta_6)|}{cos(\beta_6)}\right] \tag{4.6}$$

$$AF_{TSV} = -\left(\frac{V_1}{V_6}\right)\left(M^* \frac{V_1 \Delta T^* C_{ax}}{V_6\,s\,cos(\beta_6)} + \frac{M^* - 1}{cos(\beta_6)} \left|\frac{V_6}{V_1} sin(\beta_6) - sin(\beta_1)\right|\right) \tag{4.7}$$

$$AF_{CV} = -\left(\frac{V_1}{V_6}\right)\left(\frac{M^*}{cos(\beta_6)} \left|\frac{V_1}{V_6} sin(\beta_6) - sin(\alpha_1)\right| + -\frac{M^* - 1}{cos(\beta_6)} \left|\frac{V_6}{V_1} sin(\beta_6) - sin(\beta_1)\right|\right) \tag{4.8}$$

$$\zeta_{Marsh} = 0.0021 \sum_i AF_i \tag{4.9}$$

For the CFD and the available experimental values, the secondary loss coefficient is computed according to the usual splitting of the outlet losses as the sum of inlet,

profile and secondary losses (Eq. 4.10)

$$\zeta_{sec} = \zeta - \zeta_{in} - \zeta_{prof} \tag{4.10}$$

The values are compared in Tab. 4.5. The numerical values do not have an overall good agreement with the correlations both at nominal and high Reynolds conditions. The maximum deviation is ≈0.45%, occurring at high Reynolds. The misprediction is not coherent with the scatter obtained in [100] (≈0.15%). On the other hand, at low Mach the prediction is slightly better because of the increased endwall losses adduced to the stronger secondary flows. Greater differences exist with respect to the experimental values. CFD underestimates losses for all simulated conditions. The best agreements is found at $Re_{6,is}$=120,000. In this condition, experiments match correlations, even though a 0.5% difference exists compared to the CFD. At $Re_{6,is}$=70,000, the numerical endwall losses are approximately half as the experimental ones, which can be adduced to the stronger circulation of the secondary flows predicted by RANS, which indicates that the loss induced by the mixing has not occurred yet.

Table 4.5 Loss Budgets in percentage

$Ma_{6,is}$ $Re_{6,is}$	ζ	ζ_{in}	ζ_{prof}	ζ_{end}	$\zeta_{CD} + \zeta_{sec}$	ζ_{exp}
0.9 70,000	6.22	1.74	3.77	0.71	1.11	1.5
0.9 120,000	6.34	2.03	3.67	0.63	1.08	1.1
0.7 70,000	7.41	2.33	4.08	0.98	1.20	1.9

4.5 2D Unsteady Simulations

The third part of the numerical activity performed on the SPLEEN cascade is focused on the study of the unsteady performance of the blade under the periodic passing wakes imposed by means of a wake generator. The simulations have been run using two different approaches:

- a "Coupled" approach, where both the bar and blade are simulated. The unsteady interaction is studied by means of a sliding mesh technique
- a "Segregated" approach, where only the blade is simulated, while the effect of wake passing is considered imposing the experimental traces of total pressure, incidence angle and turbulence quantities at the inlet of the bar domain.

Nominal operating point and low-Mach conditions have been simulated in this part of the activity.

The setup of the sliding mesh approach consists on the coupling of a multi-block mesh for the bar domain and a hybrid grid for the blade domain. The hybrid grid for the blade is the same one used for the steady simulation, while the bar mesh contains around 100,000 elements. A picture of the mesh is shown in Fig. 4.35. The simulations for the coupled approach have been run using the sliding mesh technique described in Sec. 4.5.1, while similarly to the three-dimensional case, the $\gamma - \tilde{Re}_{\theta t}$ model has been used. Because of the high relative Mach number of the bar, the flow field experiences a shock which greatly affects the turbulence flow field upstream of the cascade. In order to solve this problem, the V-version of the production terms of both k and ω has been used (see Appendix C). Time integration is performed using a second order Backward Euler Implicit method, using 120 time-steps per period. The dependency on the boundary conditions, time-step and turbulence model are all reported in Appendix B.

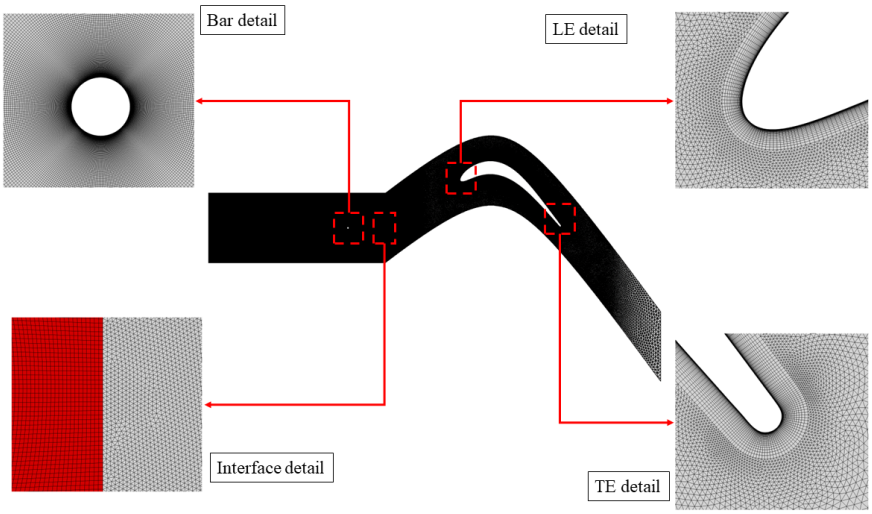

Fig. 4.35 Unsteady mesh characteristics

4.5.1 Sliding mesh implementation

The relative movement between the moving bar and the stationary blade is simulated using a sliding mesh technique. The computation of the fluxes across the interface requires the definition of a left state ($U^-_{x_\alpha}$), coming from the upstream cell and a right state ($U^+_{x_\alpha}$) coming from the downstream cell. The whole procedure can be summarized in three different steps which are performed during the pre-processing phase of the grid, assuming that the spatial periodicity of the upstream and the downstream domain is the same:

- Step 1: Define the intersections between the hanging faces on the upstream and the downstream domains. This step is performed upon defining the number of time-steps enforced for the simulation of a single pass of the rotating domain, which allows to set the displacement of the hanging faces at each time-step
- Step 2: A time-dependent reconstruction stencil is built for each cell adjacent to a hanging face. The reconstruction stencil contains two levels of neighbors from the very same domain and the $N^(2)$ neighbors of the intersecting cells from the coupled domain. This step allows to keep the reconstruction stencil centered even in the case of domains in relative motion.
- Step 3: A second order reconstruction is then enforced using the weighted LSQ procedure described in Sec. 3.1.1.

A graphical schematic of the reconstruction process is shown in Fig. 4.36. In order to avoid the computation of the reconstruction coefficients on the fly, the LSQ system inversion associated with cells across the interface is performed once before the start of the simulation for all the relative position between the moving rows. Once the reconstruction coefficients are available, the left value is computed according to the usual second order reconstruction:

$$U^-_{x_\alpha} = U_\alpha + \nabla_\alpha \cdot (\mathbf{x}_{x_\alpha} - \mathbf{x}_\alpha) \tag{4.11}$$

On the other hand, the right value is computed using an inverse distance weighted average of the reconstructed values of the flow variables in the center points of the intersecting faces x_γ and x_β, respectively:

$$U^{+}_{x_\beta} = U_\beta + \nabla_\beta \cdot (\mathbf{x}_{x_\beta} - \mathbf{x}_\beta) \tag{4.12}$$

$$U^{+}_{x_\gamma} = U_\gamma + \nabla_\gamma \cdot (\mathbf{x}_{x_\gamma} - \mathbf{x}_\gamma) \tag{4.13}$$

$$U^{+}_{x_\alpha} = \frac{U^{+}_{x_\gamma} \, ||\mathbf{d}_{\alpha\gamma}|| + U^{+}_{x_\beta} \, ||\mathbf{d}_{\alpha\beta}||}{||\mathbf{d}_{\alpha\beta} + \mathbf{d}_{\alpha\gamma||}} \tag{4.14}$$

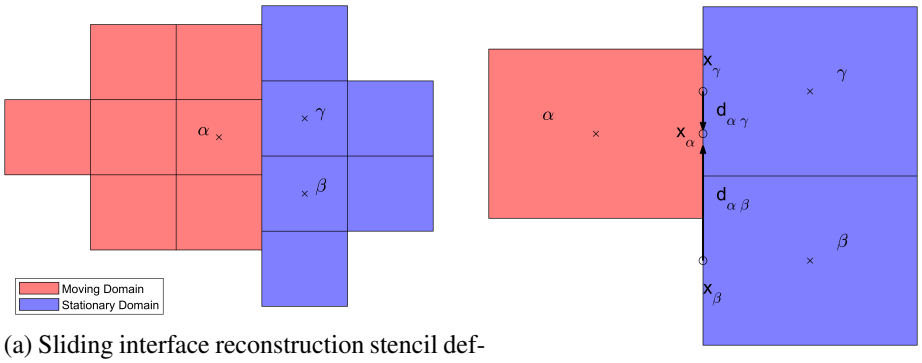

(a) Sliding interface reconstruction stencil definition

(b) Interface value reconstruction

Fig. 4.36 Interface treatment

While the implementation is described for two-dimensional test cases, the same procedure has been tested for unstructured meshes three-dimensional meshes with both linear and annular periodicity.

4.5.2 Blade loading

Figure 4.37 shows the comparison of steady and unsteady predictions of the loading, along with the experimental measurements. The effect of the bar wake is evident in the front part, where the acceleration over the SS decreases due to the reduced incidence of the flow. For both the isentropic Mach numbers, the separation bubble over the PS is not evident in the loading prediction, disappearing in the time-averaged loading predictions. The effect of the boundary conditions is more evident in the aft region of the SS. At $Ma_{6,is}$=0.9, the velocity peak increases compared to the steady case. The increase is more evident in the experiments compared to the CFD. Moreover, the diffusion rate of the experiments is almost constant. The same happens

for the CFD, in the region 0.65<X/Cax<0.85. The diffusion is slower downstream of $X/Cax \approx$0.85, which is an indication of the transition of the boundary layer to a turbulent state. A similar behavior is evidenced by the case at low Mach number. The variation of the incidence induced by the bar passing event, reduces the acceleration over the SS, while the effect of the PS separation is mitigated. Steady numerical and experimental evidence a separation bubble over the SS, in the region 0.75<X/Cax<0.85. The bubble is not evident in the unsteady case due to the wake induced transition, and the isentropic Mach profile appears flatter.

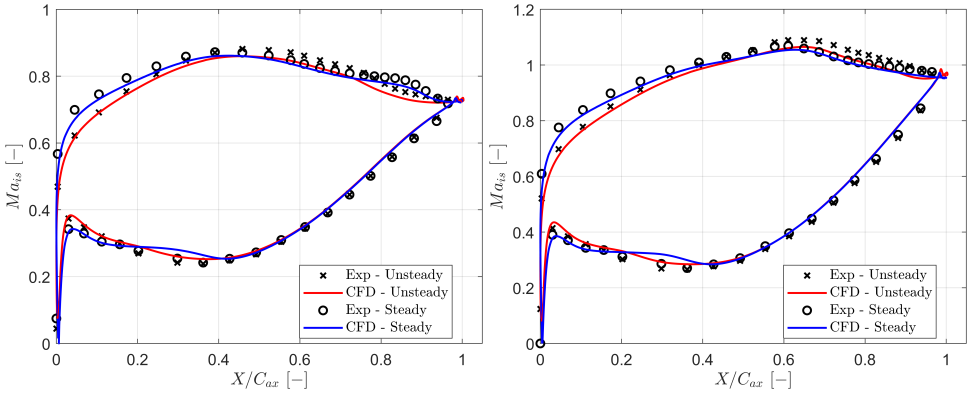

Fig. 4.37 Comparison of Steady and Unsteady loading: (a) $Ma_{6,is}$=0.7 $Re_{6,is}$=70,000, (b) $Ma_{6,is}$=0.9 $Re_{6,is}$=70,000

4.5.3 Wake induced transition

Boundary Layer Development

The impact of wake induced effects on the development of the SS boundary lower is addressed in Fig. 4.38, which shows a space-time diagram contour with the shape factor H. H is computed by integrating the velocity profile throughout the boundary layer, to get the momentum thickness θ and the displacement thickness δ. The edge of the boundary layer is determined by means of local flow vorticity. The contour plots also indicate the trajectory of the wake by means of red and black dashed lines. The former indicate the Leading Edge of the wake, while the latter its Trailing Edge. On the other hand, the black dashed line indicates the wake center. The trajectory is computed using the same procedure shown of Coull and Hodson [102]. The wake center is positioned midway through the local maximum of tangential flow velocity

and its local minimum. They correspond to the leading edge and the trailing edge, respectively. In addition to the wake trajectory, the plots show three slope lines corresponding to 30%, 50% and 88% of the local isentropic velocity. The starting position of the lines is arbitrary and is set at the curvilinear coordinate of the upmost separation point and the phase corresponding to the TE of the wake.

In the front part of the blade, the boundary layer is laminar, and the passage of the wake is felt only downstream of S/S_0>0.18. The passage of the wake is associated with a reduction of the shape factor, caused by the so-called negative jet effect ([103], [104]), which makes the boundary layer fuller. After the velocity peak, the negative pressure gradient promotes the thickening of the boundary layer which becomes more susceptible to the disturbance of the free-stream flow, which is affected by the passage of the wake. At $Ma_{6,is}$=0.9, an intermittent separation is present in the region comprised between $0.675 < S/S_0 < 0.875$. The first separation occurs at $S/S_0 \approx 0.75$, while the reattachment line closely follows the $U = 0.3U_{is}$ slope. On the other hand, the $U = 0.5U_{is}$ line follows a region after the reattachment which is featuring a higher shape factor, indicating the presence of laminar attached flow. The high value of H compared to the typical shape factor of a laminar flow (H=2.0-2.2) is due to the unsteady state of the boundary layer.

The experimental investigations of [105], indicate that the two lines ($U = 0.3U_{is}$ and $U = 0.5U_{is}$) indicate the presence of the calmed region ([106],[107]), which characterize a laminar boundary layer, which is not prone to separation. The slope corresponding to $U = 0.88U_{is}$ covers a region of low shape factor. The experimental investigations by [108] indicate that this line marks the transport of the leading edge of turbulent spots in zero pressure gradient boundary layers. It also corresponds to the findings of ([102]). On the other hand, the line at $U = 0.5U_{is}$ corresponds to the trailing edge of the spots.

In the low Mach case, the peak velocity moves upstream, meaning that the diffusion of the flow is anticipated compared to the high Mach case. The separation region consequently moves upstream, and is associated with high values of the shape factor. The transition mechanism is the same as the one reported for the high Mach case, which can be inferred by the fact that the reattachment line is still inclined at the $U = 0.3U_{is}$ slope. The low shape factor is again confined between the $U = 0.5U_{is}$ and $U = 0.88U_{is}$ slopes. Differently from the high Mach case, the calmed region is

characterized by a small separation bubble, which is probably induced by the higher diffusion encountered in the case of $Ma_{6,is}$=0.7, for S/S_0>0.68.

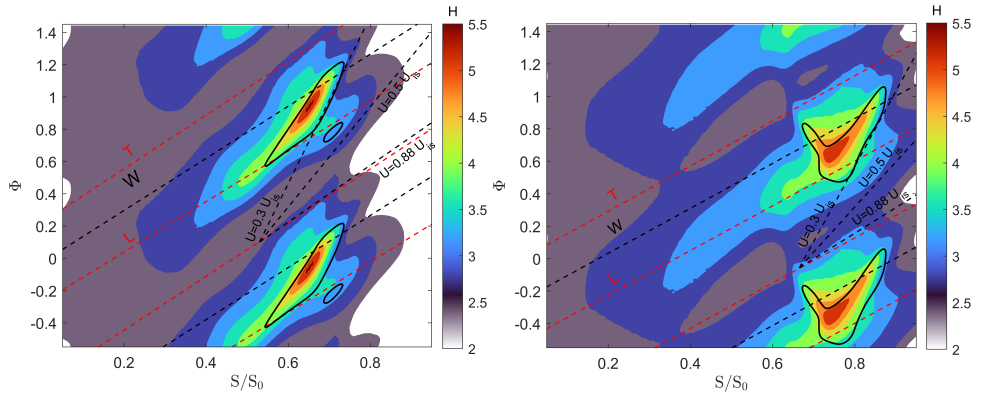

Fig. 4.38 Shape factor: (a) $Ma_{6,is}$=0.7, (b) $Ma_{6,is}$=0.95

The comparison of the experimental phase-resolved shear wall shear-stress and the CFD predictions is shown in Fig. 4.39. The normalization of both the numerical and experimental quantities is carried out using the first measurement point close to the blade LE, at the same phase. The isoline of null wall shear stress, marking the separation region, along with the slope lines marking the reattachment and the propagation of turbulent spots are added over the experimental predictions to facilitate the comparison between numerical data and measurements. The figure also shows the experimental standard deviation of the electric voltage provided by the thin films, which is correlated to an increased turbulence activity in the boundary layer ([91]). On the other hand, the becalmed region corresponds to relatively low values of $STD(E)$ ([109]).

At $Ma_{6,is}$=0.9, the experimental wall shear stress shows no evident sign of the wake passing events. Increased values of τ are only found for S/S_0>0.85. In this attached flow region, the wake passing induces an increase of the wall shear stress which are also found in the CFD predictions. Despite the mismatch in terms of absolute value, this region extends up to $S/S_0 \approx$0.65, which is in accordance with the experiments. Regarding the distribution of the electric voltage standard deviation, there is a good agreement between the predictions of the separation region from the CFD and the development of the separation bubble over the SS from the experiments. Regions of high standard deviation confine well the upstream separation and the later reattachment. A mismatch between the measurements and the predictions

appears at $S/S_0 \approx 0.78$ and $\Phi \approx 0.55$. A high standard deviation is found inside the separation bubble hinting at the fact that the reattachment predicted by the CFD is late. Moreover, the lower values of $STD(E)$ found at $S/S_0 \approx 0.0.9$ and $\Phi \approx 0.2$, suggest that the separation region should extend towards deeper curvilinear coordinates. This is in accordance with the predictions of the loading, where the numerical prediction of the isentropic Mach show a faster pressure recovery compared to the experiments, which can be adduced to the reattaching separation bubble and a faster transition of the boundary layer to a turbulent state. It is noteworthy that the numerical slopes also are in good agreement withe the regions marked by a high standard deviation.

For the low Mach case, the comparison between experiments and CFD yields similar conclusions with respect to the high Mach case. It must be said that the measurements refer to a different spanwise position ($z/H \approx 45\%$) since midspan values were not available. Once again, it can be inferred that the numerical results yield the correct reattachment location, even though a mismatch in the propagation of the flow disturbance is present. Most notably, for $S/S_0 > 0.9$, CFD predicts a fully reattached flow with increased wall shear stress in the region between the $U = 0.3U_{is}$ and the $U = 0.5U_{is}$ slopes. The experiments show instead a low standard deviation of the voltage, suggesting that the boundary layer is more stable and less affected by the free-stream disturbances. This is also in agreement with the fact that the shape factor from CFD is low, indicating a fuller velocity profile.

4.5.4 Interaction of the bar wake with blade boundary layer

In order to have a more complete view of the interaction between the bar wake and the SS boundary layer, time resolved fluctuations of the static pressure over the SS are shown in Fig. 4.40. The numerical traces are re-phased to facilitate the comparison between the measurements and the CFD predictions. As a matter of fact, a difference in phase between experimental and numerical traces exists for all tested conditions (see App. B). The origin of the phase difference is thought to te related to various effects, namely the misprediction of the free-stream velocity which governs the convection of the bar wake through the cascade, errors in the prediction of the incidence angle and possibly the fact that while non-dimensional conditions are matched, dimensional conditions are different which might generate differences in the isentropic velocity of the flow. In order to evidence the positions of the measurement location, with respect to the boundary layer status, the separation

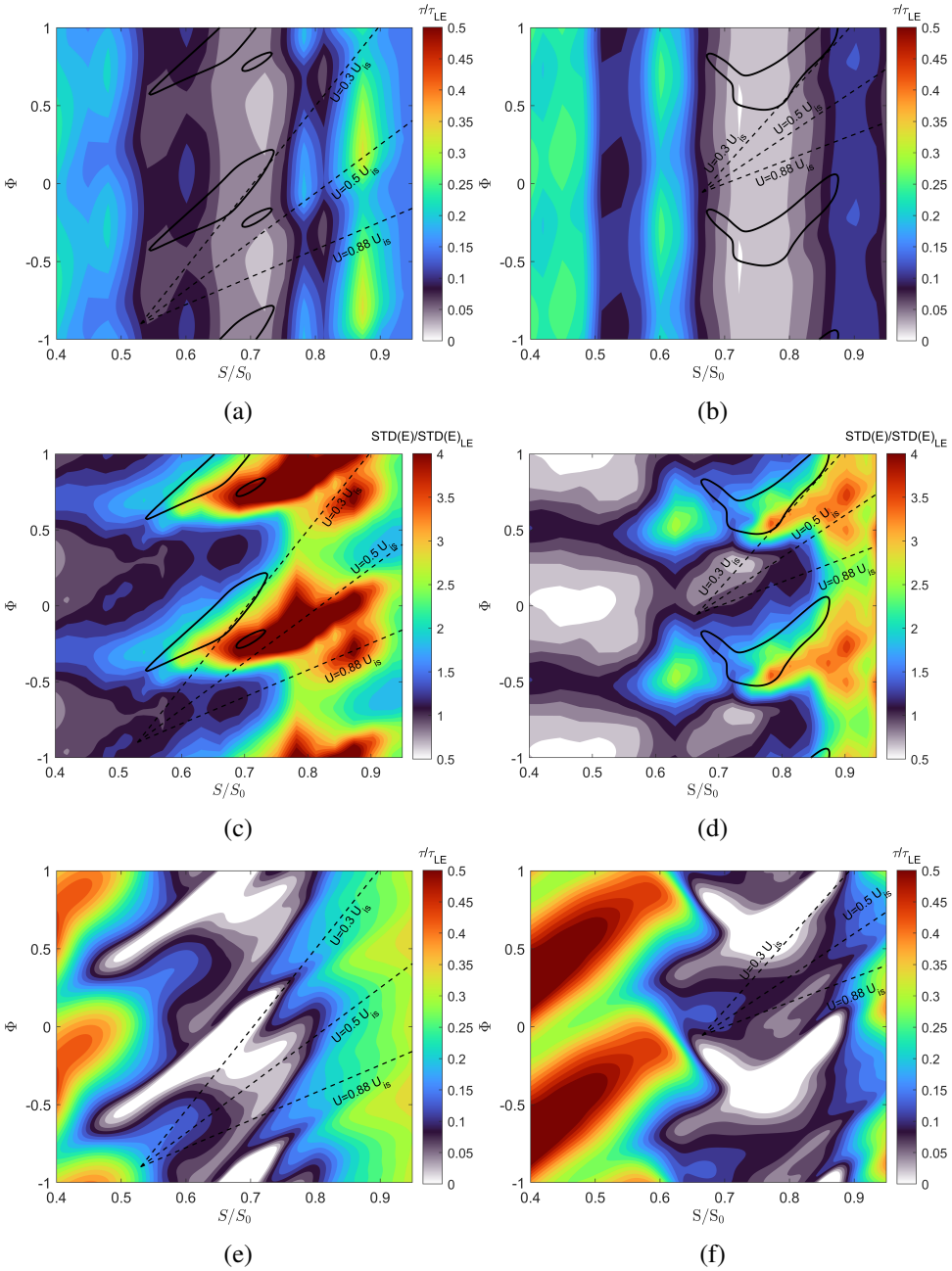

Fig. 4.39 Wall shear stress fluctuations: (a-c-e) $Ma_{6,is}$=0.7, (b-d-f) $Ma_{6,is}$=0.9

and reattachment regions retrieved from the isentropic Mach distribution over the SS, are also plotted. The positions of the Kulite pressure transducers over the blade is shown in Fig. 4.41, along with the predictions of the shock forming in the cascade in two different instants.

In the LE region, the pressure traces are characterized by a sine-like shape, which results from the passage of the wake and its bending over the front part of the blade. CFD overpredicts the amplitude of the fluctuations but is generally able to reproduce the experimental shape. For the low-Mach case, in the region between the separation and the reattachment, the wake induced disturbance appears as a pressure through, while a flat profile is retrieved in the undisturbed region. After the reattachment, in correspondence of the low shape factor region, the pressure fluctuation is the lowest. For the high-Mach case, the behavior is quite different. As a matter of fact, after the sine-like shape over the front region, the pressure traces still evidence peaks downstream of the velocity peak. Numerical predictions are in accordance with the experiments, even though an additional (rather small) peak in the pressure trace is present. This will be discussed later in the section, and is adduced to the presence of a shock sweeping over the SS of the blade, which also acts as a modulator for the intermittent separation of the boundary layer. The shock signature is not present downstream of S/S_0 =0.753. At $S/S_0 = 0.9$, which also represents the last measurement location, the pressure fluctuations still account for $0.05P_{01}$, which is more than twice the residual fluctuation found at $Ma_{6,is}$ =0.7 ($\approx 0.05P_{01}$). For both investigated Mach numbers, the experimental overshoots/undershoots with respect to the clean free-stream flow, travel at $\approx 0.50U_{is}$, which is in accordance with the roll-up of Kelvin-Helmotz instabilities (see [110]).

In order to evidence the flow phenomena predicted by the CFD, responsible for the evidenced pressure fluctuations, Fig. 4.42 shows the analysis of the flow field over selected surfaces. They are parallel to the local SS tangential vector, while their distance from the blade is set as a percentage of the average free-stream location (d_{fs}). The surfaces are placed at 10%, 50% and 100% of d_{fs}, respectively. The first row of the plot refers to the wall pressure fluctuations, while cyan curves are used to evidence separated flow regions. The other plots show the contours of the tangential velocity fluctuations. It is taken positive when aligned with the cascade from the LE to the TE of the blade.

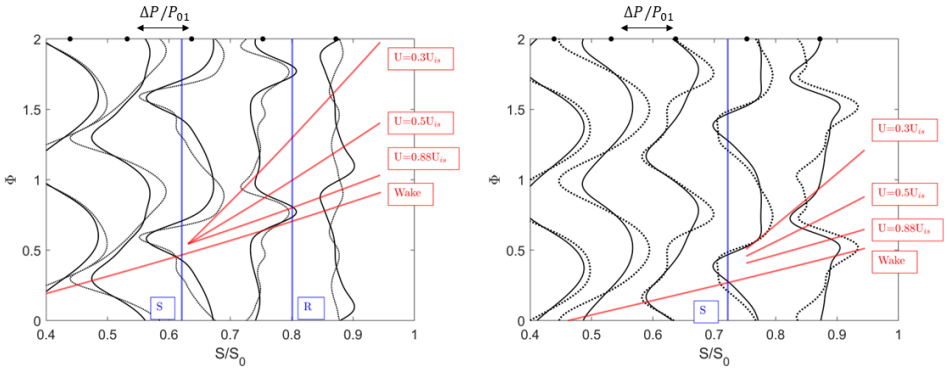

(a) (b)

Fig. 4.40 Static pressure fluctuations: (a) $Ma_{6,is}$=0.70 $Re_{6,is}$=70,000 and (b) $Ma_{6,is}$=0.90 $Re_{6,is}$=70,000

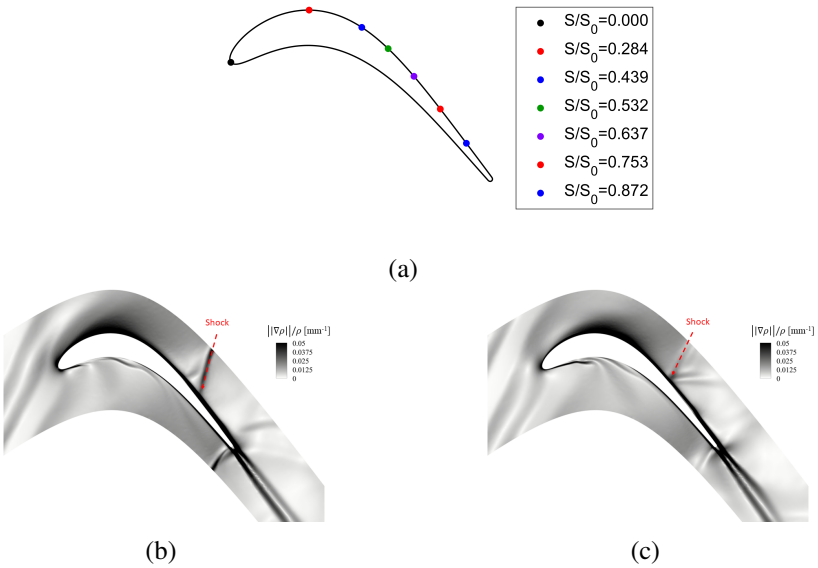

(a)

(b) (c)

Fig. 4.41 Kulite pressure transducers location and CFD shock predictions.

At $Ma_{6,is}$=0.7, three different propagation velocities are responsible for the pressure fluctuations. In the front part of the blade, the pressure fluctuations induced by the passage of the wake propagate at 70% of the isentropic velocity. Through of pressure are associated to the passage of the clean flow, while the peaks are associated with the center of the wake. The pressure increase is induced by the negative jet-effect. After the velocity peak occurring at S/S_0=0.41, the pressure propagation speed changes and becomes aligned with the $U=0.5U_{is}$ slope, which is the same slope for the separation and reattachment location. After the flow reattaches, another change of the slope is present. As a matter of fact, the pressure fluctuations propagate at the local flow velocity, which for the wall pressure is taken at $d = 0.1d_{fs}$.

In the near wall region, the tangential velocity fluctuation travel at a speed equal to $U=0.5U_{is}$ (a positive value indicates that we are in presence of the bar wake LE). In the aft region, after the reattachment, the propagation occurs at the local flow speed $U=U_{loc}$. This feature of the reattached flow region is common to all wall distances, indicating that the reattached flow boundary layer is less dependent on the free-stream disturbance, but still convects the upstream disturbances generated in the boundary layer. The disturbance present in the diverging region of the SS, where the intermittent separation/reattachment occurs, is visible at the other wall distances as well. This indicates that near wall fluctuations propagate through the aft portion of the blade, moving towards higher wall distances. Differently from the aft region, the propagation of tangential velocity fluctuations in the boundary layer over the front region, heavily depends on the wall distance. It increases from $0.5U_{is}$ at $d_{wall}=10\%d_{fs}$ to $0.7U_{is}$ and $0.88U_{is}$ at $d_{wall}=50\%d_{fs}$ and $d_{wall}=100\%d_{fs}$, respectively. The latter is also similar to the propagation speed of the wake, which is computed from the $d=100\%d_{fs}$ fluctuations.

The high-Mach case features similar characteristics with respect to the low-Mach case. The propagation speeds are in fact equal to the other case. There are two major differences, though. Firstly, the separation point moves downstream which causes the pressure fluctuations to be still high in the aft region. Secondly it is evident that the flow is also affected by the passage of a shock over the SS. It induces flow field separation, along with the passage of the clean flow. As a matter of fact, the separation isoline is characterized by a left-running bump, which closely follows the shock propagation over the SS. Moreover, as anticipated in the previous discussion of the Kulite transducers measurements, the low-Mach case present a though pressure

after the velocity peak, in the unsteady pressure traces. It is associated with the flow separation over the SS.

4.5.5 Blade wake

The predictions of the energy loss coefficient at the outlet measurement plane are reported in Fig. 4.43, for both the investigated Mach numbers. Steady results are also plotted to highlight the effect of the wake interaction over the profile loss under wake passing. At high Mach, the experiments show similar losses compared to the steady case. The width of the wake increases slightly due to the passage of the bar wake. The CFD overestimates the losses for both conditions, while the core of the wake is misplaced towards the SS of the blade. Moreover, similarly to the steady case, the wake is thinner compared to the experiments, which is adduced to RANS deficiencies in reproducing the mixing of the flow in the shear layer of the blade wake. Unsteady results are slightly better than the steady case, tough, indicating that the underestimation of the turbulent mixing is partially balanced by the unsteady nature of the flow. The wake also thickens over the SS, which is also another improvement compared to the steady predictions.

At low Mach, the effect of unsteady wake passing is more evident compared to the high Mach case. This is probably induced by the fact that at the Strouhal number at $Ma_{6,is}$=0.7 is higher compared to the $Ma_{6,is}$=0.9 case (1.19 and 0.95, respectively). A high mismatch is present in both cases, especially in the prediction of the core loss. A slightly better agreement is present in the unsteady case, which also manages to correctly retrieve the position of the wake center at Y/G=-0.09. A major difference between the low Mach and the high Mach case is found in the free-stream region, where the local total pressure is higher than the averaged total pressure obtained at PL02. This behavior is present only in the CFD, but is in accordance with other numerical investigations (see [104]). The reason behind the negative loss coefficient is thoroughly described in Sec. 4.5.6, where the unsteady traces of the total pressure at the outlet measurement planes are analyzed.

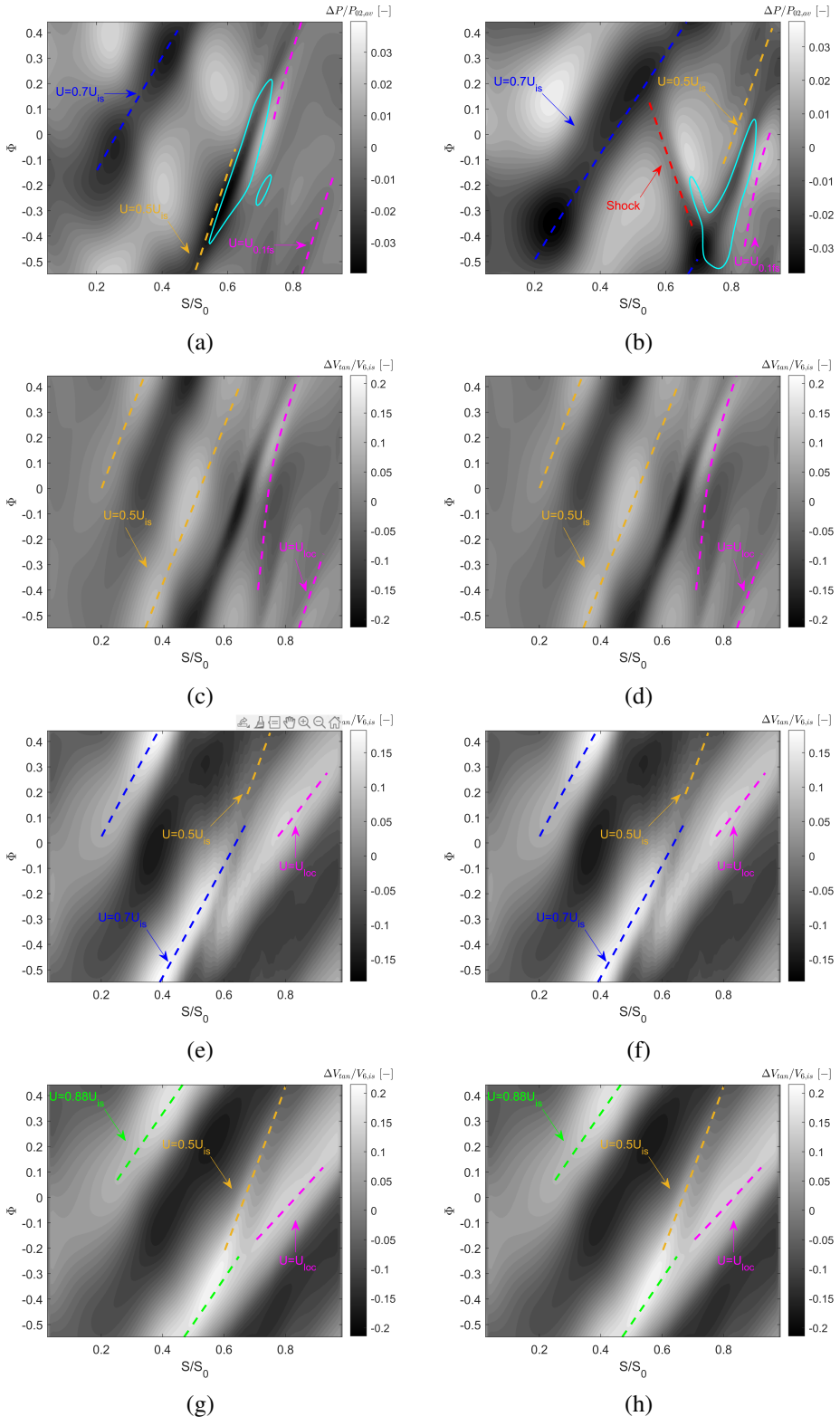

Fig. 4.42 Flow field fluctuations: left - $Ma_{6,is}$=0.7, right - $Ma_{6,is}$=0.9. (a)-(b) wall pressure fluctuations, (c-(d)) d_{wall}=10% of free-stream position, (e)-(f) d_{wall}=50% of free-stream position, (g)-(h) d_{wall}=100% of free-stream position

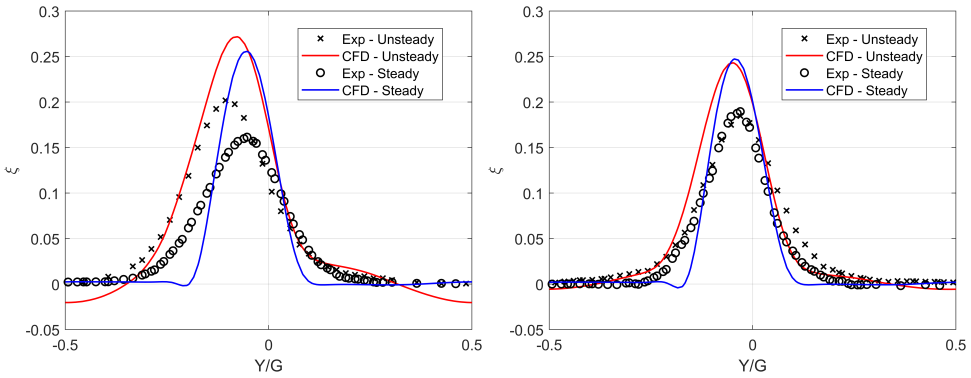

Fig. 4.43 Time averaged losses: (a) $Ma_{6,is}$=0.70 $Re_{6,is}$=70,000; (b) $Ma_{6,is}$=0.90; $Re_{6,is}$=70,000

4.5.6 Energy Loss Coefficient

Figure 4.44 shows the contours of the numerical and the experimental phase-resolved energy loss coefficients. The maps are characterized by a very different behavior moving along the pitch of the cascade. A strip of high kinetic energy loss coefficient is found for $Y/G \approx 0$, which corresponds to the blade wake. In this region the max loss coefficient is higher than 0.3. On the other hand, peaks and lows alternate in the free-stream. This occurs both on the PS and the SS sides of the wake, with a shift in phase resulting from the different propagation speeds of the flow (and the pressure gradient). The unsteady mechanism driving the fluctuations of total pressure was described for a low pressure turbine operating at low Mach conditions in [104]. It must be noted that regions of negative ξ feature a higher total pressure compared to the peak found at PL02. The peaks of total pressure at PL02 are around $0.025P_{02,av}$ and $0.0190.025P_{02,av}$, for $Ma_{6,is}$=0.9 and $Ma_{6,is}$=0.7, respectively. The corresponding peaks at PL06 are $0.075P_{02,av}$ and $0.055P_{02,av}$, respectively. The magnification of the total pressure peak from PL02 to PL06 confirm that the unsteady behavior of the cascade flow cannot be solely adduced to wake kinematics. As a matter of fact, if the total pressure peak from PL02 simply convects through the cascade, a negative energy loss coefficient should appear over the SS side of the blade wake at PL06. Moreover, the peak should be lower due to the additional mixing of the bar wake throughout the cascade. Despite this, the maps evidence that a convective pattern is still present, with both the SS and the PS structures arising periodically over the pitch of the blade. This feature also suggests that the overall flow field at PL06 is

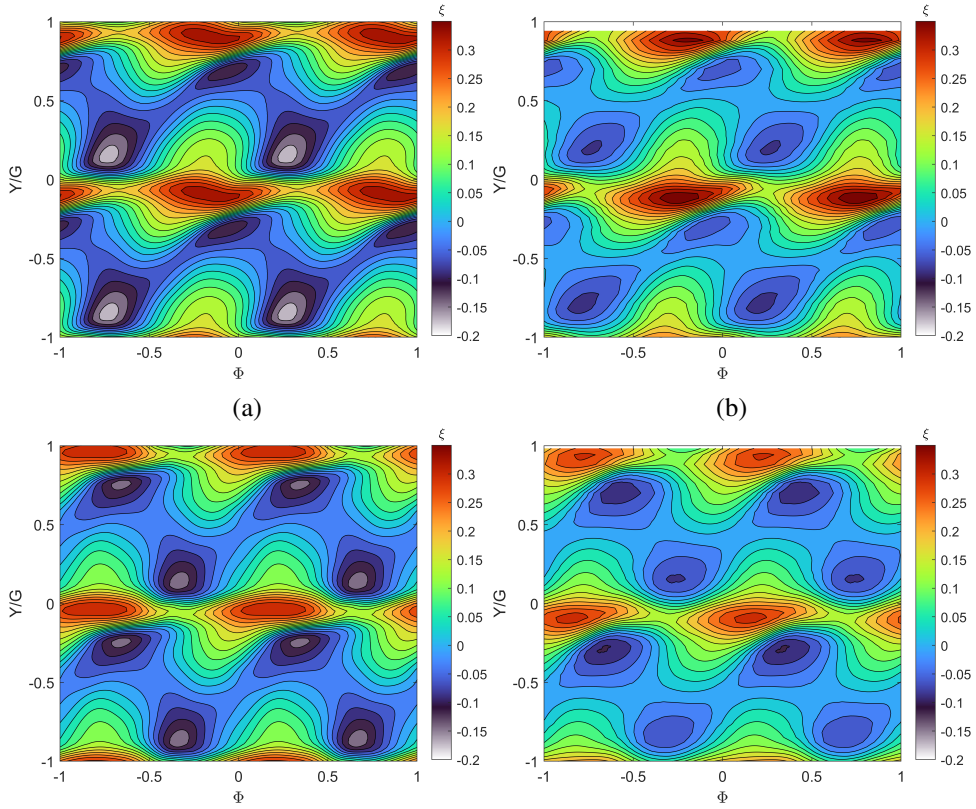

Fig. 4.44 Energy loss coefficient fluctuation: (a) Experimental $Ma_{6,is}$=0.70 $Re_{6,is}$=70,000; (b) CFD $Ma_{6,is}$=0.70 $Re_{6,is}$=70,000; (c) Experimental $Ma_{6,is}$=0.90 $Re_{6,is}$=70,000; (d) CFD $Ma_{6,is}$=0.90 $Re_{6,is}$=70,000;

mainly dependent on the interaction between the bar wake and the cascade, while secondary unsteady behavior, like the intermittent separation bubble arising over the SS, plays a minor role. This is also caused by the usage of RANS closures, which do not allow to solve small scale features like Kelvin-Helmotz roll-ups of at the interface between the separation bubble and the free-stream. CFD predictions agree well with the measurements both in terms of energy loss coefficient topology and magnitude at both Mach numbers.

In order to highlight the unsteady mechanism responsible for the fluctuations of loss coefficient at Plane 06, the unsteady cascade flow field is shown in Fig. 4.45. The plots show the unsteady flow vectors, which are obtained by subtracting the time-averaged flow field to the instantaneous one. The contours refer to the local total pressure, normalized by the average total pressure measured at PL02.

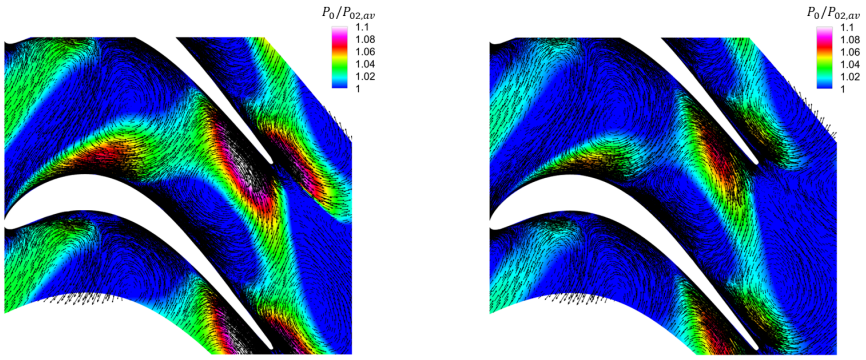

(a) (b)

Fig. 4.45 Unsteady vectors and wake transport through the passage: (a) $Ma_{6,is}$=0.9; (b) $Ma_{6,is}$=0.7

The vectors evidence the typical structure of the wake flow in a stationary frame of reference, with the typical negative jet effect. As soon as the bar wake approaches the blade, it starts bowing and begins its stretching across the cascade. The wake is accumulated close to the blade SS because of the pressure gradient, and local increases of total pressure arise both over the PS and the SS. The local compression of the flow occurs in two separate instants, but at similar axial locations, close to the LE of the blade. The SS peak originates downstream of the bar wake, while an opposite situation occurs over the PS, where the local compression occurs upstream of the wake, in correspondence of the clean inflow passage. This unsteady behavior has a twofold nature.

Figure 4.46 reports the pressure derivative for two different time steps, while isolines refer to the local total pressure ratio $P_0/P_{02,av}$, highlighting regions where the total pressure increases. The analysis is shown for the high-Mach case, but similar conclusions can be drawn from the low-Mach case. The two time steps have been chosen to highlight instants corresponding to the wake entering the cascade and the wake inside the cascade after a partial acceleration. The total pressure peak in the front region is associated to the passage of the flow across a region with a positive pressure derivative. The phenomenon is typically referred to as "energy-separation". This effect is responsible for the local compression of the flow at the LE region. It is induced by the reduced flow incidence over the LE of the wake, which accumulates flow closer to the SS. Similarly, the PS peak corresponds to an increased incidence downstream of the wake, which contributes to flow accumulation closer to

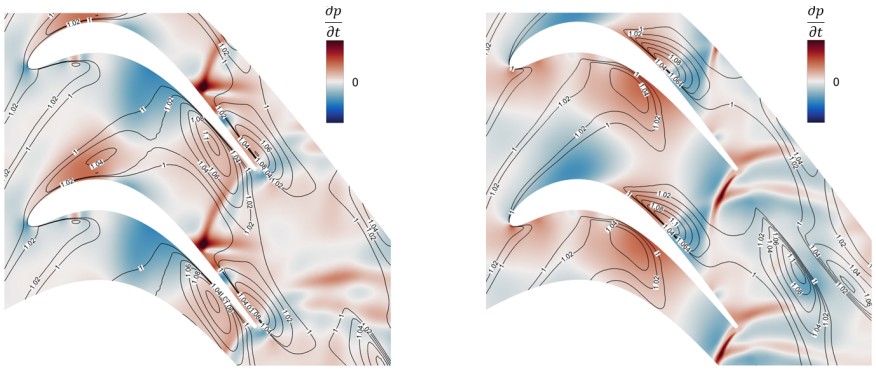

(a) (b)

Fig. 4.46 Unsteady pressure field and total pressure variation for $Ma_{6,is}$=0.9: (a) Φ=0.75, (b) Φ=1.35

the wall. After the initial compression, the local patches of increased total pressure convect through the cascade. The convective nature is also confirmed by the fact, that additional regions of positive pressure derivatives form in correspondence of the TE region without retaining an effect over both the strength of the peak and the shape of the patch. It must be said that the residence time of the patch in the high pressure derivative region in the aft portion of the blade is lower due to the higher flow velocity at the exit of blade.

The Mach number has two primary effects on the total pressure/energy loss coefficient patches found at PL06. Firstly, the phase for the patches is different, which is adduced to the different Strouhal numbers. On the other hand, the fluctuations found for $Ma_{6,is}$=0.9 are stronger in comparison to the low-Mach case. This effect is probably adduced to the different loading of the blade in the front part, which affects bar wake bowing and eventually flow accumulation over the blade wall. Despite this, other blade profiles, with different accelerations over the front part, should be tested to confirm this hypothesis.

CFD predictions agrees well with the measured pattern, but tend to overestimate the fluctuations found during the experimental campaign. The high energy loss coefficient, in correspondence of the blade wake (Y/G≈1) are also present in the time-averaged losses (Fig. 4.43). The same happens for regions of low energy loss, which explains the negative loss coefficient found at low-Mach.

4.5.7 Outlet turbulence

The last part of the analysis for the SPLEEN cascade details the measurements of the turbulent field at the outlet measurement plane. Figure 4.47 shows the space-time diagram of the turbulence intensity fluctuations over Plane 06. The turbulence intensity fluctuation in the free-stream (Y/G≈0.5) is around 0.6%, indicating that the flow is quite uniform. The small variations can be addressed to the residual turbulence of the bar wake which convects through the cascade. On the other hand, a different behavior in the region of the blade wake (-0.1<Y/G<0.1), where two evident peaks of turbulence intensity are present on the PS and on the SS, respectively. The two peaks are indicated in the diagram as "A" and "B". They appear slightly later compared to the trough of kinetic energy loss coefficient, which was previously associated with the passage of the bar wake across the cascade. The phenomenon is present for both Mach numbers, but the fluctuations present at $Ma_{6,is}$=0.7 are lower. At $Ma_{6,is}$=0.9, the PS and the SS peaks retain a similar increase of turbulence intensity (≈1.3%). At $Ma_{6,is}$=0.7, the peak of turbulence intensity arising over the PS (Δ TI=1.3%) is higher than the one occurring on the SS (Δ TI=0.6%).

It must be noted that CFD predicts a different shape of the turbulence intensity maps in the free-stream compared to the experiment. As a matter of fact, the experimental shape is in accordance with wake bowing and stretching across the passage. Peaks of turbulence first arrive at PL06 on the SS side, while the pitchwise position increases with the phase, moving towards the PS. This transport of the bar wake is highlighted in the figure by means of dashed arrows. While CFD evidences a streak of increased turbulence intensity as well, a region of low intensity marks the passage of the clean flow through PL06. The misprediction of the space-time TI diagram can be adduced to various effects, namely the overall misprediction of the wake bowing, the outlet flow angle as well as the limited accuracy of RANS models in properly predicting the production of turbulent kinetic energy across the bar wake throughout the cascade. As a matter of fact, this behavior is characteristic of the turbulent field and not of the loss coefficient, which confirms the proper prediction of the transport of entropy streaks through the cascade, despite the magnified effects of the energy-separation.

As previously stated, the CFD predictions manage to capture the same effects evidenced by the experiments, while the quantitative predictions depend on the Mach number. The increase of turbulence intensity is underestimated at $Ma_{6,is}$=0.9, which

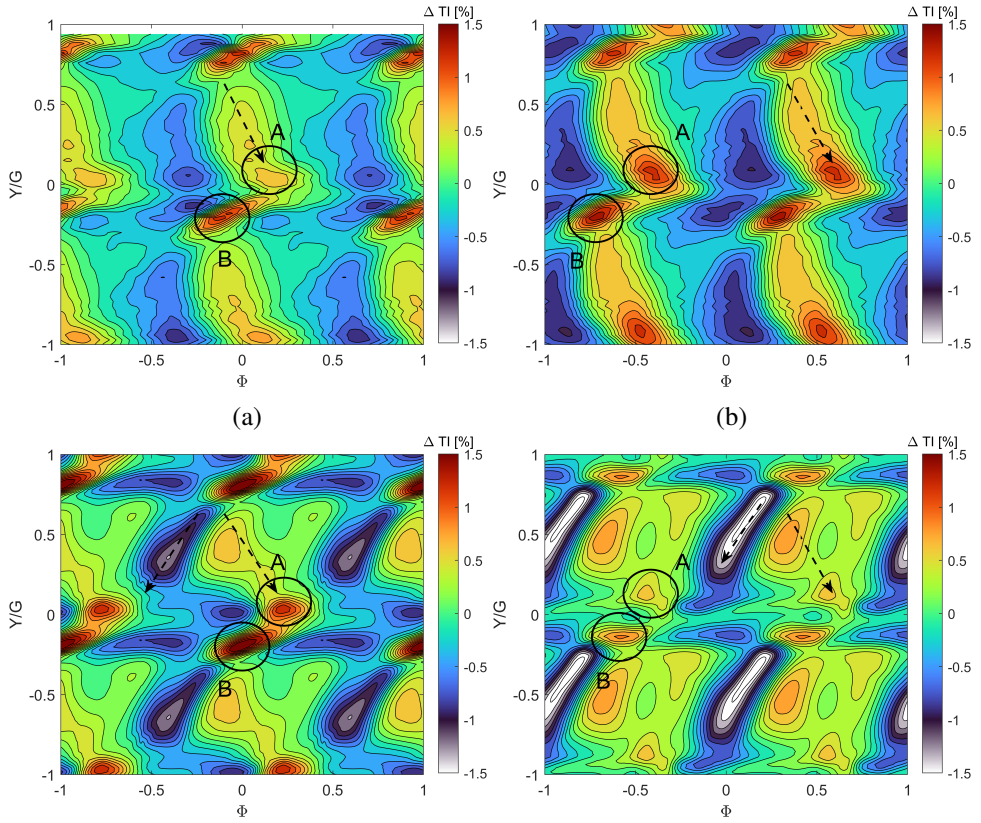

Fig. 4.47 Turbulence intensity fluctuations: (a-c) $Ma_{6,is}$=0.70 $Re_{6,is}$=70,000; (b-d) $Ma_{6,is}$=0.90; $Re_{6,is}$=70,000. Experiments on top, CFD at the bottom.

predicts a peak of ≈0.65%, roughly half the value measured during the experimental campaign. On the other hand, CFD overestimates the measurements at $Ma_{6,is}$=0.7, where the max predicted peak is around 1.5 %, compared with the 1.2% measured during the experimental campaign.

The origin of the two peaks close to the blade wake is addressed in Fig. 4.48, where the turbulence fluctuations are shown for two different time instants, close to the outlet measurement plane. The isolines refer to the normalized total pressure, which allows to locate the bar wake through the cascade. Both peaks on the PS and the SS arise from the interaction between the blade wake and the free-stream flow. At Φ=0.64, the level of turbulence in the wake is the lowest, which corresponds to the passage of the clean flow from the cascade. This also corresponds to the low shape factor region in the aft region of the SS. The increase of turbulence corresponds to the passage of the LE of the bar wake at the TE plane of the cascade. The production

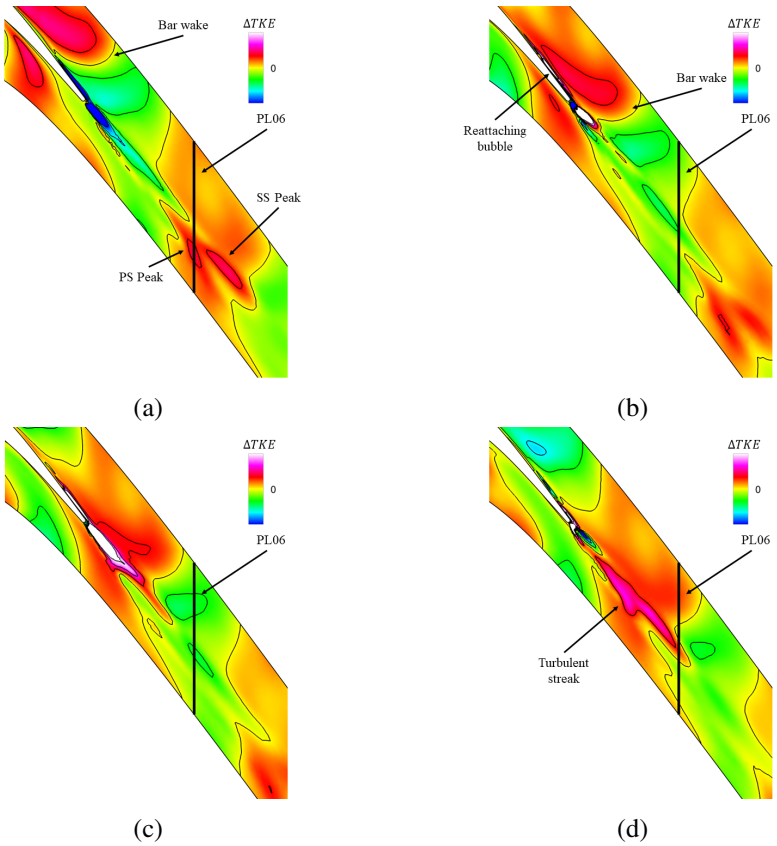

Fig. 4.48 Turbulence kinetic energy fluctuations, Ma_{6is}=0.90: (a) Φ=0.64, (b): Φ=0.91, (**c**): Φ=1.08, (d) Φ=1.31

of turbulent kinetic energy starts on the SS first because of the migration of the bar wake (Φ=0.91). The increase over the PS occurs as the bar wake crosses the TE on that side of the blade (Φ=1.08). Eventually, the peak of turbulence intensity convects towards PL06, with the SS peak reaching the plane first (Φ=1.31) and the PS peak arriving later Φ=0.64.

Chapter 5

Conclusions and Future Perspectives

The thesis reports the main activities performed during the research period to improve the performance and the numerical accuracy of the Finite-Volume Solver HybFlow. The thesis covers three broad topics related to the development of CFD solver intended for turbomachinery applications.

The first chapter of the thesis covers the implementation of a novel linear solver. The original strategy present in the code (Additive Schwarz Method), despite being memory efficient, leads to a huge decrease in performance for a high number of block divisions, due to the inherently explicit formulation of the block interface. On the other hand, the original subdivision among the blocks was not able to guarantee proper partition over high number of processors. In order to overcome these issues, the block-division strategy was removed and used mainly as a preconditioner for the Newton-Krylov nonlinear solver, while the partition of the grid is now performed using the well-known graph partitioner *Metis*. The overall Jacobian assembly procedure was instead modified to avoid numerical inaccuracies related to the choice of constant perturbation, even though the overall procedure has remained unchanged. Eventually, the GMRES solver has been parallelized using MPI-based routines, to improve the performance of the solver when a high number of processors is used. During the activity, new solver setups have been implemented. A new preconditioner based on an Algebraic Multigrid algorithm for the GMRES has been developed and tested in a wide range of setups defining the overall cycle shape and sweeps between coarse and fine levels. The performance of the GMRES solver has eventually been compared to a more common point-implicit smoother (LU-SSOR), while

implementing a CFL evolution law to speed-up steady simulations. It was shown that the AMG-GMRES and the LU-SSOR produce in general better convergence time compared to the ILU-GMRES solver, which is also more memory demanding. The choice between the AMG-GMRES and the LU-SSOR is instead dictated by the overall setup of the simulation, in particular the CFL number. As a matter of fact, the cost for building and applying the AMG-preconditioner is non negligible during the first iterations of simulations adopting a CFL evolution law, and in general when a low CFL value is imposed. For this reason the LU-SSOR performs better at low CFL values, while the AMG-GMRES is to be preferred in the case of fast steady convergence and for its robustness compared to the point implicit smoother. In the last part of the chapter, the scalability of the solver has been addressed, indicating a better parallel performance of LU-SSOR compared to the AMG-GMRES in the current implementation. Additional analysis of the solvers should be performed on finer meshes in order to confirm the results found on two-dimensional laminar/turbulent test cases found in the present activity. The analysis of the scalability over very fine meshes, using both implicit and explicit solvers is essential for the later implementation of Large Eddy Simulations capabilities in HybFlow.

The second chapter addresses the implementation of a high-order reconstruction scheme in the HybFlow. Two different methodologies have been implemented and tested over two different inviscid flows, and transitional test cases, spanning a flat plate, a low pressure turbine blade and a high pressure turbine vane with heat transfer. Two different test cases have been used to assess the capability of the implementation to achieve the nominal order of convergence of the methods. It was shown that both methodologies can achieve the nominal order of accuracy, even if the Successive Correction Method converges to smaller error levels for the same reconstruction order as the LSQ. The flat plate with zero pressure gradient test case allowed to test the effect of the reconstruction order over the prediction of by-pass and nearly by-pass transition of boundary layers. For higher order methods, the discrepancy between the cell averaged flow gradients and the cell center flow gradients, can become detrimental to the accuracy of the solver, as the prediction of the transition point gets increasingly delayed, while the skin friction coefficient is underestimated by 30% at the transition onset. On the other hand, the proper model behavior can be achieved by substituting the cell center gradients, with average gradients computed with the Green-Gauss formula, yielding the proper reconstruction of the boundary layer. The validation of the implemented method

for turbomachinery test cases has been performed using the T106C and the LS89 rotor blade and high pressure vane, respectively. The application of high order discretization is beneficial for the prediction of separating boundary layers, where the position of the separation/reattachment points can be detected with roughly half the elements of second order simulations. On the other hand, the effect of heat transfer predictions is limited and the high-order implementation provides no particular advantage over common second-order reconstruction. It is thought that such behavior is induced by the higher Reynolds number of the test-case, where large gradients in the near-wall region and the presence of an attached boundary layer limit the impact of high-order reconstruction compared to the low-pressure turbine test-case. Additional efforts can be devoted to the introduction of a consistent treatment for curved elements, which are necessary to fully achieve high-order reconstruction in the wall vicinity. Moreover, the choice of primitive variables reconstruction, in the place of the conservative one, should be taken into consideration, which is thought to be another possible cause behind the small effect of the reconstruction scheme over heat transfer predictions.

The third chapter addresses the application of the code to the SPLEEN cascade, which is representative of a high-speed low pressure turbine cascade operated at cruise Reynolds numbers. The analysis allowed to investigate the performance of the implemented transition sensitive RANS closures on this new setup. Initially, a sensitivity analysis to the model performed over a wide range of operating conditions, allowed to choose the $\gamma - \tilde{Re}_{\theta t}$ as the most suitable one compared to the $k - \overline{v^2} - \omega$. Both models tend to overpredict the peak of the losses in the wake center, while underpredicting its size, which is a typical shortcoming of RANS closures. The full three-dimensional cascade was analyzed to investigate the development of secondary flow structures and associated losses in the test-case. The simulations addressed in detail the effect of the turbulence profile imposed as an inlet boundary condition, hinting at the necessity of detailed turbulence measurements for a faithful reproduction of the flow-field in the cascade. Despite this, the agreement between the predictions and the experiments is good and the proper secondary flow distribution and turbulence intensity retrieved from the experimental campaign is achieved. Eventually the wake-blade interaction was simulated at the midspan section, using both the experimental profiles of the wake and a coupled simulation. To this end, a sliding mesh technique is implemented to study the coupling between the domains in relative motion. After an initial sensitivity to the setup, the results allowed to

investigate the effects of the wake induced transition comparing the predictions of the loading, wall shear stress and unsteady pressure measurements over the suction side of the blade. Despite the overall agreement between measurements and predictons, the results obtained through the unsteady approach are still not satisfactory. This leaves some space in the development of the code in terms of more accurate turbulence modelling, more suited to low-Reynolds conditions, such as Large Eddy Simulation (LES).

References

[1] W.Kyle Anderson and Daryl L Bonhaus. An implicit upwind algorithm for computing turbulent flows on unstructured grids. *Computers & Fluids*, 23(1):1–21, 1994.

[2] P.L Roe. Approximate riemann solvers, parameter vectors, and difference schemes. *Journal of Computational Physics*, 43(2):357–372, 1981.

[3] E. Turkel. Preconditioning techniques in computational fluid dynamics. *Annual Review of Fluid Mechanics*, 31(Volume 31, 1999):385–416, 1999.

[4] Jonathan M. Weiss, Joseph P. Maruszewski, and Wayne A. Smith. Implicit solution of preconditioned navier-stokes equations using algebraic multigrid. *AIAA Journal*, 37(1):29–36, 1999.

[5] Mauro Carnveale. *Development of Large Eddy Simulation Modelling for Turbomachinery Application*. PhD thesis, Università degli studi di Firenze, 2011.

[6] Christopher Michalak and Carl Ollivier-Gooch. Globalized matrix-explicit newton-gmres for the high-order accurate solution of the euler equations. *Computers & Fluids*, 39(7):1156–1167, 2010.

[7] Shenren Xu, Pavanakumar Mohanamuraly, Dingxi Wang, and Jens-Dominik Müller. Newton–krylov solver for robust turbomachinery aerodynamic analysis. *AIAA Journal*, 58(3):1320–1336, 2020.

[8] Dimitri J. Mavriplis and Karthik Mani. Unstructured mesh solution techniques using the nsu3d solver. In *52nd Aerospace Sciences Meeting*, 2014.

[9] Yousef Saad. *Iterative Methods for Sparse Linear Systems*. SIAM, 2003.

[10] Ning Qin, David K. Ludlow, and Scott T. Shaw. A matrix-free preconditioned newton/gmres method for unsteady navier–stokes solutions. *International Journal for Numerical Methods in Fluids*, 33(2):223–248, 2000.

[11] Matthew MacLean and Todd White. Implementation of generalized minimum residual krylov subspace method for chemically reacting flows. In *50th AIAA Aerospace Sciences Meeting including the New Horizons Forum and Aerospace Exposition*, 2012.

[12] Peterson Wong and David W. Zingg. Three-dimensional aerodynamic computations on unstructured grids using a newton–krylov approach. *Computers & Fluids*, 37(2):107–120, 2008.

[13] Todd T. Chisholm and David W. Zingg. A jacobian-free newton–krylov algorithm for compressible turbulent fluid flows. *Journal of Computational Physics*, 228(9):3490–3507, 2009.

[14] Olivier Dubois, Martin J. Gander, Sébastien Loisel, Amik St-Cyr, and Daniel B. Szyld. The optimized schwarz method with a coarse grid correction. *SIAM Journal on Scientific Computing*, 34(1):A421–A458, 2012.

[15] Victorita Dolean and Stephane Lantieri. A hybrid domain decomposition and multigrid method for the acceleration of compressible viscous flow calculations on unstructured triangular meshes. *International Journal of Computational Fluid Dynamics*, 14(4):287–304, 2001.

[16] P. Adami, F. Martelli, and V. Michelassi. Three-Dimensional Investigations for Axial Turbines by an Implicit Unstructured Multi-Block Flow Solver. volume Volume 1: Aircraft Engine; Marine; Turbomachinery; Microturbines and Small Turbomachinery of *Turbo Expo: Power for Land, Sea, and Air*, page V001T03A108, 05 2000.

[17] Lei Zhao and Chuhua Zhang. A parallel unstructured finite-volume method for all-speed flows. *Numerical Heat Transfer, Part B: Fundamentals*, 65(4):336–358, 2014.

[18] George Karypis and Vipin Kumar. A fast and high quality multilevel scheme for partitioning irregular graphs. *SIAM Journal on Scientific Computing*, 20(1):359–392, 1998.

[19] https://github.com/ivan-pi/fmetis.

[20] Andrea Arnone, Meng-Sing Liou, and Lousi Povinelli. Multigrid time-accurate integration of navier-stokes equations. In *11th Computational Fluid Dynamics Conference*.

[21] Antony Jameson. Time dependent calculations using multigrid, with applications to unsteady flows past airfoils and wings. In *10th Computational Fluid Dynamics Conference*, 1991.

[22] K. Stüben. A review of algebraic multigrid. *Journal of Computational and Applied Mathematics*, 128(1):281–309, 2001. Numerical Analysis 2000. Vol. VII: Partial Differential Equations.

[23] M. Raw. Robustness of coupled algebraic multigrid for the navier-stokes equations. In *34th Aerospace Sciences Meeting and Exhibit*, 1996.

[24] D. J. Mavriplis and A. Jameson. Multigrid solution of the navier-stokes equations on triangular meshes. *AIAA Journal*, 28(8):1415–1425, 1990.

[25] V. Venkatakrishnan. On the accuracy of limiters and convergence to steady state solutions. In *31st Aerospace Sciences Meeting*, 1993.

[26] Tony Arts, Marie Lambert de Rouvroit, and A. William Rutherford. Aero-thermal investigation of a highly-loaded transonic linear turbine guide vane cascade. Technical report, von Karman Institute for Fluid Dynamics, 1990.

[27] Lucian Ivan and Clinton P.T. Groth. High-order solution-adaptive central essentially non-oscillatory (ceno) method for viscous flows. *Journal of Computational Physics*, 257:830–862, 2014.

[28] R.C. Swanson and S. Langer. Steady-state laminar flow solutions for naca 0012 airfoil. *Computers & Fluids*, 126:102–128, 2016.

[29] V. Venkatakrishnan. Viscous computations using a direct solver. *Computers & Fluids*, 18(2):191–204, 1990.

[30] R. Kannan and Z. J. Wang. A study of viscous flux formulations for a p-multigrid spectral volume navier stokes solver. *Journal of Scientific Computing*, 41(2), 2009.

[31] Giove De Cosmo and Simone Salvadori. Implementation of non-reflecting boundary conditions in a finite volume unstructured solver for the study of turbine cascades. In *Proceedings of 13th European Conference on Turbomachinery Fluid dynamics and Thermodynamics*, 2019.

[32] Z.J. Wang, Krzysztof Fidkowski, Rémi Abgrall, Francesco Bassi, Doru Caraeni, Andrew Cary, Herman Deconinck, Ralf Hartmann, Koen Hillewaert, H.T. Huynh, Norbert Kroll, Georg May, Per-Olof Persson, Bram van Leer, and Miguel Visbal. High-order cfd methods: current status and perspective. *International Journal for Numerical Methods in Fluids*, 72(8):811–845.

[33] Vincent Brunet, Emma Croner, Alexandre Minot, Jérôme de Laborderie, Eric Lippinois, Stéphane Richard, Jean-François Boussuge, Jérôme Dombard, Florent Duchaine, Laurent Gicquel, Thierry Poinsot, Guillaume Puigt, Gabriel Staffelbach, Luis Segui, Olivier Vermorel, Nadège Villedieu, Jean-Sébastien Cagnone, Koen Hillewaert, Michel Rasquin, Ghislain Lartigue, Vincent Moureau, Vincent Couaillier, Emeric Martin, Marta de la Llave Plata, Jean-Marie Le Gouez, and Florent Renac. Comparison of Various CFD Codes for LES Simulations of Turbomachinery: From Inviscid Vortex Convection to Multi-Stage Compressor. volume Volume 2C: Turbomachinery of *Turbo Expo: Power for Land, Sea, and Air*, page V02CT42A013, 06 2018.

[34] Andrea Cassinelli, Francesco Montomoli, Paolo Adami, and Spencer J. Sherwin. High Fidelity Spectral/hp Element Methods for Turbomachinery. volume Volume 2C: Turbomachinery of *Turbo Expo: Power for Land, Sea, and Air*, page V02CT42A020, 06 2018.

[35] Timothy Barth and Paul Frederickson. Higher order solution of the euler equations on unstructured grids using quadratic reconstruction. In *28th Aerospace Sciences Meeting*, 1990.

[36] Luis Cueto-Felgueroso, Ignasi Colominas, Xesús Nogueira, Fermín Navarrina, and Manuel Casteleiro. Finite volume solvers and moving least-squares approximations for the compressible navier–stokes equations on unstructured grids. *Computer Methods in Applied Mechanics and Engineering*, 196(45):4712–4736, 2007.

[37] Antonis F. Antoniadis, Dimitris Drikakis, Pericles S. Farmakis, Lin Fu, Ioannis Kokkinakis, Xesús Nogueira, Paulo A.S.F. Silva, Martin Skote, Vladimir Titarev, and Panagiotis Tsoutsanis. Ucns3d: An open-source high-order finite-volume unstructured cfd solver. *Computer Physics Communications*, 279:108453, 2022.

[38] H.Q. Yang, Z.J. Chen, Andrzej Przekwas, and Jonathan Dudley. A high-order cfd method using successive differentiation. *Journal of Computational Physics*, 281:690–707, 2015.

[39] Grégoire Pont, Pierre Brenner, Paola Cinnella, Bruno Maugars, and Jean-Christophe Robinet. Multiple-correction hybrid k-exact schemes for high-order compressible rans-les simulations on fully unstructured grids. *Journal of Computational Physics*, 350:45–83, 2017.

[40] Oliver Friedrich. Weighted essentially non-oscillatory schemes for the interpolation of mean values on unstructured grids. *Journal of Computational Physics*, 144(1):194–212, 1998.

[41] Krzysztof Michalak and Carl Ollivier-Gooch. Limiters for unstructured higher-order accurate solutions of the euler equations. In *46th AIAA Aerospace Sciences Meeting and Exhibit*, 2008.

[42] Carl Ollivier-Gooch and Michael Van Altena. A high-order-accurate unstructured mesh finite-volume scheme for the advection–diffusion equation. *Journal of Computational Physics*, 181(2):729–752, 2002.

[43] A. Menasria, P. Brenner, and P. Cinnella. Improving the treatment of near-wall regions for multiple-correction k-exact schemes. *Computers & Fluids*, 181:116–134, 2019.

[44] Shayan Hoshyari, Ehsan Mirzaee, and Carl Ollivier-Gooch. Efficient convergence for a higher-order unstructured finite volume solver for compressible flows. *AIAA Journal*, 58(4):1490–1505, 2020.

[45] Carl Ollivier-Gooch. High-order eno schemes for unstructured meshes based on least-squares reconstruction. In *35th Aerospace Sciences Meeting and Exhibit*, 1997.

[46] Florian Haider, Pierre Brenner, Bernard Courbet, and Jean-Pierre Croisille. Parallel implementation of k-exact finite volume reconstruction on unstructured grids. In *High Order Nonlinear Numerical Schemes for Evolutionary PDEs*, pages 59–75, Cham, 2014. Springer International Publishing.

[47] Dimitri Mavriplis. Revisiting the least-squares procedure for gradient reconstruction on unstructured meshes. In *16th AIAA Computational Fluid Dynamics Conference*, 2003.

[48] Alireza Jalali and Carl F. Ollivier Gooch. Higher-order finite volume solution reconstruction on highly anisotropic meshes. In *21st AIAA Computational Fluid Dynamics Conference*, 2013.

[49] G. R. Cowper. Gaussian quadrature formulas for triangles. *International Journal for Numerical Methods in Engineering*, 7(3):405–408, 1973.

[50] Peter Wriggers. *Computational Contact Mechanics (2nd Edition)*. Springer, 2006.

[51] Alireza Jalali and Carl Ollivier Gooch. Accuracy assessment of finite volume discretizations of diffusive fluxes on unstructured meshes. In *50th AIAA Aerospace Sciences Meeting including the New Horizons Forum and Aerospace Exposition*, 2012.

[52] R.L. Taylor O.C. Zienkiewicz and J.Z. Zhu. *The Finite Element Method: Its Basis and Fundamentals (7th Edition)*. Elsevier, 2013.

[53] Maurin Lopez and D. Keith Walters. Prediction of transitional and fully turbulent flow using an alternative to the laminar kinetic energy approach. *Journal of Turbulence*, 17(3):253–273, 2016.

[54] Jan Michálek, Michelangelo Monaldi, and Tony Arts. Aerodynamic Performance of a Very High Lift Low Pressure Turbine Airfoil (T106C) at Low Reynolds and High Mach Number With Effect of Free Stream Turbulence Intensity. *Journal of Turbomachinery*, 134(6):061009, 08 2012.

[55] Roberto Pacciani, Michele Marconcini, Atabak Fadai-Ghotbi, Sylvain Lardeau, and Michael A. Leschziner. Calculation of High-Lift Cascades in Low Pressure Turbine Conditions Using a Three-Equation Model. *Journal of Turbomachinery*, 133(3):031016, 11 2010.

[56] Bing Cui Xiaole Wang and Zuoli Xiao. Numerical investigation on ultra-high-lift low-pressure turbine cascade aerodynamics at low reynolds numbers using transition-based turbulence models. *Journal of Turbulence*, 22(2):114–139, 2021.

[57] Jayson Babajee and Tony Arts. Investigation of the Laminar Separation-Induced Transition With the γ-$\mathrm{Re}_{\theta t}$ Transition Model on Low-Pressure Turbine Rotor Blades at Steady Conditions. volume Volume 8: Turbomachinery, Parts A, B, and C of *Turbo Expo: Power for Land, Sea, and Air*, pages 1167–1178, 06 2012.

[58] Koen Hillewaert, Corentin Carton de Wiart, Guillaume Verheylewegen, and Tony Arts. Assessment of a High-Order Discontinuous Galerkin Method for the Direct Numerical Simulation of Transition at Low-Reynolds Number in the T106C High-Lift Low Pressure Turbine Cascade. volume Volume 2B: Turbomachinery of *Turbo Expo: Power for Land, Sea, and Air*, page V02BT39A034, 06 2014.

[59] Site Hu, Chao Zhou, Zhenhua Xia, and Shiyi Chen. LES and CDNS Investigation of T106C Low Pressure Turbine. volume Volume 2C: Turbomachinery of *Turbo Expo: Power for Land, Sea, and Air*, page V02CT39A029, 06 2016.

[60] Abdelkader Benyahia. Mise en oeuvre et évaluation d'un modèle de transition à équations de transport pour la simulation d'écoulements en turbomachines. 2012.

[61] D. Keith Walters and Davor Cokljat. A Three-Equation Eddy-Viscosity Model for Reynolds-Averaged Navier–Stokes Simulations of Transitional Flow. *Journal of Fluids Engineering*, 130(12):121401, 10 2008.

[62] Frank Haselbach, Heinz-Peter Schiffer, Manfred Horsman, Stefan Dressen, Neil Harvey, and Simon Read. The Application of Ultra High Lift Blading in the BR715 LP Turbine . *Journal of Turbomachinery*, 124(1):45–51, 02 2001.

[63] J. D. Denton. Loss Mechanisms in Turbomachines. Volume 2: Combustion and Fuels; Oil and Gas Applications; Cycle Innovations; Heat Transfer; Electric Power; Industrial and Cogeneration; Ceramics; Structures and Dynamics; Controls, Diagnostics and Instrumentation; IGTI Scholar Award:V002T14A001, 05 1993.

[64] Klaus Gersten Hermann Schlichting. *Boundary Layer Theory (9th Edition)*. Springer, 2017.

[65] Frank Mangrem White. *Viscous Fluid FLow (2nd Edition)*. McGraw-Hill, 1991.

[66] Mark V. Morkovin. On the many faces of transition. In C. Sinclair Wells, editor, *Viscous Drag Reduction*, pages 1–31, Boston, MA, 1969. Springer US.

[67] J. L. Kerrebrock and A. A. Mikolajczak. Intra-Stator Transport of Rotor Wakes and Its Effect on Compressor Performance. *Journal of Engineering for Power*, 92(4):359–368, 10 1970.

[68] H. Pfeil, R. Herbst, and T. Schro¨der. Investigation of the Laminar-Turbulent Transition of Boundary Layers Disturbed by Wakes. *Journal of Engineering for Power*, 105(1):130–137, 01 1983.

[69] B. J. Abu-Ghannam and R. Shaw. Natural transition of boundary layers—the effects of turbulence, pressure gradient, and flow history. *Journal of Mechanical Engineering Science*, 22(5):213–228, 1980.

[70] Robert Edward Mayle. The Role of Laminar-Turbulent Transition in Gas Turbine Engines. volume Volume 5: Manufacturing Materials and Metallurgy; Ceramics; Structures and Dynamics; Controls, Diagnostics and Instrumentation; Education; IGTI Scholar Award; General of *Turbo Expo: Power for Land, Sea, and Air*, page V005T17A001, 06 1991.

[71] W. R. Hawtorne. Rotational flow through cascades part I. The components of vorticity. *The Quarterly Journal of Mechanics and Applied Mathematics*, 8(3):266–279, 01 1955.

[72] Carl Heinz Sieverding. Recent Progress in the Understanding of Basic Aspects of Secondary Flows in Turbine Blade Passages. *Journal of Engineering for Gas Turbines and Power*, 107(2):248–257, 04 1985.

[73] H. P. Wang, S. J. Olson, R. J. Goldstein, and E. R. G. Eckert. Flow Visualization in a Linear Turbine Cascade of High Performance Turbine Blades. *Journal of Turbomachinery*, 119(1):1–8, 01 1997.

[74] H. P. Hodson and R. G. Dominy. The Off-Design Performance of a Low-Pressure Turbine Cascade. *Journal of Turbomachinery*, 109(2):201–209, 04 1987.

[75] A. P. Weiss and L. Fottner. The Influence of Load Distribution on Secondary Flow in Straight Turbine Cascades. *Journal of Turbomachinery*, 117(1):133–141, 01 1995.

[76] M. W. Benner, S. A. Sjolander, and S. H. Moustapha. The Influence of Leading-Edge Geometry on Secondary Losses in a Turbine Cascade at the Design Incidence . *Journal of Turbomachinery*, 126(2):277–287, 06 2004.

[77] J. K. K. Chan, M. I. Yaras, and S. A. Sjolander. Interaction Between Inlet Boundary Layer, Tip-Leakage and Secondary Flows in a Low-Speed Turbine Cascade. Volume 1: Turbomachinery:V001T01A091, 06 1994.

[78] Kristina S. Hermanson and Karen A. Thole. Effect of inlet conditions on endwall secondary flows. *Journal of Propulsion and Power*, 16(2):286–296, 2000.

[79] E. Rosa de la Blanco, H. P. Hodson, R Vazquez, and D Torre. Influence of the state of the inlet endwall boundary layer on the interaction between pressure surface separation and endwall flows. *Proceedings of the Institution of Mechanical Engineers, Part A: Journal of Power and Energy*, 217(4):433–441, 2003.

[80] J. Cui, V. Nagabhushana Rao, and P.G. Tucker. Numerical investigation of secondary flows in a high-lift low pressure turbine. *International Journal of Heat and Fluid Flow*, 63:149–157, 2017.

[81] Richard Pichler, Yaomin Zhao, Richard Sandberg, Vittorio Michelassi, Roberto Pacciani, Michele Marconcini, and Andrea Arnone. Large-Eddy Simulation and RANS Analysis of the End-Wall Flow in a Linear Low-Pressure Turbine Cascade, Part I: Flow and Secondary Vorticity Fields Under Varying Inlet Condition. *Journal of Turbomachinery*, 141(12):121005, 11 2019.

[82] M. Giovannini, F. Rubechini, M. Marconcini, D. Simoni, V. Yepmo, and F. Bertini. Secondary Flows in LPT Cascades: Numerical and Experimental Investigation of the Impact of the Inner Part of the Boundary Layer. Volume 2B: Turbomachinery:V02BT41A027, 06 2018.

[83] Anirban Garai, Laslo Diosady, Scott Murman, and Nateri Madavan. DNS of Flow in a Low-Pressure Turbine Cascade Using a Discontinuous-Galerkin Spectral-Element Method. volume Volume 2B: Turbomachinery of *Turbo Expo: Power for Land, Sea, and Air*, page V02BT39A023, 06 2015.

[84] *Best-Practice Guidelines for High-Fidelity Simulations Based on Detailed Analysis of a Highly-Loaded Low-Pressure Turbine Cascade*, volume Volume 13B: Turbomachinery — Axial Flow Turbine Aerodynamics of *Turbo Expo: Power for Land, Sea, and Air*, 06 2023.

[85] R. E. Mayle and A. Schulz. The Path to Predicting Bypass Transition. Volume 1: Turbomachinery:V001T01A065, 06 1996.

[86] Roberto Pacciani, Michele Marconcini, Atabak Fadai-Ghotbi, Sylvain Lardeau, and Michael A. Leschziner. Calculation of High-Lift Cascades in Low Pressure Turbine Conditions Using a Three-Equation Model. *Journal of Turbomachinery*, 133(3):031016, 11 2010.

[87] F. R. Menter, R. B. Langtry, S. R. Likki, Y. B. Suzen, P. G. Huang, and S. Völker. A Correlation-Based Transition Model Using Local Variables—Part I: Model Formulation. *Journal of Turbomachinery*, pages 413–422, 03 2004.

[88] Robin B. Langtry and Florian R. Menter. Correlation-based transition modeling for unstructured parallelized computational fluid dynamics codes. *AIAA Journal*, 47(12):2894–2906, 2009.

[89] G. Lopes, L. Simonassi, A. F. M. Torre, M. Patinios, and S. Lavagnoli. An Experimental Test Case for Transonic Low-Pressure Turbines - Part 2: Cascade Aerodynamics at On- and Off-Design Reynolds and Mach Numbers. volume Volume 10B: Turbomachinery — Axial Flow Turbine Aerodynamics; Deposition, Erosion, Fouling, and Icing; Radial Turbomachinery Aerodynamics of *Turbo Expo: Power for Land, Sea, and Air*, page V10BT30A027, 06 2022.

[90] Loris Simonassi, Gustavo Lopes, Samuel Gendebien, Antonino Federico Maria Torre, Marios Patinios, Sergio Lavagnoli, Nicolas Zeller, and Ludovic Pintat. An Experimental Test Case for Transonic Low-Pressure Turbines – Part I: Rig Design, Instrumentation and Experimental Methodology.

volume Volume 10B: Turbomachinery — Axial Flow Turbine Aerodynamics; Deposition, Erosion, Fouling, and Icing; Radial Turbomachinery Aerodynamics of *Turbo Expo: Power for Land, Sea, and Air*, page V10BT30A012, 06 2022.

[91] Loris Simonassi, Gustavo Lopes, and Sergio Lavagnoli. Effects of periodic incoming wakes on the aerodynamics of a high-speed low-pressure turbine cascade. *International Journal of Turbomachinery, Propulsion and Power*, 8(3), 2023.

[92] Sergio Lavagnoli, Gustavo Lopes, Loris Simonassi, and Antonino Federico Maria Torre. SPLEEN - High Speed Turbine Cascade – Test Case Database, June 2023.

[93] Dragan Kožulović and B. Leigh Lapworth. An Approach for Inclusion of a Nonlocal Transition Model in a Parallel Unstructured Computational Fluid Dynamics Code. *Journal of Turbomachinery*, 131(3):031008, 04 2009.

[94] A. Hatman and T. Wang. A Prediction Model for Separated-Flow Transition. *Journal of Turbomachinery*, 121(3):594–602, 07 1999.

[95] A. Boudin, J. Dombard, F. Duchaine, L. Gicquel, N. Odier, S. Lavagnoli, G. Lopes, and L. Simonassi. Analysis of rotor/stator interactions in a high-speed low-pressure turbine cascade using Large-Eddy Simulations. In *Proceedings of 15th European Conference on Turbomachinery FLuid Dynamics and Thermodynamics*, 04 2023.

[96] H. P. Hodson and R. G. Dominy. Three-Dimensional Flow in a Low-Pressure Turbine Cascade at Its Design Condition. *Journal of Turbomachinery*, 109(2):177–185, 04 1987.

[97] S. Kubacki, P. Jonak, and E. Dick. Evaluation of an algebraic model for laminar-to-turbulent transition on secondary flow loss in a low-pressure turbine cascade with an endwall. *International Journal of Heat and Fluid Flow*, 77:98–112, 2019.

[98] Michele Marconcini, Roberto Pacciani, Andrea Arnone, Vittorio Michelassi, Richard Pichler, Yaomin Zhao, and Richard Sandberg. Large Eddy Simulation and RANS Analysis of the End-Wall Flow in a Linear Low-Pressure-Turbine Cascade—Part II: Loss Generation. *Journal of Turbomachinery*, 141(5):051004, 01 2019.

[99] Fernando Gisbert, David Cadrecha, and Patxi Apoita. Prediction of the Influence of the Inlet End-Wall Boundary Layer on the Secondary Flow of a Low Pressure Turbine Airfoil Using RANS and Large-Eddy Simulations. *Journal of Turbomachinery*, 146(9):091001, 04 2024.

[100] John D. Coull. Endwall Loss in Turbine Cascades. *Journal of Turbomachinery*, 139(8):081004, 03 2017.

[101] Mizuki Okada, Loris Simonasis, Gustavo Lopes, and Sergio Lavagnoli. PIV Measurements in a high-speed low-Reynolds low-pressure turbine cascade. *Journal of Turbomachinery*, pages 1–38, 10 2023.

[102] John D. Coull and Howard P. Hodson. Unsteady boundary-layer transition in low-pressure turbines. *Journal of Fluid Mechanics*, 681:370–410, 2011.

[103] H. P. Hodson. Measurements of Wake-Generated Unsteadiness in the Rotor Passages of Axial Flow Turbines. *Journal of Engineering for Gas Turbines and Power*, 107(2):467–475, 04 1985.

[104] H. P. Hodson and W. N. Dawes. On the Interpretation of Measured Profile Losses in Unsteady Wake–Turbine Blade Interaction Studies. *Journal of Turbomachinery*, 120(2):276–284, 04 1998.

[105] D. E. Halstead, D. C. Wisler, T. H. Okiishi, G. J. Walker, H. P. Hodson, and H.-W. Shin. Boundary Layer Development in Axial Compressors and Turbines: Part 1 of 4—Composite Picture. *Journal of Turbomachinery*, 119(1):114–127, 01 1997.

[106] V. Schulte and H. P. Hodson. Unsteady Wake-Induced Boundary Layer Transition in High Lift LP Turbines. *Journal of Turbomachinery*, 120(1):28–35, 01 1998.

[107] R. J. Howell, O. N. Ramesh, H. P. Hodson, N. W. Harvey, and V. Schulte. High Lift and Aft-Loaded Profiles for Low-Pressure Turbines . *Journal of Turbomachinery*, 123(2):181–188, 02 2000.

[108] P. G. Schubauer and P. S. Klebanoff. Contributions on the mechanics of the boundary-layer transition‘. Technical report, NACA TN 3489 and NACA rep1289, 1955.

[109] Ali Mahallati and Steen A. Sjolander. Aerodynamics of a Low-Pressure Turbine Airfoil at Low Reynolds Numbers—Part II: Blade-Wake Interaction. *Journal of Turbomachinery*, 135(1):011011, 11 2012.

[110] R. D. Stieger, David Hollis, and H. P. Hodson. Unsteady Surface Pressures Due to Wake-Induced Transition in a Laminar Separation Bubble on a Low-Pressure Cascade . *Journal of Turbomachinery*, 126(4):544–550, 12 2004.

[111] F. R. Menter. Two-equation eddy-viscosity turbulence models for engineering applications. *AIAA Journal*, 32(8):1598–1605, 1994.

[112] David C. Wilcox. *Turbulence Modeling for CFD (2nd Edition)*. D C W Industries, 1998.

[113] F. R. Menter, M. Kuntz, and R. Langtry. Ten years of industrial experience with the sst turbulence model. In *Turbulence, heat and mass transfer*, volume 4, pages 625–632, New York, 2003. Begell House.

Appendix A

AMG linear solver assessment

This Appendix presents the analysis of the sensitivity of the convergence time for steady solution, for different parameters defining the setup of the AMG-preconditioned GMRES. The parameters analyzed are the following:

- Generation of groups: N_{min} and N_{max}
- Cycling strategy: it is controlled by the number of sweeps used before/after the restriction and prolongation steps as well as at the coarsest and at the finest level
- Cycle shape: V cycle or W cycle
- Number of levels visited during the coarsening algorithm

In the remaining part of the Appendix, the various setups will be denoted as follows: a letter indicates the type of cycle, a group of four numbers indicate the sweeps performed (before restriction, after prolongation, at the coarsest level, and at the finest level), while two numbers refer to the groups generation (respectively indicating N_{min} and N_{max}). An additional number will refer to the number of coarse levels generated and will be indicated as n_{lev}. The test case used for this analysis is the laminar NACA0012 airfoil on the mesh M1.

Figure A.1 shows the computational time for various setups of the simulations using an aggressive coarsening strategy (N_{min}=8 and N_{max}=12). The variability of the computational time is somehow limited. Both for the first order and the second

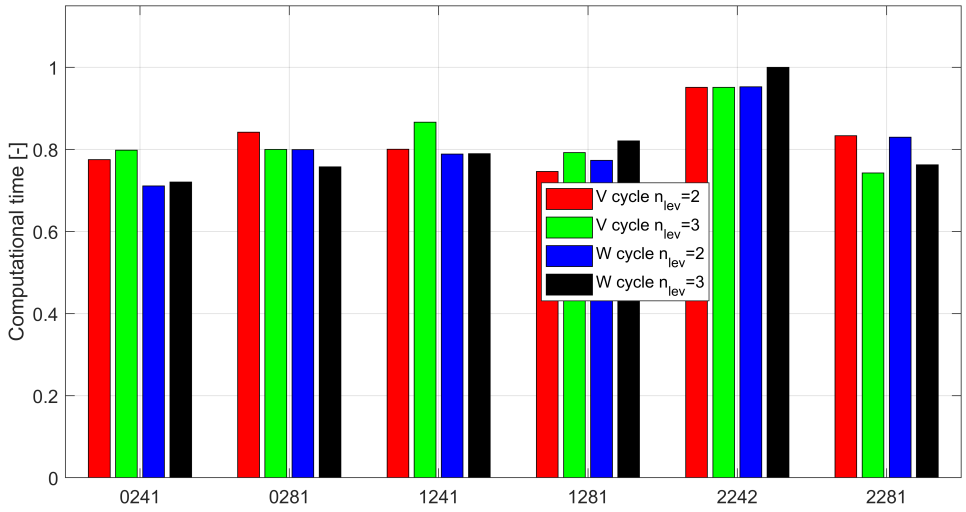

(a)

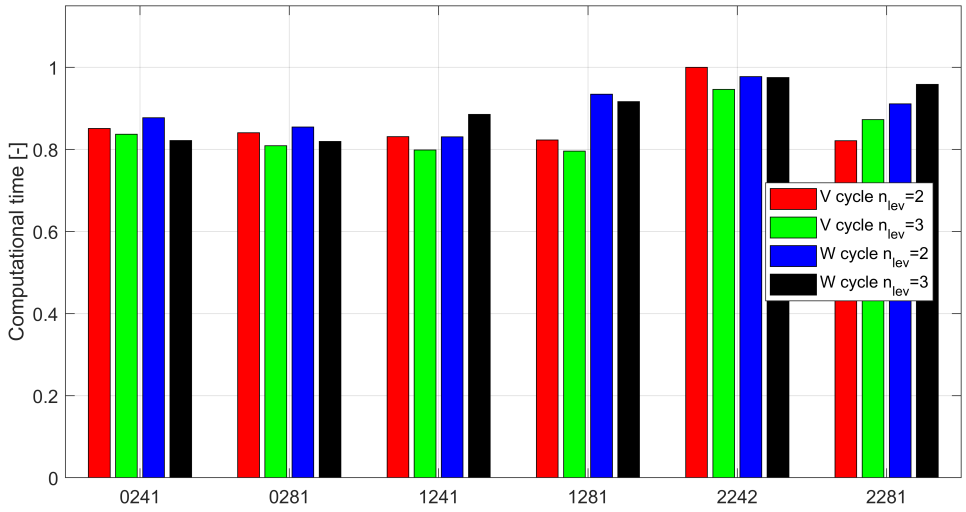

(b)

Fig. A.1 NACA0012 M1 - Effect of the discretization order: (a) 1^{st} order, (b) 2^{nd} order

order computation, the slowest strategy is obtained using the cycling 2242, which performs 2 smoothing steps at the finest level, before visiting coarser ones. This is a clear indication that increasing the number of restrictions is not beneficial to the overall convergence time. The best solutions are 0241,1281 while the strategy 2281 returns a comparable computational time only when a V cycle is adopted. On the other hand, the effect of the number of levels is mainly dependent on the order of discretization (which affects the number of linear iterations). From first order discretization results, it is evident that apart from some occurrences, the W cycle leads to a lower computational time compared to the V cycle. The opposite happens in the case of the of the second order discretization. This can be explained looking at the number of linear iterations required at each Newton step, shown in Fig. A.2 and A.3. The effect is shown for the cycle 0241-1241 and 1281, which have on average the best performance out of the tested ones. The number of linear iterations required by the 1^{st} order discretization is higher, roughly three times the number of linear iterations required by the 2^{nd} order. This is due to the fact that 2^{nd} order simulations are initialized from 1^{st} order ones. In both cases, the W cycle allows to reduce the number of iterations required by the Newton solver. Despite this, for the 1^{st} order simulations this is translated in an average reduction of the number of linear iterations of approximately 10 iterations during the final part of the simulation. On the other hand, the reduction in the 2^{nd} order setup is only of around 2-3 iterations due to the already limited number of total iterations required.

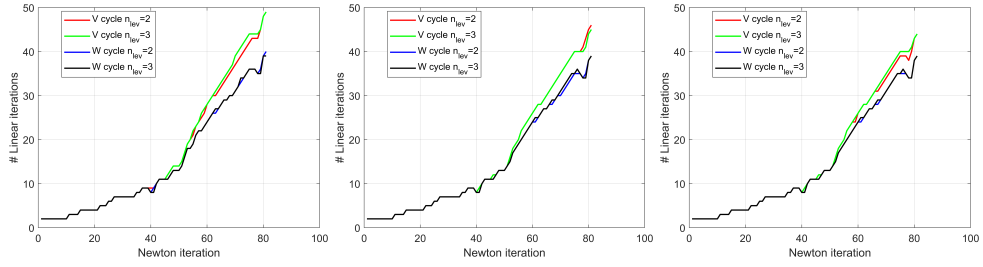

(a) (b) (c)

Fig. A.2 NACA0012 M1 - Linear iteration count for 1^{st} order solution: (a) Cycle: 0241, (b) Cycle: 1241, (c) Cycle: 1281

The breakdown of the cost associated to the application of the preconditioner is shown in Fig. A.4, which shows the computational time in seconds for each step of the linear solver (construction of the preconditioner, its application and the GMRES iterations). The analysis is performed over the last iteration of the solution, so it does not take into account the initial iterations of the simulations, where the number of

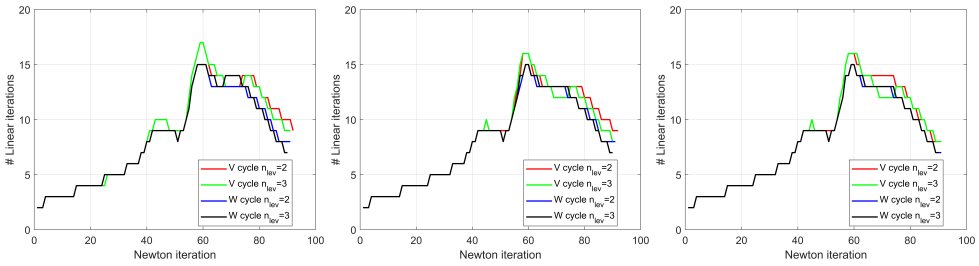

(a) (b) (c)

Fig. A.3 NACA0012 M1 - Linear iteration count for 2^{nd} order solution: (a) Cycle: 0241, (b) Cycle: 1241, (c) Cycle: 1281

inner iterations is low due to the low CFL value. The breakdown is consistent with the overall number of linear iterations. The V-shaped cycle is less effective in this conditions, compared to the W-cycle, which was already seen in Fig. A.2. For the cycles 0241 and 1241, the application of the V type of cycle takes more time than the W cycle, due to the high number of linear iterations performed. For the 1281 cycle instead, the W cycle is more demanding, but its performance is balanced by the the lower number of total iterations required to solve the nonlinear step. While the time required by the grouping is negligible over the last few-steps of the simulation, accounting for roughly 2-3% of the total computational time, it is not in the initial steps. This is shown in Fig. A.5 showing the cost for building the preconditioner

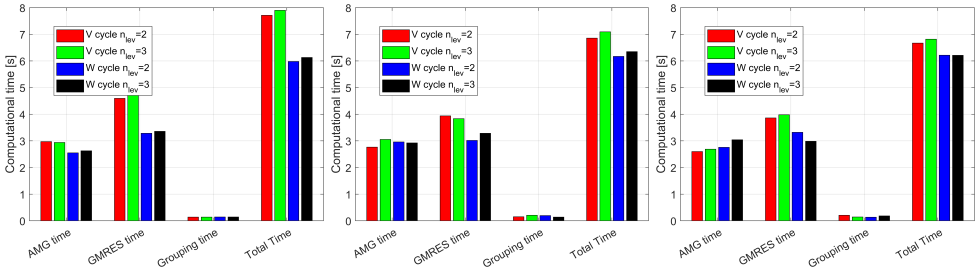

(a) (b) (c)

Fig. A.4 NACA0012 M1 - Breakdown of the overall cost over the last nonlinear iteration: (a) Cycle: 0241, (b) Cycle: 1241, (c) Cycle: 1281

and apply it to the GMRES solver when the CFL number is equal to 20. In this case, the total time necessary to build the preconditioner accounts for approximately 20-30% of the total computational time, which is a factor of 10 higher than the case of high CFL number. This also explains why the overall cycle performance highly depends on the overall nonlinear convergence (how fast the residuals drop for high CFL values). In general, the choice of the right shape of the cycle and the overall

cycling strategy becomes application dependent. For this reason, the cycle 0241 was chosen for the analysis presented in Chapter 2.

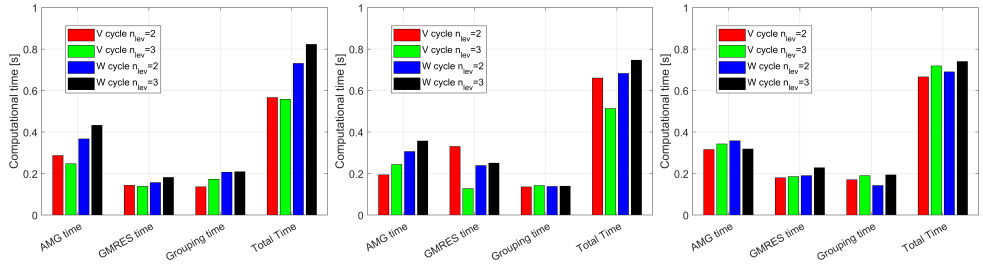

(a) (b) (c)

Fig. A.5 NACA0012 M1 - Breakdown of the overall cost at CFL=20: (a) Cycle: 0241, (b) Cycle: 1241, (c) Cycle: 1281

The effect of the coarsening is instead shown in the last part of the Appendix, where the effect of the number of cells allowed to form coarse levels is investigated. The effect of the size has been investigated only for the most promising cycles (0241,1241,1281) in Fig. A.6. In general, the aggressive coarsening yields better convergence time, regardless of the type of cycle. While the computational time reduction from a weak coarsening to a medium coarsening strategy is remarkable (on average the cost reduction is around 30 % of the computational time for the most expensive cycling strategies), the drop is less evident from medium coarsening to aggressive coarsening. In this case, the average reduction of convergence time is around 15%.

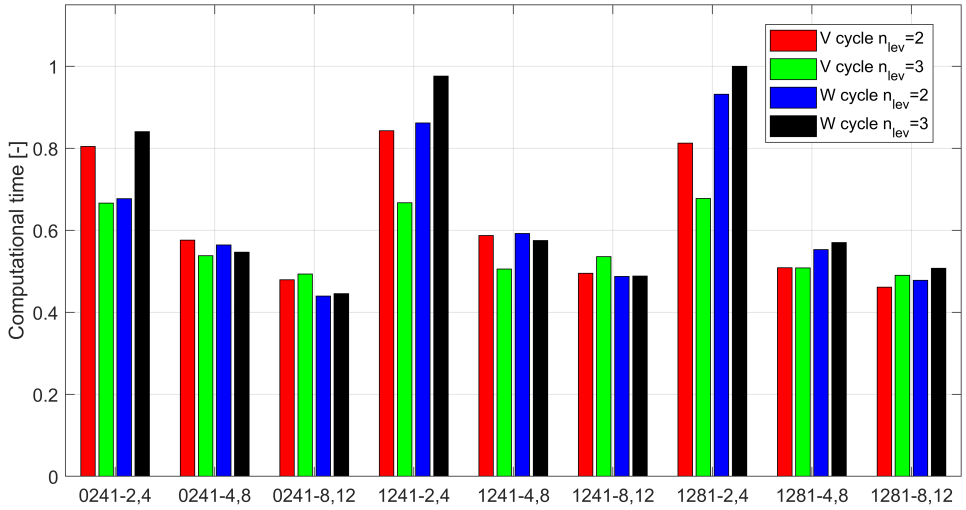

Fig. A.6 NACA0012 M1 - Effect group size

Figure A.7 shows the required linear iterations for the 1241 strategy, with different group sizes. The weak coarsening proves to yield a more stable preconditioner, especially when a W cycle is adopted. This is shown by the constant decrease of the number of iterations at each Newton step compared to the other cases. On the other hand, the overall computational time indicates that despite a lower number of GMRES iterations, the cost for building the preconditioner and its application during the linear solution outweighs the reduction of linear iterations.

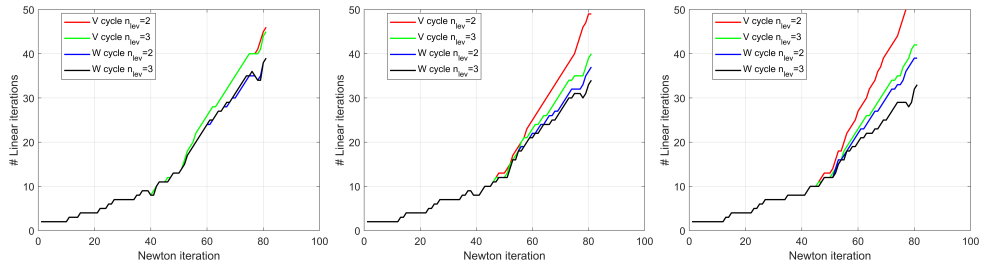

(a) (b) (c)

Fig. A.7 NACA0012 M1 - Effect of group size on linear iterations for 1241 cycle: (a) Aggressive coarsening (N_{min}=8, N_{max}=12); (b) Medium coarsening (N_{min}=4, N_{max}=8); (c) Weak coarsening (N_{min}=2, N_{max}=4).

Eventually a breakdown of the costs associated to the construction of the coarse space and the application of the preconditioner is shown in Fig. A.8, and A.9, respectively for the last iteration and for a CFL equal to 20. The sweep is performed with the V cycle with two levels explored (n_{lev}=2). Similar considerations can be drawn from different combinations of cycle shape and number of levels. For higher CFL values, the weight of the coarsening algorithm is still negligible compared to the overall cost of the nonlinear iteration. Despite this, the group size affects both the total number of iterations in the GMRES and the overall time of the AMG solver, which preconditions the system. As was shown in Fig. A.7, when an aggressive coarsening is used over the V1241-n2 cycle, the number of linear iterations tends to decrease compared to weaker coarsening strategies. For this reason, the simulations employing N_{min}=2 and N_{max}=4 take the most time out of all the tested setups.

Similarly at CFL=20, the total cost of the iterations for weak coarsening is higher. It is shown that the only case in which the weak coarsening brings some level of advantage is in the 1241 cycle, where it brings a reduction in the total GMRES due to the low number of iterations. In this case, this advantage is outweighed by the overall coarsening time and the cycling between coarse/fine levels. Eventually, the

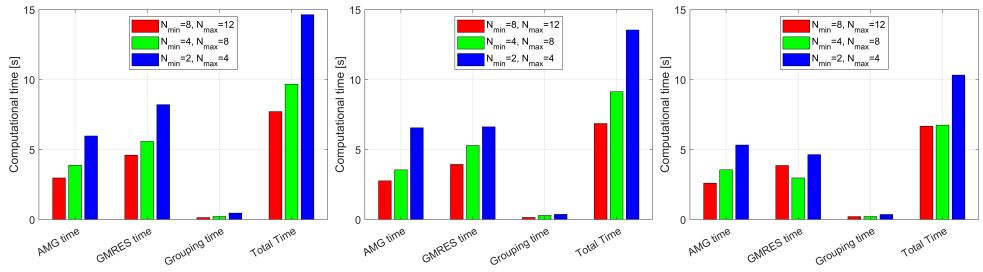

(a) (b) (c)

Fig. A.8 NACA0012 M1 - Breakdown of the overall cost varying the group size over the last iteration: (a) Cycle: 0241, (b) Cycle: 1241, (c) Cycle: 1281

cost of the weak coarsening turns out to be still twice as much as the cost of the aggressive coarsening.

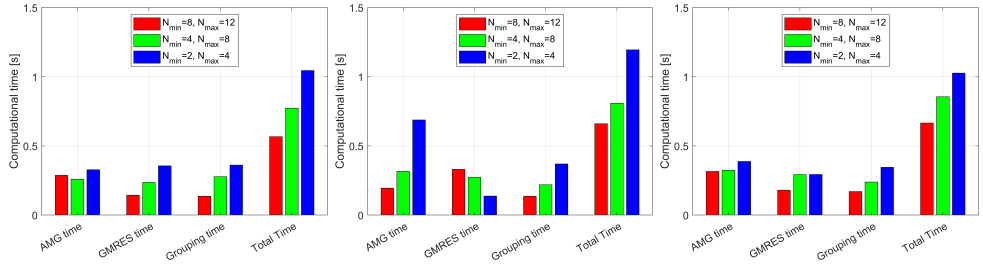

(a) (b) (c)

Fig. A.9 NACA0012 M1 - Breakdown of the overall cost varying the group size at CFL=20: (a) Cycle: 0241, (b) Cycle: 1241, (c) Cycle: 1281

Appendix B

Sensitivity analysis for 2D SPLEEN unsteady simulations

B.1 Effect of simulation setup

As mentioned in the work by Boudin et al. [95], when the experimental numerical conditions are imposed at the inlet of the blade, the acceleration in the front part of the blade is underestimated. An initial sensitivity to the inlet conditions was then performed to asses the impact of the boundary conditions on the predictions from the simulation. During the experimental investigation, the cascade was rotated by $\approx 6^{\circ}$ ([92]), to balance the variation of flow angle at the inlet plane of the bar. In addition to this, when the sliding mesh technique is employed, a one to one pitch ratio is necessary to simulate a single bar and a single blade. In this case, the pitch ratio is around 1.05. For this reason, the bar domain has been scaled, and in order to guarantee that the non-dimensional conditions of the cascade are met, the bar peripheral speed is changed accordingly. The effect of both these modifications on the numerical simulations is studied by varying the bar peripheral speed and the inlet flow angle. The "Coupled" approach, then counts five different simulations, listed in Tab. B.1. The listed incidence refers to the absolute flow angle. In general the first simulation reproduces experimental conditions in terms of St and accounts for the cascade rotation. The last setup instead reproduces the dimensional conditions in terms of bar peripheral velocity and disregards the cascade rotation. This setup is the same as the one used in [95], where the peripheral speed of the bar is set equal to the

Name	$St[-]$	$i[^\circ]$	U_{bar}	Ma_{bar}
1	0.95	5.0	Corrected	0.84
2	0.91	5.0	Experimental	0.82
3	0.95	3.0	Corrected	0.82
4	0.95	1.0	Corrected	0.80
5	0.91	-1.0	Experimental	0.77

Table B.1 Tested boundary conditions

experimental one. The other conditions investigate the effect of *St* and *i* with respect to the two limiting conditions.

The setup '5' was also used to assess the dependency on the time-step discretization. In order to check that 120 time-steps per passing could provide a reasonable tradeoff between computational time and accuracy, a second simulation was run using 240 time-steps per passing period. The results of time-step dependency are shown in Fig. B.1, where the dependency is analyzed in terms of averaged quantities (loading and energy loss coefficent, top of the figure), as well as using the phase resolved energy loss coefficient at the outlet measurement plane. As stated in Sec. 4.5, the experimental loss coefficient was retrieved from the total pressure measurements obtained with the L5HP, while the static pressure was retrieved from the pneumatic taps installed on the endwall of the cascade. In general, the impact of the time step is negligible both on averaged predictions and on unsteady quantities.

Figure B.2 evidences the effect of the boundary conditions on the numerically predicted loading. The acceleration in the front part of the blade reduces as the incidence reduces. Comparing the predictions to the experiments, the acceleration obtained for i=5° is overestimated. The opposite happens for i=-1°. A better prediction of the front acceleration is obtained for i=1° - 3°. The latter case evidences an important separation over the PS, which does not find an experimental counterpart. The effect of the Strouhal number is similar to that of the incidence as a lower peripheral velocity of the bar induces a lower deflection of the flow.

The predictions of the bar wake profile at Plane 02 is shown in Fig. B.3, where the numerical total pressure fluctuations are plotted against the pitchwise coordinate. In this case, a twofold effect is present. On one hand, the incidence variation induces a different position of the wake at PL02. This is due to the different travelling time of the wake between the bar and the measurement plane. On the other hand, also the

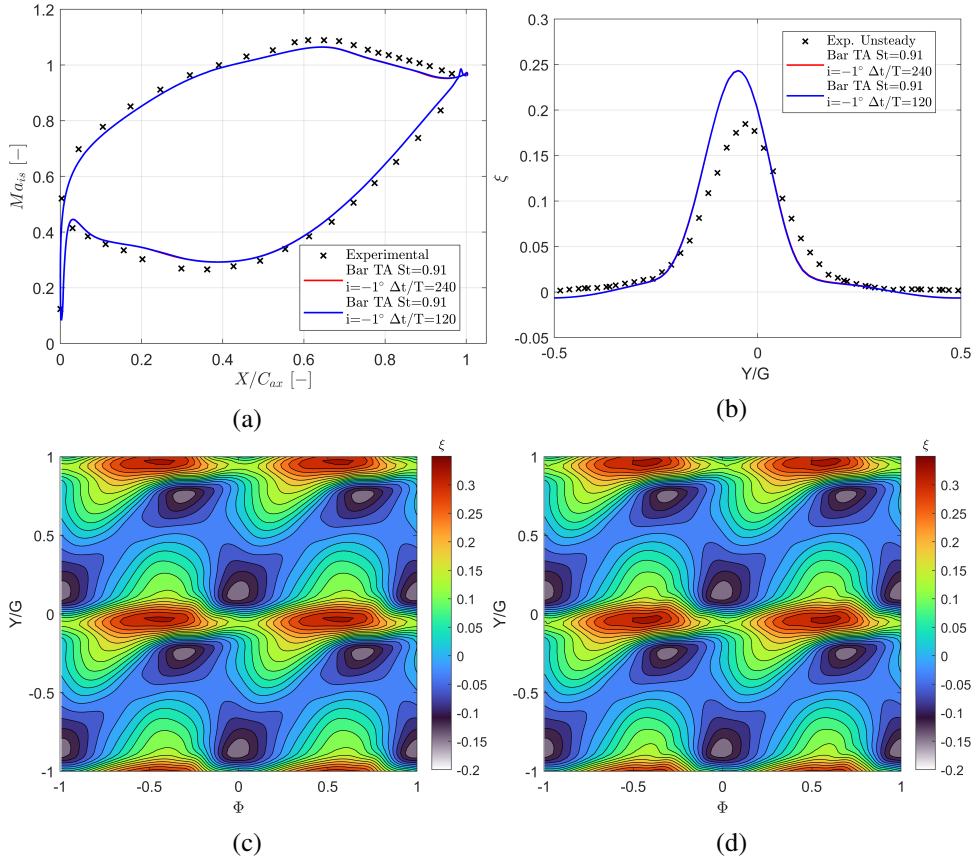

Fig. B.1 Effect of the time step

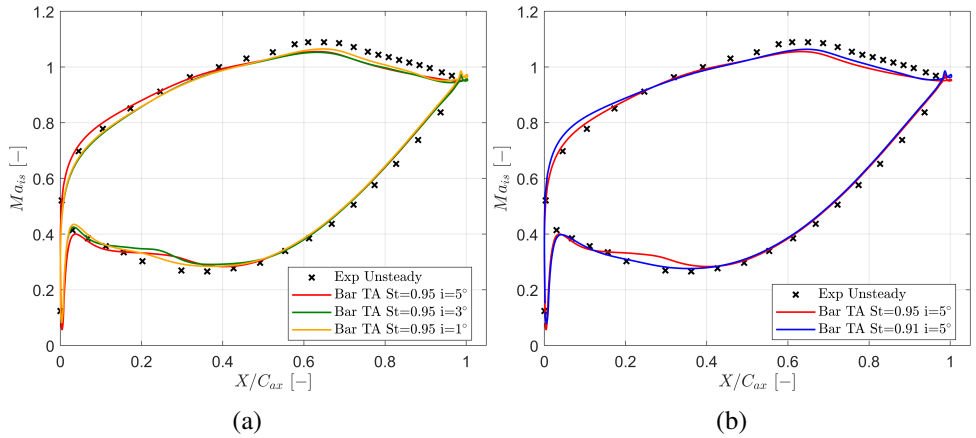

Fig. B.2 Effect of boundary conditions on loading predictions: (a) effect of prescribed incidence, (b) effect of the Strouhal number

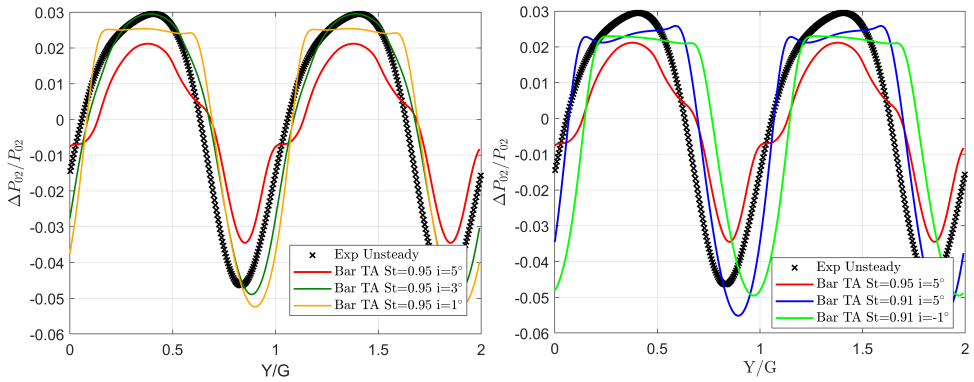

(a) (b)

Fig. B.3 Effect of boundary conditions on bar wake predictions

shape of the bar wake is affected. This is caused by the variation of the relative Mach number which affects the prediction of the shock downstream of the bar itself. The higher the Mach, the stronger the shock and shape of the wake changes accordingly. In particular for the weakest shocks (Ma_{rel}<0.8), a region with uniform conditions appears between two wake passing events. For Ma_{rel}>0.8 the shock is strong enough to produce a sine-like shape of the total pressure, inducing distributed losses also in the free-stream. In this conditions, the best prediction of the experimental shape is achieved by imposing an inlet incidence equal to 3°.

Lower sensitivity is present at the outlet measurement plane (Fig. B.4). All the simulations retrieve the same averaged losses except for the St095i5 case. The loss peak is shifted towards the PS of the blade, and it is lower in magnitude. Moreover, compared to the other cases, the wake appears thinner on the SS. For i=3°, a negative trend of the energy loss coefficient is evident in the free-stream region. This aspect is not evident in all the other simulations and is adduced to the different total pressure profile achieved at PL02. The peak of total pressure convects through the cascade, in a similar manner to the one described in Sec. 4.5, creating pockets of negative energy loss coefficient which are also present in the averaged ξ distribution.

To summarize, the predictions obtained using the setups St095i1 and St095i3 are in fact similar. The former yields a better prediction of the loading (in particular a better acceleration on the SS, in the central region of the blade, and a lower size of the PS separation), while the latter manages to reproduce correctly the total pressure deficit imposed by the wake of the bar. Eventually the St095i1 setup was used for the 'Coupled' approach simulations mainly because of the predictions in the aft

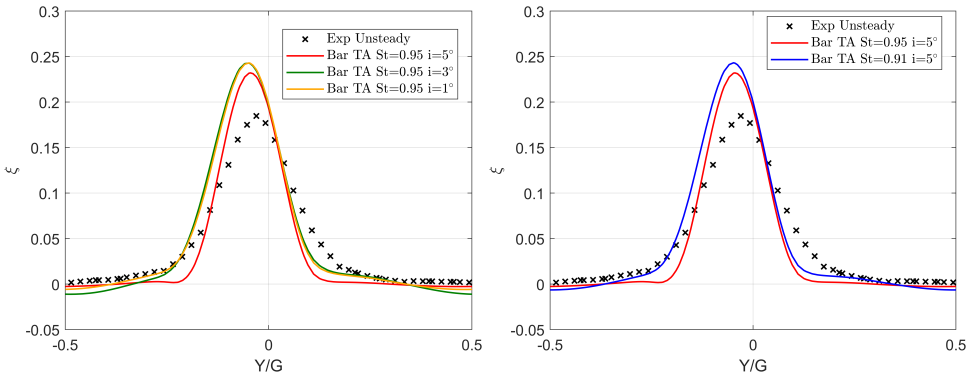

(a) (b)

Fig. B.4 Effect of boundary conditions on losses: (a) effect of prescribed incidence, (b) effect of the Strouhal number

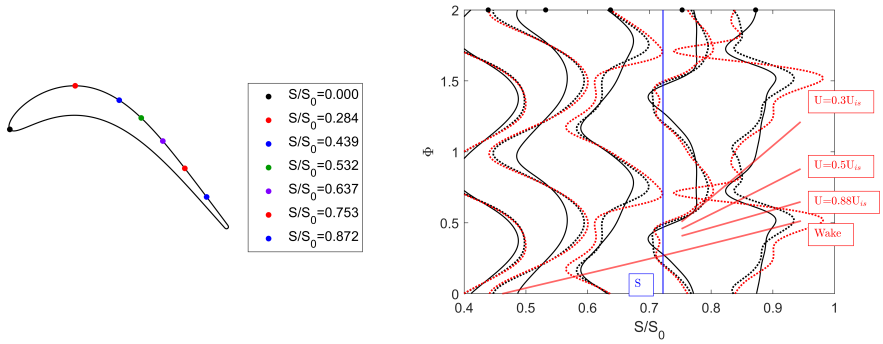

(a) (b)

Fig. B.5 Static pressure fluctuations: Experimental (black continuous curve), St095i1 (black dashed curve)and St095i3 (red dashed curve)

region of the SS and due to a local effect present in the time-resolved energy loss coefficient predicted at Plane 06. Figure B.5 evidences a high pressure fluctuation in the aft region of the SS for St095i3, which indicates a thicker boundary layer more susceptible to disturbances compared to the one predicted by St095i1. The latter is also in better agreement with the experiment. The main effect of the thick boundary layer is visible at PL06 (see Fig. B.6), where a local loss can be found on the SS side of the blade's wake. This local effect is caused by the periodic thickening of the wake after the separation over the SS, generating a similar effect as to those explained in Sec. B.2.

In order to complete the analysis regarding the boundary conditions, an additional set of simulations was run using the experimental wake profiles at the inlet mea-

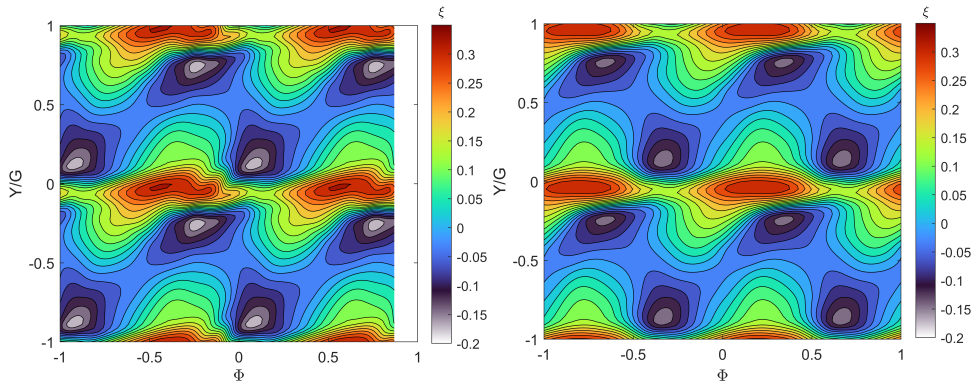

(a) (b)

Fig. B.6 Time resolved energy loss coefficient at PL06: (a) St095i3, (b) St095i1

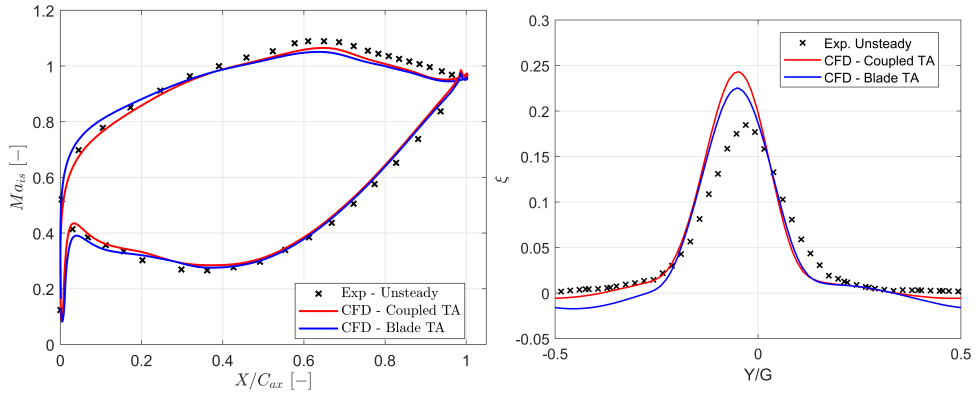

(a) (b)

Fig. B.7 Comparison of sliding mesh and wake imposed approach

surement plane. This last case will be labeled as 'Blade' approach in the remaining of the section. The experimental wake profile is prescribed by means of a moving polynomial which is swept across the inlet measurement plane at the bar peripheral speed. The interpolation is performed in such a way that the profile is constrained to be periodic over the blade periodicity rather than the bar periodicity, mimicking the effect of the domain scaling used for the sliding mesh simulations. The effect on the loading prediction and the loss prediction is shown in Fig. B.7.

The front part of the loading is captured better by the sliding mesh simulation (St095i1), while the blade approach overestimates the front acceleration and underestimates the velocity increase in the middle of the blade. Similar predictions are present on the PS, as both approaches retrieve a similar loading distribution except in the front part, due to the different incidence imposed to the blade. From the point

of view of the losses, the approaches behave similarly in the prediction of the blade wake spreading, while the loss peak predicted by the sliding mesh approach is higher than the one obtained with the wake. On the other hand, a negative energy loss coefficient is present at the outlet. The result is similar to the St95i3 case, confirming that in the unsteady prediction of the cascade losses the bar wake shape retains a major effect on the overall predictions. The difference in the free-stream is ≈0.01.

B.2 Effect of turbulence modelling

A sensitivity analysis to the transition sensitive model was also performed for the 2D unsteady simulations, both for the "Coupled" approach and the blade simulation. In this section the most meaningful comparison, in terms of profile and downstream measurements, will be presented to justify the use of the $\gamma - \tilde{Re}_{\theta t}$ transition model also for the time-resolved simulations. The time-averaged prediction of the loading is shown in Fig. B.8, where the two models are compared to the experiments. Similarly to the steady simulations, the two models yield the same isentropic Mach distribution excet for the front region of the PS. The $k - \overline{v^2} - \omega$ model predictions are heavily affected by the presence of a separation bubble which leads to a flat loading profile before the reattachment where the same Mach distribution as the $\gamma - \tilde{Re}_{\theta t}$ is obtained. The rear part of the SS is instead characterized by a slight variation of the loading compared to the $\gamma - \tilde{Re}_{\theta t}$ for 0.9<X/C_{ax}<0.95. The pressure recovery is more uniform from in the case of the $\gamma - \tilde{Re}_{\theta t}$, whose result indicate a faster transition of the boundary layer.

This is aspect can be further analyzed looking at the distributions of the shape factor over the suction side which is shown in Fig. B.9, considering the 'Coupled' approach only. The boundary layer behaves in a similar manner in the front part of the blade up to S/S_0=0.3. The $k - \overline{v^2} - \omega$ model predicts a thicker boundary layer afterwards. Flow separation occurs at approximately the same location as the $\gamma - \tilde{Re}_{\theta t}$ model, but the transition process is completely different. The $\gamma - \tilde{Re}_{\theta t}$ model predicts a fully reattached boundary layer for S/S_0>0.85, while the $k - \overline{v^2} - \omega$ yields an open and intermittent separation bubble extending towards the TE of the blade. The higher value of the shape factor, caused by the slower transition, explains the difference in the loading in the aft region of the SS, as well as the distributions of turbulence intensity and losses shown taken at PL06.

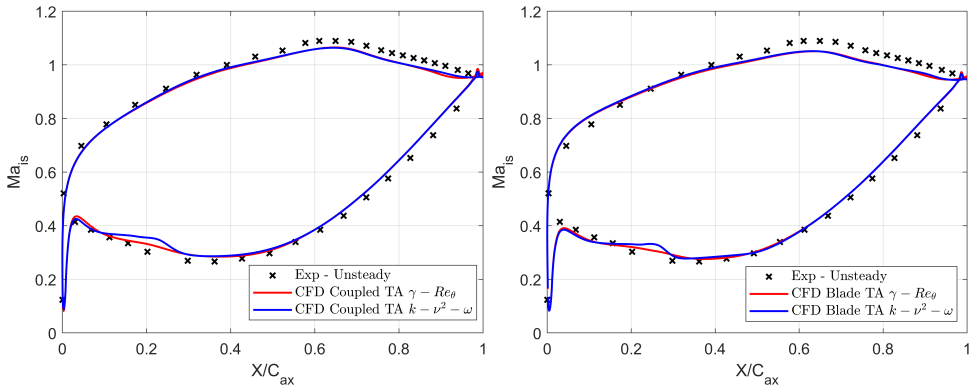

(a) (b)

Fig. B.8 Comparison of loading prediction with $\gamma - \tilde{Re}_{\theta t}$ and $k - \overline{\nu^2} - \omega$: (a) 'Coupled' approach, (b) 'Blade' approach

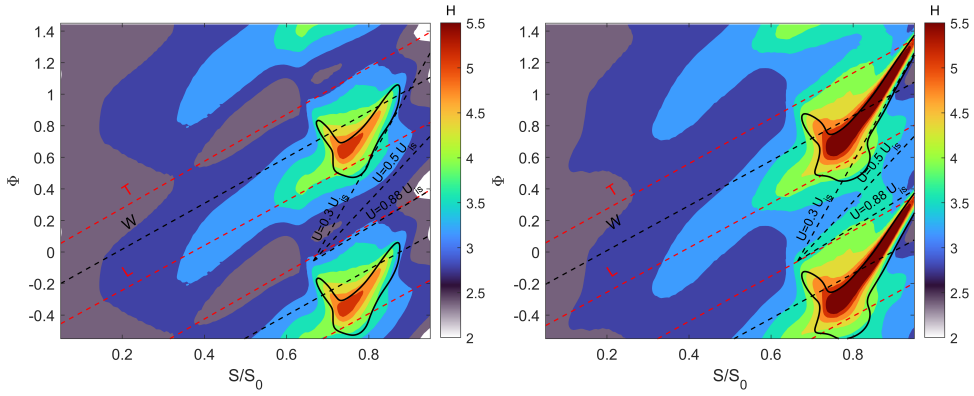

(a) (b)

Fig. B.9 Comparison of boundary layer shape factors prediction with 'Coupled' approach: (a) $\gamma - \tilde{Re}_{\theta t}$, (b) $k - \overline{\nu^2} - \omega$

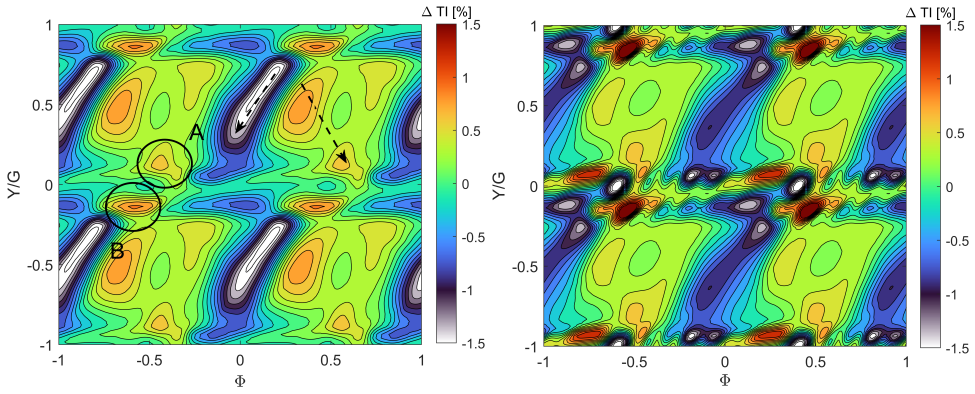

Fig. B.10 Comparison of outlet turbulence intensity prediction with the 'Coupled' approach: (a) $\gamma - \tilde{Re}_{\theta t}$, (b) $k - \overline{v^2} - \omega$

The turbulence intensity fluctuations at PL06 are shown in Fig. B.10 considering the 'Coupled' approach. The predictions of the $\gamma - \tilde{Re}_{\theta t}$ have been discussed in Chapter 4, showing how the model was in fair agreement with the experimental measurements. On the other hand, the $k - \overline{v^2} - \omega$ yields a periodic pattern of small structures indicating the breakdown of the blade's wake. This is induced by the intermittent separation over the SS. When separated boundary layer extends to the TE, the blade's wake is thickened and starts a weak, large scale oscillation. It is latter stabilized by the passage of the bar's wake which promotes the transition of the boundary layer and a fully attached flow at the TE of the blade. It must be noted that the process is periodic and triggered by the wake/boundary layer interaction rather than a local breakdown of the blade's wake due to its turbulent nature. For this reason, the behavior is not adduced to a 'scale-resolving' property of the simulation, rather to an intermittent effect fostered by the inherent unsteadiness of the flow field. The same behavior occurs in the case of the 'Blade' approach which is not shown for brevity. Hence, the considerations made regarding the 'Coupled' approach are still valid.

Eventually, the time-averaged energy loss coefficient distributions are compared in Fig. B.11. Both for the 'Coupled' approach and the 'Blade' approach, the $k - \overline{v^2} - \omega$ yields a lower loss level compared to the $\gamma - \tilde{Re}_{\theta t}$. This is not in accordance with the steady simulations, where it was shown that the intermittency based model generally yields a lower total pressure deficit in the center of the wake, while retaining a similar wake width. This is in accordance with the breakdown

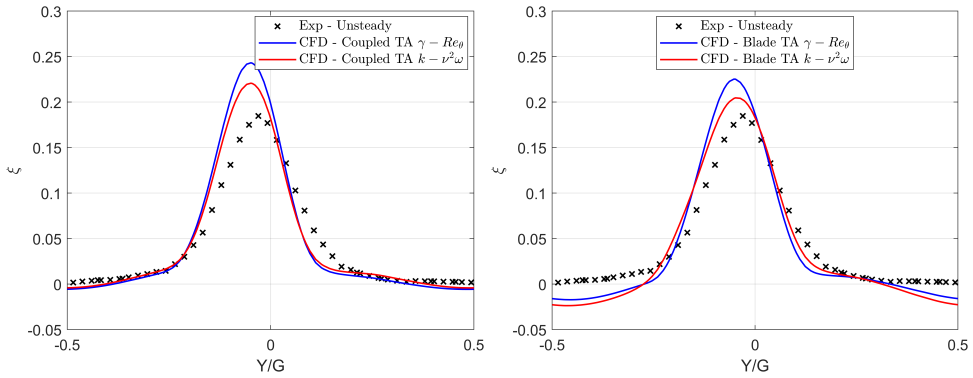

(a) (b)

Fig. B.11 Comparison of outlet energy loss coefficient with $\gamma - \tilde{Re}_{\theta t}$ and $k - \overline{v^2} - \omega$: (a) 'Coupled' approach, (b) 'Blade' approach

of the blade's wake which is present in the $k - \overline{v^2} - \omega$ simulations, while it is not present in the $\gamma - \tilde{Re}_{\theta t}$ simulations. The breakdown introduces a further level of unsteadiness in the simulation, which promotes the mixing of the wake with the free-stream flow, reducing the total pressure deficit in the wake center. The wake width predicted using the two models is similar, while negligible differences are present in the loss level in the free-stream region.

Appendix C

Implemented turbulence models

C.1 k-ω Shear Stress Transport by Menter

The first model implemented in the paper is the traditional k-ω Shear Stress Transport model by Menter [111]. The turbulent behavior of the flow is addressed by using the Boussinesq approximation, which relates turbulent stresses with the strain of the of mean flow field. With respect to common k-ω based turbulence model, the SST introduced by Menter retains good prediction in wall-bounded flows, while a blend to a k-ε-like behavior is provided for the free-stream region. Compared to the original model k-ω proposed by Wilcox ([112]), the SST retains lower sensitivity to inlet conditions.

The two transported variables account for the turbulence kinetic energy and the specific dissipation rate (which is a length scale computing variable). In their compressible form, the equations can be written as:

$$\frac{\partial(\rho k)}{\partial t}\frac{\partial(\rho U_j k)}{\partial x_j} = P_k - D_k + \frac{\partial}{\partial x_j}\left[(\nu + \mu_t \sigma_k)\frac{\partial k}{\partial x_j}\right] \tag{C.1}$$

$$\frac{\partial(\rho \omega)}{\partial t}\frac{\partial(\rho U_j \omega)}{\partial x_j} = P_\omega - D_\omega + \frac{\partial}{\partial x_j}\left[(\nu + \mu_t \sigma_\omega)\frac{\partial \omega}{\partial x_j}\right] + 2(1-F_1)\frac{\rho \sigma_{\omega 2}}{\omega}\frac{\partial k}{\partial x_j}\frac{\partial \omega}{\partial x_j} \tag{C.2}$$

The production and destruction terms of both equations can be computed as follows:

$$P_k = \tau_{ij}\frac{\partial U_i}{\partial x_j} \quad D_k = \beta^*\rho\omega k \tag{C.3}$$

$$P_\omega = \frac{\gamma}{\nu_t}\tau_{ij}\frac{\partial U_i}{\partial x_j} \quad D_\omega = \beta\rho\omega^2 \tag{C.4}$$

where τ_{ij} is the stress tensor written in compressible form:

$$\tau_{ij} = \mu_T\left(2S_{ij} - \frac{2}{3}\frac{\partial u_k}{\partial x_k}\delta_{ij}\right) - \frac{2}{3}\rho k\delta_{ij} \tag{C.5}$$

The turbulent viscosity is computed as:

$$\mu_t = \frac{\rho a_1 k}{\max(a_1\omega, \Omega F_2)} \tag{C.6}$$

Eventually, all the constants in the model can be computed as a blending between two values. Subscript '1' will be used to indicate an 'inner' value which is enforced in the near wall region, while subscript '2' will be used to indicate an 'outer' value which is enforced in the far-field. The coupling is enforced via:

$$\Phi = F_1\Phi_1 + (1-F_1)\Phi_2 \tag{C.7}$$

where the blending parameter is:

$$arg_1 = \min\left[\max\left(\frac{\sqrt{k}}{\beta^*\omega y}, \frac{500\nu}{y^2\omega}\right), \frac{4\rho\sigma_{\omega 2}k}{CD_{k\omega}y^2}\right] \quad F_1 = tanh(arg_1^4) \tag{C.8}$$

The remaining parameters are determined as follows:

$$CD_{k\omega} = \max\left(2\rho\sigma_{\omega 2}\frac{1}{\omega}\frac{\partial k}{\partial x_j}\frac{\partial \omega}{\partial x_j}, 10^{-10}\right) \quad arg_2 = \max\left(2\frac{\sqrt{k}}{\beta^*\omega y}, \frac{500\nu}{y^2\omega}\right) \quad F_2 = tanh(arg_2^2) \tag{C.9}$$

The implementation of the model follows the original development proposed by Menter. As a matter of fact, other variants are present in which the production term

σ_{k1}=0.85	$\sigma_{\omega 1}$=0.5	β_1=0.075
σ_{k2}=1.0	$\sigma_{\omega 2}$=0.856	β_2=0.0828
β^*=0.09	κ=0.41	a_1=0.31
γ_1=5/9	γ_2=0.44	

Table C.1 k-ω SST constants

in the ω equation is defined as $P^*_\omega = \frac{\gamma\omega}{k} P_k$. This form stems from the original k-ω model, but is inconsistent with the definition of the turbulent viscosity, even though it appears to be widespread in CFD community ([113]). Moreover, a production limiter is present in the definition of the turbulent kinetic energy to avoid stagnation point anomaly:

$$P^*_k = \min(P_k, 10\beta^*\rho\omega k) \tag{C.10}$$

The inlet boundary conditions are prescribed in terms of turbulence intensity and Integral Length Scale (ILS). The latter is computed as:

$$ILS = \frac{\sqrt{k}}{C_\mu \omega} \tag{C.11}$$

where the constant C_μ takes a standard value equal to 0.09. As far as wall boundary conditions are regarded, homogeneous Dirichlet conditions are specified for the turbulent kinetic energy. Similarly, a Dirichlet condition is specified for ω:

$$\omega_{wall} = 10\frac{6\nu}{\beta_1 y^2} \tag{C.12}$$

All the model coefficients are expressed in Tab. C.1 and are retrieved from [113].

C.2 $k - \overline{v^2} - \omega$ by Lopez and Walters

The transitional model by Lopez and Walters [53] is a relatively new framework in the simulation of transitional boundary layers adopting a RANS closure approach. The model variables account for total fluctuation energy k, small scale, three-dimensional velocity fluctuations $\overline{v^2}$ and a length scale variable ω. The incompressible form of the turbulence model equations is the following:

$$\frac{Dk_T}{Dt} = P_k - D_k - min(\omega k, \omega\overline{v^2}) + \frac{\partial}{\partial x_j}\left[\left(\nu + \frac{\alpha_T}{\sigma_k}\right)\frac{\partial k}{\partial x_j}\right] \tag{C.13}$$

$$\frac{D\overline{v^2}}{Dt} = P_{\overline{v^2}} + R_{BP} + R_{NAT} - \omega v^2 - D_{\overline{v^2}} + \frac{\partial}{\partial x_j}\left[\nu + \frac{\alpha_T}{\sigma_k}\frac{\partial\overline{v^2}}{\partial x_j}\right] \tag{C.14}$$

$$\begin{aligned}\frac{D\omega}{Dt} =& P_\omega + \left(\frac{C_{\omega R}}{f_W} - 1\right)\frac{\omega}{\overline{v^2}}(R_{BP} + R_{NAT}) - C_{\omega 2} f_w^2 \omega^2 + \\ & 2\beta^*(1 - F_1^*)\sigma_2 \frac{1}{\omega}\frac{\partial k}{\partial x_j}\frac{\partial \omega}{\partial x_j} + \frac{\partial}{\partial x_j}\left[\left(\nu + \frac{\alpha}{\sigma_\omega}\right)\frac{\partial\omega}{\partial x_j}\right]\end{aligned} \tag{C.15}$$

The production terms are defined as:

$$P_k = \nu_T S^2 \quad P_{\overline{v^2}} = \nu_{T,s} S^2 \quad P_\omega = \left(C_{\omega_1}\frac{\omega}{\overline{v^2}}\nu_{T,s}\right)S^2 \tag{C.16}$$

where ν_T is the turbulent viscosity. It is computed as the sum of a small scale ($\nu_{T,s}$) and a large scale ($\nu_{T,l}$) contribution:

$$\nu = \nu_{T,s} + \nu_{T,l} \tag{C.17}$$

The small scale contribution is defined as:

$$\nu_{T,s} = f_v\, f_{INT}\, C_\mu \sqrt{v_s^2}\lambda_{eff} \quad \overline{v^2}_s = f_{ss} f_W \overline{v^2} \tag{C.18}$$

The effective turbulent length scale is limited by the wall distance, in order to avoid excessive turbulence production in wall distant regions of the flow:

$$\lambda_{eff} = \min(C_\lambda d, \lambda_T) \quad \lambda_T = \frac{\sqrt{\overline{v^2}_s}}{\omega} \quad f_W = \left(\frac{\lambda_{eff}}{\lambda_T}\right)^{2/3} \tag{C.19}$$

Viscous effects due to wall vicinity are introduced through f_v:

$$f_v = 1 - \exp\left(-\frac{\sqrt{Re_T}}{A_v}\right) \quad Re_T = \frac{f_W^2\overline{v^2}}{\nu\omega} \tag{C.20}$$

while f_{ss} introduces the shear sheltering

$$f_{ss} = \exp\left[-\left(\frac{C_{SS}\nu\Omega}{\overline{v^2}}\right)^2\right] \tag{C.21}$$

The model parameter C_μ allows to introduce a realizability constraint, while f_{INT} is an intermittency based damping term:

$$C_\mu = \frac{1}{A_0 + A_S\left(\frac{S}{\omega}\right)} \quad f_{INT} = \min\left(\frac{\overline{v^2}}{C_{INT}k}, 1\right) \tag{C.22}$$

The large scale turbulent viscosity ($\nu_{T,l}$) is defined as:

$$\begin{aligned}\nu_{T,l} = \min\Big\{ & f_{\tau,l}C_{11}\left(\frac{\Omega\lambda_{eff}^2}{\nu}\right)\sqrt{v_l^2}\lambda_{eff} + \\ & \beta_{TS}C_{12}\left(\frac{\Omega d_{eff}^2}{\nu}\right)d_{eff}^2\Omega, 0.5\frac{0.5(k-\overline{v^2}_s)}{S}\Big\}\end{aligned} \tag{C.23}$$

where the *min* function again imposes a realizability constraint for the full Reynolds stresses. The parameter $\overline{v^2}_l$ represents large scale velocity fluctuations::

$$\overline{v^2}_l = \overline{v^2} - \overline{v^2}_s \tag{C.24}$$

while d_{eff} is intended to limit transitional fluctuations away from the walls.

$$d_{eff} = \frac{\lambda_{eff}}{C_\lambda} \tag{C.25}$$

In the large scale turbulent viscosity, other terms are computed as:

$$f_{\tau,l} = 1 - \exp\left(C_{\tau,l}\frac{v_l^2}{\lambda_{eff}^2\Omega^2}\right) \tag{C.26}$$

$$\beta_{TS} = 1 - \exp\left(1 - \frac{\max\left(Re_\Omega - C_{TS,crit}, 0\right)^2}{A_{TS}}\right) \tag{C.27}$$

$$Re_\Omega = \frac{d^2\Omega}{\nu} \tag{C.28}$$

The destruction terms which are also responsible for driving velocity fluctuations to 0 in the near-wall region are defined as:

$$D_k = 2\nu \frac{\partial\sqrt{k}}{\partial x_j}\frac{\partial\sqrt{k}}{\partial x_j} \qquad D_{\overline{v^2}} = 2\nu \frac{\partial\sqrt{\overline{v^2}}}{\partial x_j}\frac{\partial\sqrt{\overline{v^2}}}{\partial x_j} \tag{C.29}$$

The diffusivity α_T used for the computation of viscous terms in the equation is defined as:

$$\alpha_T = f_v\, \beta^* \sqrt{\overline{v^2}_s}\, \lambda_{eff} \tag{C.30}$$

The blending function in the cross diffusion term is computed as

$$F_1^* = 1 - [(1-F_1) f_{SS}] \tag{C.31}$$

$$F_1 = \tanh\left\{\left\{\min\left[\max\left(\frac{\overline{v^2}}{\omega d}, \frac{500\nu\beta^*}{\omega d^2}\right)\right]\right\}\right\} \tag{C.32}$$

$$CD_{k\omega} = \max\left(2\rho\sigma_{\omega 2}\frac{1}{\omega}\frac{\partial k}{\partial x_h}\frac{\partial \omega}{\partial x_j}, 10^{-10}\right) \tag{C.33}$$

The transition process is activated using R_{NAT} and R_{BP}, which are responsible for the production of small scale velocity fluctuations ($\overline{v^2}$), mimicking the effect of natural and by-pass transition, respectively.

$$R_{NAT} = C_{R,NAT}\ \beta_{NAT}\ (k - \overline{v^2})\ \Omega \tag{C.34}$$

$$R_{BP} = C_R\ \beta_{BP}\ (k - \overline{v^2})\ \omega / f_W \tag{C.35}$$

The transition terms are sensitive to characteristic time-scales, which are activated when turbulence production scale is smaller than viscous diffusion scale by means of the model parameters β_{NAT} and β_{BP}:

$$\beta_{NAT} = 1 - \exp\left(-\frac{\phi_{NAT}}{A_{NAT}}\right) \quad \beta_{BP} = 1 - \exp\left(-\frac{\phi_{BP}}{A_{BP}}\right) \tag{C.36}$$

$$\phi_{NAT} = \max\left[\left(Re_\Omega - \frac{C_{NAT,crit}}{f_{NAT,crit}}\right), 0\right] \tag{C.37}$$

$$f_{NAT,crit} = 1 - \exp\left(-C_{NC}\frac{\sqrt{k}d}{\nu}\right) \tag{C.38}$$

A_0=4.04	C_{INT}=0.95	$C_{\omega 1}$=0.44
A_s=2.12	$C_{TS,crit}$=1000	$C_{\omega 2}$=0.92
A_ν=3.8	$C_{R,NAT}$=0.02	$C_{\omega R}$=1.15
A_{BP}=0.2	C_{l1}=3.4*10$^-$6	C_λ=2.495
A_{NAT}=200	C_{l2}=1.0*10$^-$10	β^*=0.09
A_{TS}=200	C_R=0.32	Pr_θ=0.85
$C_{BP,crit}$=1.5	$C_{\alpha,\theta}$=0.035	σ_k=1
C_{NC}=0.1	C_{SS}=3.0	σ_ω=1.17
$C_{NAT,crit}$=1450	$C_{\tau,l}$=4360	$\sigma_{\omega 2}$=1.856

Table C.2 Transition model coefficients

$$\phi_{BP} = \max\left[\left(\frac{\overline{v^2}}{\nu\Omega} - C_{BP,crit}\right), 0\right] \tag{C.39}$$

The turbulent heat transfer is instead considered using a turbulent diffusivity α_Θ

$$\overline{u_i T} = \alpha_\Theta \frac{\partial T}{\partial x_i} \tag{C.40}$$

$$\alpha_\Theta = f_W \left(\frac{\overline{v^2}}{k}\right) \frac{\nu_{T,s}}{Pr_\theta} + (1 - f_W) C_{\alpha,\theta} \sqrt{\overline{v^2}} \lambda_{eff} \tag{C.41}$$

The turbulence model is implemented in its compressible form. To this end, equations are modified by transporting $\rho k, \rho\overline{v^2}$ and $\rho\omega$ and multiplying the right-hand side of the equations by the local flow density. Moreover, the compressible version of the Reynolds stress tensor is adopted:

$$\tau_{ij} = \mu_T \left(2S_{ij} - \frac{2}{3}\frac{\partial u_k}{\partial x_k}\delta_{ij}\right) - \frac{2}{3}\rho k \delta_{ij} \tag{C.42}$$

C.3 $\gamma - \tilde{Re}_{\theta t}$ by Langtry and Menter

The $\gamma - \tilde{Re}_{\theta t}$ by Langtry and Menter [88] attempts to model boundary layer transition using the concept of intermittency, while transition is controlled by an additional transported variable $\tilde{Re}_{\theta t}$, which indicates the momentum thickness Re at the transition onset. The idea behind the development of the model, is to relate the momentum thickness of the boundary layer, which needs the integration of the boundary layer

profile, with a local quantity. This is done by noting that for a Blasius boundary layer, the momentum thickness Re and the strain rate Re are proportional:

$$Re_\theta = \frac{\rho \theta U}{\mu} \quad Re_v = \frac{\rho S y^2}{\mu} \quad Re_\theta = \frac{\max(Re_v)}{C} \tag{C.43}$$

where C is a constant varying with the boundary layer shape factor. A constant value is chosen by the authors equal to 2.193.

The additional equation for the intermittency variable is the following:

$$\frac{\partial \rho \gamma}{\partial t} + \frac{\partial (\rho U_i \gamma)}{\partial x_i} = P_\gamma - E_\gamma + \frac{\partial}{\partial x_j}\left[\left(\mu + \frac{\mu_T}{\sigma_f}\right)\frac{\partial \gamma}{\partial x_j}\right] \tag{C.44}$$

The production and destruction terms are respectively:

$$P_\gamma = F_{length} c_{a1} \rho S [\gamma F_{onset}]^{0.5} (1 - c_{e1}\gamma) \quad E_\gamma = F_{turb} c_{a2} \rho \Omega \gamma (c_{e2} - 1\gamma) \tag{C.45}$$

where S and Ω are the strain and the vorticity magnitude of the flow, respectively. F_{onset} controls the location at the transition onset and can be computed as:

$$F_{onset1} = \frac{Re_v}{2.193 Re_{\theta c}} \quad F_{onset2} = \min(\max(F_{onset1}, F_{onset1}^4), 2.0) \tag{C.46}$$

$$F_{onset3} = \max(1 - \left(\frac{R_T}{2.5}\right)^3, 0) \quad F_{onset} = \max(F_{onset2} - F_{onset3}, 0.0) \tag{C.47}$$

where R_T is the turbulence Reynolds number: $R_T = \frac{\rho k}{\mu \omega}$. The quantity $Re_{\theta c}$ is the critical Reynolds number. It defines the location where the intermittency starts increasing in the boundary layer, and can be computed via the following correlation in terms of $\tilde{Re}_{\theta t}$:

$$Re_{\theta c} = \begin{cases} [\tilde{Re}_{\theta t} - (396.036 \times 10^{-2} - 120.656 \times 10^{-4}\tilde{Re}_{\theta t} + 868.230 \times 10^{-6}\tilde{Re}_{\theta t}^2 + \\ -696.506 \times 10^{-9}\tilde{Re}_{\theta t}^3 + 174.105 \times 10^{-12}\tilde{Re}_{\theta t}^4)] \ \tilde{Re}_{\theta t} \leq 1870 \\ \left[\tilde{Re}_{\theta t} - (593.11 + (\tilde{Re}_{\theta t} - 1870.0) \times 0.482)\right] \ \tilde{Re}_{\theta t} > 1870 \end{cases} \tag{C.48}$$

The length of transition is instead controlled y means of F_{length}. The quantity is obtained via a correlation:

$$F_{length} = \begin{cases} 398.189 \times 10^{-1} - 119.270 \times 10^{-4}\tilde{Re}_{\theta t} - 132.567 \times 10^{-6}\tilde{Re}_{\theta t}^2 \ \tilde{Re}_{\theta t} < 400 \\ 263.404 - 123.939 \times 10^{-2}\tilde{Re}_{\theta t} + 194.548 \times 10^{-5}\tilde{Re}_{\theta t}^2 + \\ -101.685 \times 10^{-8}\tilde{Re}_{\theta t}^3 \ 400 \leq \tilde{Re}_{\theta t} < 596 \\ 0.5 - (\tilde{Re}_{\theta t} - 596.0) \times 3.0 \times 10^{-4} \ 596 \leq \tilde{Re}_{\theta t} < 1200 \\ 0.3188 \ 1200 \leq \tilde{Re}_{\theta t} \end{cases} \tag{C.49}$$

A correction to the value of F_{length} is also implemented in order to avoid fast transition in the case of high Reynolds number flows, where the production term of the intermittency equation is activated due to the low values of $\tilde{Re}_{\theta t}$ right after transition. The correction is based on forcing a maximum value of F_{length} inside the viscous sublayer via:

$$F_{length} = (1 - F_{sublayer})F_{length} + 40F_{sublayer} \quad F_{sublayer} = e^{-(\frac{R_\omega}{0.4})^2} \tag{C.50}$$

where $R_\omega = \frac{\rho y^2 \omega}{500\mu}$.

The transport equation for the Reynolds at the transition onset is the following:

$$\frac{\partial \rho \tilde{Re}_{\theta t}}{\partial t} + \frac{\partial (\rho U_i \tilde{Re}_{\theta t})}{\partial x_i} = P_{\theta t} + \frac{\partial}{\partial x_j}\left[\sigma_{\theta t}(\mu + \mu_T)\frac{\partial \tilde{Re}_{\theta t}}{\partial x_j}\right] \tag{C.51}$$

where $P_{\theta t}$ is the production term computed as:

$$P_{\theta t} = c_{\theta t}\frac{\rho}{t}(Re_{\theta t} - \tilde{Re}_{\theta t})(1.0 - F_{\theta t}) \tag{C.52}$$

with t as a time scale ($t = \frac{500\mu}{\rho U^2}$). The term $F_{\theta t}$ deactivates the production term in the boundary layer:

$$F_{\theta t} = \min(\max(F_{wake} e^{-\frac{y}{\delta}^4}, 1.0 - \left(\frac{\gamma 1/c_{e2}}{1.0 - 1/c_{e2}}\right)^2), 1.0) \tag{C.53}$$

while F_{wake} is necessary to deactivate the blending function in wake regions. This term can be computed as

$$\Theta_{BL} = \frac{\tilde{Re}_{\theta t}\mu}{\rho U} \quad \delta_{BL} = 7.5\Theta_{BL} \quad \delta = \frac{500\Omega y}{U}\delta_{BL} \tag{C.54}$$

$$Re_{\omega} = \frac{\rho \omega y^2}{\mu} \quad F_{wake} = e^{-(\frac{Re_{\omega}}{10^5})^2} \tag{C.55}$$

The last term to be defined to fully close the set of equations is $Re_{\theta t}$ which is not to be confused with the transported variable. This last term is defined via correlations. The original one proposed by the authors of the transition model is the following:

$$Re_{\theta t} = \begin{cases} \left(1173.51 - 589.428Tu + \frac{0.2196}{Tu^2}\right) F(\lambda_\theta) \; Tu \leq 1.3 \\ 331.50\,(Tu - 005658)^{-0.671} F(\lambda_\theta) \; Tu > 1.3 \end{cases} \tag{C.56}$$

$F(\lambda_\theta$ introduces the effect of streamwise acceleration in the transition process. Another correlation is defined to determine its value:

$$F(\lambda_\theta) = \begin{cases} 1.0 - \left(-12.986\lambda_\theta - 123.66\lambda_\theta^2 - 405.689\lambda_\theta^3\right) e^{-(Tu/1.5)^{1.5}} \; \lambda_\theta \leq 0.0 \\ 1 + 0.275\left(1.0 - e^{-35.0\lambda_\theta}\right) e^{-Tu/0.5} \; \lambda_\theta > 0.0 \end{cases} \tag{C.57}$$

where the stramwise acceleration parameter λ_θ is defined as $\lambda_\theta = \frac{\rho\theta^2}{\mu}\frac{dU}{dS}$. The stremwise acceleration is computed as:

$$\frac{dU}{dS} = \left[(u/U)\frac{dU}{dx} + (v/U)\frac{dU}{dy} + (w/U)\frac{dU}{dz}\right] \tag{C.58}$$

The momentum thickness θ is present both in the definition of λ_θ and in the definition of $Re_{\theta t} = \frac{\rho U \theta}{\mu}$. For this reason, the equation for $Re_{\theta t}$ is solved iteratively. The first guess solution comes from imposing a zero-pressure gradient value for λ_θ. In the present implementation, the iterative procedure is based on a fixed point iteration.

The transition model interacts with the fully turbulent model, modifying the production and destruction terms in the transport equation for the turbulent kinetic energy, and in the definition of the blending function for the computation of the turbulent viscosity. More in detail, the original production and destruction terms P_k and D_k are substituted with $\tilde{P}_k$ and $\tilde{D}_k$ where:

$$\tilde{P}_k = \gamma_{eff} P_k \quad \tilde{D}_k = \min(\max(\gamma_{eff}, 0.1)1.0) D_k \tag{C.59}$$

The parameter γ_{eff} is an effective intermittency value, which is allowed to grow beyond 1.0. The reason behind this nonphysical (but wanted) behavior is that the transition model cannot properly model the fast turbulence production occurring in separated shear layers. This causes the model to overpredict the reattachment length and in general the size of the bubble This deficiency is overcome by substituting the flow intermittency γ in the production term of k, with the effective intermittency γ_{eff}. The latter is determined as the maximum value between γ and a separation intermittency γ_{sep} which is defined as:

$$\gamma_{sep} = \min\left(s_1 \max\left[0, (\frac{Re_v}{3.235 Re_{\theta c}}) - 1\right] F_{reattach}, 2\right) F_{\theta t} \tag{C.60}$$

The constant controlling the relationship between Re_v and $Re_{\theta c}$ is taken from a Blasius boundary layer, at the separation point, for a shape factor equal to 3.5. $F_{reattach}$ is instead defined as: $F_{reattach} = e^{-(\frac{R_T}{20})^4}$

An additional modification of the fully turbulent model concerns the blending function F_1 which is computed as:

$$R_y = \frac{\rho y \sqrt{k}}{\mu} \quad F_3 = e^{-(\frac{R_y}{120})^8} \quad \tilde{F}_1 = \max(F_1, F_3) \tag{C.61}$$

The inlet boundary conditions are prescribed assuming fully turbulent free-stream conditions, hence setting the intermittency equal to 1 and computing the inlet value

c_{e1}=1.0	c_{a1}=2.0	c_{e2}=50.0	c_{a2}=0.06
σ_f=1.0	$c_{\theta t}$=0.03	$\sigma_{\theta t}$=2.0	s_1=2.0

Table C.3 $\gamma - \tilde{Re}_{\theta t}$ model coefficients

of $\tilde{Re}_{\theta t}$ from the inlet turbulence intensity and assuming no acceleration ($\frac{dU}{dS} = 0$). Homogeneous Neumann conditions are prescribed at the wall.

The model coefficients are summarized in Tab. C.3.